Deuteration of Complex Organic Molecules in the Early Phases of Star Formation

Wiebke Riedel

München 2025

Deuteration of Complex Organic Molecules in the Early Phases of Star Formation

Wiebke Riedel

Dissertation
an der Fakultät für Physik
der Ludwig–Maximilians–Universität
München

vorgelegt von
Wiebke Riedel
aus Großenstein, Deutschland

München, den 02.12.2025

Erstgutachter: Prof. Dr. Paola Caselli
Zweitgutachter: Prof. Dr. Barbara Ercolano
Tag der mündlichen Prüfung: 12.01.2026

Contents

List of Figures

List of Tables

Zusammenfassung

Woher kommen wir? Wie entstand das Leben? Das sind Fragen, die sich die Menschheit schon immer gestellt hat. Zunächst wurden sie vor allem durch Mythologie und Religion beantwortet. Mit den Fortschritten der Naturwissenschaften in den letzten Jahrhunderten entstanden jedoch immer mehr Erkenntnisse aus den Bereichen Astronomie, Chemie und Biologie. Astrochemie und Astrobiologie liegen genau an der Schnittstelle all dieser Disziplinen.

Komplexe organische Moleküle, die aus sechs oder mehr Atomen bestehen, von denen mindestens eines ein Kohlenstoffatom ist, gelten allgemein als Vorstufe biologisch relevanter Moleküle wie z.B. Eiweiße, Fette und Aminosäuren. Früher glaubte man, dass die kalten Bedingungen, die in der Phase des prästellaren Kerns, dem frühesten Stadium der Sternentstehung, herrschen, den Grad der chemischen Komplexität auf einfachere Molekülarten beschränken würden. In der letzten Dekade meldeten jedoch mehrere Beobachtungsstudien die Existenz sauerstoffhaltiger komplexer organischer Moleküle in mehreren prästellaren Kernen.

Heutzutage ist allgemein anerkannt, dass Methanol, der einfachste Vertreter der sauerstoffhaltigen komplexen organischen Moleküle, fast ausschließlich durch aufeinanderfolgende Hydrierung von CO auf der Oberfläche von Staubkörnern entsteht. Die Entstehungsmechanismen der meisten anderen komplexen organischen Moleküle sind jedoch nach wie vor umstritten. Entstehen sie auf der Oberfläche von Staubkörnern oder in der Gasphase? Wenn sie auf Staubkörnern entstehen, wie sind dann Reaktionen zwischen zwei schweren, unbeweglichen Reaktionspartnern in den extrem niedrigen Temperaturen von prästellaren Kernen möglich, und durch welchen Mechanismus werden sie in die Gasphase freigesetzt, wo sie dann beobachtbar werden? Die in dieser Arbeit vorgestellten Projekte befassen sich mit all diesen Fragen und versuchen, durch die Verknüpfung mit dem Thema Deuterierung bessere Einschränkungen zu liefern.

Im ersten Projekt verwende ich den Gas-Staub-Chemiecode *pyRate*, um Säulendichteprofile für Methanol (CH_3OH) und sein einfach deuteriertes Isotopolog (CH_2DOH) des prototypischen prästellaren Kerns L1544 zu berechnen. Ich füge eine experimentbasierte Behandlung der reaktiven Desorption in *pyRate* hinzu, die eine individuelle reaktive Desorptionseffizienz ermittelt, welche von der Reaktionsenthalpie und der Oberflächenbedeckung des Staubkorns abhängig ist. Diese Arbeit schlägt auch eine Erweiterung des bestehenden Mechanismus vor, um die massenabhängige Aufteilung der Reaktionsenthalpie für eine Zwei-Produkt-Reaktion zu berücksichtigen. Zusätzlich werden mehrere chemische und physikalische Parameter getestet.

Im zweiten Projekt habe ich *pyRate* mit mehreren nichtdiffusiven Reaktionsmechanismen aktualisiert, die auf der (geringen) Wahrscheinlichkeit beruhen, dass beide Reaktionspartner in unmittelbarer Nähe zueinander gebildet werden. Dazu gehören Eley-Rideal-Reaktionen, photo-

dissoziationsinduzierte Reaktionen und Drei-Körper-Reaktionen. Zunächst untersuche ich ihren Einfluss auf die Bildung und Deuterierung von Methanol.

Im dritten Projekt erweitere ich jedoch das chemische Netzwerk von Molekülen mit sieben Atomen auf Moleküle mit neun Atomen, wodurch die Bildung und Deuterierung größerer komplexer organischer Moleküle berechnet werden kann. Hier konzentriere ich mich auf drei sauerstoffhaltige komplexe organische Moleküle: Acetaldehyd (CH_3CHO), Methylformiat (CH_3OCHO) und Glycoaldehyd (CH_2OCHO), für die Beobachtungen mehrerer deuterierter Isotopologe aus dem protostellaren Stadium vorliegen.

Summary

Where do we come from? How was life created? Those are questions humankind has always wondered. First, they were mostly answered by mythology and religion. With the advancements of the natural sciences in the last centuries, however, more and more insights from the fields of astronomy, chemistry and biology emerged. Astrochemistry and astrobiology are right at the intersection of all of those disciplines.

Complex organic molecules (COMs), molecules made up of six or more atoms, at least one of which is a carbon atom, are commonly considered to be the precursors of biologically relevant molecules as e.g. proteins, lipids and amino acids. It was previously believed that the cold conditions prevailing in the pre-stellar core phase, the earliest stage of star formation, would restrict the degree of chemical complexity to simpler molecular species. However, in the last decade, several observational surveys reported the existence of O-bearing COMs in multiple pre-stellar cores

Nowadays, it is generally accepted that methanol, the simplest of the O-bearing COMs, is produced almost exclusively by successive hydrogenation of CO on the surface of dust grains. The formation mechanisms of most other COMs, however, still remain a field of open debate. Are they formed on the surface of dust grains or in the gas phase? If they formed on grains, how are reactions between two heavy, immobile reaction partners in the extremely low temperatures of pre-stellar cores possible and by which mechanism are they released into the gas phase, where they become observable? The projects presented in this thesis touch all of these questions and try to provide better constraints by linking them to the topic of deuteration.

In the first project, I use the gas-grain chemical code *pyRate* to derive column density profiles for methanol (CH_3OH) and its singly deuterated isotopologue (CH_2DOH) of the prototypical pre-stellar core L1544. I introduce an experiment-based treatment of reactive desorption into *pyRate*, that derives an individual reactive desorption efficiency, depending on the reaction enthalpy and surface coverage of the dust grain. This work proposes an extension of the existing recipe to consider the mass-dependent partitioning of the reaction enthalpy for a two-product reaction.

In the second project, I update *pyRate* with multiple non-diffusive reaction mechanisms, that rely on the (small) probability that both reaction partners are formed in close proximity to each other. These include Eley-Rideal reactions, photodissociation-induced reactions and three-body reactions. Initially, I investigate their influence on the formation and deuteration of methanol.

In the third project, however, I extend the chemical network from species with seven atoms to nine atoms, making it possible to calculate the formation and deuteration of larger COMs. Here, I focus on three O-bearing COMs: acetaldehyde (CH_3CHO), methyl formate (CH_3OCHO) and

glycoaldehyde (CH_2OCHO), for which observational constraints of multiple deuterated isotopologues from the protostellar stage exist.

Chapter 1

Introduction

Although molecules have been detected in a variety of astronomical objects, including the envelopes surrounding evolved stars and even other galaxies, astrochemistry is strongly linked with the field of star- and planet formation. The evolution of a cold, dense cloud into a main-sequence star with its own planetary system is also accompanied by an increasing chemical complexity of its molecular content, which originated organic life at least one occasion - in our own Solar System.

This introduction presents the main concepts of star formation and the methods used in the simulation of chemical processes in the early phases of the formation process. Section 1.1 introduces the field of astrochemistry. Section 1.2, which is mostly based on Stahler & Palla (2004) and Draine (2011), gives a broad overview about the interstellar medium, including its gas- and dust content. Section 1.3 describes the phases of star formation with particular emphasis on the early phases of low-mass star formation, as they are the most relevant for this thesis. This section is mainly based on Stahler & Palla (2004). Section 1.4, presents the physical and chemical structure of pre-stellar cores, and lays out important chemical processes in detail, which is mainly based on Yamamoto (2016). Finally, Section 1.5 describes the methods used in a rate-equation astrochemical code, mainly based on Sipilä et al. (2015a) and Bovino & Grassi (2024).

1.1 Astrochemistry

Astrochemistry is a branch of astronomy that studies the formation and destruction of molecules - their chemistry - in the extreme conditions of the interstellar medium. Since the discovery of the first molecule, methylidyne (CH; McKellar 1940), in 1940, over 340 molecules have been detected in the interstellar medium or circumstellar shells (McGuire 2022, [1]). Most of the observed molecules consist of two to twelve atoms. However, even some larger molecules,

[1] https://cdms.astro.uni-koeln.de/classic/molecules

e.g. polycyclic aromatic hydrocarbons[2] or fullerenes[3], have been found. The more complex molecules with six atoms or more are exclusively of organic nature, containing at least one carbon atom, which earned them the term: *complex organic molecules (COMs)* (Herbst & van Dishoeck 2009) or *interstellar complex organic molecules (iCOMs)* (Ceccarelli et al. 2017).

Chemistry in space works surprisingly similar as on Earth with a few exceptions that are caused by the extreme physical conditions, mainly the low densites and temperatures. Typical densities in pre-stellar cores, the main environment investigated in this thesis, range from 1×10^4 to $10^7\,\mathrm{cm}^{-3}$, which is orders of magnitude lower than the densities that can be realised in the ultra-high vacuum chambers of astrochemical laboratories. In contrast to Earth, due to the low densities, the probability of a three-body reaction in the gas phase is negligible. They only become significant for densities above $10^{13}\,\mathrm{cm}^{-3}$ that exist(ed) in the inner midplane of protoplanetary disks, the atmospheres of AGB stars or the early universe (van Dishoeck 2014). An exception are reactions involving dust grains. The low densities and temperatures also prolong the lifetime of chemically reactive species considerably, which is why free radicals, molecular ions and highly unsaturated hydrocarbon molecules play an important role in the chemistry of pre-stellar cores (Yamamoto 2016). The typical gas- and dust temperatures are extremely low, ranging between 7 - 15 K (Caselli & Ceccarelli 2012), which causes endothermic reactions to be inefficient. Astrochemistry is, therefore, ruled almost exclusively by exothermic reactions.

The field of astrochemistry is a highly interdisciplinary field, which profits from the combined work of three large subfields: observations, theoretical models and laboratory (Öberg & Bergin 2021). At the heart of astronomy, and also astrochemistry, are certainly observations in several parts of the electromagnetic spectrum, conducted by outstanding telescope facilities, both ground-based and spaced-based. In the observation of cold sources, rotational or ro-vibrational transitions play a prominent role, as their energies are typically sufficiently low to be excited even at $T \leq 20\,\mathrm{K}$, causing them to emit at submillimeter, millimeter and radio wavelengths, where they are observable by ground-based telescopes (e.g. ALMA[4] , IRAM[4],..). Observations of light hydrides, as e.g. HD and H_2O, have to be performed from space (e.g. HST[4]) or at very high altitudes (SOFIA[4]), as the far-infrared wavelengths are blocked by the absorption of atmospheric gases. With the launch of JWST[4], operating in the optical and infrared regime, interest in the observations of interstellar ices has been renewed and delivered interesting new puzzle pieces from the solid state (e.g. McClure et al. 2023, Rocha et al. 2024). In addition to remote observations, the relative closeness of our own solar system allowed for a multitude of missions to other planets, moons and asteroids, even with the possibility of sample returns, that can be

[2]The term polycyclic aromatic hydrocarbons, typically abbreviated as PAHs, summarizes organic molecules, that consist of multiple fused aromatic rings. An aromatic molecule is a planar ring molecule, that has $4n+2\ \pi$ electrons, with n being a non negative integer value.

[3]Fullerenes are carbon allotropes: molecules solely consisting of carbon atoms. They are connected by single or double bonds that form a (partially) closed mesh. They exist in several shapes e.g. spheres, ellipsoids or tubes. The most famous representative is the buckminsterfullerene C_{60}.

[4]Atacama Large Millimeter/submillimeter Array (ALMA), Institut de Radioastronomie Millimétrique (IRAM) 30m telescope & Northern Extended Millimeter Array (NOEMA), Herschel Space Telescope (HST), Stratospheric Observatory for Infrared Astronomy (SOFIA), James Webb Space Telescope (JWST).

analysed in laboratories on Earth.

The prediction, analysis and interpretation of astrochemical observations is aided by a variety of models. To this regard, astrochemical models are an essential tool to understand the details of chemical behaviour in different environments. Distinctly different approaches for chemical models have been developed over the years. Microscopic or kinetic Monte Carlo models trace the motions and reactions of every atom and molecule in the gas phase, on the surface of dust grains and the inside of their icy mantles based on parameterised probabilities. They are typically employed to study small reactive systems, such as the surface formation of methanol (Cuppen et al. 2009), or to analyse laboratory experiments (e.g. Simons et al. 2020). Chemical codes based on rate-equations, on the other hand, only compute average formation and destruction rates for the molecules contained in their chemical networks. This approach, however, makes it feasible to derive time-dependent abundances of hundreds of molecular species, described by thousands of chemical reactions.

All of these efforts, both observational and modelling, would not be possible without the invaluable experimental knowledge obtained by astrochemical laboratories. They provide a multitude of necessary molecular and chemical data, ranging from spectroscopy of gas phase molecules and ices and collisional excitation cross sections, needed for the analysis of observations, to all the parameters included in a chemical model (e.g. rate coefficients of chemical reactions, branching ratios, diffusion, binding and activation energies, etc.). Most of this information is nowadays carefully collected and stored in publicly accessible databases.

1.2 The interstellar medium

1.2.1 Interstellar gas

Only 5% (Planck Collaboration 2014) of the total mass-energy content of our universe resides within baryonic matter, made up of protons and neutrons, while the vast majority lies within dark matter (26.8%) and dark energy (68.2%). Still, the multitude of stars and planets, the structures that enabled organic life at least once, consists mostly of this small fraction. Again, the greater part ($\approx 90\%$) of the baryonic mass in galaxies is incorporated in stars. The remainder ($\approx 10\%$) are in form of a dilute gas, filling the space between the stars, the *interstellar medium* (ISM). The ISM is simultaneously the reservoir of material from which stars form and the medium into which stellar material is ejected during various phases of their lifetimes.

The simplest element, hydrogen (H), is also the most abundant one, making up 90% of the particles, followed by helium (He) with about 8%. Only 2% of the particles consists of elements heavier than helium, customarily summarized as "metals" by astronomers. Nevertheless, they are essential for the formation of the variety of molecules found in the ISM. The most abundant "metals": carbon ($n_C/n_H = 2.7 \times 10^{-4}$), nitrogen ($n_N/n_H = 6.8 \times 10^{-5}$) and oxygen ($n_O/n_H = 4.9 \times 10^{-4}$; Asplund et al. 2009) are crucial components of organic matter. In general, the heavier the element, the lower its abundance. However, the elemental abundances are set by the primordial and stellar nucleosynthesis processes, partially favouring the formation of certain elements, as e.g. iron (Fe), the element with the highest binding energy per nucleon.

The ISM consists of several distinct phases of varying density and temperature, that are roughly in pressure equilibrium with each other (McKee & Ostriker 1977). Hydrogen is present either in molecular (H_2), neutral (H; or HI) or ionized form (H^+, HII). The most extended phase, the hot ionised medium (HIM), was likely created by supernova explosions (SNEs), pushing gas outwards, thereby creating large bubbles, filled with a hot (T=10^6 K), low-density (n = 0.003 cm^{-3}) gas. Although SNEs are rare, due to the low density, their remnants cool only very slowly, leading to a large network of rarefied, interconnecting bubbles. Once the hot regions cooled enough to allow for the recombination of protons and electrons, radiative cooling ensures an efficient cooling process, resulting in the warm neutral medium (WNM), with temperatures of 8000 K and densities around n = 0.3 - 0.5 cm^{-3}. The WNM surrounding OB stars can be ionised by UV photons, creating the warm ionized medium (WIM). The cold neutral medium (CNM) has lower temperatures (T = 80 K) and higher densities (n = 50 cm^{-3}). It will, once compressed and cooled, become the molecular phase, where temperatures (T = 10 K) are sufficiently low and densities ($n \geq 300$ cm^{-3}) are sufficiently high, that star formation can occur.

1.2.2 Interstellar dust

Although interstellar dust grains make up only about 1% of the gas mass, they are an essential component of the interstellar medium, due to their interplay with radiation, gas phase molecules and also each other. They exhibit a distribution of sizes, roughly following the power-law $dn/da \propto a^{-3.5}$, between a minimum size $a_{\rm min}$ and a maximum one $a_{\rm max}$, referred to as the Mathis-Rumpl-Nordsieck (MRN) distribution. Typically used sizes for $a_{\rm min}$ and $a_{\rm max}$ are 0.005 µm and 0.25 µm (Mathis et al. 1977, with a = 0.1 µm being the average size. The grains consist of a core of refractory material, consisting of a mix of amorphous silicates and carbonaceous material, which only vaporizes for temperatures above 1200 K. The core is surrounded by an icy mantle that is usually entirely sublimated at temperatures above 200 K. Heavy elements tend to deplete from the gas phase into the mantle and core. Dust grains lock up almost the entirety of the available silicon (Si), magnesium (Mg) and iron (Fe) and around 70% of the oxygen (O) and 30% of the carbon (C) (van Dishoeck 2014).

Dust grains interact with photons from the interstellar radiation field by absorption and scattering, causing the light from background stars to appear attenuated and redder, an effect termed *extinction*. The structure of the extinction curve, usually expressed as the normalized extinction ratio $A_\lambda/A_{\rm V}$ or the color difference $E(\lambda - V)/E(B - V)$[5] with respect to wavelength λ, reveals detailed information about the dust grain's chemical composition and size distribution. The radiative heating of the grains is (partially) counteracted by radiative cooling in form of a modified black body radiation, providing information about the dust temperature $T_{\rm dust}$ and gas column density $N_{\rm mol}(H_2)$ of the source. Molecules from the gas phase adsorb onto dust grains, where they can diffuse over the surface, undergo chemical reactions and desorb into the gas phase again. In this, the dust grain's role is thought to be not the one of an active catalyst in the chemical

[5]The wavelength dependent extinction A_λ is given by: A_λ=$m(\lambda) - M(\lambda) + 5\log(d)$, where $m(\lambda)$ is the apparent magnitude, $M(\lambda)$ the absolute magnitude and d the distance. The color excess $E(\lambda_1 - \lambda_2)$ is the difference between two extinction values (=$A_{\lambda_1} - A_{\lambda_2}$). The color excess $E(B-V) = (B-V)_{\rm obs} - (B-V)_{\rm int}$ is measured as the difference of the apparent magnitudes $(B - V)_{\rm obs}$ and absolute magnitudes $(B - V)_{\rm int}$ in the B and V photometric band.

sense (van Dishoeck 2014), but of a molecular storage, bringing together reaction partners in close proximity for a prolonged period of time. Finally, the dust grains interact with each other by sticking together, thereby growing in size, coagulating into larger and larger bodies, that will constitute the *planetesimals*, from which planets form.

1.3 The formation of stars

The life of stars, from their birth to their death, can be described as a cycle. One generation of stars influences the properties of the interstellar medium, from which the subsequent generations will form. The cycle starts with the condensation of diffuse material (Figure 1.1, a) into a dense core (b), which collapses gravitationally. Once the central densities and temperatures are sufficiently high, a protostar is formed. Surrounding gas and dust accrete onto the central protostar, causing feedback in the form of bipolar jets and molecular outflows perpendicular to the forming disk (c, Class 0/I). After the dissipation of the envelope, a planet-forming disk is revealed (d, Class II), which will also eventually clear out and reveal planets (e, Class III). Once the star has entered the main-sequence phase, burning hydrogen in its centre, it will remain there for the majority of its life. Finally, the star dies. Depending on its mass, the death of a star happens in distinctly different scenarios. Low-mass ($M \leq 2M_\odot$ [6]) and intermediate-mass stars ($2M_\odot < M < 8M_\odot$) shed their envelope, resulting in planetary nebula, while their cores contract into a white dwarf. Stars with $M > 8M_\odot$ explode in a supernova explosion, while their cores contract either into a neutron star (for stars with $8M_\odot < M < 20M_\odot$) or a black hole (for high-mass stars with $M > 20M_\odot$). The expelled material is fed into the surrounding interstellar medium, enriching it with metals[7]. Eventually the gas will cool and condense again, starting the star formation cycle anew.

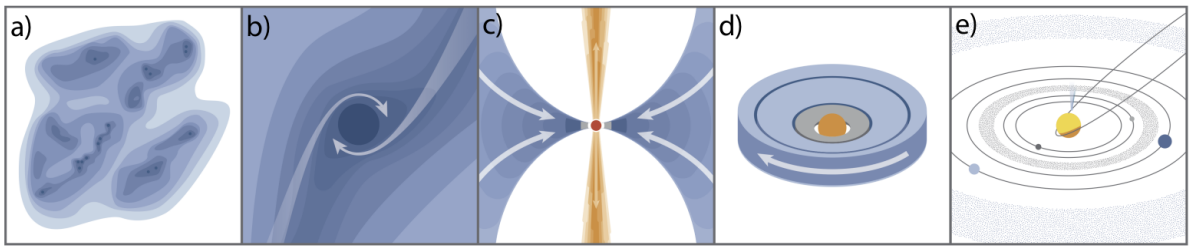

Figure 1.1: Schematic of the early phases of low-mass star and planet formation. Figure published in Öberg & Bergin (2021). Image credit: K.Peek.

This thesis focuses on the formation of low-mass stars, which is due to multiple reasons: (i) The process of star formation strongly favours the formation of stars below $1M_\odot$, as described by the stellar initial mass function, resulting in more low-mass star formation sites in close

[6]The mass of a star is usually expressed in $M_\odot$ (solar masses), being the mass of our own Sun $M = 1.988 \times 10^{30}$ kg
[7]In astronomy, deviating from the chemical definition, metals are defined as elements heavier than helium.

proximity to us, where they can be observed with greater detail. (ii) Their formation and main-sequence life times are much longer than those of their high-mass counterparts, resulting in more observable objects, for which one can also observably differentiate different evolutionary stages. Additionally, (iii) they are typically created from chemically-rich molecular gas, which is sufficiently cool to promote an extremely efficient deuteration process.

The following sub-chapters explain the individual processes of low-mass star formation and their impact on the chemistry of the surrounding gas in more detail.

1.3.1 Low-mass star formation

When seen in visible light, molecular, or dark clouds, appear simply as dark regions in the night sky; entirely devoid of stellar emission. Although they were already noticed by the early astronomers William and Caroline Herschel (Herschel 1785), it has not been until the beginning of the last century that they have been established as optically opaque clouds situated in the interstellar medium of our galaxy (Barnard 1919, Wolf et al. 1923). It took another few decades to realize, that despite being dense and rich enough in dust to achieve a significant obscuration of background stars, they contain very little atomic hydrogen, but most of their gas content is locked in molecular form (e.g. Weinreb et al. 1963, Wilson et al. 1970). In recent years, advancements in the development of modern millimeter and submillimeter telescopes have led to a far more complex understanding of the physics and chemistry of molecular clouds. In particular, it has been established that they consist of a hierarchy of smaller self-similar substructures (Bergin & Tafalla 2007) situated within larger ones, ranging from filaments - elongated overdense structures that span a few parsec in length - to dense cores - only about 0.1 pc in size (Pineda et al. 2023).

1.3.1.1 Stability of the cloud

Most of the phases in the interstellar medium are in a state of pressure equilibrium. The dynamics of molecular clouds, however, are mainly dictated by gravity, causing them to self-gravitate, fragment into smaller structures and eventually collapse. An approximate understanding of the cloud's stability and the conditions of its collapse can be achieved by use of the *virial theorem*. Let us consider a molecular cloud that maintains an equilibrium state solely by gravity and thermal pressure:

$$\frac{1}{2}\frac{\partial^2 I}{\partial t^2} = W + 2U, \tag{1.1}$$

where I is the cloud's moment of inertia, W the gravitational potential energy and U the energy contained in the thermal motion of the gas. While the gravitational potential energy W is negative, generating an attractive force directed towards the center of the cloud, the thermal pressure U is positive, generating repulsive forces that counteract gravity. An equilibrium state, meaning that the cloud remains stable, is realised if $\frac{\partial^2 I}{\partial t^2} = 0$ and consequently $2U = -W$. In case $2U < -W$, the cloud will contract and if $2U > -W$, it will disperse into the surrounding medium again.

For an isothermal, spherically symmetric cloud of mass M and radius R, made up of an ideal gas, the terms W and U can be expressed as:

$$W = -\frac{3}{5}\frac{GM^2}{R}, U = \frac{3}{2}\frac{Mk_\mathrm{B}T}{\mu m_\mathrm{H}}, \tag{1.2}$$

where G is the gravitational constant, k_B the Boltzmann constant, μ the mean molecular weight and m_H the mass of an H atom.

Then, assuming the cloud fulfils the requirement of contraction $W > |2U|$, one can derive some useful approximate quantities. First, ignoring the thermal pressure term, the equation of motion for a thin shell with an initial radius R_ini is given by:

$$\frac{\mathrm{d}^2 r}{\mathrm{d}t^2} = -\frac{GM(r)}{r^2} \tag{1.3}$$

Due to mass conservation, the mass within the collapsing sphere stays constant and can be simply described by $M(r) = \frac{4\pi}{3}\rho_\mathrm{ini}R_\mathrm{ini}^3$. An approximate solution can be obtained by assuming a constant acceleration, meaning that $a(t) = \frac{\mathrm{d}^2 r}{\mathrm{d}t^2} = \frac{2R_\mathrm{ini}}{t^2}$, resulting in the *free-fall time*:

$$t_\mathrm{ff} = \sqrt{\frac{3}{2\pi G\rho_\mathrm{ini}}} \approx 7\times10^6\mathrm{yr}\left(\frac{M}{10^5\mathrm{M}_\odot}\right)^{-1/2}\left(\frac{R}{25\mathrm{pc}}\right)^{3/2}, \tag{1.4}$$

which is the time that a pressure-less homogenous sphere of initial density ρ_ini needs to collapse into a point.
Then taking the thermal pressure term into account again and expressing the density in terms of the number density $n = \rho/\mu m_\mathrm{H}$, one can derive the *Jeans length*:

$$-\frac{3}{5}\frac{GM^2}{R} > 2\times\frac{3}{2}\frac{Mk_\mathrm{B}T}{\mu m_\mathrm{H}} \tag{1.5}$$

$$R > \sqrt{\frac{15k_\mathrm{B}T}{4\pi G(\mu m_\mathrm{H})^2 n}} \rightarrow \lambda_\mathrm{J} \approx 0.19\mathrm{pc}\left(\frac{T}{10\mathrm{K}}\right)^{1/2}\left(\frac{n_{\mathrm{H}_2}}{10^4\mathrm{cm}^{-3}}\right)^{-1/2} \tag{1.6}$$

and the *Jeans mass*, which is the minimum mass that a cloud needs for collapse if it is solely supported by thermal pressure:

$$M_\mathrm{J} = \frac{4\pi}{3}n\mu m_\mathrm{H}\lambda_\mathrm{J}^3 \rightarrow M_\mathrm{J} \approx 1\mathrm{M}_\odot\left(\frac{T}{10\mathrm{K}}\right)^{3/2}\left(\frac{n_{\mathrm{H}_2}}{10^4\mathrm{cm}^{-3}}\right)^{-1/2} \tag{1.7}$$

The Jeans mass decreases with decreasing temperature T and increasing number density n, meaning it is more likely for colder and denser clouds to collapse. For a giant molecular cloud with typical values of $T = 15\,\mathrm{K}$ and $n_{\mathrm{H}_2} = 10^2\,\mathrm{cm}^{-3}$, the Jeans mass assumes a value of around $10\mathrm{M}_\odot$, which is much smaller than average masses of giant molecular clouds. However, observations suggest that giant molecular clouds are relatively stable and likely do not undergo

global collapse. Moreover, the star formation rate resulting from the above described simple approximation is around one order of magnitude higher (Zuckerman & Palmer 1974), than the one observed (Robitaille & Whitney 2010). Both suggest that additional sources of support against gravitational collapse must be present, which is indeed the case as molecular clouds are usually also supported by kinetic motions of the bulk, such as rotation and turbulence, and magnetic fields. Rather than globally, star formation occurs within smaller dense substructures of molecular clouds, the *dense cores*, which are around the size suggested by the Jeans mass.

1.3.1.2 Collapse

The collapse of the dense core progresses in several phases. In the initial phase, the collapse is still isothermal. The heat produced by the gravitational collapse can be radiated away, as the gas is optically thin and cools efficiently by collisional excitation of gas molecules and their radiative de-excitation. As the density increases in the larger cloud and the gas temperature remains constant, the Jeans mass decreases, meaning that smaller fragments could begin to collapse independent of the larger structure. The opacity is mainly caused by the presence of dust particles. As the density inside the core increases, the opacity increases. Once the density becomes so high that the gas becomes optically thick, the heat cannot be radiated away any more and the temperature rises. The collapse proceeds adiabatically, meaning no heat is exchanged with the surroundings. The thermal pressure increases due to the rising temperature, until an equilibrium between gravity and thermal pressure is achieved again. The collapse at the centre of the core comes to a halt, forming a *first hydrostatic core*. The envelope continues to collapse and its material accretes onto the first core, further increasing its mass and temperature. When the temperature reaches 2000 K, the H_2 molecules inside the first core dissociate and thereby absorb energy that would otherwise provide thermal pressure. The centre of the core enters a second, very short, collapse phase, after which hydrostatic equilibrium is re-established and the *second hydrostatic core* continues to accrete infalling material.

1.4 Pre-stellar cores

Dense cores can be subdivided into different categories. *Starless cores* are centrally concentrated (Ward-Thompson et al. 1999) structures with densities above 10^5 cm^{-3} (Crapsi et al. 2005, Keto & Caselli 2008) and extremely low central temperatures ranging around 6 K to 10 K (Crapsi et al. 2007). *Pre-stellar cores* are a subset of starless cores, comprising only the most evolved ones, that are very centrally peaked and experience contraction motions. Once a protostar has formed in the core it is termed *protostellar core*.
Pre-stellar cores typically possess a density and temperature gradient. The density profile is usually best described by a centrally flattened inner region up to a characteristic radius r_0 and an $r^{-\alpha}$ decline for the outer part (Tafalla et al. 2002, Chacón-Tanarro et al. 2019b):

$$n_{\mathrm{H_2}}(r) = \frac{n_0}{1 + \left(\frac{r}{r_0}\right)^{\alpha}}, \tag{1.8}$$

where α is the asymptotic power index and is typically in the range of 2 to 3. The temperature distribution has a similar shape, however, with the lowest temperature at the centre $T_{\rm in}$ increasing towards the outer part of the core $T_{\rm out}$:

$$T(r) = T_{\rm out} - \frac{T_{\rm out} - T_{\rm in}}{1 + \left(\frac{r}{r_{\rm t0}}\right)^{\alpha_{\rm t}}}. \tag{1.9}$$

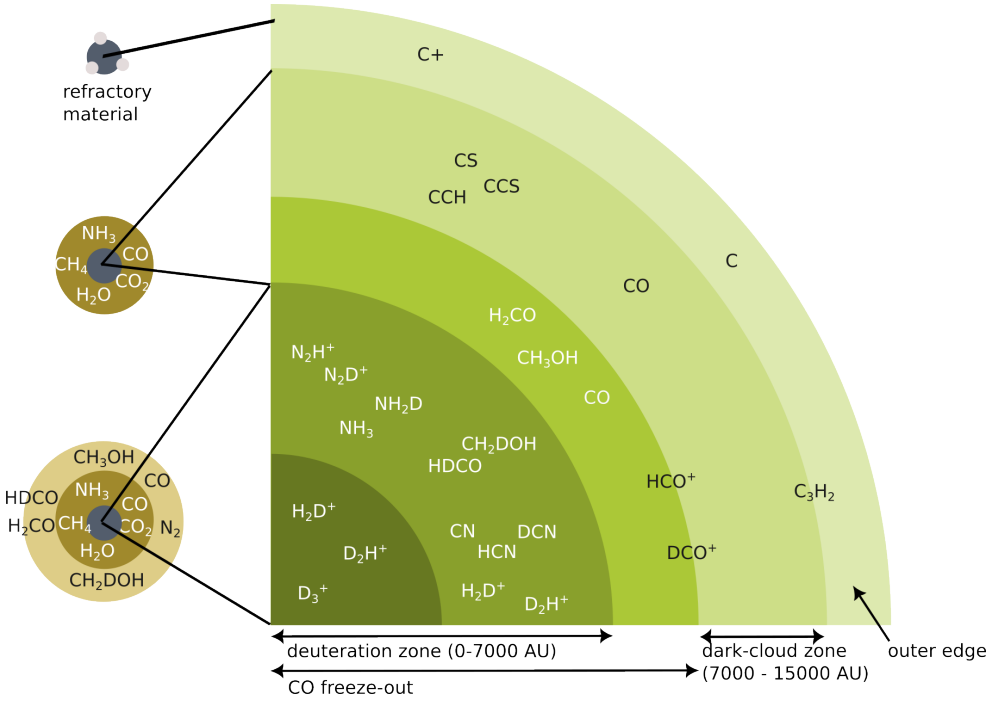

Figure 1.2: Schematic summary of the chemical structure of a pre-stellar core. The sizes of the specific zones are derived from the observed chemical structure of the pre-stellar core L1544.

The gradient in physical properties (e.g. density, temperature, visual extinction) profoundly impacts the ongoing chemistry and creates distinct zones with their own chemical behaviour (Caselli & Ceccarelli 2012, Ceccarelli et al. 2014):

- The **outer edge** represents the transition zone between the pre-stellar core and the surrounding molecular cloud. Here, the visual extinction drops below 4 mag and photochemistry becomes important. Carbon is mostly present in form of C^+ in the gas phase, enabling carbon-chain chemistry. Water ice forms efficiently on the surface of dust grains and is partially photo-evaporated into the gas phase.

- In the **dark-cloud zone**, chemistry is dominated by ion-molecule reactions, starting the carbon and oxygen chemistry, and neutral-neutral reactions, converting atomic nitrogen into N_2. Carbon is mostly locked in CO.

- The **zone of CO freeze out** represents the region where the density increases above 10^5 cm^{-3} and the temperatures drop below 10 K. There, the freeze-out timescale ($\approx 10^9/n_{\rm H}$; Jones & Williams 1985) is much shorter than the free-fall time scale (see equation 1.4), and consequently gas phase molecules adsorb onto the surface of dust grains in high rates, forming thick icy mantles. Each species possess their unique evaporation temperature, hence desorbes at different radii, resulting in an onion-like chemical structure of the core. The existence of a "complete depletion zone", where more than 99.9% of all species heavier than He are frozen out onto the dust grain, in the very centre of the core has been confirmed observationally for the pre-stellar core L1544 Caselli et al. 2022.

- The **deuteration zone** is the zone, where deuterium fractionation via the reaction H_3^+ + HD $\leftrightarrow$ H_2D^+ + H_2 proceeds efficiently (more details can be found in Section 1.4.2).

1.4.1 Important chemical processes

The following presents an overview about basic chemical reactions in dense cores. The focus of this chapter lies heavily on introducing the beginning of chemistry in the gas phase, and the subsequent carbon chemistry that is relevant for the formation of complex organic molecules discussed in this thesis.

Dense cores are the birthplace of chemical complexity in the star- and planet formation process. Their chemistry is initiated by the reaction of the most abundant element - hydrogen - with itself, forming the most abundant molecule: molecular hydrogen (H_2). When two, free hydrogen atoms form an H_2 molecule in its ground electronic state, the formed molecule has to dispose of 4.48 eV of dissociation energy (Draine 2011). Since the diatomic homonuclear molecule is highly symmetric, it does not have a permanent electric dipole moment and is therefore not able to remove internal energy by electric dipole radiation. Electric quadrupole transitions are available, but possess very low rates. Hence H_2 is only efficiently formed in the presence of a third body that removes the internal energy of the formed molecule.

The most commonly available third body in molecular clouds are interstellar dust grains. Hydrogen atoms attach to the grain, become weakly bound and diffuse in a random process over the surface until they encounter other hydrogen atoms to react with. The dissociation energy is relaxed by interaction with the grain's surface, which also typically results in an ejection of the H_2 molecule into the gas phase (e.g. Gould & Salpeter 1963, Hollenbach & Salpeter 1971). More recently, it has been shown that H_2 formation can also occur at relatively high temperatures of up to 250 K (Grieco et al. 2023) and on very small grains or even polycyclic aromatic hydrocarbons (PAHs; Habart et al. 2004, Boschman et al. 2015).

In contrast to diffuse clouds, the density and visual extinction in the inner parts of dense cores are high enough that H_2 can efficiently self-shield against interstellar UV radiation (Draine & Bertoldi 1996) and is only photodissociated at its edges. Hence, hydrogen is locked almost exclusively in its molecular form. In the absence of UV photons, cosmic rays (CRs), being able to penetrate deep into the core's interior, become the main ionising agent, ionising the abundant H_2 molecule to H_2^+, which in turn reacts quickly with H_2 again to form H_3^+:

$$H_2 + CR \rightarrow H_2^+ + e^- + CR \tag{1.10}$$
$$H_2^+ + H_2 \rightarrow H_3^+ + H. \tag{1.11}$$

The H_3^+ ion readily reacts with several neutral atoms, both initiating carbon (reaction 1.12) and oxygen chemistry (reaction 1.13), in a proton transfer reaction followed by multiple hydrogen abstraction reactions with H_2. Finally dissociative recombination reactions form a neutral molecule:

$$C \xrightarrow{H_3^+} CH^+ \xrightarrow{H_2} CH_2^+ \xrightarrow{H_2} CH_3^+ \xrightarrow{e^-} CH/CH_2 \tag{1.12}$$
$$O \xrightarrow{H_3^+} OH^+ \xrightarrow{H_2} H_2O^+ \xrightarrow{H_2} H_3O^+ \xrightarrow{e^-} H_2O/OH/O. \tag{1.13}$$

Once CH_3^+ and H_3O^+ are formed, they can react with atomic oxygen or carbon respectively to form HCO^+:

$$CH_3^+ + O \rightarrow HCO^+ + H_2 \tag{1.14}$$
$$H_3O^+ + C \rightarrow HCO^+ + H_2, \tag{1.15}$$

which is transformed into the stable CO molecule by a dissociative recombination with an electron:

$$HCO^+ + e^- \rightarrow CO + H. \tag{1.16}$$

Once the density is sufficiently high, CO (and most other species) *freeze-out catastrophically* (Caselli et al. 1999, 2022). The freeze-out of CO is of particular importance for multiple reasons: (i) CO is the starting point of the formation of methanol (and other COMs) on the grains; (ii) on CO covered surfaces, the intermolecular forces between adsorbed molecules and the underlying surface molecules are less strong, due to the weak dipole moment of the CO molecule (especially with respect to water). A high CO surface coverage could, therefore, promote an enhanced diffusion process for selected surface molecules, possibly boosting the formation of various COMs by diffusive reaction mechanisms even at the low temperatures of pre-stellar cores (Molpeceres et al. 2024); (iii) reactive/chemical desorption is experimentally found to be significantly more efficient from CO covered surfaces as from water ice surfaces (Minissale et al. 2016b).

On the grain surface, the chemistry is mostly dominated by hydrogenation reactions, as hydrogen, due to its low binding energy, is able to scan the surface for reaction partners even at extremely low temperatures (≈ 10 K), while most other species are immobile. The successive hydrogenation of oxygen, carbon, nitrogen and carbon monoxide results in the formation of the closed-shell end products - water (H_2O), methane (CH_4), ammonia (NH_3) and methanol (CH_3OH):

$$\mathrm{O} \xrightarrow{\mathrm{H}} \mathrm{OH} \xrightarrow{\mathrm{H}} \mathrm{H_2O} \tag{1.17}$$

$$\mathrm{C} \xrightarrow{\mathrm{H}} \mathrm{CH} \xrightarrow{\mathrm{H}} \mathrm{CH_2} \underset{-\mathrm{H_2}}{\overset{\mathrm{H}}{\longleftrightarrow}} \mathrm{CH_3} \underset{-\mathrm{H_2}}{\overset{\mathrm{H}}{\longleftrightarrow}} \mathrm{CH_4} \tag{1.18}$$

$$\mathrm{N} \xrightarrow{\mathrm{H}} \mathrm{NH} \xrightarrow{\mathrm{H}} \mathrm{NH_2} \xrightarrow{\mathrm{H}} \mathrm{NH_3} \tag{1.19}$$

$$\mathrm{CO} \underset{-\mathrm{H_2}}{\overset{\mathrm{H}}{\longleftrightarrow}} \mathrm{HCO} \underset{-\mathrm{H_2}}{\overset{\mathrm{H}}{\longleftrightarrow}} \mathrm{H_2CO} \underset{-\mathrm{H_2}}{\overset{\mathrm{H}}{\longleftrightarrow}} \mathrm{CH_2OH/CH_3O} \underset{-\mathrm{H_2}}{\overset{\mathrm{H}}{\longleftrightarrow}} \mathrm{CH_3OH}. \tag{1.20}$$

The formation of complex organic molecules, other than methanol, is still under active debate, with the central question being whether they are mainly formed in the gas phase or on the surface of dust grains. In the former case, simpler molecules are formed by the efficient hydrogenation reactions (1.17 - 1.20), desorbed nonthermally into the gas phase and then processed further by gas phase reactions to form COMs (e.g. Balucani et al. 2015, Skouteris et al. 2018, Vazart et al. 2020). In the latter case, COMs are formed by radical-radical or radical-molecules reactions, that often involve the intermediate products of the hydrogenation chains (reaction 1.17 - 1.20; e.g. Garrod et al. 2008, Jin & Garrod 2020, Molpeceres et al. 2024). Likely, a combination of both theories is necessary to explain the existence of the multitude of COMs observed.

The proposed formation pathways for acetaldehyde ($\mathrm{CH_3CHO}$), methyl formate ($\mathrm{CH_3OCHO}$) and glycoaldehyde ($\mathrm{CH_2OHCHO}$) on the grain surface are:

$$\mathrm{CH_3} + \mathrm{HCO} \rightarrow \mathrm{CH_3CHO} \tag{1.21}$$

$$\mathrm{CO} + \mathrm{CH_3} \rightarrow \mathrm{CH_3CO} + \mathrm{H} \rightarrow \mathrm{CH_3CHO} \tag{1.22}$$

$$\mathrm{CH_3O} + \mathrm{HCO} \rightarrow \mathrm{CH_3OCHO} \tag{1.23}$$

$$\mathrm{CO} + \mathrm{CH_3O} \rightarrow \mathrm{CH_3OCO} + \mathrm{H} \rightarrow \mathrm{CH_3OCHO} \tag{1.24}$$

$$\mathrm{CH_2OH} + \mathrm{HCO} \rightarrow \mathrm{CH_2OHCHO} \tag{1.25}$$

Even after their formation, COMs (and other molecules) can be further processed by chemical reactions on the grain's surface. Here, *abstraction reactions* play an essential role. Abstraction reactions are chemical reactions, in which a radical (e.g. H, $\mathrm{CH_3}$, $\mathrm{NH_2}$, OH) abstracts a hydrogen atom from the COM, thereby preferably resulting in a closed-shell end product (e.g $\mathrm{H_2}$, $\mathrm{CH_4}$, $\mathrm{NH_3}$, $\mathrm{H_2O}$) and in a parent molecule of the COM (Molpeceres et al. 2025):

$$\mathrm{CH_3OH} + \text{e.g } \mathrm{H, CH_3, NH_2, OH} \rightarrow \mathrm{CH_3O/CH_2OH} + ... \tag{1.26}$$

$$\mathrm{CH_3CHO} + \text{e.g } \mathrm{H, CH_3, CH_3O, CN, NH_2, OH} \rightarrow \mathrm{CH_3CO} + ... \tag{1.27}$$

$$\mathrm{CH_3OCHO} + \text{e.g } \mathrm{H, CH_3, CH_3O, CN, NH_2, OH} \rightarrow \mathrm{CH_2OCHO/CH_3OCO} + ... \tag{1.28}$$

$$\mathrm{CH_2OHCHO} + \text{e.g } \mathrm{H, CH_3, CH_3O, CN, NH_2, OH} \rightarrow \mathrm{CH_2OHCO/CHOHCHO/OH_2CCHO} + ... \tag{1.29}$$

Due to the large number of hydrogen atoms and their high mobility, those parent molecules are likely to be quickly hydrogenated again, but they can also react with other reaction partners to form other COMs, as e.g. $CH_3OCO + OH/NH \rightarrow CH_3OCOOH/CH_3OCONH$. Furthermore, if the reaction partner is hydrogen again, the addition reactions can result in the formation of other end products, as there might exist multiple reaction channels with their individual branching ratios (indicated on top of the arrows):

$$\begin{aligned} CH_3CO + H &\xrightarrow{0.9} CH_3CHO \\ &\xrightarrow{0.03} CH_2CO + H \\ &\xrightarrow{0.03} CH_4 + CO \\ &\xrightarrow{0.03} CH_3COH \end{aligned} \tag{1.30}$$

$$CH_2OCHO + H \xrightarrow{1.0} CH_3OCHO \tag{1.31}$$

$$CH_3OCO + H \xrightarrow{1.0} CH_3OCHO \tag{1.32}$$

$$CH_2OHCO + H \xrightarrow{1.0} CH_2OHCHO \tag{1.33}$$

$$\begin{aligned} CHOHCHO/OH_2CCHO + H &\xrightarrow{0.5} CH_2OHCHO \\ &\xrightarrow{0.5} OHCCHO + H_2. \end{aligned} \tag{1.34}$$

Unfortunately, the branching ratios (and partially individual activation energies) are rarely measured experimentally or determined by quantum chemical calculations, with the exception of methanol (e.g.:Hidaka et al. 2009, Minissale et al. 2016c, Chuang et al. 2016) and acetaldehyde (Molpeceres et al. 2025). In the absence of other information, branching ratios are usually weighted equally, as it is the case for the reactions involving methyl formate and glycoladehyde. Hence, the inclusion of abstraction reactions into chemical network tends to decrease the surface abundances of the COM end products slightly. On the other hand, the gas phase abundances are usually increased as the *cyclic addition-abstraction*-scheme, destroying and re-forming the COM, is able to enhance the reactive desorption efficiency[8] beyond the efficiency of a single formation reaction.

Alternatively to surface formation, also possibly efficient gas phase formation routes have been proposed and their rates have been partially determined by experiments or quantum chemical calculations. Vazart et al. (2020) checked several formation pathways for acetaldehyde in the literature, and thereby verified the following reaction, which seems to be a major formation route for acetaldehyde (in warm environments):

$$C_2H_5 + O \rightarrow CH_3CHO + H. \tag{1.35}$$

[8]The process that the energy released in an exothermic reaction, taking place on the surface of the dust grain, is used to desorb the reaction product(s) into the gas phase is referred to as reactive or chemical desorption.

Moreover, possibly viable formation pathways for the production of methyl formate in the gas phase have been proposed to follow upon the desorption of methanol from the grain surface (Balucani et al. 2015):

$$CH_3OH + OH \rightarrow CH_3O \tag{1.36}$$
$$CH_3 + CH_3O \rightarrow CH_3OCH_3 \tag{1.37}$$
$$CH_3OCH_3 + \text{e.g.}CH, F, Cl, CN \rightarrow CH_3OCH_2 + HF, HCl, ... \tag{1.38}$$
$$CH_3OCH_2 + O \rightarrow CH_3OCHO + H. \tag{1.39}$$

First the methoxy radical (CH_3O) forms by the reaction of methanol with the hydroxy radical (OH), which has been studied experimentally by Shannon et al. (2013) and found to be surprisingly efficient due to the formation of a hydrogen-bonded complex of both reaction partners that allows reaction 1.36 to proceed via reactive tunneling. After that, dimethyl ether (CH_3OCH_3) is formed by radiative association of CH_3 and CH_3O, which is a reaction type that is typically inefficient for smaller molecules, but can become important for larger stable COMs. However, the reaction rate of this essential reaction 1.37 has never been measured directly and can only be estimated. Subsequently, multiple common radicals can abstract a hydrogen from the dimethyl ether, resulting in CH_3OCH_2, which in turn is oxidized to form methyl formate.

Skouteris et al. (2018) proposed the existence of an "ethanol tree", from which, among others, both acetaldehyde and glycoaldehyde can form from ethanol (CH_3CH_2OH) in the gas phase in a top-down chemistry:

$$\begin{aligned} CH_3CH_2OH + OH &\rightarrow CH_3CHOH + H_2O \\ CH_3CHOH + O &\rightarrow CH_3CHO + OH \end{aligned} \tag{1.40}$$

$$CH_3CH_2OH + Cl, OH \rightarrow CH_2CH_2OH \tag{1.41}$$
$$CH_2CH_2OH + O \rightarrow CH_2OHCHO. \tag{1.42}$$

In recent years, a lot of progress has been made in all subfields of astrochemistry, regarding the formation processes of large COMs. However, there still remain many open questions that need to be investigated in more detail.

1.4.2 Deuterium fractionation

The lightest elements and their stable isotopes - hydrogen ($^1_1$H), deuterium ($^2_1$H or D), helium ($^3_2$He, $^4_2$He) and small amounts of lithium ($^7_3$Li) and beryllium ($^7_4$Be) - were formed already in the first three minutes after the birth of the universe in the Big Bang nucleosynthesis. While the heavier elements are created exclusively by nuclear fusion in stars, deuterium is consumed in stellar interiors, causing the locally measured isotopic ratio to be lower than its primordial value. Multiple independent measurements conducted in the Local Bubble found average D/H ratios between 1.52×10^{-5} (Linsky 2003, Linsky et al. 2006) and 2.0×10^{-5} (Prodanović et al. 2010) and a deuterium astration factor $f_D = (D/H)_{primordial}/(D/H)_{ISM} \leq 1.4$.

In molecular clouds, deuterium is locked up mostly in molecular form as HD, resulting in a HD/H_2 ratio of 3.04×10^{-5} to 4.0×10^{-5}. For other molecules, however, the D/H ratio can be increased by up to four orders of magnitude in a process called *deuterium fractionation* or *deuteration*. Particular chemical reactions, the *isotopic exchange reactions*, preferentially transfer one isotope to another molecular species, thereby altering the isotopic ratios in those species. The most important isotopic exchange reaction, initiating the fractionation of deuterium, is the reaction between the H_3^+ ion and HD (Watson 1974):

$$H_3^+ + HD \leftrightarrow H_2D^+ + H_2 + 232\,K. \tag{1.43}$$

Reaction 1.43 is exothermic by 232 K, allowing it to proceed efficiently in forward direction, but strongly hindering the backward reaction for temperatures below 30 K. The exothermicity is caused by the the lower zero-point energy of H_2D^+ with respect to H_3^+, due to its higher mass. Here it is implicitly assumed that H_2 is mostly in para-state [9] , as the barrier of the backwards reaction is overcome easier when H_2 is in its ortho-state that possesses a higher internal energy (175 K; Ceccarelli et al. 2014) than its para-state, rendering the fractionation process inefficient. The ortho-to-para ratio in cold molecular clouds, however, is expected to be below 10^{-3} (Flower et al. 2006, Pagani et al. 2009). Deuterium fractionation is further enhanced by the catastrophic freeze-out of CO and O in the inner parts of the cloud, as those are the main destruction partners of H_3^+ and its deuterated isotopologues. Therefore, dense cores, with their low temperatures ($T = 6 - 15$ K) and relatively high densities ($n_H \geq 10^5\,cm^{-3}$), harbour the perfect conditions for an extremely efficient deuteration process.

Subsequently, deuterium is distributed in a set of chemical reactions from H_2D^+ to other molecular species. Firstly, H_2D^+ itself is further deuterated by successive reactions with HD (Hugo et al. 2009), thereby also increasing the abundances of D_2H^+ and D_3^+:

$$H_2D^+ + HD \leftrightarrow D_2H^+ + H_2 + 187\,K \tag{1.44}$$

$$D_2H^+ + HD \leftrightarrow D_3^+ + H_2 + 234\,K. \tag{1.45}$$

Secondly, H_2D^+ (or D_2H^+ and D_3^+) transfers its deuterium atom to other neutral gas phase species. The deuterated ions eventually recombine with an electron, which can cause the ejection of a deuterium atom, producing atomic deuterium in the otherwise molecular gas:

$$H_2D^+ + X \rightarrow DX^+ + H_2 \quad \text{with e.g. X = CO, } N_2\text{, ...} \tag{1.46}$$

$$DX^+ + e^- \rightarrow X + D. \tag{1.47}$$

The atomic deuterium is partially adsorbed onto the surface of dust grains, where it proceeds to deuterate surface species and can be fractionated further by either direct H-D substitution reactions (as e.g. for H_2CO; Hidaka et al. 2009):

$$H_2CO + D \leftrightarrow HDCO + H \tag{1.48}$$

$$HDCO + D \leftrightarrow D_2CO + H \tag{1.49}$$

[9] In the H_2 molecule, the nuclear spins of the two protons couple - forming either a high energy triplet state, ortho-H_2 ($I = 1$, $M_I = 1, 0, -1$), or a low energy singlet state, para-H_2 ($I = 0$, $M_I = 0$).

or addition-abstraction cycles (as e.g. CH_3OH Hidaka et al. 2009):

$$CH_3OH + H/D \rightarrow CH_2OH + H_2/HD \tag{1.50}$$
$$CH_2OH + D \rightarrow CH_2DOH. \tag{1.51}$$

Additionally, laboratory experiments (Ratajczak et al. 2009, Gálvez et al. 2011) showed that H-D exchange between H_2O (or HDO) and other components of the icy mantles occurs. The experiments identified this process to be efficient for grain temperatures $T_{\rm grain} \geq 120\,{\rm K}$, which coincides with the sublimation phase, where large parts of the mantle are re-organised and sublimated into the gas phase. In a similar fashion, it has been shown that the exchange is also promoted by photolysis (Weber et al. 2009).

1.4.3 Inheritance versus reset

Surprisingly, multiple observational surveys conducted in the last decade (e.g. Bacmann et al. 2012, Jiménez-Serra et al. 2016, Scibelli & Shirley 2020, Scibelli et al. 2024, 2025) found that COMs were formed (and possibly released) into the gas phase already in the earliest phase of star formation, the pre-stellar core phase. However, COMs were also found in observations and samples of solar system bodies (e.g. Crovisier et al. 2004, Drozdovskaya et al. 2021). Between those two phases of stellar life, millions or even billions of years have passed, raising the question to which extent the chemical composition found today is inherited from the earlier phases or to which extent the chemistry has been reset and started anew.

The study of fractionation is a key tool in answering this question. The incorporation of a deuterium atom into the molecular structure provides a chemical marker to connect the formation of this molecule to an environment in which it can be efficiently formed, namely low-temperature and ion-molecule reactions driven environments, i.e. the pre-stellar phase or the midplane of protoplanetary disks. Currently, first efforts have been made to build up a catalogue of D/H and D_2/D ratios of multiple molecules in various astronomical objects, mainly from the pre-stellar and protostellar phase (see as an example Figure 1.3).

Comparing these values hinted to some trends with respect to molecular species, functional groups, evolutionary phase and mass of the star formation site, that can be summarized as follows:

- H_2O exhibits generally lower D/H ratios as the COMs, which is likely caused by an earlier epoch of formation, already in the relatively warm, diffuse cloud phase, whereas e.g. CH_3OH and other COMs are only formed after CO freeze-out in the pre-stellar phase (Taquet et al. 2014).

- The COMs seem to experience systematic variations in their D/H ratio in the protostellar stage (Jørgensen et al. 2018), also likely reflecting their individual formation pathways and times:

  - **2%:** H_2CO, HNCO, CH_2CO, HCOOH, CH_3OH, NH_2CHO
  - **4%:** CH_3OCH_3

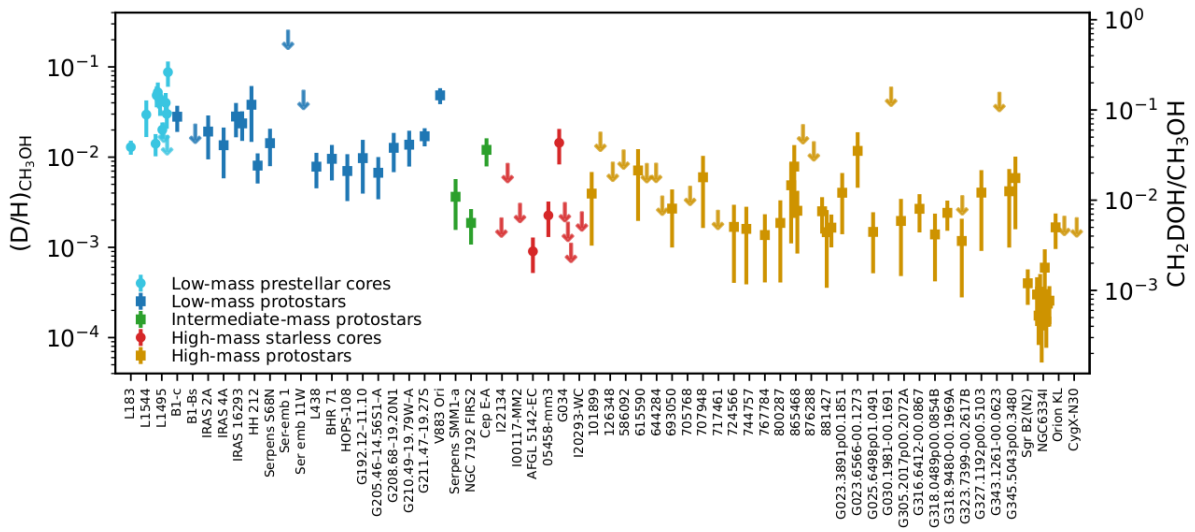

Figure 1.3: The column density ratios N_{CH_2DOH}/N_{CH_3OH} (right axis) and $(D/H)_{CH_3OH}$ ratio (left axis) of various low-mass, intermediate-mass, and high-mass pre- and protostellar objects. Note that the D/H ratios in this figure were derived from the column density ratio by correcting for the statistical weight - $N_{CH_2DOH}/N_{CH_3OH} = 3\ (D/H)_{CH_3OH}$. Figure published in van Gelder (2022).

  - **5-6%:** CH_3OCHO, CH_2OHCHO, CH_3CH_2OH
  - **8%:** CH_3CHO .

- The deuteration of the functional groups of the same COM can proceed with different efficiency. For example: the methyl group (CH_3) of methanol is deuterated more efficiently than the hydroxy group (OH), due to the higher rate of the abstraction-addition process (reaction 1.52) compared to the D-atom addition (reaction 1.53; Hidaka et al. 2009):

$$CH_3OH \xrightarrow[-H_2]{H,D} CH_2OH \xrightarrow{D} CH_2DOH \tag{1.52}$$

$$CH_3O \xrightarrow{D} CH_3OD. \tag{1.53}$$

  This results in a higher $[CH_2DOH]/[CH_3OH]$[10] ratio and lower $[CH_3OD]/[CH_3OH]$ ratio, which is why CH_2DOH is readily observed in pre-stellar cores (e.g. Chacón-Tanarro et al. 2019a, van Gelder 2022, Spezzano et al. 2025), while for CH_3OD the first detection has been reported only very recently (Kulterer et al. 2025) towards the pre-stellar cores L1448 ($[CH_2DOH]/[CH_3OD] = 2.8$ - 8.5) and tentatively towards B213-C6 ($[CH_2DOH]/[CH_3OD] = \leq 5.7$). For the pre-stellar core L1544, only estimates for upper limits exist, pointing towards $[CH_2DOH]/[CH_3OD] \geq 10$ (Bizzocchi et al. 2014), which is much higher than the statistically expected ratio of 3.

[10] $[CH_2DOH]/[CH_3OH]$ is the ratio of the column densities of e.g. CH_2DOH and CH_3OH, which is oftentimes also written as $N(CH_2DOH)/N(CH_3OH)$

- van Gelder (2022) found hints for the existence of a slight evolutionary trend of the D/H ratio of methanol from pre-stellar (average = 3.4×10^{-2}) to proto-stellar phase (average = 2.2×10^{-2}; see also Lin et al. 2023a, Spezzano et al. 2025).
- The D/H ratio for methanol is found to be on average lower in high-mass protostars (average D/H = 1.1×10^{-3}) when compared to their low-mass counterparts (average D/H = 2.2×10^{-2};van Gelder 2022). Chemical modeling suggests that the difference is caused by either higher temperature (≤ 20 K) or a shorter lifetime of the high-mass pre-stellar phase.
- There are some measurements of the D/H ratio of methanol in comets that have similar values as were found in the protostellar stage: $< 3 \times 10^{-2}$ for the comet C/1995 O1 (Hale-Bopp, Crovisier et al. 2004) and 0.71×10^{-2} - 6.63×10^{-2}) for 67P (Drozdovskaya et al. 2021). These values are suggestive of at least partial inheritance from the pre-stellar phase.

1.4.4 L1544

The prototype of pre-stellar cores is certainly L1544, situated at a distance of 172 pc (Galli et al. 2019) on the edge of the Taurus molecular cloud (see Figure 1.4). The core's popularity among astrochemists is motivated both by its remote location, where protostellar feedback and other interactions with the larger cloud are minimal, and its dynamically and chemically evolved state.

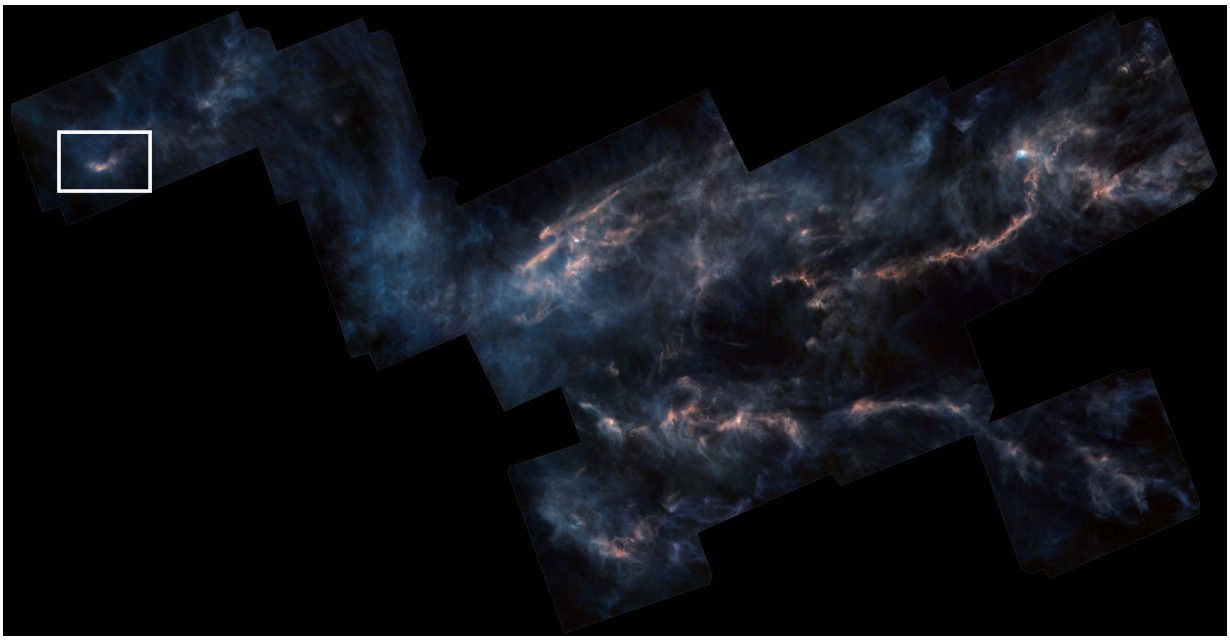

Figure 1.4: Herschel four-color image of the Taurus molecular cloud. The pre-stellar core is indicated by the white box in the upper left corner. Credit: ESA/Herschel/NASA/JPL-Caltech, R.Hurt

L1544 exhibits a high molecular hydrogen volume density ($n_{\mathrm{H}} = 1.66 \times 10^7$ cm^{-3}) and extremely

low gas and dust temperature ($T_{\rm gas}$ = 6.5 K, $T_{\rm dust}$ = 6.3 K) in its center (Keto & Caselli 2010, see also Crapsi et al. 2007, Chacón-Tanarro et al. 2019b). The extreme physical conditions cause the freeze-out of most molecular species, with the existence of a "complete depletion zone" in the inner 1800 AU where 99.9% of species heavier than He are frozen out onto dust grains (Caselli et al. 2022). Additionally, they promote a very efficient deuteration process, that was traced in several molecular species, e.g.: $[N_2D^+]/[N_2H^+]$ = 0.26, $[DCO^+]/[HCO^+]$ = 0.035 (Redaelli et al. 2019), $[HDCO]/[H_2CO]$ = 0.03, $[CH_2DOH]/[CH_3OH]$ = 0.08 (Chacón-Tanarro et al. 2019a), $[HDCS]/[H_2CS]$ = 0.3 (Spezzano et al. 2022), [c-C_3HD]/[c-C_3H_2] = 0.17 (Giers et al. 2022), [CCD]/[CCH] = 0.15, [DCN]/[HCN] = 0.05, [DNC]/[HNC] = 0.08 (Giers et al. 2023).

The core shows clear evidence of chemical segregation. Spezzano et al. (2016) found that c-C_3H_2, which forms through gas phase reactions from C, peaks in the southern part of the core, while CH_3OH, which forms on the surface of dust grains from CO, peaks in the northern part of the core. This behaviour is attributed to an uneven illumination of the core, due to a sharp drop in $N(H_2)$ of the surrounding molecular cloud. Further mapping of 39 different molecular species (Spezzano et al. 2017) revealed that the molecules can be classified into four families: (i) the c-C_3H_2 family (carbon-chains), (ii) the dust peak family (nitrogen-bearing species), (iii) the methanol peak family (oxygen-bearing molecules) and (iv) the HNCO peak family (HNCO, CH_3CCH), peaking at distinct locations in the core.

Surprisingly, Jiménez-Serra et al. 2016 (see also Lefloch et al. 2018) observed several larger COMs, including e.g.: acetaldehyde (CH_3CHO), methyl formate (CH_3OCHO) and dimethyl ether (CH_3OCH_3). Those results inspired several modelling approaches, either mainly focused on COM formation in the gas phase (Vasyunin et al. 2017), following the desorption of methanol from the grain surface, or mainly focused on non-diffusive chemistry on the surface of dust grains (Jin & Garrod 2020).

1.5 Astrochemical models

Astrochemical models are an essential tool to understand the complexities of chemical behaviour in different physical environments. They provide predictions for observational projects and aid to understand their results. In contrast to laboratory experiments, they are able to follow the chemistry in physical conditions that are difficult to attain in a laboratory set up and for extremely long periods of time.

Rate equation based astrochemical models, as the one used in this thesis, solve a system of coupled first-order ordinary differential equations that assume the form of a rate equation 1.54. The chemical evolution of species X with number density n(X) is simply given by the rate of its formation subtracted by the rate of its destruction:

$$\frac{{\rm d}n({\rm X})}{dt} = \text{rate of formation of species X} - \text{rate of destruction of species X}. \tag{1.54}$$

Depending on the amount of molecular reactants, there are unimolecular, bimolecular and termolecular reactions, although the latter becomes only relevant for the relatively high densities (as e.g. in the midplane of protoplanetary disks or the early universe).

The rate of a unimolecular reaction A → B, in units of $cm^{-3}s^{-1}$, is given by:

$$\text{Rate} = -\frac{dn(A)}{dt} = \frac{dn(B)}{dt} = kn(A), \tag{1.55}$$

where k is the rate coefficient [s^{-1}] and n(A) the number density of species A [cm^{-3}]. In this case, the rate is the destruction rate for species A, but the formation rate for species B. Unimolecular reactions are typically reactions with photons or cosmic rays as reactive agents.
The rate of a bimolecular reaction A + B → C + D is given by:

$$\text{Rate} = -\frac{dn(A)}{dt} = -\frac{dn(B)}{dt} = \frac{dn(C)}{dt} = \frac{dn(D)}{dt} = kn(A)n(B), \tag{1.56}$$

where k is the rate coefficient [cm^3s^{-1}] and n(A) and n(B) the number densities of species A and B respectively. In bimolecular reactions, the rate is the destruction rate for species A and B, but the formation rate for species C and D.

1.5.1 Gas-Phase chemistry

The rate coefficients of most chemical reactions in the gas phase obey the *Arrhenius equation*:

$$k(T) = A(T_{\text{gas}}) \exp\left(-\frac{E_A}{k_B T_{\text{gas}}}\right), \tag{1.57}$$

where $A(T)$ is the temperature-dependent pre-exponential factor, E_A a possible activation energy of the chemical reaction, k_B the Boltzmann-constant and T_{gas} the gas temperature. State-of-the-art astrochemical models, however, use a slightly altered version, the *modified Arrhenius equation*:

$$k = \alpha \left(\frac{T_{\text{gas}}}{300\text{K}}\right)^{\beta} \exp\left(\frac{-\gamma}{T_{\text{gas}}}\right), \tag{1.58}$$

which parametrizes the physical quantities specific to the particular chemical reaction with parameters α, β and γ. While the α parameter ([cm^3 s^{-1}]) is the temperature-independent part of the pre-exponential factor $A(T)$, the second term, including parameter β (dimensionless), expresses the temperature dependence of $A(T)$. The third term, containing the γ parameter ([K]), is analogous to equation 1.57 with γ being E_A/k_B.

Table 1.1 summarizes the basic types of gas phase chemical reactions. Additionally, they are explained individually in the following sections.

1.5.1.1 Bond formation processes

Radiative association reactions
Chemical reactions between positive ions or neutral molecules and other neutrals, resulting in one associated product, need to dissipate the energy released in the exothermic reaction to stabilize. In the absence of a third body, this can only happen by radiative de-excitation:

Table 1.1: Types of gas phase reactions.

		typ. rate coeff.
Bond formation processes		
Radiative association	$A + B \rightarrow AB + h\nu$	10^{-17} - 10^{-11} cm^3 s^{-1}
Associative detachment	$A^- + B \rightarrow AB + e^-$	10^{-9} cm^3 s^{-1}
Bond rearrangement processes		
Ion-molecule	$A^+ + BC \rightarrow AB^+ + C$	10^{-9} - 10^{-8} cm^3 s^{-1}
Charge transfer	$A^+ + BC \rightarrow A + BC^+$	10^{-9} cm^3 s^{-1}
Neutral-neutral	$A + BC \rightarrow AB + C$	10^{-11} - 10^{-9} cm^3 s^{-1}
Bond destruction processes		
Dissociative recombination	$A^+ + e^- \rightarrow C + D$	10^{-7} -10^{-6} cm^3 s^{-1}
Collisional dissociation	$AB + C \rightarrow A + B + C$	10^{-26} cm^{3}s^{-1}
Photodissociation	$AB + h\nu \rightarrow A + B$	10^{-10} - 10^{-8} s^{-1}
Cosmic-ray dissociation	$AB + CR \rightarrow A + B$	
Ionization		
Photoionization	$A + h\nu \rightarrow A^+ + e^-$	
Cosmic-ray ionization	$A + CR \rightarrow A^+ + e^-$	
Recombination		
Radiative recombination	$A^+ + e^- \rightarrow A + h\nu$	10^{-12} cm^3 s^{-1}
Cation-anion recombination	$A^+ + B^- \rightarrow A + B$	10^{-7} cm^3 s^{-1}
Electron attachment	$A + e^- \rightarrow A^- + h\nu$	10^{-16} - 10^{-15} cm^3 s^{-1}

$$A + B \leftrightarrow AB^* \rightarrow AB + h\nu. \tag{1.59}$$

The total rate coefficient for the formation of the final product AB is:

$$k = \frac{k_1 k_2}{k_{-1} + k_2}, \tag{1.60}$$

where k_1 is the rate coefficient for the first reaction step, producing AB^* in the forward direction and k_{-1} the rate coefficient for the backward direction. The rate coefficient for the second reaction step, de-exciting AB^* into the stable molecule AB is denoted by k_2.
For a diatomic molecule (e.g. H_2), the backward reaction from AB^* to A + B is relatively fast, as there is only one vibrational mode available for excitation. This energy can be directly used to dissociate the molecule again. For more complex molecules with N atoms, however, the excess energy is distributed among the $3N$-5 (linear molecule) or $3N$-6 (non-linear molecule) vibration

modes. The backward dissociation reaction occurs only if sufficient energy is concentrated in a specific eligible vibrational mode. Consequently, the rate coefficient for the backward reaction k_{-1} decreases for an increasing number of vibrational degrees of freedom.
The rate coefficient for the second step k_2 depends on the available transitions and their oscillator strengths, which in turn depend strongly on the particular molecule. The rate coefficient k_2, therefore, varies in the range of 10^2-$10^6\,s^{-1}$. Generally, k_2 has a higher value for larger, more complex molecules, as they have more radiative pathways for the stabilization. Although, this process is generally slow, it can still be important for the formation of a molecule for which no other pathways exists.

Associative detachment
Chemical reactions between negative ions and neutrals, producing an associated molecule by ejecting an electron ($A^- + B \rightarrow AB + e^-$) are called associative detachment reactions. They have very high rate coefficients ($10^{-9}\,cm^3\,s^{-1}$), due to the attractive force between the negative ion and an induced dipole moment in the neutral molecule. However, the abundances of negative ions in molecular clouds are low, resulting in low total formation or destruction rates for this reaction type. For a detailed explanation of the properties of the rate coefficient see Section 1.5.1.2.

1.5.1.2 Bond rearrangement processes

Ion-molecule reactions
In molecular clouds, the ionisation fraction $x(e^-)$ [11] is not entirely zero, but ranges around 10^{-6} and 10^{-8} (Caselli et al. 1998, Bergin et al. 1999). In the outer parts of the cloud, at low visual extinctions, atoms and molecules are mainly ionized by photoionization with UV photons from the interstellar radiation field. For the inner, more shielded parts, at high visual extinctions, ionization by penetrating cosmic-rays becomes the dominant ionization source.
Chemical reactions between ions and neutral molecules play an important role for gas phase chemistry in molecular clouds:

$$A^+ + BC \rightarrow AB^+ + C, \tag{1.61}$$

as the majority of them have high rate coefficients of the order of $\approx 10^{-9}\,cm^{-3}\,s^{-1}$. The electrical field of the ion polarizes the neutral molecule and induces a temporary dipole moment in it. The resulting long-range attractive electrostatic force between the ion and the neutral molecule increases the reaction cross-section compared to neutral-neutral reaction by up to two orders of magnitude. The rate coefficient for exothermic ion-molecule reactions can be estimated by the theoretically derived Langevin rate k_L:

$$k_L = 2\pi e \sqrt{\frac{\alpha}{\mu}}, \tag{1.62}$$

[11] The ionisation fraction $x(e^-)$ is defined as the ratio between the electron number density $n(e^-)$ and the H_2 number density $n(H_2)$.

which depends only on the polarizability α of the neutral molecule and the reduced mass μ of the system, and not on the temperature, meaning their activation energy is zero.

The Langevin rate is an accurate estimate for most ion-molecule systems. Some, however, present a significant temperature dependence in experiments. Possible causes are: (i) possible activation energy barriers, for reactions that require a rearrangement of chemical bonds, resulting in a decrease of the rates for decreasing temperatures or (ii) formation of temporary reaction complexes, enabling quantum tunneling through activation energy barriers, resulting in an increase of the rates for very low temperatures. Additionally, the presence of a permanent dipole moment in the neutral molecule can increase the reaction by a factor 10-100 at low temperatures.

Charge transfer reactions

A variation of ion-molecule reactions are the charge transfer reactions: ($A^+ + BC \rightarrow A + BC^+$), in which simply the electrical charge is exchanged between the reactants. Consequently, they possess rate coefficients that are of a similar order of magnitude as the ones for ion-molecule reactions ($\approx 10^{-9}\,cm^3\,s^{-1}$).

Neutral-neutral reactions

Although reactions between two neutral species often possess reaction barriers, they are also important in the formation of more complex molecules. Interactions are mainly caused by three mechanisms, depending on the properties of the specific reaction partners:

1. **Dipole-dipole interactions:** If both neutral molecules possess a permanent electric dipole moment, an attractive force will occur between those. At low temperatures the dipole moments tend to lock to each other, resulting in a potential proportional to r^{-3}.

2. **Dipole-induced dipole interactions:** The permanent dipole of the first molecule introduces an electric field at position of the second molecule, causing an induced dipole moment in it. In case the second molecule also possesses a permanent dipole moment, it will also induce a dipole moment in the first molecule. The potential is proportional to r^{-6}, independent of temperature.

3. **Dispersion interactions:** When electrons move asymmetrically with respect to the nuclei, an instantaneous dipole moment is created, which produces an attractive force between neighbouring molecules. The potential is proportional to r^{-6}.

1.5.1.3 Bond destruction processes

Dissociative recombination

Ion-molecule reactions possess high rate coefficients in the conditions of dense cores. Consequently, molecular ions are abundant gas phase species. The recombination of a molecular ion with an electron often results in a repulsive state of the neutral molecule, followed by its splitting into two (or more) neutral products:

$$A^+ + e^- \rightarrow B + C. \tag{1.63}$$

This process is termed dissociative recombination and plays an essential role in the formation of neutral molecules from their parent molecular ions. Dissociative recombination reaction often have multiple reaction channels, that have innate branching ratios. Knowing the branching ratio of various reaction channels is crucial in the evaluation of the channel's efficiency. For example, the formerly believed efficient gas phase formation of methanol:

$$CH_3^+ + H_2O \rightarrow CH_3OH_2^+ \tag{1.64}$$
$$CH_3OH_2^+ + e^- \rightarrow CH_3OH + H, \tag{1.65}$$

comprised of an ion-molecule reaction followed by a dissociative recombination reaction of $CH_3OH_2^+$, was deemed inefficient after experiments determined the branching ratio of reaction 1.65 to be only 6% (Geppert et al. 2005). Unfortunately, the measurement of branching ratios were challenging in the past and could only be achieved with the recent development of suitable laboratory equipment (e.g. storage rings). Hence, many important reactions still remain to be properly measured.

Collisional dissociation
The collision of two gas phase molecules can result in a dissociation of the molecules into smaller fragments. However, this reaction type only becomes important for high densities and energies as e.g. in shocks around young stars.

Photodissociation and - ionization
The interstellar medium is filled with ambient UV radiation generated by surrounding stars, which is called the *interstellar radiation field (ISRF)*. If molecules are exposed to UV radiation, they might be *photodissociated*, or *photoionized*.
Photodissociation occurs in three distinct scenarios:

- **Direct dissociation**, in which a molecule is directly excited in a bound-free transition to a repulsive electronic state. Therefore, this scenario occurs in a broad range of UV radiation.
- **Predissociation**, in which a molecule is excited to a rovibronic level of a bound electronic state. In case the rovibronic state is coupled to a repulsive state, the molecule is dissociated with a certain probability, depending on the coupling strength and the lifetime of the excited state. This photodissociation scenario occurs only at the transition frequencies from the ground electronic state to the electronically excited state.
- **Fluorescent decay**, in which a molecule is excited to a bound electronic state and then decays fluorescently to a continuum state of a ground electronic state.

For molecular clouds, photoprocesses are mostly important in the lower density gas at their edges, in regions in which the visual extinction A_V is only a few magnitudes at most. In the

inner parts of the cloud, the UV radiation is attenuated exponentially by its interaction with dust particles. The photodissociation rate coefficient is expressed as:

$$k = k_0 \exp(-\gamma A_V), \tag{1.66}$$

where k_0, ranging around 10^{-9}-10^{-11} s^{-1}, is the unattenuated photodissociation rate and γ a scaling factor, depending on the molecular species and grain model. These values are tabulated for an increasing number of species and are usually included in the chemical network. Abundant molecular species (e.g. H_2, CO_2) that predominantly dissociate via extraordinarily thin predissociative lines are additionally protected by an effect called *self-shielding*, in which the molecules at the surfaces of the cloud become photoionized and thereby consume the available UV photons in a certain frequency range. A related effect, called *mutual shielding*, occurs if other molecules possess transition lines that coincidentally overlap with those of abundant molecules and are therefore also shielded from UV photons. The self-shielding can be different for rarer isotologues, e.g. ^{13}CO and $C^{18}O$. They are less abundant, rendering their self-shielding capabilities less efficient as compared to the main isotopologue. Those molecules undergo isotope-selective photodissociation, thereby fractionating the molecular species.

However, secondary UV photons are also produced deep inside the cloud by a process known as *cosmic-ray-induced UV radiation* (Prasad & Tarafdar 1983, Gredel et al. 1989). In this process, cosmic-rays penetrate through the cloud, thereby ionize the abundant H_2 molecules, which release energetic electrons. The electrons then excite H_2 molecules, which relax by emitting UV photons.

Cosmic-ray dissociation and - Ionization
Since cosmic-rays are able to penetrate into the interior of molecules clouds, they can also directly dissociate or ionize molecules. The rate constant for cosmic-ray dissociation and ionization is expressed by:

$$k_{CR} = \alpha\zeta, \tag{1.67}$$

where α is a tabulated value specific to the molecule and ζ the cosmic-ray ionization rate. A value of $\zeta = 1.3 \times 10^{-17}$ s^{-1} is customarily used as canonical value. However, the value is expected to be highly specific to the environment of the particular source (Pineda et al. 2024).

1.5.1.4 Recombination reactions

Radiative recombination
In radiative recombination reactions, a free electron neutralizes a positively charged ion, thereby relaxing excess energy by emission of a photon.

Cation-anion recombination
In cation-anion recombination reactions, a positively and a negatively charged ion neutralize each other without association. Their typical rate coefficients are relatively high, ranging around

10^{-7} cm^3 s^{-1} due to the long-range attractive force between the ions.

Electron attachment
In electron attachment reactions, a free electron recombines with a neutral molecule, possibly releasing excess energy by emission of a photon. These reactions are rare and inefficient, with typical rate coefficients ranging only around 10^{-16}-10^{-15} cm^3 s^{-1}.

1.5.2 Grain chemistry

Although dust grains account for only 1% of the mass of a molecular cloud, they play an essential role in the formation of common and abundant molecules as e.g. H_2, CH_3OH and other COMs. Their advantages as a chemical environment, compared to the gas phase, are threefold (van Dishoeck (2014)) : (i) they function as a reservoir, where molecules can be stored in close proximity for prolonged periods of time, (ii) thereby making it more likely that moderate activation energies can be overcome, and (iii) they can act as third body in reactions that absorb the released reaction enthalpy and prevent the product from immediate dissociation.

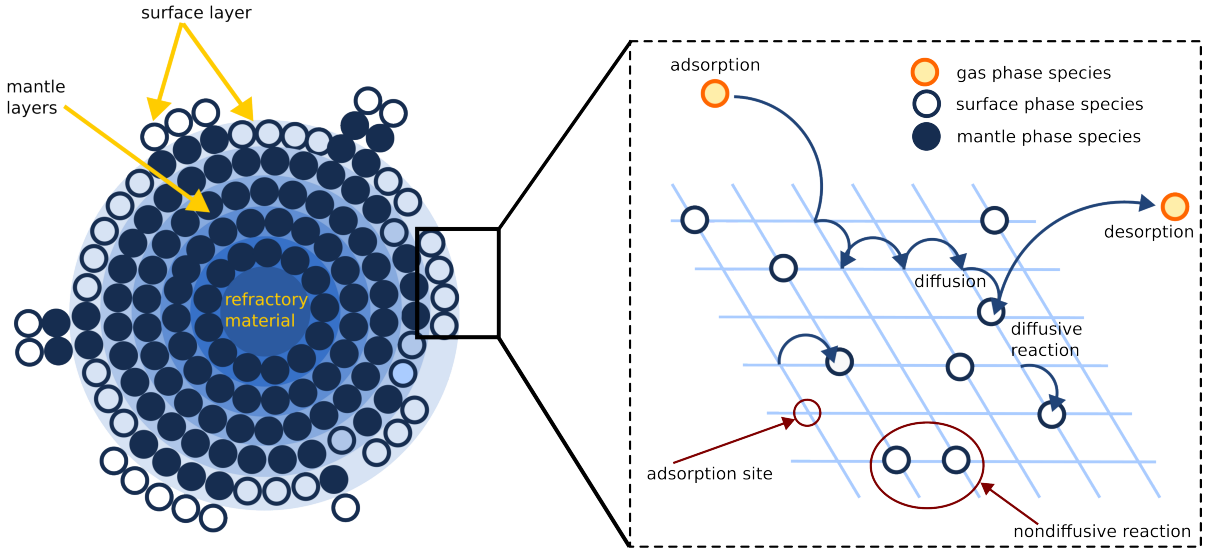

Figure 1.5: Schematic of an idealized interstellar dust grain; adapted from Yamamoto (2016).

In general, astrochemical models strongly idealize the properties of dust grains to keep the computational cost manageable. Figure 1.5 schematically summarizes the most common simplifications. Dust grains are usually assumed to be spherical with a singular radius of 0.1 µm. Recently, most astrochemical models use a three-phase model, consisting of three distinct phases: the gas phase, the surface phase and the mantle or bulk phase beneath the surface, with possible subdivision into individual layers for the latter two phases. In this scenario, the surface phase is both the place where the majority of chemical reactions are ongoing and where the exchange

of molecules with the gas phase happens. In contrast, the mantle phase is either assumed to be chemically inert, as is the case for the models presented in this work, or a slow diffusion and reaction process is allowed to occur (e.g.: Garrod 2013, Vasyunin et al. 2017).

The grain surface is represented by a lattice structure, where the intersections, the binding sites, are local potential minima. In a process called adsorption, gas phase molecules collide with the grain surface, stick to it and remain bound in those sites by either the attraction of weak van der Waals forces (physisorption) or strong chemical bonds to another surface molecule (chemisorption). The reverse process, called desorption, releases grain surface molecules into the gas phase. Here, one typically distinguishes between thermal desorption and nonthermal desorption processes, which include photodesorption (by primary and secondary UV photons), cosmic-ray induced desorption, reactive/chemical desorption, cosmic-ray induced and shock-related sputtering.

While on the surface, molecules can undergo diffusive or non-diffusive chemical reactions. In the Langmuir-Hinshelwood mechanism, molecules scan the surface diffusively for a suitable partner to react with. The diffusion process can either occur thermally, if the species is energetic enough to overcome the potential barrier (defined by the diffusion energy E_d) or by quantum tunneling through it. In addition to the diffusive reactions, molecules can also react non-diffusively with reactants that are formed in adjacent binding sites by preceding diffusive reactions, resulting in three-body or sequential reactions, or by preceding photodissociation reactions, resulting in photodissociation-induced reactions. Alternatively, they can arrive from the gas phase and react directly with a bound molecule, resulting in an Eley-Rideal reaction.

Table 1.2: Types of Grain Surface Reactions.

Gas-grain interactions	
Adsorption	$A \rightarrow A_S$
Thermal desorption	$A_S \rightarrow A$
Cosmic-ray induced desorption	$A_S + CR \rightarrow A$
Photodesorption	$A_S + h\nu \rightarrow A$
Reactive desorption	$A_S + B_S \rightarrow AB$
Surface phase reactions	
Grain surface reactions	$A_S + B_S \rightarrow AB_S$
Photodissociation	$AB_S \rightarrow A_S + B_S$

Notes. Plain letters denote gas phase species, while species with an additional subscript S denote grain surface species. $h\nu$ symbolizes a photon, while CR is a cosmic-ray.

Table 1.2 summarizes the basic types of chemical reactions occurring on the grain surface or as interaction with the gas phase. In the following, each of these processes and their mathematical formulation are described in more detail.

1.5.2.1 Adsorption

The rate of adsorption of species X[12] is given by:

$$\frac{\mathrm{d}n(\mathrm{X})}{\mathrm{d}t} = k_{\mathrm{acc,X}} n(\mathrm{X}) = S_{\mathrm{X}} v_{\mathrm{X}}(T) \sigma_{\mathrm{d}} n_{\mathrm{d}} n(\mathrm{X}), \tag{1.68}$$

where $k_{\mathrm{acc,X}}$ is the accretion rate coefficient, which is a product of the sticking coefficient S_{X}, the thermal velocity of species X in the gas phase, the geometric grain cross section $\sigma_{\mathrm{d}} = \pi r_{\mathrm{d}}^2$ and the number density of dust particles n_{d}.

The thermal velocity is equal to the mean speed of a Maxwell-Boltzmann distributed gas of species X at temperature T_{gas}:

$$v_{\mathrm{X}}(T_{\mathrm{gas}}) = \sqrt{\frac{8 k_{\mathrm{B}} T_{\mathrm{gas}}}{\pi m_{\mathrm{X}}}}, \tag{1.69}$$

where k_{B} is the Boltzmann constant and m_{X} the mass of species X.

In this work, the sticking coefficient - or sticking probability - is set 0.0 for ionic species and 1.0 for neutral species, with the exception of species for which experimental, temperature-dependent formulae are available: Cuppen et al. (2010) for H and D, He et al. (2016) for H_2, N_2, CO, O_2, CH_4, CO_2 and respective isotopologues.

1.5.2.2 Diffusive surface reactions

The reaction rate of a *Langmuir-Hinshelwood reaction*, a chemical reaction proceeding diffusively, between surface species $\mathrm{X_S}$ and $\mathrm{Y_S}$ is given by the following expression:

$$\frac{\mathrm{d}N(\mathrm{X_S})}{\mathrm{d}t} = \frac{\mathrm{d}N(\mathrm{Y_S})}{\mathrm{d}t} = f_{\mathrm{act}}(\mathrm{X_S}, \mathrm{Y_S})[k_{\mathrm{hop,X}} N(\mathrm{X_S})] \frac{N(\mathrm{Y_S})}{N_{\mathrm{sites}}} + f_{\mathrm{act}}(\mathrm{X_S}, \mathrm{Y_S})[k_{\mathrm{hop,Y}} N(\mathrm{Y_S})] \frac{N(\mathrm{X_S})}{N_{\mathrm{sites}}}, \tag{1.70}$$

which consists of two similar terms. The first term corresponds to the rate at which species $\mathrm{X_S}$ hops to another binding site ($[k_{\mathrm{hop,X}} N(\mathrm{X_S})]$), multiplied with the probability to meet reaction partner $\mathrm{Y_S}$. The second term corresponds analogously to the rate at which species $\mathrm{Y_S}$ hops over the surface and meets reaction partner $\mathrm{X_S}$. $f_{\mathrm{act}}(\mathrm{X_S}, \mathrm{Y_S}) \in [0,1]$ denotes an efficiency of a chemical reaction to occur between species $\mathrm{X_S}$ and $\mathrm{Y_S}$ and is explained in more detail in Section 1.5.2.4. Equation 1.70 is typically abbreviated to:

$$\frac{\mathrm{d}N(\mathrm{X_S})}{\mathrm{d}t} = \frac{\mathrm{d}N(\mathrm{Y_S})}{\mathrm{d}t} = k N(\mathrm{X_S}) N(\mathrm{Y_S}) \tag{1.71}$$

with the rate coefficient $k = f_{\mathrm{act}}(\mathrm{X_S}, \mathrm{Y_S})(k_{\mathrm{hop,X}} + k_{\mathrm{hop,Y}})/N_{\mathrm{sites}}$. Here, however, the long form is presented as well to highlight its structural similarity to the non-diffusive reactions introduced in Section 1.5.2.3

[12]Throughout this thesis, gas phase species are denoted with X and Y, grain surface species adopt an additional subscript $\mathrm{X_S}$ and $\mathrm{Y_S}$.

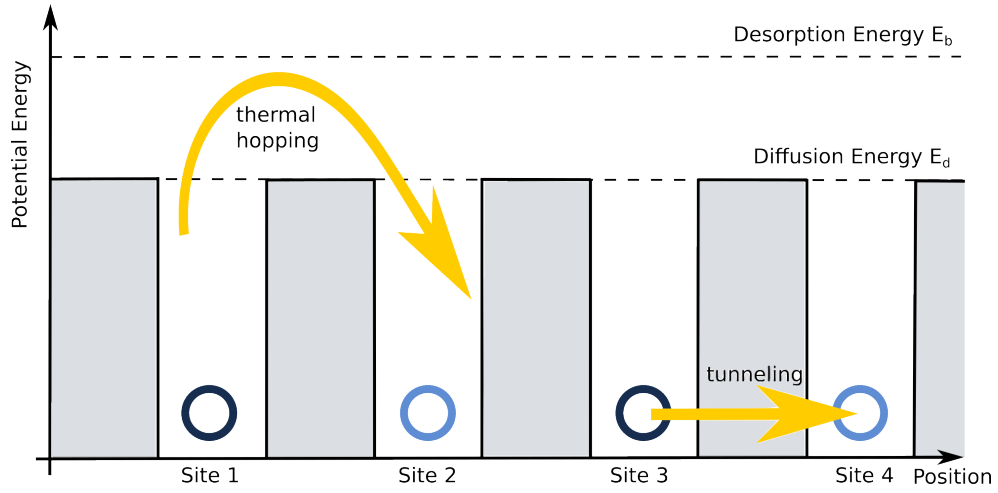

Figure 1.6: Schematic of the grain surface potential, adapted from Yamamoto (2016).

An important step in Langmuir-Hinshelwood reactions is the diffusion of one reaction partner to another one on the surface of the dust grain. Figure 1.6 schematically depicts how this process is traditionally modelled (Hasegawa et al. 1992). The diffusion energy E_d is the energy necessary for molecules to be able to leave their current binding site and diffuse over the surface into another neighbouring site. It is necessarily lower than the binding (or desorption energy), which is the energy that the molecule needs to completely desorb from the grain surface into the gas phase. Usually, the diffusion energy E_d is parametrised as a fixed ratio of the binding energy, the diffusion-to-binding energy ratio, which commonly assumes values between 0.2 and 0.7 (Furuya et al. 2022b). Diffusion proceeds either by thermal hopping of the reactant over the potential barrier or by quantum tunneling through it.

The rate of thermal diffusion, also called hopping rate, is defined by:

$$k_{\mathrm{hop,X}} = \nu_{0,\mathrm{X}} \exp(-E_{\mathrm{d,X}}/T_{\mathrm{dust}}), \tag{1.72}$$

where $\nu_{0,\mathrm{X}}$ is the attempt frequency and T_{dust} the dust or grain temperature.
The characteristic (or attempt) frequency is usually expressed as an harmonic oscillator relation:

$$\nu_{0,\mathrm{X}} = \left(\frac{2 n_\mathrm{s} E_{\mathrm{d,X}}}{\pi^2 m_\mathrm{X}}\right)^{1/2}, \tag{1.73}$$

where n_s is the surface density of binding sites, typically set to a value of $n_\mathrm{s} = 1.5 \times 10^{15}\,\mathrm{cm}^{-2}$ (Hasegawa et al. 1992, Semenov et al. 2010). Equation 1.73 produces values in the range of 10^{12}-$10^{14}\,\mathrm{s}^{-1}$. It has not been until very recently that attempt frequencies start to get reported systematically based on experimental works (see e.g. Minissale et al. 2022). In that work, values up to $10^{18}\,\mathrm{s}^{-1}$ have been found for particular species.

The rate of diffusion by quantum tunneling is defined by:

$$k_{\mathrm{tunnel,X}} = \frac{\nu_{0,\mathrm{X}}}{N_{\mathrm{sites}}} \exp\left(2\left(\frac{a}{\hbar}\right)\sqrt{2m_{\mathrm{X}}k_{\mathrm{B}}E_{\mathrm{d,X}}}\right), \tag{1.74}$$

where a is the width of a rectangular potential barrier, here assumed to be 1 Å. Typically, diffusion by quantum tunneling is enabled in addition to thermal diffusion and only for very light species as e.g. H and D (this work) or H and H_2 (Vasyunin et al. 2017).

1.5.2.3 Non-diffusive surface reactions

Multiple versions of non-diffusive reaction mechanisms were published in the literature recently (e.g.: Garrod & Pauly 2011, Ruaud et al. 2015, Chang & Herbst 2016, Dulieu et al. 2019, Shingledecker et al. 2019). They are all based on a similar principle, but vary in the detailed implementation. This work adopts and describes non-diffusive reaction mechanisms as proposed by Jin & Garrod (2020) and Garrod et al. (2022).
In general, non-diffusive reactions are treated as two-step processes, consisting of an initiating reaction that makes one reaction partner 'appear' in a binding site close to the other reaction partner, and the follow-on reaction between those reaction partners. This approach allows to use the same grain surface chemical network that is used for the diffusive reactions. Reactions proceeding non-diffusively follow a very similar structure to the diffusive reactions:

$$\frac{\mathrm{d}N(\mathrm{X_S})}{\mathrm{d}t} = \frac{\mathrm{d}N(\mathrm{Y_S})}{\mathrm{d}t} = R_{\mathrm{non-diff.}} = f_{\mathrm{act}}(\mathrm{X_S},\mathrm{Y_S})R_{\mathrm{comp}}(\mathrm{X_S})\frac{N(\mathrm{Y_S})}{N_{\mathrm{sites}}} + f_{\mathrm{act}}(\mathrm{X_S Y_S})R_{\mathrm{comp}}(\mathrm{Y_S})\frac{N(\mathrm{X_S})}{N_{\mathrm{sites}}}. \tag{1.75}$$

The diffusion rate is replaced by the completion rate $R_{\mathrm{comp}}(\mathrm{X_S})$, that describes the rate of 'appearance', meaning either the delivery from the gas phase (in the case of an Eley-Rideal reaction), or the formation by an initiating reaction, and subsequent reaction with the reaction partner $\mathrm{Y_S}$:

$$R_{\mathrm{comp}}(\mathrm{X_S}) = \frac{1}{1/R_{\mathrm{app}}(\mathrm{X_S}) + t_{\mathrm{X_S Y_S}}} \tag{1.76}$$

$$R_{\mathrm{comp}}(\mathrm{Y_S}) = \frac{1}{1/R_{\mathrm{app}}(\mathrm{Y_S}) + t_{\mathrm{X_S Y_S}}}, \tag{1.77}$$

with the formulation of the appearance rate R_{app} depending on the individual non-diffusive reaction mechanism used (see reactions 1.79 - 1.82 below). The average lifetime of both reaction partners staying in a state in which they are ready to react against an event occurring that destroys that state again (including the reaction itself) is given by:

$$t_{\mathrm{X_S,Y_S}} = \frac{1}{(\nu_{\mathrm{X_S,Y_S}}\kappa_{\mathrm{X_S,Y_S}} + k_{\mathrm{hop}}(\mathrm{X_S}) + k_{\mathrm{hop}}(\mathrm{Y_S}))}, \tag{1.78}$$

where $\nu_{X_S Y_S}$ is the larger of the characteristic vibrational frequencies of both reaction partners and $\kappa_{X_S Y_S}$ the probability to overcome the activation-energy barrier, which will be explained in detail in Section 1.5.2.4.

In the following, the different types of non-diffusive reactions and their mathematical formulation is described in detail:

- **Eley-Rideal reactions** are reactions in which a gas phase species adsorbs onto the grain surface and immediately finds a reaction partner at its adsorption site.
  The appearance rate $R_{\mathrm{app,ER}}(X_S)$ of Eley-Rideal reactions with species X is simply equal to the adsorption $R_{\mathrm{ads}}(X_S)$ of species X_S:

$$R_{\mathrm{app,ER}}(X_S) = R_{\mathrm{ads}}(X_S). \tag{1.79}$$

- **Photodissociation-induced reactions** are reactions in which a grain surface species is dissociated into two (or more) fragments by a UV photon - either directly by the interstellar radiation field or by secondary photons produced by cosmic-rays. Subsequently, one of the dissociated fragments reacts with a species in an adjacent binding site. The appearance rate of photodissociation-induced reactions $R_{\mathrm{app,PDI}}(X_S)$ is the sum of the rates of all photodissociation processes R_{photo} producing species X_S:

$$R_{\mathrm{app,PDI}}(X_S) = \sum_{\text{all photo}} R_{\mathrm{photo}}(X_S) \tag{1.80}$$

- **Three-body reactions (3B)** are reactions in which a grain surface species is formed by a diffusive reaction or an Eley-Rideal or photodissociation-induced reaction and immediately reacts further with a suitable reaction partner in its vicinity. The appearance rate of three-body reactions $R_{\mathrm{app,3B}}$ is the sum of all diffusive reactions producing species X_S, and all Eley-Rideal and photodissociation-induced reactions:

$$R_{\mathrm{app,3B}}(X_S) = \sum_{\text{all diff.reac.}} R_{\mathrm{diff.reac.}}(X_S) + \sum_{\text{all ER reac.}} R_{\mathrm{ER\,reac.}}(X_S) + \sum_{\text{all PDI reac.}} R_{\mathrm{PDI\,reac.}}(X_S) \tag{1.81}$$

- **Multiple rounds of three-body reactions** are a variation of the three-body reactions, in which a three-body reactions triggers another subsequent round of three-body reactions. Theoretically, the number of rounds is arbitrary, however, the effect on the reaction rates is usually assumed to diminish, while the computational cost quickly increases, which is why typically only a second or third round is considered. The appearance rate of a subsequent round of three-body reactions $R_{\mathrm{app,mult.\,3B}}$ is the sum of the rates of all three-body reactions $R_{\mathrm{3B\,reac.}}$ of the preceeding round producing species X_S:

$$R_{\mathrm{app,mult.\,3B}}(X_S) = \sum_{\text{all 3B reac.}} R_{\mathrm{3B\,reac.}}(X_S) \tag{1.82}$$

- **Three-body reactions with excited formation (3BEF)** are a variation of the three-body reactions, in which the energy released by the initiating reaction is sufficient for species

X_S to overcome the activation energy barrier of the follow-on reaction and immediately react with its reaction partner Y_S. This reaction type is only applied to initiating/follow-on reactions pairs, for which (i) the initiating reaction has only one reaction product, (ii) the follow-on reaction has an activation energy E_A and (iii) the exothermicity of the initiating reaction E_{reac} is larger than this activation energy. If requirements (i)-(iii) are not fullfilled, the reaction is simply treated as a regular 3B reaction. If the requirements are met, 3BEF reactions proceed only with a certain probability f_{EF}, meaning that the reaction is only treated in a fraction f_{EF} of cases as a 3BEF reaction, while in (1-f_{EF}) of cases, it is treated as a slower 3B reaction.

Equation 1.75 needs to be altered slightly:

$$\frac{\mathrm{d}N(X_S)}{\mathrm{d}t} = f_{EF}(X_S, Y_S)R_{comp}(X_S)\frac{N(Y_S)}{N_{sites}} + (1 - f_{EF})f_{act}(X_S, Y_S)R_{comp}(X_S)\frac{N(Y_S)}{N_{sites}}, \quad (1.83)$$

where f_{EF} is the fraction of successful 3BEF cases, that proceed with an efficiency f_{act} = 1. The appearance rate for 3BEF reactions is defined analogously to the one for 3B reactions (equation 1.81). Using Rice-Ramsperger-Kassel (RRK) theory [13] , one can derive a probability that the required energy is instantaneously present in the correct vibrational mode:

$$P_{EF} = \left[1 - \frac{E_A}{E_{reac}}\right]^{s-1}, \quad (1.84)$$

with s being the sum of vibrational and translational modes. By considering the competition with other processes, namely energy loss from the molecule to the grain surface and diffusion of the excited species away from the binding sites, one can derive the fraction of successful 3-BEF cases to be:

$$f_{EF} = \frac{1}{4}\left(\frac{P_{EF}}{1 + P_{EF}}\right) \quad (1.85)$$

Here, to keep equation 1.83 concise, only one initiating/follow-on reaction pair, producing species X_S close to species Y_S, is considered. However, it is possible that also species Y_S is produced adjacent to species X_S and in that case another analogous term is added. Moreover, in case there are multiple initiating/follow-on reactions pairs forming species X_S (or Y_S), the term is simply repeated with another R_{comp}. It is noteworthy that although $f_{act}(X_S, Y_S)$ and $N(Y_S)/N_{sites}$ only depend on the follow-on reaction, $\sum_i R_{comp,i}$ is not mathematically identical to $1/(1/\sum_i R_{app,i} + t_{X_S Y_S})$. It is, however, treated in this manner to keep the structure of equation 1.83 simple.

[13] RRK theory is a theory of chemical reactivity, which allows estimates of reaction rates from characteristics of the potential energy surface.

1.5.2.4 The efficiency factor

In general, chemical reactions between two radicals are barrierless. However, chemical reactions between a radical and a closed-shell molecule, even if they are exothermic, typically exhibit a more complicated reaction behaviour. Figure 1.7 depicts the potential energy diagram of the simplest variant, an exothermic reaction with an activation energy barrier that can be described by the Arrhenius equation 1.57. The activation-energy barrier is usually assumed to be a potential barrier of height E_A and width a, which needs to be overcome either thermally or by quantum tunneling.

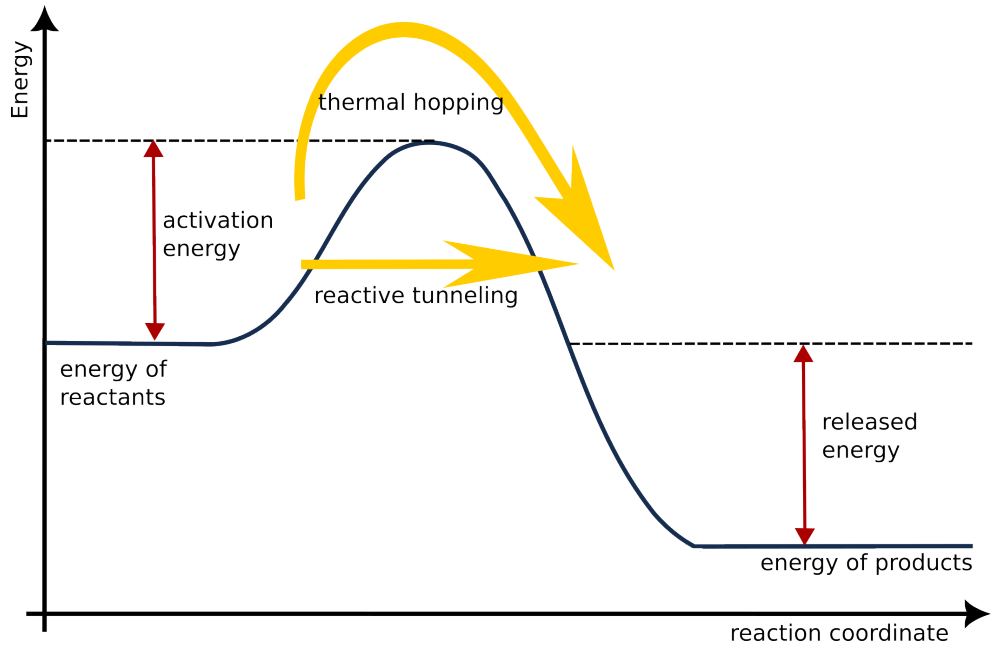

Figure 1.7: Potential energy diagram of an exothermic reaction with an activation-energy barrier. The potential barrier can either be surmounted by thermal hopping or by tunneling.

The probability to surmount the activation-energy barrier E_A (in Kelvin) by thermally hopping over it can be simply described by a Boltzmann factor:

$$\kappa = \exp(-E_A/T_{dust}), \tag{1.86}$$

where T_{dust} is the temperature of the dust grain.

The probability to quantum tunnel through the activation-energy barrier is typically described by the tunneling probability through a rectangular barrier of width a:

$$\kappa = \exp\left[-2\left(\frac{a}{\hbar}\right)\sqrt{2\mu E_A}\right], \tag{1.87}$$

where μ is the reduced mass of reactants X_S and Y_S. Both reaction 1.86 and 1.87 ensure that κ stays in the range from 0 to 1.0 and converges toward a value of 1.0 for barrierless reactions.

Different approaches to determine the reaction probability of an exothermic reaction with an activation barrier have been proposed by Hasegawa et al. (1992) and Chang et al. (2007):

- The **single collision model** (Hasegawa et al. 1992) derives the probability for the reaction to occur upon encounter of both reactants, assuming that the reaction either happens at the first attempt or not at all. The efficiency factor f_{act} is simply set to the parameter κ:

$$f_{\mathrm{act}}(\mathrm{X_S}, \mathrm{Y_S}) = \kappa_{\mathrm{X_S Y_S}}. \tag{1.88}$$

- The **reaction-diffusion competition model** (Chang et al. 2007) considers that reactants on the grain surface, unlike in the gas phase, can stay in close proximity for an extended period of time and therefore have multiple attempts to react with each other. The reaction probability is treated as a competition process between reaction and diffusion (and possibly desorption). The efficiency factor f_{act} is given by the following equation:

$$f_{\mathrm{act}}(\mathrm{X_S}, \mathrm{Y_S}) = \frac{\nu_{\mathrm{X_S Y_S}} \kappa_{\mathrm{X_S Y_S}}}{\nu_{\mathrm{X_S Y_S}} \kappa_{\mathrm{X_S Y_S}} + k_{\mathrm{hop}}(\mathrm{X_S}) + k_{\mathrm{hop}}(\mathrm{Y_S})}, \tag{1.89}$$

  where $\nu_{\mathrm{X_S Y_S}}$ is taken to be the larger of the characteristic vibrational frequencies of both reactants following the approach by Garrod & Pauly (2011), Jin & Garrod (2020), and $k_{\mathrm{hop}}(\mathrm{X_S})$ and $k_{\mathrm{hop}}(\mathrm{Y_S})$ are the diffusion rates of species $\mathrm{X_S}$ and $\mathrm{Y_S}$ respectively.

1.5.2.5 Desorption

In the past three decades, a multitude of different methods for the desorption of molecules from the surface of interstellar dust grains have been proposed in the literature. In this work, the four most common methods: thermal desorption, photodesorption, cosmic-ray induced desorption and reactive or chemical desorption, are used. Other methods include sputtering by heavy cosmic-rays (Dartois et al. 2015, Dartois et al. 2019) or shock-related sputtering of the grain mantles (e.g. May et al. 2000, Jiménez-Serra et al. 2008).

Most desorption methods, independent of their particular mechanism, depend on the binding energy of the respective molecule. Recently, increasing experimental and theoretical evidence emerged that the binding energy is not well described by a unique value, but rather a binding energy distribution (e.g.: Ferrero et al. 2020, Bovolenta et al. 2020, Tinacci et al. 2022, Kakkenpara Suresh et al. 2024), which also depends on the structure and contents of the ice matrix. Although there has been some work to integrate binding energy distributions into astrochemical models (e.g. Grassi et al. 2020), the proposed treatment quickly becomes prohibitively computationally costly when combined with a large network. Therefore, binding energies are still typically assumed to be a single value for each species.

Thermal desorption

The rate of thermal desorption of species X is given by:

$$\frac{\mathrm{d}n(\mathrm{X_S})}{\mathrm{d}t} = -k_{\mathrm{td,X}} n(\mathrm{X_S}) = -\nu_{0,\mathrm{X}} \exp\left(-\frac{E_{\mathrm{D,X}}}{T_{\mathrm{d}}}\right) n(\mathrm{X_S}), \tag{1.90}$$

where $k_{\mathrm{td,X}}$ is the thermal desorption rate coefficient, which is a product of the characteristic frequency $\nu_{0,\mathrm{X}}$ and an exponential factor including the binding or desorption energy $E_{\mathrm{D,X}}$ of species X and the dust temperature T_{dust}.

While thermal desorption is the main desorption mechanism for 'warm' sources e.g. hot cores and corinos, its significance is limited in pre-stellar cores as their extremely low temperatures suppress the exponential term. However, for light species with low binding energies, namely H and H_2, it is the main source of desorption for the outer warmer ($\geq$ 15 K) part of the core's envelope.

Cosmic-ray Induced desorption

Cosmic-rays are high-energy particles that are accelerated to high velocities, extending even into the ultrarelativistic realm (Draine 2011).

When a dust grain is struck by a cosmic-ray, the resulting energy deposition causes a sudden increase in grain temperature, which leads to the thermal desorption of grain species into the gas phase while the grain remains in this hot state. A simple, but widely used description of cosmic-ray desorption was proposed in Hasegawa & Herbst (1993). They estimated that cosmic-rays in the 20-70 MeV nucleon^{-1} energy range deposit an energy of 0.4 MeV into the grain. This energy deposition result in an increase in temperature to a value $T_{\rm max}$ of 70 K. The rate of cosmic-ray induced desorption of species X is given by the product of the thermal desorption rate $k_{\rm td,X}(T_{\rm max})$ and an efficiency factor $f(a, T_{\rm max})$ for a grain of radius a:

$$k_{\rm crd,X} = f(a, T_{\rm max}) k_{\rm td,X}(T_{\rm max}). \tag{1.91}$$

The efficiency factor $f(a, T_{\rm max})$ is the ratio of the cooling time of the grains $\tau_{\rm cool}$ to the heating interval $\tau_{\rm heat}$. This work adopts two different methods to determine the efficiency factor $f(a, T_{\rm max})$:

1. The Hasegawa & Herbst (1993) model proposes constant values for the cooling $\tau_{\rm cool}$ and heating $\tau_{\rm heat}$ times. For a grain with a radius of 0.1 µm, the efficiency factor $f(a, T_{\rm max})$ yields: 10^{-5} s/3.16×10^{13} s = 3.16×10^{-19}.

2. A refinement, introduced in Sipilä et al. (2021), in which the cooling time $\tau_{\rm cool}$ is dynamically calculated from the individual time-dependent desorption rates of the surface molecules. Additionally, the heating time $\tau_{\rm heat}$ can be calculated by using different cosmic-ray fluxes.

Photodesorption

When a dust grain is struck by a (primary or secondary) UV photon, it can desorb certain molecular species from the surface of the dust grain. The rate of photodesorption of species X is given by:

$$k_{\rm pd,X} = F_{\rm ISRF}\, G_{\rm CR}\, \gamma\, \sigma_{\rm d}, \tag{1.92}$$

where $F_{\rm ISRF}$ is the flux of interstellar UV photons, $G_{\rm CR}$ the efficiency of CR-induced UV flux, γ is the photoyield of species X and $\sigma_{\rm d}$ the geometric grain cross section. In this thesis, photodesorption is only applied to species for which experimental photoyields are available, namely CO, N_2, CO_2 (Öberg et al. 2009a), H_2O (Öberg et al. 2009b), NH_3 (Martín-Doménech et al. 2018) and their deuterated isotopologues. It is noteworthy that methanol itself is not undergoing photodesorption in the model presented in this thesis, which is consistent with experimental

findings, which showed that photodesorption of methanol is negligible as it is rather dissociated into smaller fragments (Bertin et al. 2016, Cruz-Diaz et al. 2016).

Reactive/Chemical desorption

Reactive desorption is a process in which the energy released in an exothermic chemical reaction on the surface of the dust grain is (partially) used to desorb one (or multiple) reaction products. To describe the reactive desorption process, every exothermic surface reaction is duplicated and multiplied either with the fraction of reactions resulting in successful desorption of the reaction product into the gas phase, termed the reactive desorption efficiency f_{rd} (reaction 1.93), or with the fraction of reactions resulting in the reaction product staying on the grain surface $(1 - f_{\mathrm{rd}})$ (reaction 1.94):

$$\frac{\mathrm{d}n(\mathrm{X})}{\mathrm{d}t} = f_{\mathrm{rd}} \cdot kn(\mathrm{X_s})n(\mathrm{Y_S}) \tag{1.93}$$

$$\frac{\mathrm{d}n(\mathrm{X_S})}{\mathrm{d}t} = (1 - f_{\mathrm{rd}}) \cdot kn(\mathrm{X_s})n(\mathrm{Y_S}) \tag{1.94}$$

In case that the eligible reaction has two reaction products, the respective reaction is duplicated considering every combination of possible desorption behaviour: (i) both products stay on the surface, (ii) the first product desorbs, while the second product stays behind, (iii) the second product desorbs, while the first product stays behind and (iv) both products desorb into the gas phase.

Multiple parametrizations for the derivation of the reactive desorption efficiency f_{rd}, that can be easily included into a rate equation code have been proposed and tested in the literature:

1. A single constant value, typically $f_{\mathrm{rd}} = 1\%$, which is justified by the most recent generation of dedicated laboratory experiments (e.g. Minissale & Dulieu 2014, Chuang et al. 2018, Oba et al. 2018, Furuya et al. 2022a, Santos et al. 2023) that estimated the reactive desorption efficiency f_{rd} to be in the range of 1-3% for individual reactions.

2. Garrod et al. (2007) proposed a formula, derived by RRK theory, that derives an individual reactive desorption efficiency for each product, depending on the exothermicity of the reaction, independent of the surface content and its coverage. The method assumes that reactive desorption occurs only for single product reactions. For two-product reactions, it is presumed that the energy is lost to lateral translation along the grain surface and no desorption occurs. Typically, free parameters are chosen in a way that the upper limit for the reactive desorption efficiency is 1%.

3. Minissale et al. (2016b) proposed a semi-empirical formula that derives an individual reactive desorption efficiency for each product, depending on the exothermicity of the reaction and the surface coverage, taking into account experimental results that find the reactive desorption process from water ice to be negligible. Chapter 2 in this thesis (Riedel et al. 2023) describes an update to this mechanism accounting for the mass-dependent partitioning of energy for reactions with multiple products.

4. A combination of parametrization 2 and 3, proposed in Borshcheva et al. (2025), where the reactive desorption efficiency is computed using the formula by Garrod et al. (2007), but only applied to the non-water surface fraction.

1.6 Contents of this thesis

After introducing the theoretical fundamentals involved in this thesis, the following chapters present the results and discussion of three modelling and one observational collaborative project concerning the deuteration of complex organic molecules. Here, I summarize each chapter:

- Chapter 2 introduces an experiment-based treatment of reactive desorption into the gas-grain chemical code *pyRate*. Furthermore, this Chapter focuses on the improvement of models, describing the formation and deuteration of methanol in pre-stellar cores and identifies critical chemical and physical parameters.
- Chapter 3 adds multiple non-diffusive reaction mechanisms to *pyRate*, exploring and quantifying their impact on the formation and deuteration of methanol. Moreover the influence of several other methods and parameters are evaluated, including the derivation of reaction probabilities, the inclusion of abstraction reactions and the efficiency of the reactive desorption process.
- Chapter 4 extends the deuterated chemical network to molecular species, consisting of up to nine atoms. This chemical network is subsequently applied in combination with the non-diffusive reaction mechanisms, developed in Chapter 3, to predict the formation and deuteration of acetaldehyde, methyl formate and glycoaldehyde in pre-stellar cores. The obtained values are compared to available observations of the protostellar system IRAS 16292-2422 B.
- Chapter 5 discusses a collaborative project (PI:Silvia Spezzano), which reports the first detection of the doubly deuterated methanol isotopologue CHD_2OH in the pre-stellar core L1544. The observations are compared to several models, developed in Chapter 3, emphasizing the importance of abstraction reactions. Additionally, predictions for the formation and deuteration of the pre-stellar cores HMM1 and L694-2 are made and compared to observationally obtained values.
- Chapter 6 provides a brief summary of the main conclusions of the works presented in this thesis, along with prospective research directions that build upon the methods developed and results obtained here.

Chapter 2

Modelling deuterated isotopologues of methanol towards the pre-stellar core L1544

The contents of this chapter were published in Astronomy & Astrophysics.

Abstract

Context. In the extremely cold and dark environments of pre-stellar cores, methanol is formed on the surface of interstellar dust grains and released into the gas phase via non-thermal desorption mechanisms. Gaseous methanol constitutes the starting point for the formation of many massive complex organic molecules and is therefore of utmost importance for the build-up of chemical complexity.
Aims. We aim to improve upon a previous model for the prediction of column densities and deuterium fractions of non-deuterated and singly deuterated methanol. Thereby, we try to identify crucial chemical and physical parameters for which the study of deuteration could provide valuable additional constraints.
Methods. We employed a gas-grain chemical code to devise a model that is in agreement with the observed column density and deuterium fraction profiles of the innermost region of the pre-stellar core L1544. For that purpose, we developed a new treatment of reactive desorption, deriving an individual reactive desorption efficiency for every product species in a chemical reaction that depends on the reaction enthalpy and type of the underlying surface. Furthermore, we explored several options to promote the diffusion of hydrogen and deuterium atoms over the surface of interstellar dust grains in order to increase methanol formation.
Results. Our fiducial model employs diffusion via the quantum tunnelling of hydrogen and deuterium atoms, resulting in CH_3OH and CH_2DOH column densities that are approximately an order of magnitude lower than the observed values, which is an improvement over the results of the previous model by a factor of 10. The $N(CH_2DOH)/N(CH_3OH)$ ratio is reproduced within

a factor of 1.2 for the centre and 1.8 for the position of the methanol peak. Given the large uncertainties that chemical models typically have, we consider our predictions to be in agreement with the observations. In general, we conclude that a diffusion process with a high diffusion rate needs to be employed to obtain methanol column densities that are in accordance with the observed values. Also, we find that the introduction of abstraction reactions into the methanol formation scheme suppresses deuteration when used in combination with a high diffusion rate.

Keywords: ISM: abundances - ISM: clouds - ISM: molecules - astrochemistry

2.1 Introduction

Methanol (CH_3OH) is the simplest O-bearing complex organic molecule (COM) in the interstellar medium and an important precursor of saturated, more massive COMs that are formed in the gas phase. Previous work, however, showed theoretically (Garrod et al. 2006a) and experimentally (Geppert et al. 2005) that the presumed gas-phase formation route is very inefficient and unable to account for the observed gas-phase abundances. Simultaneously, the formation of methanol on the surface of dust grains was proposed and experimentally investigated in an extensive manner in several independent projects (e.g. Watanabe & Kouchi 2002; Fuchs et al. 2009). It was concluded that formaldehyde and methanol can be produced by multiple successive addition reactions of CO with diffusive hydrogen atoms. The measured significant isotope effect for hydrogen and deuterium suggests that hydrogenation and deuteration on the surface proceeds via quantum tunnelling reactions (Hidaka et al. 2007) and therefore progresses at a much higher rate than in the gas phase. Additionally, the existence of so-called abstraction reactions, which remove H_2 from the molecule and thereby reverse the addition reaction, was postulated and found in various laboratory experiments (e.g. Hidaka et al. 2009; Minissale et al. 2016c). However, there seems to be some disagreement about the exact reaction scheme and the magnitude of the reaction rates of the different experimental approaches.

For the production of more advanced COMs in the gas phase, methanol needs to desorb from the surface of the dust grains. In hot cores and corinos, the desorption of the molecular contents of the surface phase does proceed very efficiently via thermal evaporation and photoevaporation. In the cold and dark environment of pre-stellar cores, however, these mechanisms are negligible. Therefore, only very low abundances of methanol were expected to exist in the gas phase of pre-stellar cores. Surprisingly, several surveys, for example Bacmann et al. (2012), Cernicharo et al. (2012), and Jiménez-Serra et al. (2016), conducted towards dark molecular clouds found comparatively high abundances of methanol and other COMs.

In order to explain these unexpected findings, astrochemical models need to employ other mechanisms for the evaporation of surface molecules. One promising candidate, reactive desorption, is based on the energy released in an exothermic chemical reaction, which can lead to the desorption of the reaction product(s). Nowadays, most chemical codes include a simple treatment of reactive desorption following the recipe described by Garrod et al. (2007). According to those authors, a (nearly) constant reactive desorption efficiency, typically 1%, is employed independent

of the desorbing molecule. However, recent laboratory experiments have found that the reactive desorption efficiency is strongly dependent on the chemical reaction and the type of underlying surface (Minissale et al. 2016b; Chuang et al. 2018).

In this paper we developed an updated version of the description of reactive desorption presented by Vasyunin et al. (2017), itself based on the experiments by Minissale et al. (2016b). Our work is motivated by the column density maps of CH_3OH and CH_2DOH and the theoretical predictions presented by Chacón-Tanarro et al. (2019a). They carried out single-dish observations with the Institut de Radioastronomie Millimétrique (IRAM) 30m telescope (also Bizzocchi et al. 2014; Vastel et al. 2014; Spezzano et al. 2016), showing that CH_3OH peaks in an asymmetric ring around the dust peak, with the strongest emission in the northern part of the pre-stellar core. Chacón-Tanarro et al. (2019a) analysed the formaldehyde and methanol column densities along a cut set by the position of the dust and the offset methanol peak.

An important aim of this work is to improve upon the theoretical column density profiles made by the chemical code pyRate (hereafter model S16; Sipilä et al. 2015a, 2019b), particularly to get more accurate predictions about the deuteration of methanol. Additionally, we compared our predictions with the results of the chemical code presented in Vasyunin et al. (2017, hereafter the V17 model). These two models were used in Chacón-Tanarro et al. (2019a), who found that the V17 model produced acceptable results for non-deuterated methanol (CH_3OH). However, the column density profile for singly deuterated methanol (CH_2DOH) had to be obtained using the N(CH_2DOH)/N(CH_3OH) ratio predicted by pyRate since the MONACO code (Vasyunin et al. 2017) does not treat deuteration, whereas pyRate includes an extensive description of deuterium chemistry. To carry out a similar analysis in a consistent manner, we implemented an updated version of the reactive desorption mechanism used in Vasyunin et al. (2017) into pyRate.

Vasyunin et al. (2017) and Chacón-Tanarro et al. (2019a) both find that diffusion via the quantum tunnelling of atomic and molecular hydrogen had to be employed in order to explain the observed methanol column density profile. In the present paper, we employed tunnelling diffusion for hydrogen and deuterium atoms for our fiducial model, neglecting the tunnelling diffusion of molecular hydrogen. However, we also explore the option to promote thermal diffusion by decreasing the diffusion-to-binding energy ratio, $E_\mathrm{d}/E_\mathrm{b}$, which determines the threshold for the diffusion of molecules over the surface of an interstellar dust grain via thermal hopping, from 0.55 to the lowest value reported in the experimental literature (0.2; Furuya et al. 2022b). Moreover, we test several alternative sets of input parameter to see how well they are able to explain the observed deuterium fraction profile.

The paper is structured as follows: Section 2.2 describes the new reactive desorption mechanism and the chemical and physical model in detail. Section 2.3 describes the results of the fiducial model and compares them with the observationally obtained column density and deuterium fraction profiles from Chacón-Tanarro et al. (2019a) and with the results of the V17 model Vasyunin et al. (2017). Section 2.4 discusses multiple modifications to the chemical and physical parameters and their effects on the results. Section 2.5 presents our conclusions. Appendices A.1 and A.2 provide additional information on the chemical parameters and reaction schemes used.

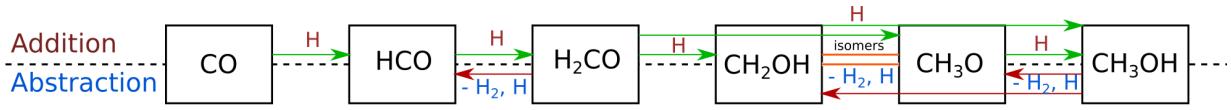

Figure 2.1: Reaction scheme for the formation of non-deuterated CH_3OH by successive hydrogenation. Hydrogen molecules can also be segregated from CH_3OH or its precursors via abstraction reactions.

2.2 Model

2.2.1 Treatment of reactive desorption

For the extension of the reactive desorption mechanism, we adopted the physical scenario proposed and experimentally justified by Minissale et al. (2016b). The mechanism is implemented following Vasyunin et al. (2017), but it is modified for this paper, as detailed below.

Minissale et al. (2016b) developed a formula that expresses the reactive desorption efficiency, RD, as a function of reaction and surface-dependent properties:

$$RD = \exp\left(-\frac{E_\mathrm{b} N}{\epsilon \Delta H}\right), \tag{2.1}$$

where ΔH is the reaction enthalpy, E_b the binding energy, N the number of the degrees of freedom (translational, rotational and vibrational) of the reaction product and ϵ the fraction of kinetic energy retained by the reaction product. We assumed that the available reaction enthalpy is distributed equally into all the degrees of freedom, N, and that only the energy going into the vertical translational degree of freedom is used for the desorption of an atom or a molecule from the surface of a dust grain. Therefore, for one-product reactions, $1/N$ of the reaction enthalpy is distributed into motion perpendicular to the surface of the dust grain. The number of degrees of freedom, N, of the product can be simply derived as $N = 3n_\mathrm{atoms}$, with n_atoms being the number of atoms of the reaction product. This approach has the effect that the less complex molecules, consisting of fewer atoms, can use a larger share of the reaction enthalpy for vertical motion off the surface. For the more complex molecules, the total number of degrees of freedom increases quickly with increasing number of atoms, due to the fact that larger molecules have more possibilities for vibrational excitation. However, the number of translational degrees of freedom stays the same. As a consequence, a smaller share of the reaction enthalpy is converted into vertical motion. For example, a forming CO molecule, with only 2 atoms, receives 1/6 of the reaction enthalpy for vertical motion, while a forming CH_3OH molecule, with 6 atoms, receives only 1/18.

The dependence of the reactive desorption efficiency on the type of surface is expressed by the fraction of kinetic energy, ϵ, received by the reaction product with mass m when colliding with a surface element with an effective mass M:

$$\epsilon = \left(\frac{M - m}{M + m}\right)^2. \tag{2.2}$$

In the experiments by Minissale et al. (2016b), the effective mass, M, is a parameter that needs to be fitted. It was found to be typically much larger than the mass of a single atom or molecule of the surface species, but is more consistent with a collective behaviour of also the neighbouring molecules that is induced by the rigidity of the surface. The more rigid the surface, the higher the effective mass of the surface element M and the easier it is for the reaction products to bounce off from the surface into the gas phase. For the effective masses we mostly kept the values adopted by Vasyunin et al. (2017), namely $M = 48$ amu for a H_2O surface and $M = 100$ amu for a CO-surface, with the exception of the effective mass for bare grain, where we took the somewhat lower value of $M = 120$ amu that has been suggested as a common value for carbonaceous and silicate grains following the experiments conducted by Minissale et al. (2016b). Every surface that does not consist of H_2O or bare grain is treated as if it were CO. Considering that grain surfaces in the inner, very cold regions of pre-stellar cores are covered, aside from CO itself, by species with a similar molecular weight (e.g. N_2, H_2CO and CH_3OH), this seems to be a reasonable approximation given the lack of more detailed measurements. To consider that a grain surface might be covered by a mixture of bare surface, H_2O or CO, we followed the average surface composition of the dust grains over time, starting with a bare grain surface, which is then quickly covered by water ice and later on CO. Then, we scaled the individual reactive desorption efficiencies for a reaction i by the fraction of the surface sites that are covered by the particular surface type, j:

$$RD_{\mathrm{tot}}(i,t) = \sum_j RD_{\mathrm{j}}(i) \cdot \frac{n_j^*(t)}{n_{\mathrm{tot}}^*(t)}, \tag{2.3}$$

where RD_{j} is the individual reactive desorption efficiency for either bare grain H_2O or CO, n_j^* the number of surface sites inhabited by surface type j and n_{tot}^* the total number of surface sites. The largest difference between the procedure applied in this paper and the one presented in Vasyunin et al. (2017) is the treatment of reactions with more than one reaction product. Vasyunin et al. (2017) treated multi-product reactions identically to one-product reactions, so that every reaction product receives the entire available reaction enthalpy. This approach clearly violates energy conservation. However, this simplification was considered to be negligible for the chemical network that was used in Vasyunin et al. (2017) as it includes mostly two-product reactions involving heavier reactants that proceed inefficiently at the low grain temperatures typical of pre-stellar cores.

In contrast, the method presented in this paper includes a recipe for the mass-dependent partitioning of the total reaction enthalpy in the case of a two-product reaction. We assumed that the desorbing molecules are first isolated from the surface and then undergo an elastic collision with the surface of the grain to gain velocity in the vertical direction. Considering the conservation of linear momentum, one can derive an expression for the kinetic energy, E_{kin}, received by a product species i:

$$E_{\mathrm{kin}}(\mathrm{i}) = E_{\mathrm{kin}} \cdot \frac{m_{\mathrm{j}}}{m_{\mathrm{i}} + m_{\mathrm{j}}} = \frac{N_{\mathrm{trans}}}{N_{\mathrm{tot}}} \cdot \Delta H \cdot \frac{m_{\mathrm{j}}}{m_{\mathrm{i}} + m_{\mathrm{j}}}. \tag{2.4}$$

The kinetic energy received by species i is scaled by the fraction of the mass of the other reaction partner (species j) and the combined mass of both reaction products. Additionally, we derived the share of the reaction enthalpy that goes into kinetic energy as the fraction of the number of translational degrees of freedom to the total number of degrees of freedom. We note that the number of translational degrees of freedom is the combined number for both reactants: $N_{\rm trans} = 3n_{\rm prod}$, where $n_{\rm prod}$ is the number of products. The total number of degrees of freedom is similarly defined as the sum of the individual degrees of freedom for both reaction partners: $N_{\rm tot} = \sum_i 3n_{\rm atoms,i}$, with $n_{\rm atoms,i}$ being the number of atoms of reaction product i. Here, we considered that the vertical motion that is responsible for the desorption is only one of three translational degrees of freedom. This introduces an additional factor of 1/3. Finally, we could derive an equation for the reactive desorption efficiency of a two-product reaction (2.5), which simplifies to Eq. (2.1) if the occurring reaction has only one reaction product:

$$RD_{\rm i} = \exp\left(-\frac{1}{\epsilon}\left(\frac{E_{\rm b}}{\Delta H}\right)\left(\frac{1}{3}\frac{N_{\rm trans}}{N_{\rm tot}}\frac{m_{\rm j}}{m_{\rm i}+m_{\rm j}}\right)^{-1}\right). \tag{2.5}$$

The new approach has the effect that the lighter of the two products gets the larger share of the kinetic energy and consequently has an increased reactive desorption efficiency, while the one for the heavier product is decreased. For example, considering the reaction

$$\rm H_2CO + H \rightarrow HCO + H_2, \tag{2.6}$$

with HCO being approximately 14 times more massive than H_2, the HCO molecule receives only 1/15 of the kinetic energy, whereas the molecular hydrogen gets 14/15. This results in a reactive desorption efficiency for a CO surface of 54.0% for the H_2 molecule and only 1.5×10^{-36}% for the HCO molecule. The procedure presented in Vasyunin et al. (2017) would provide an efficiency of 63.1% for H_2 and 0.1% for the HCO molecule. However, there are no similar reactions efficient at low temperatures in the Vasyunin et al. (2017) model.

2.2.2 Chemical model

We incorporated the new description of reactive desorption into the rate-equation-based chemical code pyRate, described in more detail in Sipilä et al. (2015a, 2019b). It tracks the chemical evolution both in the gas phase and on the grain surface. The basis of the chemical network is the 2014 public release of the Kinetic Database for Astrochemistry (KIDA) gas-phase network (kida.uva.2014, Wakelam et al. 2015), which was extended by deuterium chemistry for molecules with up to seven atoms. The code also tracks the various spin states of the light hydrogen-bearing species H_2, H_2^+ and H_3^+ and their deuterated isotopologues, as well as multiply protonated or deuterated species involved in the water and ammonia formation networks. All together, the network includes $\approx$ 74000 gas-phase reactions and $\approx$ 2100 grain surface reactions. For the inclusion of abstraction reactions into the methanol formation pathway in the models presented in this work, we refer to the chemical network proposed by Hidaka et al. (2009) and depicted in Figure 2.1 (representation with H) and Figure A.1 (more extensive representation with H and D). We adopted atomic initial abundances (see Table 2.1) taken from Semenov et al. (2010), as

Table 2.1: Initial chemical abundances with respect to n_H.

Species	Initial abundance	Species	Initial abundance
He	9.00×10^{-2}	S^+	8.00×10^{-8}
pH_2	5.00×10^{-1}	Si^+	8.00×10^{-9}
oH_2	5.00×10^{-4}	Na^+	2.00×10^{-9}
HD	1.60×10^{-5}	Mg^+	7.00×10^{-9}
H	1.00×10^{-8}	Fe^+	3.00×10^{-9}
D	1.00×10^{-8}	P^+	2.00×10^{-10}
C^+	1.20×10^{-4}	Cl^+	1.00×10^{-9}
N	7.60×10^{-5}	F	2.00×10^{-9}
O	2.56×10^{-4}		

Notes. [(a)] from Semenov et al. (2010)

they were also used for the S16 model, whose improvement is the main aim of this work. Also, we employed a three-phase model, consisting of a gas phase, a chemically active surface phase, and a chemically inert mantle phase. The dust grains were assumed to be spherically symmetric with a radius of 0.1 μm.

For exploring our new treatment of reactive desorption, the choice of binding energies E_b and formation enthalpies H_{form} is crucial. The values of E_b and H_{form} are displayed in Table (A.1). The binding energies are taken from Semenov et al. (2010). Most of the formation enthalpies are adopted from Du et al. (2012). For the other remaining species, the data sources are marked in Table A.1 in the appendix. Unfortunately, experimental values for deuterated molecules are quite scarce. For this reason, we applied the same values as for the non-deuterated isotopologues, with the exception of the species marked with a star in Table (A.1), for which we found individual values in the NIST Chemistry WebBook [1].

2.2.3 Physical model

As mentioned in Section 2.1, one of the main aims of this work is to improve the theoretical predictions made by the chemical code pyRate for the column density profiles of CH_3OH and CH_2DOH and to compare these again to the observational (Chacón-Tanarro et al. 2019a and theoretical profiles from the V17 model (Vasyunin et al. 2017). For that purpose, we extensively explored the chemical evolution in the pre-stellar core L1544 with a one-dimensional physical model. It was derived from the one presented in Keto & Caselli (2010) and described in more detail in Sipilä et al. (2019a). The model provides radius-dependent, but time-independent, values for the H_2-density $n(H_2)$, the gas temperature T_{gas}, the dust temperature T_{dust} and the visual extinction A_V as shown in Figure 2.2. The core model consists of 35 concentric shells spanning the core radius of 0.32 pc. The chemistry is solved separately for each shell, yielding a spherically

[1] https://webbook.nist.gov/chemistry

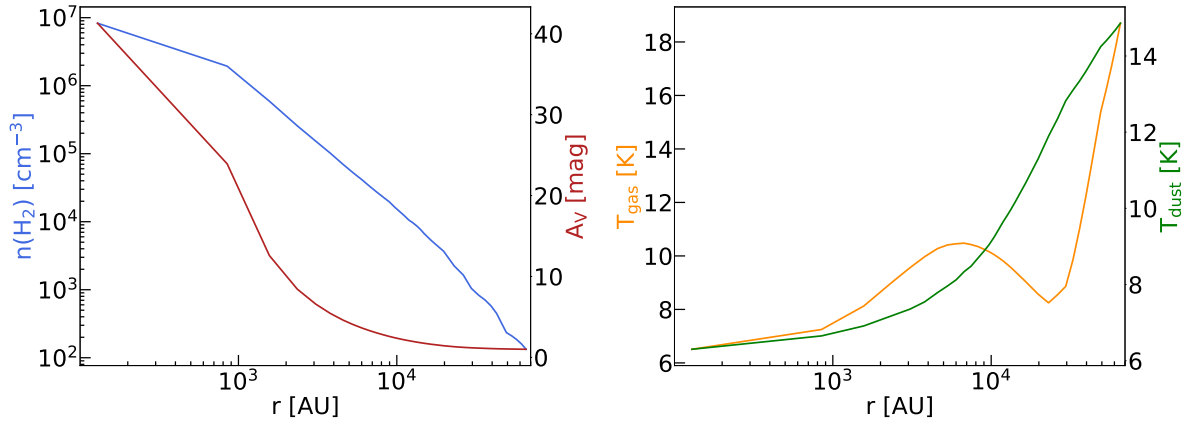

Figure 2.2: Physical model developed in Keto & Caselli (2010) that yields static radial profiles of the H_2 density, $n(H_2)$ (blue, in logarithmic scale), the visual extinction, A_V (red), the gas temperature, T_{gas} (orange), and the dust temperature, T_{dust} (green).

symmetric spatio-temporal evolution of molecular abundances. We calculated column densities by integrating along the line of sight for different impact factors from the core centre. Afterwards, the column density distribution was convolved with a 30" Gaussian beam, corresponding to the angular resolution of the observations by Chacón-Tanarro et al. (2019a).

Taking the core model as a basis, we ran several simulations varying multiple chemical and physical parameters. All presented models include the new treatment for reactive desorption with individual efficiencies for every exothermic surface reaction and various surface types, as described in Section 2.2.1. An overview of the various models is presented in Table 2.2.

2.3 Results

2.3.1 Fiducial model

We selected the 1D-4 model as our fiducial model because it is the closest to V17 in terms of parameter space. In the fiducial model, the diffusion of H and D atoms by quantum tunnelling is enabled, while abstraction reactions as shown in Figure 2.1 (or their deuterated analogues) are not included. This choice is discussed in more detail in Section 2.4.1.1.

We calculated column density profiles for all species observed by Chacón-Tanarro et al. (2019a), for several time steps in the range of 10^5 yr to 10^6 yr in the fiducial model. Figure 2.3 shows the molecular abundances with respect to H_2 and Figure 2.4 shows the column density profiles for H_2CO, CH_3OH and CH_2DOH for four different time steps (1×10^5 yr, 3×10^5 yr, 5×10^5 yr, and 1×10^6 yr). We note that these species freeze out onto dust grains in the very cold centre of the pre-stellar core and then peak at a density of $n(H_2) \approx 10^4$ cm^{-3}, which corresponds to a radius of $\approx$ 5200 AU in the theoretical profiles, offset from the position of the dust peak. For a time of $t = 3.5 \times 10^5$ yr, the CH_3OH abundance reaches its maximum value of approximately

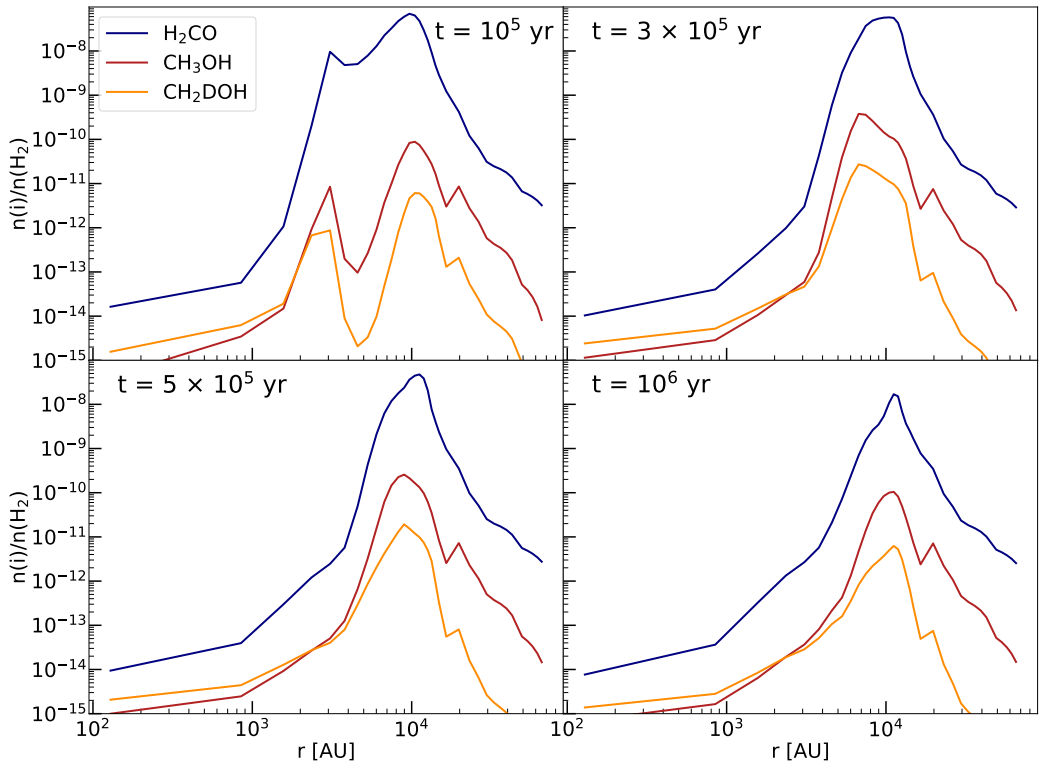

Figure 2.3: Gas-phase abundance profiles of H_2CO, CH_3OH, and CH_2DOH for the 1D-4 model for four different time steps ranging from 10^5 yr (left) to 10^6 yr (right). The best-fit time is $t = 3 \times 10^5$ yr.

4×10^{-10}, which is in good agreement with values observed in various pre-stellar cores (e.g. Scibelli & Shirley 2020, Harju et al. 2020, Spezzano et al. 2020, Punanova et al. 2022).

In Chacón-Tanarro et al. (2019a), the time step in the S16 model was chosen such that the simulated CO column density approximately matched the observed one (Caselli et al. 1999), which occurred at a very early time of $3{\times}10^4$ yr. However, S16 did not include CO self-shielding, and is therefore probably underestimating the total amount of CO. For this very early time step, the S16 model produces a centrally flat CH_3OH column density profile with an amplitude of $N \approx 1 \times 10^{11}$ cm^{-2}, under-producing the observed values for methanol of 3.9×10^{13} cm^{-2} at the dust peak and 5.9×10^{13} cm^{-2} at the methanol peak by roughly two orders of magnitude. On the other hand, the $N(CH_2DOH)/N(CH_3OH)$ ratio in the S16 model approaches unity, thereby overestimating the observed deuterium fraction of 0.07 by a factor of 10. We note that the chemical network that was used for the S16 model includes reactions like $CH_2DOH + H_3O^+ \rightarrow CH_3OHD^+ + H_2O$, or analogues for other deuterated forms of methanol, with the effect of

increasing the deuterium fraction. We do not permit this sort of exchange to happen in the revised chemical network, as this would require the addition of a (hydrogen) atom as well as the exchange of a hydrogen and a deuterium atom between the different functional groups of methanol, which we consider unlikely.

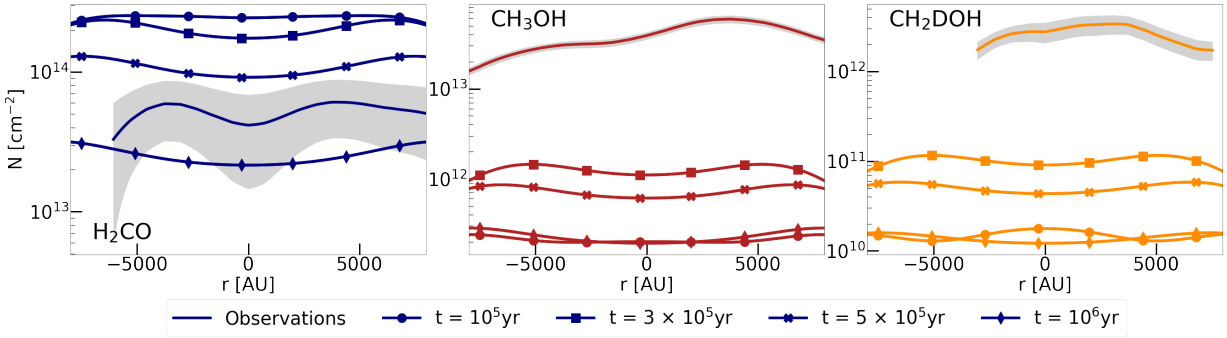

Figure 2.4: Column density profiles of H_2CO, CH_3OH, and CH_2DOH for the 1D-4 model for four different time steps ranging from 10^5 yr to 10^6 yr. The lines with markers show the modelled results, integrated along the line of sight and convolved with a 30" beam. The solid lines show the observationally obtained column density profiles obtained by Chacón-Tanarro et al. (2019a) by taking a cut through the dust and methanol peaks. The grey-shaded areas indicate the error bars of the column densities. The position of the dust peak is at $r = 0$ AU, while $r > 0$ AU is the direction towards the methanol peak.

To estimate a new best-fit time for the fiducial model, we calculated the χ^2 values of the observed central column density versus the corresponding values in the fiducial model for different time steps and species. Subsequently the time step where the sum of the χ^2 values of all species is minimised was taken as the best-fit time. For the 1D-4 model, this corresponds to a best-fit time of $t = 3{\times}10^5$ yr, which is roughly consistent with estimations from other molecules (e.g. Redaelli et al. 2019, 2021). Additionally, it coincides with the occurrence of the highest methanol column density in the probed time frame. For $t = 3.0{\times}10^5$ yr, the fiducial model reaches a column density of methanol of $\approx 1.5 \times 10^{12}$ cm^{-2}, which is roughly an order of magnitude lower than the column densities determined by the observations. Given the large uncertainties that chemical modelling typically experiences, this is an acceptable agreement (Vasyunin et al. 2004, 2008, Wakelam et al. 2010, and references therein).

Figure 2.5 compares the modelled deuterium fraction $N(CH_2DOH)/N(CH_3OH)$ with the observed one. At the early time step ($t = 1 \times 10^5$ yr), the deuterium fraction profile is slightly higher than the observed one, but the shape of the profiles are nearly identical. The modelled deuterium fraction flattens with time. This behaviour can probably be explained by the use of the static physical model that is employed here. At the best-fit time of $t = 3 \times 10^5$ yr, the deuterium fraction assumes an almost completely flat profile with a value of ≈ 0.08. At the intermediate ($t = 5 \times 10^5$ yr) and late ($t = 1 \times 10^6$ yr) time steps, the $N(CH_2DOH)/N(CH_3OH)$ ratio starts to decrease slightly, but stays at a level that is in agreement with the observed one.

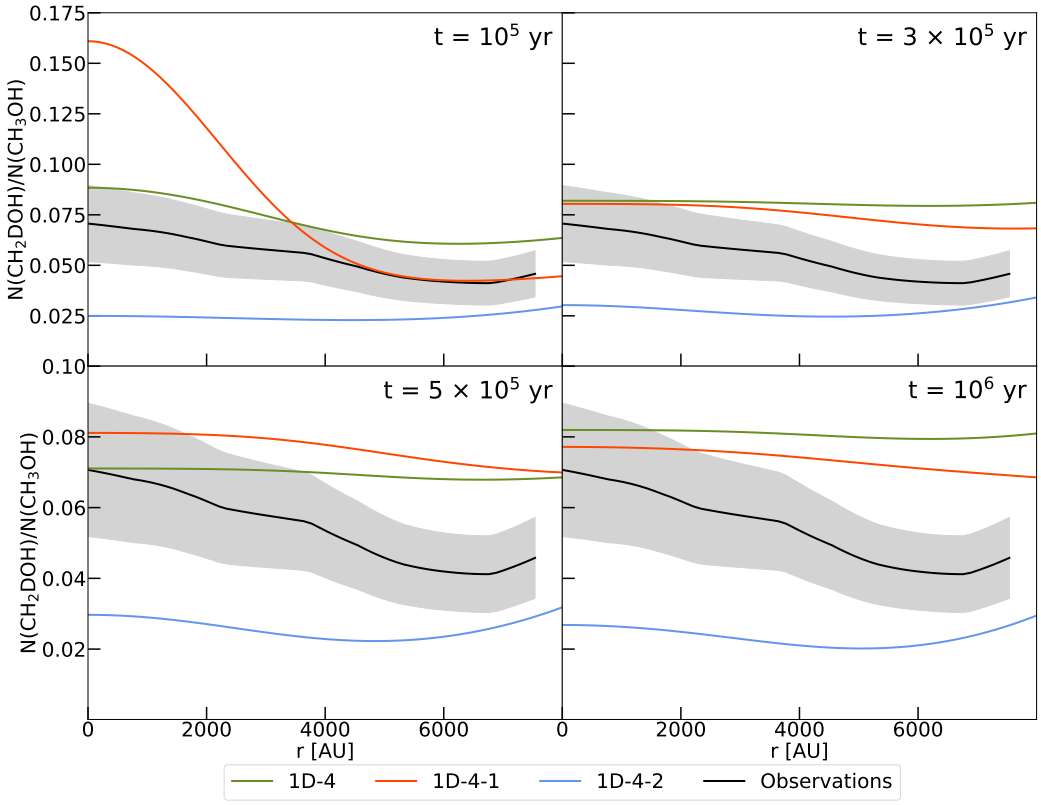

Figure 2.5: Modelled ratio between singly deuterated methanol (CH_2DOH) and non-deuterated methanol (CH_3OH) for the 1D-4 model for four different time steps ranging from 10^5 yr (top left) to 10^6 yr (bottom right). Additionally, we show two variations of this model: one with four layers in the chemically active surface phase instead of one (1D-4-1), and one with a two-phase model (1D-4-2; see also Table 2.2 and Section 2.3.2 for a more detailed explanation). The coloured lines show the column density ratio of the models, while the black line indicates the observed ratio (errors as grey-shaded areas).

2.3.2 Comparison with V17

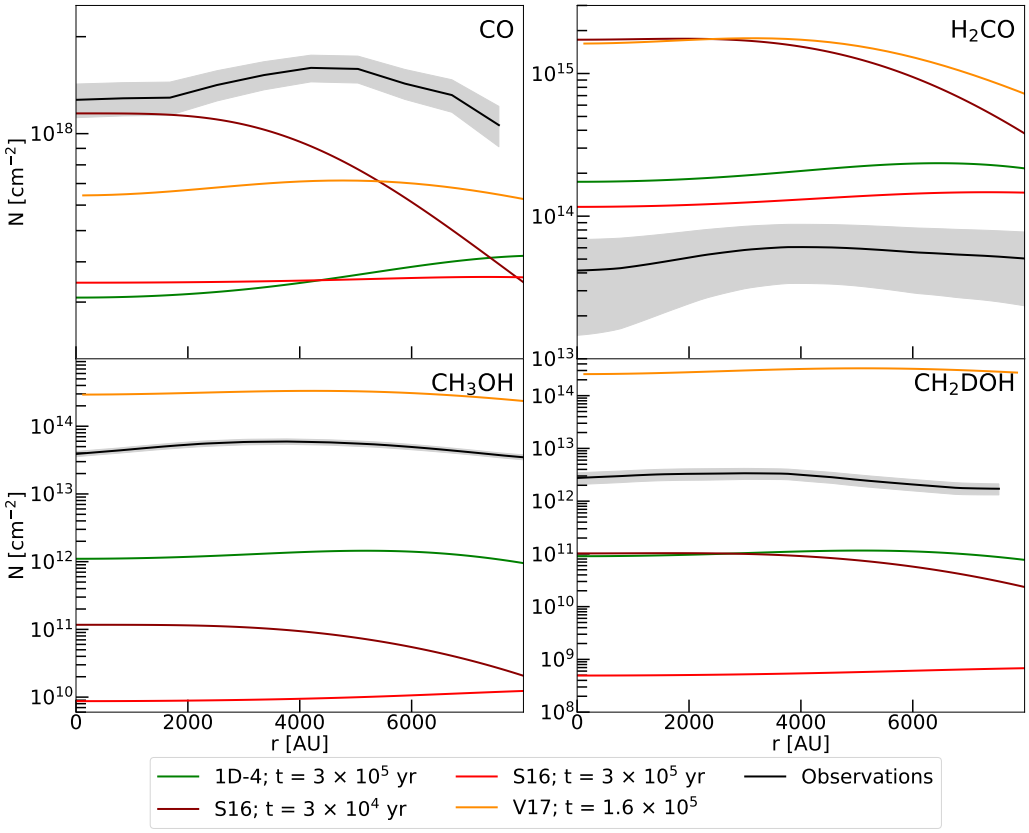

Figure 2.6: Comparison of the models presented in Chacón-Tanarro et al. (2019a) – S16 (obtained with pyRate) and V17 (obtained with MONACO) – to the 1D-4 model (fiducial model) computed with an updated version of pyRate. The column density profiles are shown at different time steps: $t = 1.6 \times 10^5$ yr for V17, $t = 3.0 \times 10^4$ yr and $t = 3.0 \times 10^5$ yr for S16, and $t = 3.0 \times 10^5$ yr for 1D-4. The observed profiles are depicted in black (errors as grey-shaded areas). The CO column densities were obtained using observations of $C^{17}O$ and the average isotopic ratios of $^{16}O/^{18}O = 557$ and $^{18}O/^{17}O = 3.6$ in the local interstellar medium (Wilson et al. 1999).

The fiducial model (1D-4) shows a much better agreement for the column densities of non-deuterated methanol than the S16 model, which was produced by an earlier version of pyRate, when compared to the V17 model produced by the chemical code MONACO and presented in Vasyunin et al. (2017) and Chacón-Tanarro et al. (2019a) (see our Figure 2.6). We set the values of the various physical parameters to correspond to those in V17 as closely as possible. Still, several differences remain between MONACO and pyRate, and these cannot be fully understood without a detailed direct comparison of the two models, which is out of the scope of this paper.

Here, we point out some of the most noticeable differences. The chemical models are not identical, as we used different chemical networks. MONACO is specialised to describe the formation of COMs, while pyRate concentrates on the description of deuteration. V17 does not consider deuteration at all. Also, pyRate's chemical network contains 'backward' abstraction reactions adopted from Hidaka et al. (2009). We removed them for several models presented in this paper, including the fiducial model 1D-4, in order to compare our model to the V17 model. In V17, these reactions are deliberately left out due to their badly constrained reaction rates.

Both codes use a so-called three-phase grain model with multiple layers as opposed to a simpler two-phase model. Three-phase models usually consist of three distinct phases: the gas, the ice surface and the bulk phase, which again can be subdivided into individual layers. Two-phase models only distinguish between gas and surface phase. In most astrochemical codes, the bulk is simply a chemically inert storage of accreted molecules, while the chemical reactions occur solely in the gas and surface phase. A two-phase model has no such storage. Every molecule on the grain can react or desorb at any time. The introduction of layers into a grain model enables the storage of molecules in the bulk in the order that they are accreted. Gas-phase molecules can only accrete to the surface phase, where they can react with another surface molecule. The surface phase usually consists of only one layer. If all binding sites in the surface phase are filled, molecules are transferred continuously into the bulk phase, which keeps growing.

The MONACO code has a more advanced description of the physical processes taking place on dust grains than most other astrochemical codes. In MONACO, the bulk experiences a slow type of diffusion and species are therefore able to meet one another and react, instead of just being stored away. Moreover, the surface phase consists not only of the uppermost layer, but of the first four layers in order to also allow atoms to be diffused in the vertical direction. The fiducial model presented in this paper also uses a multilayer dust model, but with a chemically inactive bulk phase and only one layer in the surface phase, which reduces the surface area on which methanol and its precursors can be hydrogenated.

To evaluate the consequences of our choice to use only one layer in the chemically active surface phase in our models, we also tested a modification of our fiducial model, 1D-4-1, where we set the number of layers in the surface phase to four and, as a reference, a two-phase model of the fiducial model setup, 1D-4-2, where the entirety of the ice is available for reactions. For 1D-4-1, we find that both the CH_3OH and the CH_2DOH column densities are increased by a factor of a few in comparison to the fiducial model in the entire considered time frame. This makes sense as with the increase in layers in the surface phase the model approaches the two-phase model, showing consistently higher column densities for both isotopologues of methanol. This behaviour is credited both to an increased overall production of methanol and an increased reactive desorption efficiency in the very centre of the pre-stellar core, due to a higher coverage of the surface with CO. However, the deuterium fraction of the two-phase model is quite low (see also Section 2.4.1.2), as the increase in column densities for CH_2DOH is lower than for CH_3OH. Surprisingly, this is not the case for the model with four layers in the surface phase, as is depicted in Figure 2.5. Instead, we find a considerable increase in the deuterium fraction compared to the fiducial model for early time steps, reaching a value of up to ≈ 0.16 at $t = 1 \times 10^5$ yr. The deuterium fraction of the model with four layers in the surface phase drops slightly below that of

the fiducial model for time steps around when the methanol column density peaks, but increases again above it for later time steps.

Both models, the fiducial and V17, employ a similar form of diffusion. The diffusion-to-binding energy E_d/E_b is set to a constant value of 0.55, as suggested by Minissale et al. (2016a), for all surface species. Additionally, both codes consider the inclusion of diffusion by quantum tunnelling. Although, while pyRate only follows the tunnelling diffusion of H (and D), MONACO also traces that of H_2.

The mechanism for reactive desorption in the two codes is similar: it is altered here for chemical reactions with multiple products to ensure that it adheres to the conservation of energy, and it is identical for reactions with a single product. If one does not introduce abstraction reactions in the formation scheme of methanol, reactions with two reaction products are considered to be negligible, as the formation just proceeds by successive addition reactions of H. We note that even though the procedure for single product reactions is the same in both codes, they can produce unequal reactive desorption efficiencies owing to the fact that we used different sets of enthalpies and binding energies. The binding energies and formation enthalpies for the models presented in this work and in the S16 model are adopted from Semenov et al. (2010), Du et al. (2012), the NIST Chemistry WebBook[2] and KIDA [3]. Detailed information can be found in Table A.1. As little modification as possible has been made to the list of these values, as the main aim of this work is to improve the result of the S16 model. Only if necessary for the calculation of the reactive desorption efficiencies, values have been added. This concerns all values adopted from the NIST Chemistry WebBook and KIDA. For the V17 model, the enthalpies are also mostly taken from Du et al. (2012) and the binding energies from Minissale et al. (2016b). Apparently, discrepancies between the two codes also exist for some of the reactions involved in the hydrogenation chain towards methanol:

$$\mathrm{HCO + H} \xrightarrow[\text{pyRate:15.4\%}]{\text{MONACO:5.4\%}} \mathrm{H_2CO} \tag{2.7}$$

$$\mathrm{CH_2OH/CH_3O + H} \xrightarrow[\text{pyRate:0.05\%/0.08\%}]{\text{MONACO:0.64\%}} \mathrm{CH_3OH.} \tag{2.8}$$

For example for reaction 2.7 and 2.8 the two codes yield very different reactive desorption efficiencies. In pyRate, H_2CO is desorbed more efficiently before it has the opportunity to react further and eventually form CH_3OH, which is also less likely to desorb from the surface of the dust grain compared to the formation scenario in MONACO.

Figure 2.6 presents the column density profiles of CO, H_2CO, CH_3OH and CH_2DOH of models 1D-4, S16 and V17. In the case of V17, the CH_2DOH column density was derived by scaling the CH_3OH column density with the respective deuteration ratio from S16, as MONACO does not include a description of deuterium chemistry. We note that the column density profiles are shown at different time steps. The V17 model and the S16 model presented in Chacón-Tanarro et al. (2019a) showed the time steps when the CO column density in the respective model is comparable to the observed value. For V17 this corresponds to $t = 1.6 \times 10^5$ yr, which

[2]https://webbook.nist.gov/chemistry
[3]https://kida.astrochem-tools.org

coincides with the peak of the COM abundances. The same estimation for S16 yields a very early time step of $t = 3.0 \times 10^4$ yr. The resulting column densities are shown in Figure 2.6 as the dark red line. We have derived a new best-fit time corresponding to the lowest χ^2 value of the observed column densities versus the corresponding values in the 1D-4 model: t = 3.0×10^5 yr. This time step corresponds roughly with the peak of the methanol abundance in the 1D-4 model and is also in good agreement with the one estimated by the V17 model, varying only by a factor of 2. In Figure 2.6 we show the results for the S16 model and the 1D-4 model at the new best-fit time step as bright red or green line, respectively. The S16 model produces less non-deuterated and singly deuterated methanol at this later time step, which is caused by gas-phase chemical reactions where atom exchanges between the two functional groups of methanol were allowed. Such reactions are not allowed in the present work. The 1D-4 model, on the other hand, is more consistent with the results of the V17 model, though it still underestimates the column densities of methanol by roughly an order of magnitude. The V17 model overestimates the CH_3OH column density and as consequence also CH_2DOH column density, which was credited to a likely overestimation of the reactive desorption efficiency. All models overestimate the amount of gas-phase H_2CO. The V17 and S16 models, which are evaluated at a time step to match the observed CO column densities, are off by more than an order of magnitude, whereas S16 at $t = 3.0 \times 10^5$ yr and 1D-4 produce only twice the observed column density. Although the V17 model and the newly developed fiducial model, 1D-4, still differ for the CH_3OH column density by almost two orders of magnitude (one order of magnitude of overestimation by V17 and one order of magnitude underestimation by 1D-4), we are able to confirm qualitatively some results of Vasyunin et al. (2017). The most important conclusion is that we are only able to reconcile our models with the observed values if we consider some form of enhanced diffusion on the surface of dust grains. One possibility to get a higher diffusion rate is to enable diffusion by quantum tunnelling of H and D atoms in the models. Other options are discussed below. Also, similar to Vasyunin et al. (2017), we conclude that other forms of non-thermal desorption, for example cosmic-ray-induced desorption (CRD) and photo-desorption, seem to have a negligible impact on the release of methanol and its precursors into the gas phase.

2.4 Discussion

In addition to the comparison with the V17 model, we explored various alterations of our model, mainly to investigate the effect on the deuteration of methanol and possibly improve the agreement between the predicted and observed $N(CH_2DOH)/N(CH_3OH)$ ratio. An overview of the various models and their modified chemical and physical parameters is presented in Table 2.2. The 1D-4 model was picked as the fiducial model because of its closeness to V17 in terms of parameter space. However, for most of the variations of the other physical parameters, we used the 1D-3 model as the point of reference, comprising the abstraction reactions, as most other modelling works include them. In Table 2.2, models that are derived by modifying the fiducial model 1D-4 are indicated with a star (*) and those derived from 1D-3 with a dagger (†). We only varied one physical parameter at a time, in order to undoubtedly ascribe the altered results to the made modifications. For the discussion of the effects of the variations,

we roughly divided them into chemical and physical variations. We collected an overview of the resulting $N(CH_2DOH)/N(CH_3OH)$ ratios for all presented models at four different time steps for the positions of the dust peak and of the methanol peak in Table 2.3.

Table 2.2: Overview of the various models investigated in this work.

Model	tunnelling diffusion	thermal diffusion	E_d/E_b [a]	abstraction reactions	gas-grain model	cosmic-ray ionisation rate	other modifications
Chemical variation:							
1D-1†	✗	✓	0.55	✓	3 phases	1.3×10^{-17} s^{-1}	
1D-2⋆	✗	✓	0.55	✗	3 phases	1.3×10^{-17} s^{-1}	
1D-3	✓	✓	0.55	✓	3 phases	1.3×10^{-17} s^{-1}	
1D-4	✓	✓	0.55	✗	3 phases	1.3×10^{-17} s^{-1}	
1D-4-1⋆	✓	✓	0.55	✗	3 phases	1.3×10^{-17} s^{-1}	4 active surface layers
1D-4-2⋆	✓	✓	0.55	✗	2 phases	1.3×10^{-17} s^{-1}	
1D-5†	✗	✓	0.2	✓	3 phases	1.3×10^{-17} s^{-1}	
1D-6⋆	✗	✓	0.2	✗	3 phases	1.3×10^{-17} s^{-1}	
1D-7†	✓	✓	0.55	✓	2 phases	1.3×10^{-17} s^{-1}	
1D-8†	✓	✓	0.55	✓	3 phases	1.3×10^{-17} s^{-1}	no reactive desorption for reactions with 2 products
1D-9†	✓	✓	0.55	✓	3 phases	1.3×10^{-17} s^{-1}	reduced E_A [b] for deuterated species by 200 K
1D-10†	✓	✓	0.55	✓	3 phases	1.3×10^{-17} s^{-1}	$H_{form}(XH) = H_{form}(XD)$ [c] (see Table A.1)
Physical variation:							
1D-11†	✓	✓	0.55	✓	3 phases	1.3×10^{-17} s^{-1}	decreased T_{gas} by 1 K throughout the core
1D-12†	✓	✓	0.55	✓	3 phases	$\mathscr{L}$-model [d]	
1D-13†	✓	✓	0.55	✓	3 phases		dynamic mechanism for CR- desorption [e]

Notes. Only the chemical and physical properties that vary between models are listed. The 1D-4 model is the fiducial model presented in Section 2.3.1. Models that take the 1D-4 model as starting point are marked with a star (⋆). Models that take the 1D-3 model, including the abstraction reactions, as a starting point are marked with a dagger(†). [(a)] E_d is the diffusion energy and E_b the binding energy [(b)] E_A is the activation energy of the reaction [(c)] $H_{form}(XH)$ is the formation enthalpy of a non-deuterated species and $H_{form}(XD)$ is the formation enthalpy of a deuterated species [(d)] from Padovani et al. (2018) [(e)] from Sipilä et al. (2021)

2.4.1 Chemical variation

2.4.1.1 1D-1 to 1D-6: Combining enhanced diffusion and abstraction reactions

As already pointed out in Section 2.3.2, to explain the observed magnitudes of molecular abundances and column densities, we had to introduce some type of enhanced diffusion of atoms on the grain surface. In V17 and the fiducial model, this is realised by enabling the diffusion of H (and D) via quantum tunnelling. Laboratory experiments on an amorphous solid water surface (Hama et al. 2012) as well as a CO surface (Kimura et al. 2018) actually suggest that the diffusion of H and D is dominated by thermal hopping, even at temperatures around 10 K. This was concluded since a significant isotope effect, which is expected if the diffusion proceeds

mainly via quantum tunnelling, could not be observed. Therefore, we explored both the option for an increased, fast thermal diffusion and the diffusion of H and D atoms by quantum tunnelling.

For the former, a value of the diffusion-to-binding energy, E_d/E_b, has to be chosen. Due to the lack of detailed experimental data, most chemical codes apply only one value for the diffusion-to-binding energy to every surface species. In reality, it is likely that different species have an individual diffusion-to-binding energy that extends over a wider range of values, depending on the various types of potential wells present. Reasonable values of the diffusion-to-binding energy cover the range of 0.2 to 0.7 (Furuya et al. 2022b). As a first approximation, we assumed that the comparatively large number of hydrogen and deuterium atoms might fill up the deeper potential wells quite quickly, making the shallower potential wells more relevant for the diffusion process. For that reason, we adopted the lowest debated value of 0.2 for the diffusion-to-binding energy. As a reference, we also tested the option of introducing no enhanced diffusion – neither fast thermal diffusion nor tunnelling diffusion – only employing a typically assumed value for the diffusion-to-binding energy of 0.55, leading to slow thermal hopping. Additionally, we decided to run two models for every explored type of diffusion process: one with only addition reactions and one with addition and abstraction reactions.

Models 1D-1 and 1D-2, employing slow thermal diffusion with a diffusion-to-binding energy E_d/E_b of 0.55, serve as references to the models with enhanced diffusion. Both produce CH_3OH column densities around 10^7 cm^{-2}, which is several orders of magnitude lower than the observed value of 10^{13} cm^{-2}. Models 1D-3 and 1D-4, additionally employing the diffusion via tunnelling for H and D atoms, as well as models 1D-5 and 1D-6, relying on fast thermal hopping, show significantly higher column densities of the order of 10^{12} cm^{-2}. These results deviate only within a factor of 10 from the observed values and are thereby matching the observation. Therefore, we conclude that some form of enhanced diffusion of H and D atoms over the grain surface has to take place in order to reach similar column densities as the ones measured in the pre-stellar core L1544.

The column densities in the models that employ fast thermal hopping are higher for early time steps ($t = 1 \times 10^5$ yr) and intermediate time steps ($t = 5 \times 10^5$ yr) – up to a factor of 6 for CH_3OH and up to a factor of 4 for CH_2DOH – but decline earlier than in the models with tunnelling diffusion. Moreover, we find that the CH_3OH column density profiles in the 1D-4 model including only addition reactions are lower (by up to a factor of 3) than for the 1D-3 model comprising both addition and abstraction reactions. The CH_2DOH column density profiles, on the other hand, are higher (by up to a factor of 2.5) in the models with addition reactions only. For the 1D-5 and 1D-6 model, employing fast thermal hopping, this effect is even more pronounced with a factor of up to 10 for CH_3OH and up to eight for CH_2DOH.

In addition to the order of magnitude of column densities, we attempted to reproduce the deuterium fraction $N(CH_2DOH)/N(CH_3OH)$ as closely as possible. This ratio is likely less affected by the individual modelling choices, as the effects on CH_3OH and CH_2DOH are probably similar for most parameter selections. Figure 2.7 depicts the ratio of the column densities of singly deuterated methanol (CH_2DOH) and non-deuterated methanol (CH_3OH). Models 1D-1 and 1D-2 show a similar level of deuteration reaching a central value of ≈ 0.05 for the best-fit time of $t = 3.0 \times 10^5$ yr. 1D-1, the model that includes addition and abstraction reactions, has a slightly higher deuterium fraction than the one with only addition reactions. The slightly higher

Table 2.3: $N(CH_2DOH)/N(CH_3OH)$ ratio at the centre of the pre-stellar core, r_{cen}, and the radius of the methanol peak, r_{max} = 5200 AU.

Model	t = 1×10^5 yr		t = 3×10^5 yr		t = 5×10^5 yr		t = 1×10^6 yr	
	r_{cen} [%]	r_{max} [%]	r_{cen} [%]	r_{max} [%]	r_{cen} [%]	r_{max} [%]	r_{cen} [%]	r_{max} [%]
1D-1	3.8	3.3	5.4	4.6	6.2	5.0	6.6	5.1
1D-2	3.8	3.3	5.2	4.5	5.9	4.8	6.4	4.9
1D-3	3.0	0.5	3.3	1.1	2.4	1.6	4.8	4.2
1D-4*	8.8	6.2	8.2	8.0	7.1	6.9	6.3	6.1
1D-4-1	16.1	4.5	8.0	7.3	8.1	7.5	7.7	7.2
1D-4-2	2.5	2.3	3.0	2.5	3.0	2.2	2.7	2.0
1D-5	1.1	0.2	1.3	0.5	1.7	1.3	2.0	2.3
1D-6	5.8	4.9	8.0	7.7	11.4	11.3	13.6	13.5
1D-7	0.1	0.04	0.2	0.04	0.2	0.04	0.1	0.03
1D-8	4.3	0.8	6.8	2.3	5.7	3.0	3.5	1.4
1D-9	7.0	1.4	2.7	1.1	3.4	2.2	6.3	5.5
1D-10	3.0	0.5	3.2	1.1	2.3	1.5	4.6	4.0
1D-11	3.0	0.5	4.3	1.4	2.2	1.4	4.9	4.2
1D-12	0.8	0.1	2.3	1.1	3.1	2.2	7.4	6.9
1D-13	3.9	0.7	2.7	1.0	2.3	1.5	4.3	3.7

Notes. The position of the methanol peak is determined by the profile of the fiducial model at the best-fit time. An overview of the chemical and physical properties of the various models is given in Table 2.2. The model marked with a star is the fiducial model and $t = 3 \times 10^5$ yr is the best-fit time obtained as described in Section 2.3.1. The observed values are $N(CH_2DOH)/N(CH_3OH)(r_{cen}) = 7.1\% \pm 1.9\%$ for the centre and $N(CH_2DOH)/N(CH_3OH)(r_{max}) = 4.5\% \pm 1.2\%$ for a radius of 5200 AU.

deuterium fraction is expected theoretically and can be explained by the following: reaction 2.9 has a much higher activation energy than the competing reaction 2.10, leading to its isomer. Therefore, the hydrogenation of H_2CO preferably proceeds via the latter reaction:

$$H_2CO + H \xrightarrow{E_A=5.16\times10^3\,K} CH_2OH \tag{2.9}$$

$$H_2CO + H \xrightarrow{E_A=2.00\times10^3\,K} CH_3O. \tag{2.10}$$

However, the deuteration of CH_3O is not able to produce CH_2DOH in our chemical network, as this would require an exchange of atoms between the two functional groups. It is only able to react to CH_3OD in the presence of D. CH_2DOH can only be produced by deuteration of CH_2OH. Including abstraction reactions into the chemical network opens up another channel for the formation of CH_2DOH via the abstraction of non-deuterated methanol:

$$CH_3OH + H/D \xrightarrow{E_A=3.62\times10^3/3.24\times10^3\,K} CH_2OH + H_2/HD \quad (2.11)$$

$$CH_3OH + H/D \xrightarrow{E_A=5.56\times10^3/5.16\times10^3\,K} CH_3O + H_2/HD. \quad (2.12)$$

Reaction 2.11 is favoured in comparison to the analogue including its isomer 2.12. A similar effect on the deuterium fraction of the molecular abundances was discussed for the static 0D-models in Taquet et al. (2012). They found large enhancements for the $N(CH_2DOH)/N(CH_3OH)$ ratio in the high density case ($n_H \geq 1 \times 10^6\,cm^{-3}$) eventually reaching values above unity, while there was no significant increase for the low density case ($n_H = 1 \times 10^4\,cm^{-3}$ - $1 \times 10^5\,cm^{-3}$). Aikawa et al. (2012), on the other hand, could not fully confirm these results with their 1D radiative hydrodynamics model.

In contrast to the models with slow thermal diffusion, the models that include a form of enhanced diffusion – either fast thermal hopping or tunnelling diffusion – show the opposite behaviour when it comes to the inclusion of abstraction reactions (see Figure 2.7). The models with only addition, 1D-4 and 1D-6, have an up to 8 times higher $N(CH_2DOH)/N(CH_3OH)$ ratio at certain time steps than the one where addition and abstraction reactions are included. The downside of this increased deuterium fraction is that the increased amount of CH_2DOH apparently causes a decrease in the amount of CH_3OH that is produced.

Models 1D-3 and 1D-5, comprising addition and abstraction reactions, are not able to reproduce the observed $N(CH_2DOH)/N(CH_3OH)$ ratio as well. They only match the level of the observations for the innermost part of the core at early time steps ($t = 1 \times 10^5$ yr), but decline too quickly with increasing radius. For late time steps ($t = 1 \times 10^6$ yr), the deuterium fraction is increasing again to a level, where the intermediate radii (r=2000AU - r=6000) match the observational profile. The innermost part, however, shows less deuteration than both the outer ring and the observations.

By looking at the reaction rates of for example model 1D-3, one can see that at a time step close to the peak in methanol formation ($\approx t = 5 \times 10^5$ yr), the magnitude of the addition reaction rates and the one from the abstraction reactions approach each other and basically become almost equal in value, meaning that the net formation of methanol does proceed much more slowly. We therefore suspect that the reaction rates for the abstraction reactions are too high/much higher than in reality.

Having assessed that some form of enhanced diffusion is needed, it is not possible to decide based on our modelling results which of the processes of enhanced diffusion matches the observations better. For times before the time step when the methanol column density peaks, the fiducial model, employing tunnelling diffusion, has a higher $N(CH_2DOH)/N(CH_3OH)$ ratio profile than the 1D-6 model, relying on thermal hopping. The former is slightly above the observed values, but reproduces the observed shape of the profile very well. The latter is well within the area of uncertainty of the observations. It has, however, a much flatter profile than is observed. The profile of the fiducial model flattens with time, until both models become nearly identical at the best-fit time of 3.0×10^5 yr. After the time step when the methanol column density peaks, the $N(CH_2DOH)/N(CH_3OH)$ ratio of the fiducial model decreases and begins to match the observed values quite closely for time steps beyond $t = 5.0 \times 10^5$ yr. The $N(CH_2DOH)/N(CH_3OH)$ ratio of

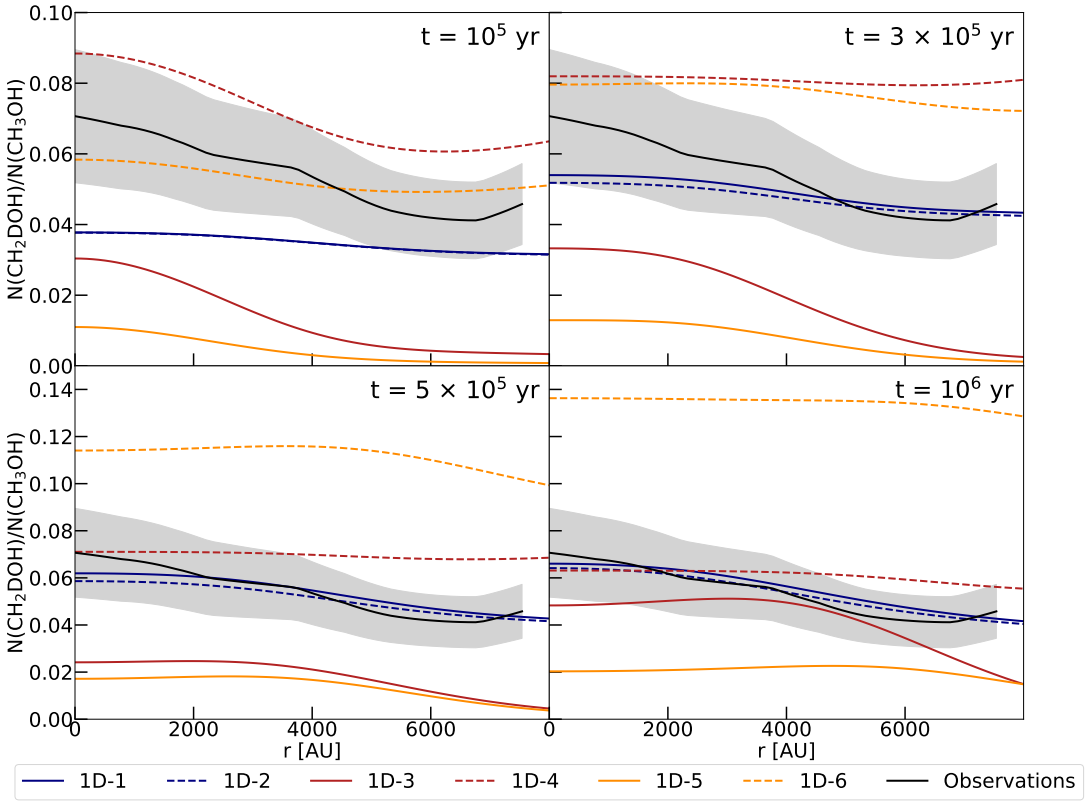

Figure 2.7: Modelled ratio between singly deuterated methanol (CH_2DOH) and non-deuterated methanol (CH_3OH) for several models at four different time steps ranging from 10^5 yr to 10^6 yr. The best-fit time is $t = 3 \times 10^5$ yr. We show two models with slow thermal hopping (E_d/E_b = 0.55; blue lines), two models with slow thermal hopping and tunnelling diffusion of H and D (red lines), and two models with fast thermal hopping (E_d/E_b = 0.2; orange lines). The solid lines indicate models with addition and abstraction reactions, while the dashed lines indicate models with only addition reactions. The black line shows the observed ratio (errors as grey-shaded areas).

the 1D-6 model starts increasing far above the observed values, until it reaches values of almost 0.14 for late times ($t = 1 \times 10^6$ yr).

2.4.1.2 1D-7: Variation of the grain model

As described in Section 2.2.2, the grain model is a three-phase model, consisting of a gas phase, a chemically active surface phase and a chemically inert mantle phase, for most of the models presented here (see also Table 2.2). Other modelling tasks performed with pyRate (Sipilä et al. 2016) show that the choice of the grain model can have a significant effect on the magnitude of the deuterium fraction. Therefore, we decided to run a simulation with a simpler two-phase model, consisting only of a gas phase and a chemically active surface phase. A mantle phase, where frozen-out molecules are stored without chemical alteration is not considered in this model. The 1D-7 model presented in this section is identical to the 1D-4-2 model, but for the inclusion of abstraction reactions for methanol in 1D-7 in contrast to 1D-4-2.

The resulting column density profiles and the $N(CH_2DOH)/N(CH_3OH)$ ratio are depicted in Figs. 2.8 and 2.9, respectively. The two phase model, 1D-7, does produce a much lower deuterium fraction than the three-phase model. The deuterium fraction in the two phase model is of the order 10^{-3} to 10^{-4} compared to 10^{-2} in the fiducial model, in model 1D-3 and in the observed $N(CH_2DOH)/N(CH_3OH)$ ratio. This finding is consistent with previous results that deuteration on the surface is hindered by using only two phases (Sipilä et al. 2016). The two-phase model produces higher column densities than model 1D-3 or model 1D-4 for CH_3OH. They are of the order of 10^{13} cm^{-2}, differing only a factor of a few from the observed values. The column densities of CH_2DOH on the other hand are one or two orders of magnitude lower than in the three phase model and CH_2DOH is thereby severely under-produced.

An explanation for this behaviour is that in two phase models, deuterium atoms on the surface of dust grains tend to get locked into deuterated forms of water, ammonia and methane, forming quite stable bonds that are not easily broken up again. Additionally, the aforementioned molecules are not readily desorbed into the gas phase, which hinders the release of deuterium atoms by the dissociation of gas-phase species. As a consequence, the majority of deuterium is trapped in the molecular ice contents and deuteration of other surface species, including methanol, is suppressed in two phase models compared to the more advanced multilayer models.

2.4.1.3 1D-8: Variation of the reactive desorption mechanism

The reactive desorption mechanism that was in place in pyRate before the extension to the more advanced treatment, described in Section 2.2.1, allowed only the reactive desorption of exothermic surface reactions with a single reaction product. Additionally, the mechanism applied the same reactive desorption efficiency, typically 1%, to every eligible reaction and did not distinguish between surface types. In fact that is the case for most other reactive desorption mechanisms used in the literature, except for the one presented here and the one in Vasyunin et al. (2017).

The new reactive desorption mechanism extends its application to chemical reactions with two reaction products. It is now interesting to quantify the consequences of this change. We

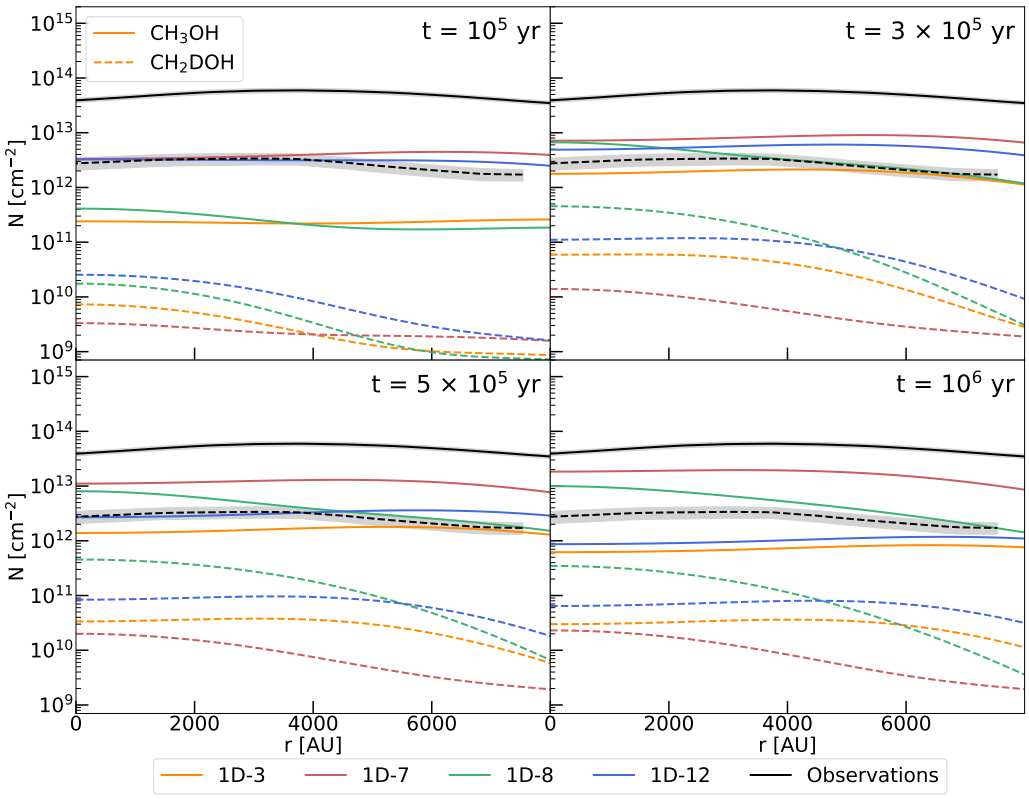

Figure 2.8: Modelled column density profiles of non-deuterated methanol (CH_3OH) and singly deuterated methanol (CH_2DOH) for several models at four different time steps ranging from 10^5yr to 10^6yr. We present the varied models that show the largest effects in terms of the amount of methanol in the gas phase: 1D-7 (two-phase model), 1D-8 (only reactive desorption with one product), and 1D-12 (location-dependent cosmic-ray ionisation rate). The black lines show the observed profiles (errors as grey-shaded areas). The solid lines indicate the CH_3OH column densities, and the dashed lines indicate the CH_2DOH column densities.

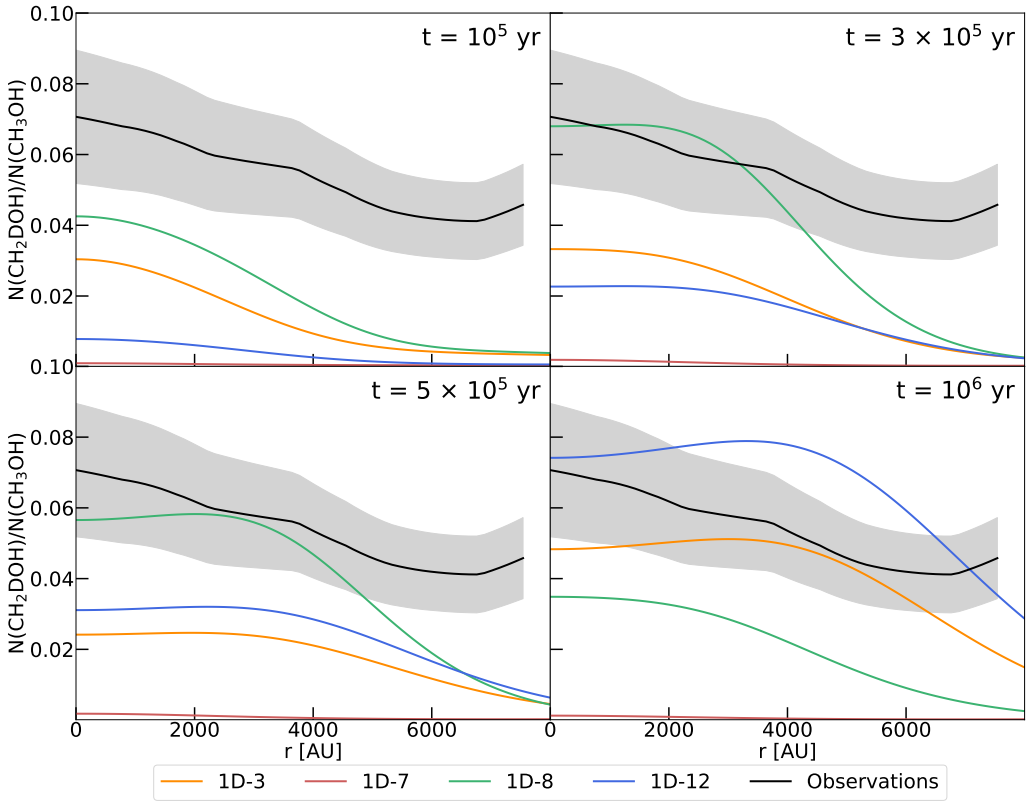

Figure 2.9: Modelled ratio between singly deuterated methanol (CH_2DOH) and non-deuterated methanol (CH_3OH) for several models at four different time steps ranging from 10^5yr to 10^6yr. We present the varied models that show the largest effects in terms of the amount of methanol in the gas phase: 1D-7 (two-phase model), 1D-8 (only reactive desorption with one product), and 1D-12 (location-dependent cosmic-ray ionisation rate). The black line shows the observed ratio (errors as grey-shaded areas).

note that the newly developed mechanism yields a larger reactive desorption efficiency for the lighter reaction partner and a lower efficiency for the heavier one, depending on their mass ratio. In model 1D-8, we apply the modified reactive desorption mechanism only to reactions with one product. We anticipate that fewer of the light species are expelled from the surface of the dust grains. Although the reactive desorption mechanism is in place for all exothermic surface reactions, we also expect to hinder a specific effect caused by the existence of the abstraction reactions. For example for reaction 2.13:

$$H_2CO + H \rightarrow HCO + H_2, \tag{2.13}$$

the new reactive desorption mechanism yields on a CO-surface an efficiency of 54% for the H_2 and of 1.5×10^{-36}% for HCO. The abstraction reactions cause the expulsion of significant amounts of H_2, HD, and D_2, while the desorption of the larger reaction partner is negligible.

The column densities of CH_3OH and CH_2DOH in the 1D-8 model are increased compared to the 1D-3 model (see Figure 2.8). The difference between the two models grows with time, from a factor of ≈ 2 at early time steps ($t = 1 \times 10^5$ yr) to a factor of ≈ 16 at late time steps ($t = 1 \times 10^6$ yr) for CH_3OH or from ≈ 2.5 to ≈ 12 for CH_2DOH. This results in a $N(CH_2DOH)/N(CH_3OH)$ profile (see Figure 2.9) that is very similar in shape to the 1D-3 model, but slightly higher than that of the 1D-3 model around the time steps before the methanol column density peaks in the 1D-3 model, as the CH_2DOH column density increases more quickly than the one of CH_3OH in the 1D-8 model. This could indicate that the determined reactive desorption efficiencies do not describe the physical reality very well, and in particular that our mechanism is overestimating the efficiency with which lighter particles are expelled from the surface. However, light particles, as for example H, H_2 and their deuterated isotopologues, are especially important for the formation of methanol on dust grains, as it proceeds by successive addition of hydrogen and deuterium atoms. Indeed, there are hints that some of the assumptions made to set up the mechanism might not be fulfilled. For example, Fredon et al. (2021) pointed out that the equal distribution of energy into all the degrees of freedom of the reaction product is unlikely to occur, and it is more likely that one or multiple degrees of freedom are favoured against the others. However, since the present work represents the first step to a more advanced treatment, we kept our assumptions simple and as general as possible. Further work could investigate different options for the partitioning of the available reaction enthalpy.

2.4.1.4 1D-9: Variation of the activation energy

The formation of methanol proceeds by the successive hydrogenation of CO along HCO, H_2CO and CH_2OH/CH_3O to CH_3OH. Reactions 2.14 to 2.16,

$$CO + H \xrightarrow{E_A = 1.76 \times 10^3\ \mathrm{K}} HCO \tag{2.14}$$

$$H_2CO + H \xrightarrow{E_A = 5.16 \times 10^3\ \mathrm{K}} CH_2OH \tag{2.15}$$

$$H_2CO + H \xrightarrow{E_A = 2.00 \times 10^3\ \mathrm{K}} CH_3O, \tag{2.16}$$

have an activation barrier. Their corresponding activation energies E_A are indicated on top of the arrows. The remaining reactions are barrier-less. The reactions leading to deuterated analogues of these species have similar activation energies, at times with somewhat lower values. A complete overview is shown in Appendix A.2 for both addition and abstraction reactions.

The exact values of the activation energies, especially the difference for reactions leading to non-deuterated and deuterated isotopologues, could potentially have a large impact on the $N(CH_2DOH)/N(CH_3OH)$ ratio. Therefore, we explored how the results are affected by a small variation in the activation energy. Specifically, we aimed to test if decreasing the activation energies for reactions producing deuterated isotopologues could lead to a significant increase in the $N(CH_2DOH)/N(CH_3OH)$ ratio. Hence, we decided to decrease the activation energy for those reactions by 200 K. We only varied the activation energy of specific addition reactions (marked with a star in the overview in Appendix A.2). The abstraction reactions were left untouched.

Undertaking this variation produces a slightly higher CH_2DOH column density (see Figure A.2). For early times (t=1 × 10^5 yr), the 1D-9 model shows a twice as high CH_2DOH column density as compared to the 1D-3 model. The difference between the two models decreases towards the time step when the methanol column density peaks at $t = 3.0 \times 10^5$ yr. At this time step, the 1D-8 model has a slightly lower CH_2DOH column density profile as compared to the 1D-3 model. After the temporal methanol peak, the difference increases for intermediate ($t = 5.0 \times 10^5$ yr) and late ($t = 1 \times 10^6$ yr) time steps to a factor between 1 and 2. The CH_3OH column densities differ by a negligible amount between the two models (see Figure A.2). Consequently, the $N(CH_2DOH)/N(CH_3OH)$ profile (see Figure A.3) experiences an increase as well. For early time steps the $N(CH_2DOH)/N(CH_3OH)$ ratio reaches high values of up to 16.6 at t=1.15×10^5 yr and is for several other time steps well within the area of uncertainty of the observed profile for the very inner centre of the core (0.055 - 0.091) but is declining significantly more steeply at larger radii. The ratio decreases rapidly at the time when the methanol column density peaks, and increases again at late times (t=1×10^6 yr), hitting the area of uncertainty, but presenting only a small upward shift compared to the 1D-3 model.

2.4.1.5 1D-10: Variation of the formation enthalpies

The incorporation of the more sophisticated reactive desorption mechanism required to expand the list of tabulated formation enthalpies H_{form}, which are necessary to compute the reaction enthalpies ΔH. The complete list of formation enthalpies (and binding energies) of species involved in exothermic surface reactions is shown in Appendix A.1. Since experimental data for deuterated isotopologues are scarce, we have for the most part adopted the same formation enthalpy values for the deuterated isotopologues as for their non-deuterated counterparts. In a few cases, however, we were able to find experimentally measured values for the deuterated analogues in the NIST Chemistry WebBook [4]. The adopted values are marked with a star in Table A.1. The formation enthalpies of the non-deuterated molecules do not differ strongly from the values of their deuterated analogues. For most species, there is a difference of approximately 4 kJ/mol or less for singly deuterated, up to 7 kJ/mol for doubly deuterated and up to 13 kJ/mol

[4] https://webbook.nist.gov/chemistry/

for triply deuterated analogues.This list of formation enthalpies and binding energies was used for all the presented models.

In order to secure that changing the formation enthalpies for only some of the deuterated isotopologues has no significant effect, we ran a model in which we adopted the same values for non-deuterated and deuterated isotopologues. The column density profiles for CH_3OH and CH_2DOH of this model are shown in Figure A.2 and the deuterium fraction profiles are shown in Figure A.3. The effect on both the CH_3OH and CH_2DOH column densities and on the $N(CH_2DOH)/N(CH_3OH)$ ratio is vanishingly small. The difference with respect to the reference model, 1D-3, ranges around 4% for the best-fit time ($t = 3.0 \times 10^5$ yr.)

2.4.2 Physical variation

2.4.2.1 1D-11: Variation of the gas temperature

Based on observations of the NH_3 (1,1) and (2,2) lines and especially their relative strengths, there is reason to believe that the determined gas temperatures in the used physical model by Keto & Caselli (2010) are too high at the intermediate densities, where the maximum of the CO desorption and methanol formation occurs. In principle, lower temperatures should help promote the deuteration process. Therefore, we decided to test a model, in which we decreased the gas temperature throughout the entire core by 1 K, as a first approximation for a revised temperature profile.

The obtained column density profiles for both isotopologues of methanol, non-deuterated and singly deuterated (see Figure A.2), are quite close to the reference model 1D-3. The CH_3OH column densities of the 1D-3 model are a bit higher until the time step when the methanol column density peaks, which is reversed after the methanol column densities start decreasing again. The CH_2DOH column densities in the 1D-11 model are a little higher than in the 1D-3 model around the methanol peak, but are lower before and almost identical after the peak. The deuterium fraction in the 1D-11 model (see Figure A.3) increases less quickly, but the maximum value does reach a slightly higher maximum value than the 1D-3 model at a later time step. After the time step of the methanol peak the $N(CH_2DOH)/N(CH_3OH)$ ratios become very similar.

2.4.2.2 1D-12: Variation of the cosmic-ray ionisation rate

UV photons are not able to penetrate the inner, denser parts of molecular clouds with visual extinctions $A_V \geq 1$, as they are already efficiently absorbed by the outer layers of the cloud. Therefore, cosmic rays take their place as the main ionising agents in the central parts, constituting the start of the ion-molecule chemistry. The penetrating cosmic rays will ionise molecular hydrogen to form H_2^+, which then in turn reacts again with the large reservoir of hydrogen molecules, thereby forming the H_3^+ ion. This particular ion can react with deuterated molecular hydrogen HD in the following reversible reaction:

$$H_3^+ + HD \rightleftharpoons H_2D^+ + H_2. \tag{2.17}$$

The direction of the reaction from left to right is strongly favoured due to the lower zero-point energy of H_2D^+ for temperatures below 30 K, which pre-stellar cores usually exhibit (strictly true only if all reactants and products are in para form Pagani et al. 1992). Additionally, CO, the main destroyer of H_3^+ is mostly frozen out on dust grains in the very inner part of the pre-stellar core. These convenient conditions promote a very efficient deuteration process in the inner parts of the core, which also quickly translates the high D/H ratios to more complex molecules.

While we used the canonical value of the cosmic-ray ionisation rate per hydrogen molecule $\zeta(\mathrm{H}) = 1.3 \times 10^{-17}\,\mathrm{s}^{-1}$ for most of the models presented here, for the 1D-12 model we used a physical model that is attenuating the cosmic-ray ionisation rate depending on its distance from the centre. The $\mathscr{L}$-model, presented in Padovani et al. (2018) and already tested in the context of the pre-stellar core L1544 by Redaelli et al. (2021), increases the cosmic-ray ionisation rate from $\zeta(\mathrm{H}) = 2.02\times10^{-17}\,\mathrm{s}^{-1}$ in the innermost cell to $\zeta(\mathrm{H}) = 4.89\times10^{-17}\,\mathrm{s}^{-1}$ at the outer boundary of the core.

The 1D-12 model exhibits higher CH_3OH and CH_2DOH column densities as compared to the 1D-3 model (see Figure 2.8). Especially for early times ($t = 1 \times 10^5$ yr), the CH_3OH column densities are a factor of 13 higher than in the 1D-3 model. However, the difference to the 1D-3 model is decreasing over time: at intermediate times ($t = 5 \times 10^5$ yr) it is approximately a factor of 2 and even lower at late times ($t = 1 \times 10^6$ yr). The shape of the column density profile (see Figure 2.9) is almost identical between the two models, with small deviations at early times. For the increase in the singly deuterated methanol, we see a time-delayed behaviour compared to the non-deuterated isotopologue. CH_2DOH is amplified by a factor of 3 at early times ($t = 1\times10^5$ yr), but it never gets to the values observed for CH_3OH. Nevertheless, the amplification for CH_2DOH overtakes the one for CH_3OH after the time step when the methanol column density peaks, which results in a larger deuterium fraction magnitude than in the 1D-3 model for the later time steps. The largest $N(CH_2DOH)/N(CH_3OH)$ ratio of ≈ 0.74 is reached at late times ($t = 1 \times 10^6$ yr).

2.4.2.3 1D-13: Variation of the cosmic-ray desorption mechanism

A frequently adopted model for the CRD is the one laid out in Hasegawa & Herbst (1993). It is also used for all the models presented in this work so far. The model assumes that cosmic rays in the 20-70MeV nucleon^{-1} energy range deposit 0.4 MeV of energy into the dust grain, heating it up to a temperature $T_{\max}$ of 70 K. The CRD rate coefficient for molecule i is calculated as the product of the thermal desorption rate, $k_{\max}(\mathrm{i}, \mathrm{T}_{\max})$, of i at the temperature $T_{\max}$ and an efficiency term $f(a, T_{\max})$ for a grain of radius a:

$$k_{\mathrm{CR}}(i) = f(a, T_{\max}) k_{\mathrm{therm}}(i, T_{\max}). \tag{2.18}$$

The efficiency factor $f(a, T_{\max})$ is determined as the ratio between the cooling time of the grains τ_{cool} to the heating interval τ_{heat}. The Hasegawa & Herbst (1993) model adopts constant values for these quantities, for example $f(a, T_{\max}) = 1 \times 10^{-5}\,\mathrm{s}/3.16 \times 10^{13}\,\mathrm{s} = 3.16 \times 10^{-19}$ for a grain of 0.1 μm. A revised version of CRD presented by Sipilä et al. (2021) refines the description of the process by introducing two major modifications to the established scheme. On one hand, the grain cooling time τ_{cool} is determined now by a dynamic mechanism taking into account the individual sublimation rates of the surface molecules as a function of their time-dependent ice

abundances. On the other hand, several different cosmic-ray fluxes can be considered for the calculation of the heating intervals $\tau_{\rm heat}$.

In order to test how this new mechanism affects the formation of methanol and its deuterated isotopologues, we chose the cosmic-ray flux presented in Léger et al. (1985), as this is the one most consistent with the canonical value of the cosmic-ray ionisation rate $\zeta(\mathrm{H}) = 1.3 \times 10^{-17}\,\mathrm{s}^{-1}$, which we used for the other models. The impact on singly and non-deuterated methanol formation seems to be minor compared to the 1D-3 model. This results fits well with the finding that the desorption of species involved in the methanol formation scheme is dominated by reactive desorption, rather than CRD. The CH_3OH column density profile (see Figure A.2) is slightly decreased, especially for the earlier time steps , while the CH_2DOH profile is not significantly changed, resulting in a little higher $N(CH_2DOH)/N(CH_3OH)$ ratio (see Figure A.3). It reaches its highest value of 0.088 at $t = 1 \times 10^5$ yr in the very inner centre. However, the decline is again much steeper than is observed.

2.5 Conclusion

We have presented several models for predicting column densities and deuterium fractions of methanol and its deuterated isotopologues in pre-stellar cores. As a comparison to observed quantities, we used single-dish observations of H_2CO and CH_3OH and some of their deuterated isotopologues towards the pre-stellar core L1544 conducted and analysed by Chacón-Tanarro et al. (2019a).

All our models use a novel treatment of reactive desorption of molecules from the surface of interstellar dust grains. The treatment is experimentally justified (Minissale et al. 2016b) and derives an individual reactive desorption efficiency for every species, depending on the forming chemical reaction(s) and the type of underlying surface.

The results of our fiducial model were compared to the results of the models V17 (MONACO) and S16 (pyRate) presented in Chacón-Tanarro et al. (2019a). The fiducial model includes thermal diffusion (diffusion-to-binding energy ratio $E_\mathrm{d}/E_\mathrm{b} = 0.55$) as well as the diffusion of hydrogen and deuterium atoms via quantum tunnelling. The chemical network does not comprise abstraction reactions for the methanol reaction scheme. We estimated a best-fit time that coincides with the occurrence of the methanol peak at 3.0×10^5 yr. At this time step, we find a better agreement with the observations than for the S16 model. The column densities of CH_3OH and CH_2DOH are still underestimated. However, instead of a more than two orders of magnitude deviation, we are able to reduce the difference to approximately an order of magnitude. This improvement is not possible without increasing the diffusion rate on the surface of the dust grain. The observed $N(CH_2DOH)/N(CH_3OH)$ can be reproduced quite closely. Additionally, we find that increasing the number of layers in the chemically active surface phase from one to four, which allows the atoms to also diffuse in the vertical direction as in the V17 model, increases the column densities of non-deuterated and singly deuterated methanol as well as their D/H ratio in the time frame in question.

Previous work by Vasyunin et al. (2017) and Chacón-Tanarro et al. (2019a) shows that to reproduce the observed order of magnitude for the methanol abundances, it is necessary to

both employ an increased rate of surface diffusion and to disregard abstraction reactions from the reaction scheme. Therefore, we also explored various types of diffusion processes: slow thermal hopping ($E_d/E_b = 0.55$), fast thermal hopping ($E_d/E_b = 0.2$), and slow thermal hopping ($E_d/E_b = 0.55$) combined with the diffusion of H and D atoms via quantum tunnelling. From these tests, we conclude that a form of enhanced diffusion over the surface needs to take place to explain the observational results. Only employing slow thermal hopping produces CH_3OH and CH_2DOH column densities that are several orders of magnitudes below the observed ones. However, we cannot decide based solely on our models which enhanced diffusion process — fast thermal hopping or tunnelling diffusion — matches the observed $N(CH_2DOH)/N(CH_3OH)$ ratio profiles better. The two produce D/H ratios of a similar level that are in good agreement with the observed values. For the best-fit time, the two options have nearly identical profiles.

We also tested both options, employing either addition and abstraction reactions or only addition reactions, for every explored diffusion process. In general, we conclude that including abstraction reactions following Hidaka et al. (2009), in combination with an increased diffusion rate, leads to $N(CH_2DOH)/N(CH_3OH)$ ratios that are a factor of a few lower than in the models that only include addition reactions. We ascribe this behaviour to the fact that the reaction rates of the abstraction reactions become comparable to the addition reactions when combined with enhanced diffusion processes.

Furthermore, we explored other modifications to our model that we suspected would have an effect on the $N(CH_2DOH)/N(CH_3OH)$ ratio:

- A two-phase model resulted in higher CH_3OH and CH_2DOH column densities; the deuterium fraction is severely underestimated, by more than one order of magnitude.
- Reactive desorption applied only to reactions with one reaction product resulted in higher CH_3OH and CH_2DOH column densities and thus a slightly better agreement with the observations.
- A location-dependent cosmic-ray ionisation rate resulted in higher CH_3OH and CH_2DOH column densities that only differ from the observations by a factor of 2 to 3.

Only small effects on the CH_3OH and CH_2DOH column density and deuterium fraction profiles were found for the following model changes:

- A decrease in the activation energy by 200 K leading to deuterated isotopologues (as opposed to non-deuterated species).
- Inclusion of individual formation enthalpies for some deuterated isotopologues as opposed to using the same formation enthalpies for hydrogenated and deuterated isotopologues.
- Decrease in the gas temperature by 1 K throughout the entire core.
- Refinement of the used cosmic-ray desorption mechanism following Sipilä et al. (2021).

Further work needs to be carried out on quantifying the reactive desorption mechanism. On the one hand, there is reason to question the assumption of equal partitioning of energy into all the degrees of freedom. Also, some of our results could hint at the fact that light particles are desorbed too easily into the gas phase with the employed mechanism. On the other hand, it would be interesting to investigate how the reactive desorption mechanism influences other species that are formed on the surface of dust grains.

Additionally, a closer look into the intricacies of the surface diffusion processes, especially of H and D, is needed. Particularly interesting would be to explore the effects of introducing different types of potential wells in which species can be trapped. Other reaction mechanisms, such as the Eley-Rideal mechanism, which is not treated by many chemical codes, or non-diffusive chemistry could play an important role in the formation and deuteration of methanol. These mechanisms will be the subject of a future paper.

We conclude that to obtain a reasonable match with the observational column density and deuterium fraction profiles, it is necessary to employ a form of enhanced diffusion process – either fast thermal hopping or diffusion via quantum tunnelling. Furthermore, the inclusion of abstraction reactions in the methanol formation scheme while also using a fast diffusion process leads to $N(CH_2DOH)/N(CH_3OH)$ ratios that are a factor of a few lower than without the abstraction reactions.

Chapter 3

Forming deuterated methanol in pre-stellar core conditions

The contents of this chapter were published in Astronomy & Astrophysics. Credit: Riedel, W., Sipilä, O., Redaelli, E., et al. 2025, A&A, 701, A291.

Abstract

Context. The formation mechanisms for most complex organic molecules (COMs) are still debated. Either COMs form mostly on the surface of dust grains or mostly by reactions between simpler hydrogenation products upon their desorption into the gas phase. Methanol, the simplest of the O-bearing COMs, plays a key role in both scenarios.
Aims. Our aim is to improve the suitability of our models for the formation and deuteration of COMs in the extremely cold conditions of pre-stellar cores, where chemical reactions between heavier reactants on the surface of dust grains are hindered by the reactant's immobility. Initially, we focused our efforts on CH_3OH and its singly deuterated isotopologue CH_2DOH.
Methods. We updated a gas-grain chemical code capable of deuterium chemistry by including various non-diffusive reaction mechanisms: Eley-Rideal reactions, photodissociation-induced reactions, and three-body reactions. Moreover, we added the reaction $H_2CO + CH_3O \rightarrow CH_3OH + HCO$ to our chemical network, which was found to contribute significantly to methanol formation in both microscopic kinetic Monte Carlo simulations and laboratory experiments. We performed several 1D simulations of the pre-stellar core L1544, where we derived column density profiles for CH_3OH and CH_2DOH and compared our model results with more conventional modelling approaches and available gas-phase observations.
Results. We show that multiple models with different parameter sets provide column density profiles that are in reasonable agreement with the observed values. On the one hand, when applying a single collision reaction probability, either an increase in the reaction rate by the occurrence of diffusion by quantum tunneling or a lowered diffusion-to-binding energy ratio ($E_d/E_b = 0.2$) for thermal diffusion is needed to match the observed methanol levels. On the other hand, when applying reaction-diffusion competition, reactions proceeding by thermal

diffusion with a conservative diffusion-to-binding energy ratio (E_d/E_b = 0.55) are sufficient to reach observed column densities. We find that, in contrast to other COMs, the introduced non-diffusive mechanisms play only a secondary role in the formation and deuteration of methanol. Additionally, we find only a negligible contribution from $H_2CO + CH_3O \rightarrow CH_3OH + HCO$.

Keywords: ISM: abundances - ISM: clouds - ISM: molecules - astrochemistry

3.1 Introduction

Currently, over 330 molecules[1] have been discovered in the interstellar medium, and their numbers are rapidly growing as observers make use of today's outstanding telescope facilities in the radio, millimetre, and far-infrared regime. Around 47% of the detected molecules are considered to be large, consisting of six atoms or more. Interestingly, all of these larger molecules contain at least one carbon atom, which is why they are commonly called complex organic molecules (COMs; Herbst & van Dishoeck 2009) or interstellar COMs (iCOMs; Ceccarelli et al. 2017). The apparent dominance of carbon chemistry, both in the interstellar medium and on Earth, together with other chemical markers (e.g. D/H ratios), strongly suggest that the precursors of the building blocks of organic life on our planet were formed - and possibly conserved to some extent - in the earliest stages of star formation (Caselli & Ceccarelli 2012).

The consensus is that methanol is formed almost exclusively on the surface of dust grains by successive H-addition reactions to CO (e.g. Watanabe & Kouchi 2002, Fuchs et al. 2009, Santos et al. 2022). The formation scenarios of most other COMs, however, are still under debate. The present and ongoing discussion concerns the degree to which either gas-phase or grain-surface and ice mechanisms dominate the production of COMs in general. In the former case, this would occur as common grain mantle components (e.g. H_2O, CO_2, NH_3, CH_4, and CH_3OH; Boogert et al. 2015), which are formed mostly by the hydrogenation of atoms or simple molecules, are released into the gas phase by thermal and nonthermal desorption processes and then further processed by gas-phase reactions to form more complex molecules. In the case in which grain-surface chemistry is dominant, production could occur through diffusive or non-diffusive reactions, or through energetic processing (e.g. UV photolysis). The products would then be desorbed into the gas via thermal or nonthermal means, depending on the environment. Although these two possibilities are sometimes presented as either-or options for all COMs (e.g. Ceccarelli et al. 2023), it is apparent from astrochemical models that certain COMs have highly effective gas-phase production mechanisms, while others do not, with many still unexplored. Understanding the early formation mechanisms of methanol is extremely relevant in both formation scenarios, as it plays an important role in both of them. In a scenario where grain surface mechanisms dominate, COMs are usually assumed to form by radical-radical or radical-neutral reactions in which HCO, CH_3O, and CH_2OH, as intermediate products of the methanol formation route, play a fundamental role. In contrast, in the gas-dominated scenario, methanol

[1] https://cdms.astro.uni-koeln.de/classic/molecules

is desorbed into the gas phase subsequent to its formation on the grain surface and acts as an important precursor for larger COMs.

In the case of grain surface formation, COMs were formerly believed to form only in a lukewarm temperature regime (30-100 K) during a gradual warm-up phase of the molecular clouds. In this warm-up scenario, grain surface radicals are first produced by the irradiation of UV photons and cosmic rays. Once the grain temperature increases to about 30 K, the radicals become more mobile, diffuse over the grain surface, meet each other, and react (Garrod et al. 2006b, Garrod et al. 2008). However, detections of multiple COMs in even earlier, colder (< 15 K) stages of star formation (e.g. Öberg et al. 2010, Bacmann et al. 2012, Cernicharo et al. 2012, Jiménez-Serra et al. 2016) bring doubt regarding the warm-up scenario as the sole formation process. Alternatively, or in addition to the warm-up scenario, the introduction of non-diffusive reaction mechanisms has been proposed in various works. Hereby, the term non-diffusive chemistry consists of various reaction mechanisms, which have in common that they do not require the diffusion of species heavier than commonly present atoms (e.g. H, O, C, and N). Instead, they rely on the (small) probability that both reaction partners are formed in close proximity to each other. At the low temperatures of pre-stellar cores (6 K $\leq T_{\rm grain}$ $\leq$ 15 K), non-diffusive reaction mechanisms could be the most relevant process for the formation of COMs, as only the lightest species are expected to diffuse over the grain surface, likely excluding a diffusion-driven COM formation scenario for these conditions. Garrod & Pauly (2011) introduced a single three-body reaction, very similar to the one used in the present work, between the reactants H, O, and CO to explain the formation of CO_2 on the surface of dust grains under dark-cloud conditions. Ruaud et al. (2015) showed that Eley-Rideal reactions in combination with a complex induced reaction mechanism of gas phase carbon atoms with the grain surface are able to increase the formation rate of multiple O-bearing COMs. Chang & Herbst (2016) added a chain-reaction mechanism to their unified microscopic-macroscopic Monte Carlo code. Conceptually, their mechanism is very similar to the three-body reactions used in this work; however, it is not straightforwardly applicable to a rate-equation based code. Similar to Garrod & Pauly (2011), Dulieu et al. (2019) introduced a single three-body reaction, between H_2NO and H_2CO to reproduce the formation of formamide (NH_2CHO) in co-deposition experiments of H, NO, and H_2CO at 10 K. Their approach tracks two types of H_2NO molecules: the ones that are formed next to an active H_2CO molecule and the ones that are formed next to other molecules. Although different from the one used in this work, their treatment should produce the same results. Shingledecker et al. (2019) showed that radiolysis can efficiently form radicals and other reactive species in the grain's bulk, which are then able to react non-diffusively with neighbouring molecules and drive a rich chemistry there. The most extensive introduction and the one adopted in the present work, however, is presented in Jin & Garrod (2020) and Garrod et al. (2022).

The importance of reactions between heavy reaction partners under dark cloud conditions is supported by several co-deposition experiments of simple and abundant molecules. In experiments with CO molecules and H atoms at 13 K, Fedoseev et al. (2015) found the formation of glycoaldehyde ($HC(O)CH_2OH$) and ethylene glycol ($H_2C(OH)CH_2OH$) in addition to formaldehyde (H_2CO) and methanol (CH_3OH) formation,. The result was confirmed and extended to methyl formate ($HC(O)OCH_3$) formation in CO+H+H_2CO and CO+H+CH_3OH co-deposition

experiments at 15 K by Chuang et al. (2016). There, H_2CO and CH_3OH were only deposited simultaneously to artificially enhance their abundances to provide sufficiently high methyl formate yields to meet the detection sensitivity limits of the experimental setup. In a similar manner, Fedoseev et al. (2017) detected glycerol ($HOCH_2CH(OH)CH_2OH$ and tentatively detected glyceraldehyde ($HOCH_2CH(OH)CHO$) upon co-deposition of CO+H+$HOCH_2CHO$ at 13 K. Qasim et al (2019) showed that the formation of propanal (H_3CCH_2CHO) in co-deposition of C_2H_2+CO+H at 10 K and its subsequent hydrogenation to 1-propanol ($CH_3CH_2CH_2OH$) is possible. Moreover, the formation of the simplest amino acid, glycine (NH_2CH_2COOH) has been shown in co-deposition of CO+NH_2CH_3+O_2+H at 13 K by Ioppolo et al. (2021). Their proposed formation routes are supported by astrochemical models, performed with *MAGICKAL* (Garrod 2013), including non-diffusive reaction mechanisms. Fedoseev et al. (2022) find that ketene (CH_2CO) is formed in co-deposition of H_2O+C+CO+H at 10 K with possible further hydrogenation steps leading to acetaldehyde (CH_3CHO) and ethanol (CH_3CH_2OH) formation. However, the most relevant finding for the present work are the co-deposition experiments of H_2CO+H performed in a temperature range from 10 K to 16 K by Santos et al. (2022). The authors confirmed the predominant formation of methanol by the radical-molecule reaction H_2CO + $CH_3O \rightarrow CH_3OH$ + HCO over the simple H-addition reaction, which was formerly suggested by microscopic kinetic Monte Carlo simulations (Simons et al. 2020. What all the proposed formation pathways have in common is that they involve at least one reaction step where larger surface radicals or molecules react with one another, possibly preceded and-or followed by multiple hydrogenation steps. Before, such reaction steps were deemed inefficient, as both reaction partners are considered to be immobile on the surface of dust grains in the extremely cold conditions of pre-stellar cores. Their inclusion makes invoking non-diffusive reaction mechanisms into astrochemical models necessary. Otherwise, the efficiency of the proposed reactions could be severely underestimated. Interestingly, the found pathways do not require that the grain mantle products are energetically processed by UV photons or cosmic rays; most of the radicals are instead formed by simple surface hydrogenation addition and abstraction reactions.

The inclusion of non-diffusive reaction mechanisms into rate-equation based astrochemical codes is still under scrutiny. While microscopic Monte Carlo codes account for the exact position of each molecule at all times and can therefore accurately determine the amount of respective reactants sitting in close proximity to each other, rate-equation based codes compute only the average formation and destruction rates of the molecules included in their chemical network. Unfortunately, this large amount of information comes with a high computational cost, and hence, studies conducted with a microscopic Monte Carlo code usually use chemical networks including only a small number of species and reactions. To obtain a broad overview over the chemistry occurring in any interstellar region, rate-equation based codes are typically better suited accounting for the multitude of different species and reactions present. In the formulation of non-diffusive chemistry proposed by Jin & Garrod (2020) and Garrod et al. (2022), the probability of the second reactant being close by when the first one forms is simply estimated to be N_i/N_S. Here, N_i is the average number of atoms or molecules of species A or B on the grains, and N_S is the total number of binding sites on a grain. While this recipe is simple to integrate into a rate-equation based code, it can lead to an overestimation of reactants being formed close to each other in the case only very small numbers of the respective reactants are present on the

grain. Additionally, rate-equation based codes are unable to account for clustering of surface species, which could potentially make certain non-diffusive reactions more efficient than would otherwise be the case for a random distribution of reactants on the grain surface.

Here, we present the inclusion of non-diffusive reaction mechanisms following the formulation by Jin & Garrod (2020) and Garrod et al. (2022) into an astrochemical code capable of simulating deuterium chemistry (*pyRate*; Sipilä et al. 2015a, 2019b). The addition of non-diffusive chemistry to *pyRate* provides valuable additional information about the deuteration of COMs that could formerly not be obtained. We applied the added reaction mechanisms to methanol, the simplest of the O-bearing COMs, as it is a key species in the two major formation scenarios for COMs discussed in the current literature. To connect to our previous works (Vasyunin et al. 2017, Chacón-Tanarro et al. 2019a, Riedel et al. 2023), all the necessary modifications were performed in a step-by-step manner to enable the reader to separately evaluate the effects of each step. In a subsequent work, we will extend our chemical network to larger species and investigate the formation and deuteration of other COMs.

This paper is structured as follows: In Section 3.2 we describe the physical model and the updated chemical model in detail. In Section 3.3 we add various non-diffusive reaction mechanisms to the base model individually and in combination with each other. We discuss their importance for the formation and deuteration of methanol and compare them to more conventional modelling approaches and the observationally obtained column density and deuterium fraction profiles from Chacón-Tanarro et al. (2019a). Section 3.4 discusses additional modifications to the chosen chemical and physical parameters. Section 3.5 presents our conclusions. Appendices B.1 and B.2 provide more detailed information for some minor intermediate modification steps.

3.2 Methods

3.2.1 Introducing non-diffusive reaction mechanisms

PyRate was updated to include the non-diffusive mechanisms presented in Jin & Garrod (2020) and Garrod et al. (2022). In general, the present work follows their formulation closely, and we refer to these works for an extensive explanation of the adopted mechanisms and their respective formulation. However, for some of our purposes, namely to ensure comparability to our previous work (Riedel et al. 2023), it proved necessary to modify some equations slightly. Therefore, we lay out very briefly relevant equations below to explain these minor modifications. In Section 3.3.2, following the comparison to previous results, we switch to the original formulation of Jin & Garrod (2020) and Garrod et al. (2022) and use it for the remainder of the paper to ensure comparability to the literature.

According to the standard formulation, as detailed in Hasegawa et al. (1992), the reaction rate R_{AB} of reactants A and B in chemical reactions proceeding diffusively, is given by the following expression:

$$R_{AB} = f_{\rm act}(AB)[k_{\rm hop}(A)N(A)]\frac{N(B)}{N_{\rm S}} + f_{\rm act}(AB)[k_{\rm hop}(B)N(B)]\frac{N(A)}{N_{\rm S}}, \tag{3.1}$$

where $k_{\rm hop}(A)$ or $k_{\rm hop}(B)$ are the rates of thermal hopping (occasionally modified to account for diffusion by quantum tunneling) of molecule A or B, respectively, $N(A)$ or $N(B)$ the abundance of species A or B on the grain (here: average number of molecules on individual grain) and $N_{\rm S}$ total number of binding sites on the grain. The quantity $f_{\rm act}$ denotes the efficiency of a chemical reaction and assumes a value between 0 and 1.

Reaction rates R_{AB} for non-diffusive reactions, as detailed in Jin & Garrod (2020) and Garrod et al. (2022), follow a similar structure as equation 3.1:

$$R_{AB} = f_{\rm act}(AB)R_{\rm comp}(A)\frac{N(B)}{N_{\rm S}} + f_{\rm act}(AB)R_{\rm comp}(B)\frac{N(A)}{N_{\rm S}}, \tag{3.2}$$

where the diffusion rate $[k_{\rm hop}(A)N(A)]$ of reactant A or the diffusion rate $[k_{\rm hop}(B)N(B)]$ of reactant B is replaced by the completion rate $R_{\rm comp}(A)$ or $R_{\rm comp}(B)$ that describe the rate of 'appearance' of reactant A and subsequent reaction with reactant B (or vice versa). The completion rates are derived by equations 3.3 and 3.4:

$$R_{\rm comp}(A) = \frac{1}{1/R_{\rm app}(A) + t_{\rm AB}} \tag{3.3}$$

$$R_{\rm comp}(B) = \frac{1}{1/R_{\rm app}(B) + t_{\rm AB}}, \tag{3.4}$$

where $R_{\rm app}(A)$ and $R_{\rm app}(B)$ are the appearance rates, that depend on the specific non-diffusive mechanism used, and $t_{\rm AB}$ is the average lifetime of both reaction partners staying in a state in which they are ready to react.

Non-diffusive mechanisms are always allowed to act on the entire chemical network and in addition to the well-established diffusive reactions. The added mechanisms include the Eley-Rideal mechanism, photodissociation-induced mechanisms and three-body reactions. Eley-Rideal reactions are reactions in which a molecule from the gas phase adsorbs onto the grain surface and immediately finds a reaction partner in the vicinity of its adsorption spot. The appearance rate for a reactant is simply equal to the adsorption rate of this species. Photodissociation-induced reactions are initiated by a photon dissociating a larger molecule on the dust grain surface into two fragments, followed by a reaction of one of those fragments with another surface molecule in close proximity. The species appearance rate is calculated as the sum of photodissociation rates producing this species. Here, we adopt the description in Jin & Garrod

(2020) (or the PDI version in Garrod et al. 2022), as the proposed refinement that considers that unsuccessful immobile photo-products recombine immediately is not of importance for surface species, since they can diffuse away from their production site before they would recombine again. In three-body reactions, a molecule is initially formed either diffusively, in a reaction with at least one mobile reaction partner (e.g. H), or via the above described non-diffusive reaction mechanisms. Subsequently, the newly formed reaction product can then spontaneously react with another adjacent molecule. Here, the appearance rate is the sum of the reaction rates of all diffusive reactions producing this species. In case they are switched on, the summed reaction rates of Eley-Rideal and photodissociation-induced reactions are also added to the appearance rate. Additionally, the three-body reaction mechanism has two variations. It is possible to perform several successive rounds of three-body reactions. While the first round can be initiated by diffusive reactions, and possibly Eley-Rideal and photodissociation-induced reactions, the following rounds are initiated by the respective preceding round of three-body reactions. The cost of running multiple rounds of three-body reactions with a chemical network comprising 75000 reactions is extremely large and the effect expected to diminish with each round, which is why we limit ourselves to run models with two rounds of three-body reactions. Another option, three-body reactions with excited formation, is to assume that the reaction enthalpy released by the initiating reaction can (partially) help to overcome the activation-energy barrier of the follow-up reaction. This mechanism is only sensible in combination with the basic three-body reactions.

The above described non-diffusive reaction mechanisms can, in principle, be applied in arbitrary combination with each other. However, as running every possible combination would result in an unreasonable amount of models that also not necessarily provide more insights, we restrict ourselves to six models, involving non-diffusive chemistry. We perform a model run, where Eley-Rideal reactions (ND1/ND7), photodissociation-induced reactions (ND2/ND8) and three-body reactions (ND3/ND9) each are enabled separately. Moreover, we test a model with two rounds of three-body reactions (ND4/ND10) and a model where three-body reactions with excited formation are enabled alongside the basic version of three-body reactions (ND5/ND11). At last, we also run a model, where we combine Eley-Rideal, photodissociation-induced and three-body reactions (ND6/ND12), but none of the variations.

3.2.2 Chemical model

The chemical evolution of molecular abundances is calculated with the gas-grain astrochemical code *pyRate*, capable of simulating deuterium chemistry and described in more detail in Sipilä et al. (2015a, 2019b). The overall chemical network is based on the 2014 public release of the Kinetic Database for Astrochemistry (KIDA) gas-phase network (kida.uva.2014, Wakelam et al. 2015). Respective reactions were cloned to include deuterium chemistry for molecules with up to seven atoms and spin-state chemistry for H_2, H_2^+, and H_3^+, as well as multiply protonated species involved in the water and ammonia formation networks and their respective deuterated isotopologues. More details can be found in Sipilä et al. (2015a,b) and Sipilä et al. (2019b). In total the network includes a total of $\approx$ 75000 gas-phase and grain surface reactions, making it substantially larger than commonly used chemical networks that do not treat the chemistry

of isotopologues explicitly. The methanol formation network is the same as presented in detail in Riedel et al. (2023). If not otherwise indicated, a network without abstraction reactions is adopted. However, in Section 3.3.3, the experimentally verified (Santos et al. 2022) methanol formation pathway $H_2CO + CH_3O \rightarrow CH_3OH + HCO$ is added to the network. Moreover, in Section 3.4.2, we also present and discuss selected models including the abstraction scheme proposed by Hidaka et al. (2009).

Surface reactions are allowed to proceed through the Langmuir-Hinshelwood mechanism relying purely on thermal diffusion. Diffusion by quantum tunneling of hydrogen and deuterium atoms is not enabled in most models. We show, however, some models including both types of diffusion for the purpose of comparison to previous works (Vasyunin et al. 2017, Chacón-Tanarro et al. 2019a, Riedel et al. 2023) in Section 3.3.1. The diffusion-to-binding energy E_d/E_b is set to 0.55, a value suggested for atoms by Minissale et al. (2016a) based on their measurements of diffusion and desorption energies of O and N atoms.

Dust grains are assumed to be spherical, with a radius of 0.1 μm and a surface site density of 1.5×10^{15} cm^{-2}. We employed a three-phase grain model, including a gas phase, a chemically active surface phase and an inert mantle phase. In contrast to Jin & Garrod (2020), diffusive and non-diffusive mechanisms are carried out solely on the surface of the dust grains. Chemical reactions or any form of bulk diffusion is not included. The impact of bulk diffusion and reactions is probably small in the physical conditions of pre-stellar cores, where the grains undergo net adsorption rather than net desorption and as long as no invasive desorption mechanisms, that partially (or entirely) destroy the grain mantle, are applied. It can, however, become important if one considers the effect of cosmic-ray-driven radiation chemistry in combination with non-diffusive bulk reactions as was done in the works by Shingledecker et al. (2019), Shingledecker et al. (2020). This is beyond the scope of the present paper.

Initially, we adopted atomic initial abundances (see Table 3.1) taken from Semenov et al. (2010), as they were used for previous works (Chacón-Tanarro et al. 2019a, Riedel et al. 2023). This choice is revisited in section 3.4.3.

Besides thermal desorption, *pyRate* contains several nonthermal desorption mechanisms. In this work, we only apply cosmic-ray induced desorption and reactive desorption as nonthermal desorption mechanisms, since those can efficiently desorb methanol from the grain surface with reactive desorption presumed to be the dominant one. Photo-desorption of methanol has been shown experimentally to have negligible impact on the release of methanol from the grain surface (Bertin et al. 2016, Cruz-Diaz et al. 2016). *PyRate* contains two different options for the treatment of reactive desorption. The first option is a basic mechanism where the reaction products desorb with an efficiency of a specified, but constant value. The second option derives an individual reactive desorption efficiency for every product species that depends on the reaction enthalpy and type of underlying surface Minissale et al. (2016b) and was previously tested in Riedel et al. (2023). Most presented models apply the first option with an efficiency of 1%, as this provides a better comparability to the literature. However in Section 3.4.2, we also present the effects of the experiment-based reactive desorption mechanism for a small selection of models.

During the test phase, we found that when using the Eley-Rideal mechanism, the code will not converge to a solution, unless there is some method in place to get rid of an unphysical

buildup of H_2 on the surface of the dust grains. In Section 3.4.1, we test various options to lower the H_2 coverage, including scaling the binding energies of H_2 and its isotopologues by a factor of 0.1 and the modified binding energy treatment presented in Garrod & Pauly (2011) applied to all species or solely to H, H_2 and its isotopologues. The overall effects on the column densities of CH_3OH are small, which is why we have used the simple scaling option on all models presented in the main body of the paper.

Many chemical reactions both in the gas phase and on the surface of dust grains are exothermic but still require the reactants to overcome activation-energy barriers to react with each other. The formation scheme of methanol comprises at least two hydrogenation steps possessing considerable barriers ($CO \rightarrow HCO$; $E_A = 1.76 \times 10^3$ K, $H_2CO \rightarrow CH_3O/CH_2OH$; 2.00×10^3 K/5.16×10^3 K). However, the extremely cold environments of pre-stellar cores pose a significant obstacle for those reactions to proceed, as the reactants typically have only very low energies. Hence, the details of calculating the efficiency of reactions with activation-energy barriers are crucial for the amount of methanol (and other COMs) produced.

In previous models (see Chacón-Tanarro et al. 2019a, Riedel et al. 2023), a single collision reaction probability (hereafter: SC), which was proposed in Hasegawa et al. (1992), was applied. It derives the probability κ for the reaction to happen upon encounter of the reactants as either a Boltzmann factor, $\kappa = \exp(-E_A/T_d)$, where E_A is the activation energy of the reaction and T_d the dust temperature, or a tunneling probability, $\kappa = \exp\left(-2(a/\hbar)\sqrt{2\mu k_B E_A}\right)$, where a is the thickness of a rectangular barrier and μ the reduced mass. In Riedel et al. 2023 and the present work, reactive tunneling with a barrier thickness of 1 Å is used.

However, the formulation of non-diffusive mechanisms proposed in Jin & Garrod (2020) assumes that rates for reactions containing an activation-energy barrier are calculated using reaction probabilities derived from the reaction-diffusion competition (RDC) model proposed by Chang et al. (2007) (see also Garrod & Pauly 2011). It considers that the reaction partners are confined in the same binding site until one of them diffuses away again. Therefore, they have multiple opportunities to react with each other as opposed to just one in the SC model. In the RDC model, a reaction with an activation-energy barrier is typically significantly more likely to happen as compared to the SC model, as the reactants can undergo multiple attempts to react. Therefore, reactants have to meet less frequently to produce the same amount of successful reactions. In recent years, many modellers adopted the RDC model into their chemical models, as it can provide higher gas phase abundances without assuming a highly efficient diffusion process on the surface or an unlikely high desorption rate.

First, in Section 3.3.1, to present a consistent approach for both diffusive and non-diffusive reactions and to be fully able to compare the effects of non-diffusive chemistry to the previous models, we modified the equations presented in Jin & Garrod (2020) and Garrod et al. (2022) accordingly, which can be simply done by setting f_{act} to κ. We, also, removed the t_{AB}-term from Equations 3.3 and 3.4, as the SC model assumes that the reaction either happens on first encounter of the reactants or not at all. In Section 3.3.2, we switch from using the SC model to using the RDC model for the remainder of the paper. For that, the efficiency factor f_{act} is adjusted to be

Table 3.1: Initial chemical abundances with respect to n_H.

Species	Initial abundance	Species	Initial abundance
He	9.00×10^{-2}	S^+	8.00×10^{-8}
pH_2	5.00×10^{-1}	Si^+	8.00×10^{-9}
oH_2	5.00×10^{-4}	Na^+	2.00×10^{-9}
HD	1.60×10^{-5}	Mg^+	7.00×10^{-9}
H	1.00×10^{-8}	Fe^+	3.00×10^{-9}
D	1.00×10^{-8}	P^+	2.00×10^{-10}
C^+	1.20×10^{-4}	Cl^+	1.00×10^{-9}
N	7.60×10^{-5}	F	2.00×10^{-9}
O	2.56×10^{-4}		

$$f_{\rm act}(AB) = \frac{\nu_{AB}\kappa_{AB}}{\nu_{AB}\kappa_{AB} + k_{\rm hop}(A) + k_{\rm hop}(B)}, \tag{3.5}$$

where $\kappa_{\rm AB}$ is, as described above, either a Boltzmann factor or a tunneling probability. $k_{\rm hop}(A)$ and $k_{\rm hop}(B)$ are the rates of thermal hopping of species A or B, respectively. $\nu_{\rm AB}$ denotes the frequency of collision of both reactants, which is here taken to be the larger of the characteristic frequencies of the reactants derived by the respective equation that is presented in Hasegawa et al. (1992).

3.2.3 Physical model

We present a set of static models using a one dimensional physical model (see Figure 3.1) for H_2 density, gas temperature $T_{\rm gas}$, dust temperature $T_{\rm d}$ and visual extinction $A_{\rm V}$, which was derived from the one presented in Keto & Caselli (2010), with a more detailed description in Sipilä et al. (2019a). The chemical evolution is solved separately for 35 concentric shells spanning the entire core radius of 0.32 pc, resulting in spherical symmetric spatio-temporal evolution of molecular abundances.

The column density distribution is calculated by an integration along the line of sight for different impact factors and is subsequently convolved with a 30″ Gaussian beam to be comparable to the observations by Chacón-Tanarro et al. (2019a).

3.3 Results

In the following, various modifications are introduced in a step-by-step manner to make it possible to follow their effects separately. All presented models are listed in the order of their appearance in Table 3.2. Modified physical and chemical parameters are indicated as well.

Table 3.2: Overview of the various models investigated in this work.

Model	ER[a]	PDI[b]	3B[c]	3BEF[d]	No. rounds	RD efficiency	H_2 removal	other modifications
I1⋆	✗	✗	✗	✗	✗	exp.based	✗	
I2⋆	✗	✗	✗	✗	✗	exp.based	✗	tunnel diffusion
I3⋆	✗	✗	✗	✗	✗	exp.based	✗	fast diffusion
I4⋆	✗	✗	✗	✗	✗	exp.based	scaled E_b	
I5⋆	✗	✗	✗	✗	✗	exp.based	scaled E_b	tunnel diffusion
I6⋆	✗	✗	✗	✗	✗	exp.based	scaled E_b	fast diffusion
D1⋆	✗	✗	✗	✗	✗	1%	scaled E_b	
D2⋆	✗	✗	✗	✗	✗	1%	scaled E_b	tunnel diffusion
D3⋆	✗	✗	✗	✗	✗	1%	scaled E_b	fast diffusion
ND1⋆	✓	✗	✗	✗	✗	1%	scaled E_b	
ND2⋆	✗	✓	✗	✗	✗	1%	scaled E_b	
ND3⋆	✗	✗	✓	✗	1	1%	scaled E_b	
ND4⋆	✗	✗	✓	✗	2	1%	scaled E_b	
ND5⋆	✗	✗	✓	✓	1	1%	scaled E_b	
ND6⋆	✓	✓	✓	✗	1	1%	scaled E_b	
D4†	✗	✗	✗	✗	✗	1%	scaled E_b	
ND7†	✓	✗	✗	✗	✗	1%	scaled E_b	
ND8†	✗	✓	✗	✗	✗	1%	scaled E_b	
ND9†	✗	✗	✓	✗	1	1%	scaled E_b	
ND10†	✗	✗	✓	✗	2	1%	scaled E_b	
ND11†	✗	✗	✓	✓	1	1%	scaled E_b	
ND12†	✓	✓	✓	✗	1	1%	scaled E_b	
NM1†	✗	✗	✗	✗	✗	1%	scaled E_b	include CH_3O+H_2CO
NM2†	✗	✗	✓	✗	1	1%	scaled E_b	include CH_3O+H_2CO
BE1†	✗	✗	✗	✗	✗	1%	$E_b(H_2)$ = 640/500[e] K	
BE2†	✗	✗	✗	✗	✗	1%	dynamic E_b all species	
BE3†	✗	✗	✗	✗	✗	1%	dynamic E_b only H_2	
BE4†	✗	✗	✗	✗	✗	1%	dynamic E_b only H & H_2	
D5†	✗	✗	✗	✗	✗	1%	scaled E_b	H-abstraction reac.
D6†	✗	✗	✗	✗	✗	exp.based	scaled E_b	
D7†	✗	✗	✗	✗	✗	exp.based	scaled E_b	H-abstraction reac.
D8†	✗	✗	✗	✗	✗	1%	scaled E_b	ini.abund: 50%H/50%H_2

Notes. Only the chemical and physical properties that vary between models are listed. ⋆ Models that apply the single collision model proposed by Hasegawa et al. (1992) to derive the reaction probabilities. † Models that apply the RDC model proposed by Chang et al. (2007) to derive the reaction probabilities. [(a)] Eley-Rideal reactions , [(b)] photodissociation-induced reactions , [(c)] three-body reactions and [(d)] three-body reactions with excited formation . IX are models with intermediate modifications steps presented in Appendices B.1 and B.2, DX are models with solely diffusive reaction mechanisms, NDX are models with additional non-diffusive reaction mechanisms, NMX are models for which the chemical network was modified, and BEX are models with modified H_2 removal methods. [(e)] 640 K being the binding energy on bare grain surfaces, 500 K being the binding energy on water ice.

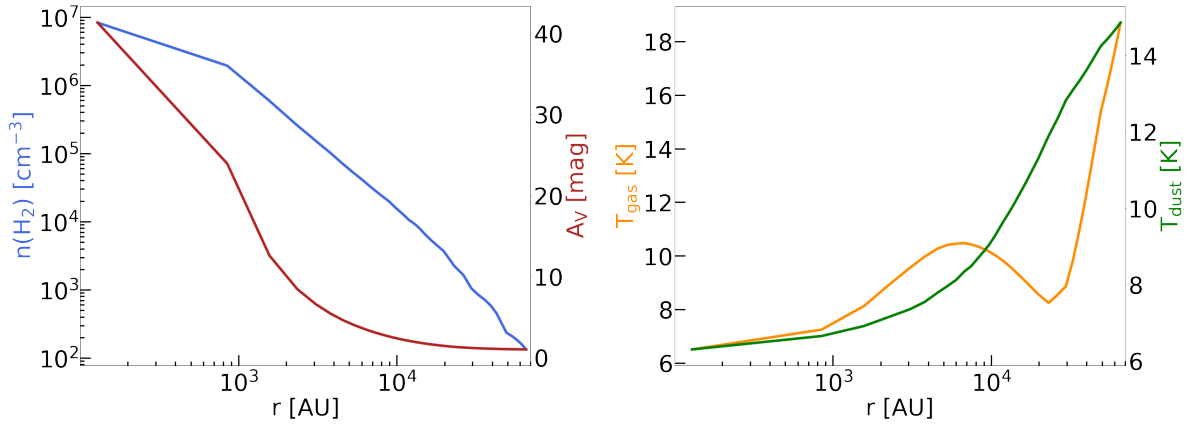

Figure 3.1: Physical model first presented in Keto & Caselli (2010) and described in more detail in Sipilä et al. (2019a) providing static radial profiles of the H_2 volume density, $n(H_2)$ (blue, logarithmic scale), the visual extinction, A_V (red), T_{gas} (orange), and the dust temperature, T_{dust} (green).

3.3.1 Applying a single collision model

The upper panel of Figure 3.2 presents the column density profiles of CH_3OH (left) and N(CH_2DOH)/N(CH_3OH) profiles (right) of various models including non-diffusive reaction mechanisms at the best-fit time of $t = 3.0\times10^5$ yr. The lower panel sets these results in comparison to previous results (Riedel et al. 2023) and the available gas phase observations by Chacón-Tanarro et al. (2019a). The single-dish observations, carried out with the Institut de Radioastronomie Millimétrique (IRAM) 30m telescope, show that CH_3OH peaks in an asymmetric ring (see also Bizzocchi et al. 2014; Vastel et al. 2014; Spezzano et al. 2016). The position of strongest emission (methanol peak) is located in the northeastern part of the ring offset from the position of the dust peak. The best-fit time is taken to be the time-step, where the χ^2 value of the observed central column density versus the corresponding value in the base model for H_2CO and CH_3OH (and their observed deuterated isotopologues) are minimised.

A purely diffusive model with a diffusion-to-binding energy ratio of E_d/E_b of 0.55 (slow thermal diffusion; model D1) is always shown as a reference. We find that applying the non-diffusive mechanisms as proposed by Jin & Garrod (2020) and Garrod et al. (2022) and modified to be consistent with the SC model as detailed above, is only adding minor contributions to the gas phase methanol reservoir, independent of the respective mechanism. While the largest impact on the CH_3OH and N(CH_2DOH)/N(CH_3OH) profiles is seen when adding three-body reactions (model ND3), a further addition of a second round of three-body reactions (ND4) or three-body reactions with excited formation (model ND5) is not increasing the methanol yield much more. Also, Eley-Rideal reactions (model ND1) only cause a slight increase in methanol production. Photodissociation-induced reactions (model ND2) have a negligible impact on the methanol reservoir. The increase for CH_3OH is typically larger than for its deuterated counterpart CH_2DOH, consequently reducing the N(CH_2DOH)/N(CH_3OH) slightly. Most of the increase in

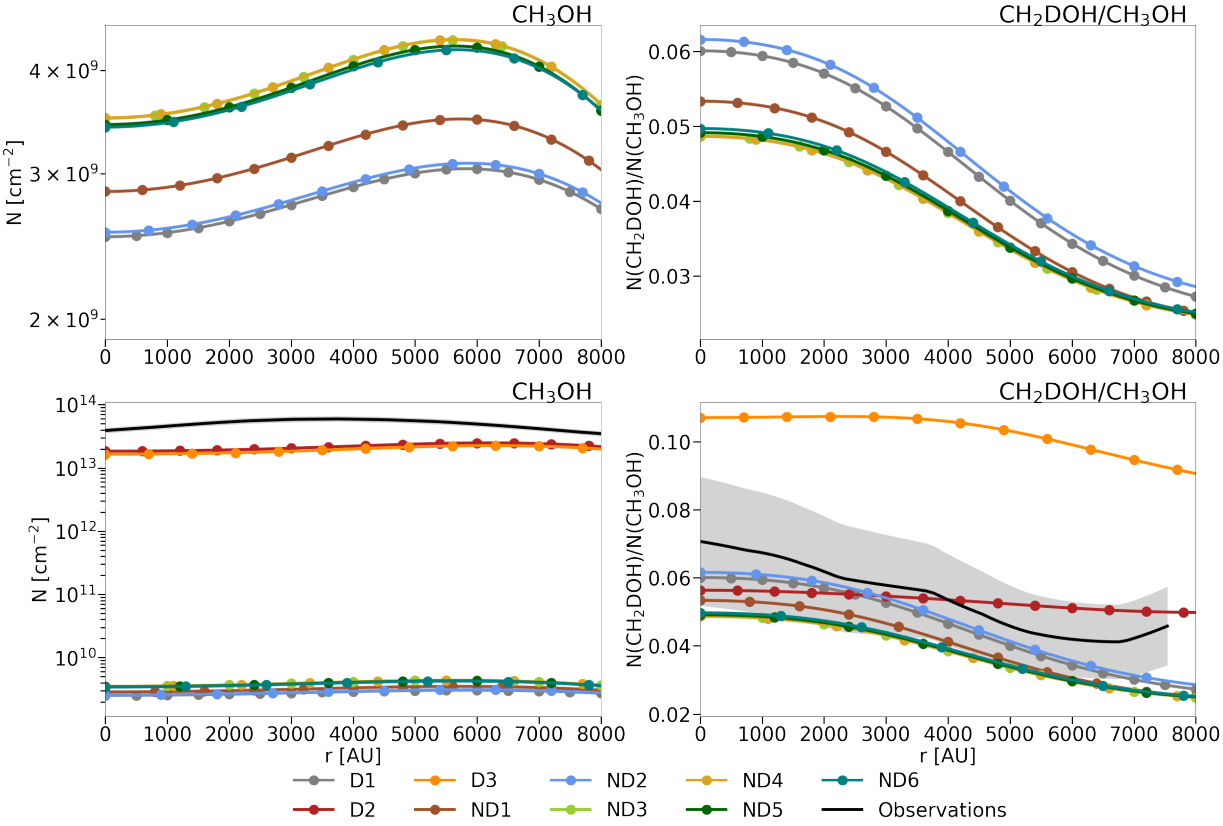

Figure 3.2: Column density profiles of CH_3OH (left) and $N(CH_2DOH)/N(CH_3OH)$ profiles (right) of various combinations of the introduced non-diffusive mechanisms (model ND1-ND6; upper panel) and of diffusive models, including the diffusion of hydrogen (and deuterium) atoms by quantum tunneling (model D2; red) or a diffusion-to-binding energy ratio of E_d/E_b of 0.2 (fast thermal diffusion; model D3; orange; lower panel). A diffusive model with a diffusion-to-binding energy ratio of E_d/E_b of 0.55 (slow thermal diffusion; model D1; grey) is shown as a reference. All models are performed within the framework of the single collision model. The observed profiles, ranging from the dust peak into the direction of the methanol peak, presented first in Chacón-Tanarro et al. (2019a), are depicted in black (errors as grey-shaded areas). The results are presented for the best-fit time of $t = 3.0 \times 10^5$ yr.

methanol can be accredited to opening up an additional pathway for simple H-addition reactions. This is particularly the case for the ND1 model, where the Eley-Rideal mechanism contributes up to 44% at the dust peak (densest part) and 13% at the methanol peak. Reactions between heavier reactants (e.g. $OH+CH_3 \rightarrow CH_3OH$ or $OH+CH_2D \rightarrow CH_2DOH$), which occur predominantly via non-diffusive reaction mechanisms, start to play a role as well and are even the dominant formation route on occasion. Especially for the formation of the methanol precursors - CH_3O and CH_2OH - the reactions $O+CH_3 \rightarrow CH_3O$ and $OH+CH_2 \rightarrow CH_2OH$ dominate the formation (for CH_3O) or are comparable to the hydrogenation reaction (for CH_2OH). These formation routes are likely favoured as they do not possess an activation-energy barrier, while the hydrogenation reactions $H+H_2CO \rightarrow CH_3O$ ($E_A = 2 \times 10^3$ K) and $H+H_2CO \rightarrow CH_2OH$ ($E_A = 5.16 \times 10^3$ K) have a substantial one. For Eley-Rideal reactions, we typically find an increased importance to the innermost part of the core, where the higher gas phase abundances result in larger adsorption rates. The photodissociation-induced and three-body reactions, however, show higher contributions at the position of the methanol peak.

Riedel et al. (2023), in agreement with Vasyunin et al. (2017) and Chacón-Tanarro et al. (2019a), conclude that an increase of the diffusion rates of hydrogen and deuterium atoms over the grain is necessary to explain the observations. They tested two available options: either allowing the diffusion to take place both by a slow thermal hopping process ($E_d/E_b = 0.55$) and additional quantum tunneling of hydrogen and deuterium atoms through a rectangular barrier with a width of 1 Å or by a fast thermal hopping process ($E_d/E_b = 0.2$). Additionally, a reference model with solely a slow thermal hopping process ($E_d/E_b = 0.55$) was performed. Both options with increased diffusion rates are able to increase the methanol column densities by several orders of magnitude compared to the reference model, but they still underproduce the observed methanol column densities by roughly an order of magnitude. However, most models presented in Vasyunin et al. (2017), Chacón-Tanarro et al. (2019a), and Riedel et al. (2023) apply an experiment-based formulation of reactive desorption proposed by Minissale et al. (2016b), which derives an individual reactive desorption efficiency for every product species in a chemical reaction, depending on the reaction enthalpy and type of underlying surface. Since this version of reactive desorption typically produces reactive desorption efficiencies much lower than 1% for heavier reaction products, this underproduction could potentially be caused by an underestimation of the desorption process. For a full comparison of the models using a form of increased diffusion rate with the models comprising non-diffusive reaction mechanisms presented here, we performed the former ones again, but with scaled H_2 binding energies and a constant reactive desorption efficiency of 1% (see Appendices B.1 and B.2 for more details).

In the framework of the SC model, we conclude, when using solely a slow diffusion process ($E_d/E_b = 0.55$), the diffusion rate of hydrogen (and deuterium) atoms is not efficient enough. Applying the non-diffusive mechanisms is only adding a minor contribution to the gas phase methanol reservoir. Models increasing the diffusion rate, especially of hydrogen (and deuterium) atoms, tested in the previous works, are more successful in that regard and are able, when using a constant reactive desorption efficiency of 1%, to increase column densities to almost the observed order of magnitude and simultaneously produce a $N(CH_2DOH)/N(CH_3OH)$ profile, which is well within the area of uncertainty of the observations.

However, available laboratory experiments (Hama et al. 2012 on an ASW surface,

Kimura et al. 2018 on a CO surface) found that the diffusion of hydrogen (and deuterium) atoms at 10 K is not dominated by quantum tunneling but rather thermal hopping, as a significant isotope effect between hydrogen and deuterium atoms has not been observed. These results are also backed up by theoretical work (Senevirathne et al. 2017).

Also, measurements for diffusion energies E_d or more commonly diffusion-to-binding energy ratios E_d/E_b are quite sparse. They are found to be species-dependent with $E_d/E_b = 0.2$ (as used for the model with a fast thermal hopping process) being the lowest value debated in the literature (Furuya et al. 2022b). However, these values were measured for CO and CH_4 and not for H. Moreover, experiments (Watanabe et al. 2010, Hama et al. 2012) conclude that potential wells on the surface of the dust grain can be divided into groups according to their depth, with Hama et al. (2012) identifying at least three different ones. Most astrochemical codes are not able to model such complicated grain surface properties, with only a few exceptions (e.g. Grassi et al. 2020), but only use a uniform diffusion-to-binding energy ratio. Additionally, Jin & Garrod (2020) find that a low value for the diffusion-to-binding energy ratio ($E_d/E_b = 0.35$ in their case) causes a quicker hydrogenation of radicals, which shortens their lifetimes and consequently could make proposed surface formation pathways for COMs less efficient.

3.3.2 Applying a reaction-diffusion competition model

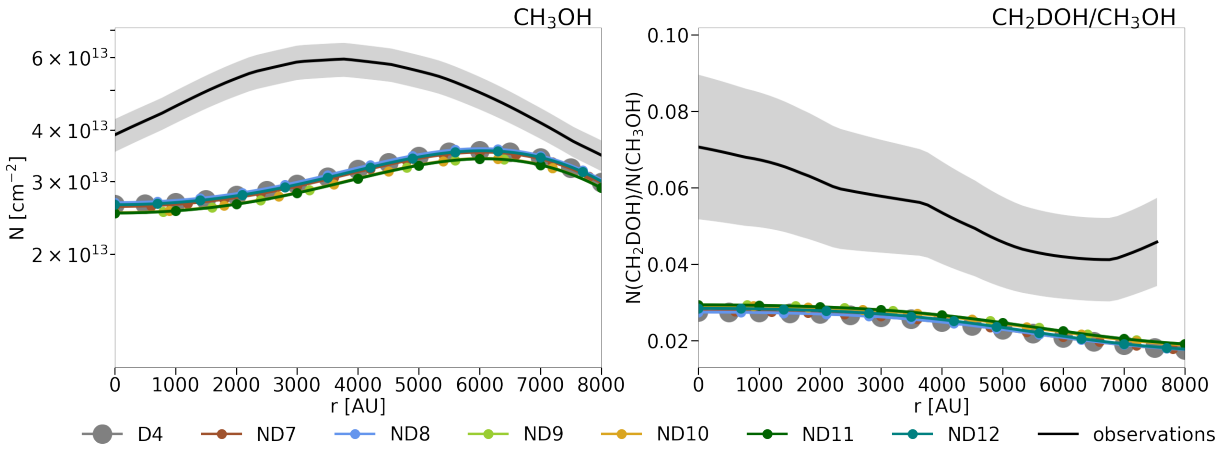

Figure 3.3: Column density profiles of CH_3OH (left) and $N(CH_2DOH)/N(CH_3OH)$ profiles (right) of various combinations of the introduced non-diffusive mechanisms (model ND7-ND12). A diffusive model with a diffusion-to-binding energy ratio of E_d/E_b of 0.55 (slow thermal diffusion; model D4; grey) is shown as a reference. All models are performed within the framework of the RDC model. The observed profiles are depicted in black (errors as grey-shaded areas). The results are presented for the best-fit time of $t = 3 \times 10^5$ yr.

Figure 3.3 presents the column density profiles of CH_3OH (left) and $N(CH_2DOH)/N(CH_3OH)$ profiles (right) of the diffusive model with a slow thermal hopping process ($E_d/E_b = 0.55$; D4) and various non-diffusive models (ND7-ND12), derived by assuming the RDC model. They are presented at the best-fit time of $t = 3.0 \times 10^5$ yr. We find that the column densities of CH_3OH and

CH_2DOH in model D4 are increased by several orders of magnitude compared to the respective model derived with the SC model (D1) due to the higher reaction probabilities of the reactions with activation-energy barriers (CO + H → HCO and CH_2OH/CH_3O + H → CH_3OH). In fact, the CH_3OH column density profile matches the observationally constrained profiles within a factor of around two, which is considered to be a good agreement for astrochemical models.

Interestingly, the $N(CH_2DOH)/N(CH_3OH)$ in model D4 is decreased by a factor of two to three compared to model D1. This decrease is caused by the change in the reaction probabilities for important formation pathways of CH_2DOH when applying the RDC model. CH_2DOH can be formed via three different pathways, starting from H_2CO: (I) the hydrogenation of H_2CO to CH_2OH and its subsequent deuteration (see reaction 3.6), (II) the deuteration of H_2CO to CHDOH and its subsequent hydrogenation (see reaction 3.7) and (III) the deuteration of H_2CO to CH_2DO and its subsequent hydrogenation (see reaction 3.8). The CH_2DOH formation from CH_3O or CH_2OD is excluded in the selected formation scheme.

$$H_2CO \xrightarrow{+H} CH_2OH \xrightarrow{+D} CH_2DOH \tag{3.6}$$

$$H_2CO \xrightarrow{+D} CHDOH \xrightarrow{+H} CH_2DOH \tag{3.7}$$

$$H_2CO \xrightarrow{+D} CH_2DO \xrightarrow{+H} CH_2DOH. \tag{3.8}$$

When applying the SC model for the calculation of reaction probabilities for reactions with an activation-energy barrier, the hydrogenation reaction of H_2CO will much more often result in the formation of the isomer CH_3O as opposed to CH_2OH due to its much higher activation-energy barrier ($E_A = 5.16 \times 10^3$ K versus $E_A = 2.00 \times 10^3$ K). Consequently CH_3O is around 10^4x more abundant than CH_2OH at the dust peak for the best-fit time. Without the inclusion of abstraction reactions (see also Section 3.4.2), a deuteration to CH_2DOH is not possible any more once CH_3O is formed. Since abstraction reactions are not considered in the first part of this work, the formation of CH_2DOH mainly proceeds via reaction 3.8 as it has the lowest activation-energy barrier: $E_A = 1.28 \times 10^3$ K compared to $E_A = 5.16 \times 10^3$ K for the other two options. When applying the RDC model, however, the formation of CH_2OH is not hindered significantly by the reaction's high activation-energy barrier, as both reactants can undergo numerous attempts to react until one of them diffuses away again. In the extremely cold environment of pre-stellar cores the diffusion rates, even of hydrogen atoms, are much lower than the typical collision frequencies ν_{AB}. Consequently, the efficiency factor f_{act} is much larger than in the SC model, resulting in an almost equal abundance of CH_2OH and CH_3O, while the abundance of CH_2DO is decreased. Additionally, the D/H ratio on the grain surface in the RDC model is lower - around two order of magnitudes at the dust peak - than in the SC model. Combined with the lower D/H ratio and the slower hopping rate of D atoms, the higher amount of CH_2OH decreases the relative CH_2DOH formation as a hydrogenation reaction of CH_2OH to form CH_3OH is more likely than the respective deuteration reaction to form CH_2DOH.

The impact of applying the various non-diffusive reaction mechanisms is again quite minor, which is in agreement with the results presented in Jin & Garrod (2020) (see Figure 11). In the models described above, methanol forms mainly by successive H/D-addition reactions to CO.

Assuming a more efficient diffusion process is not necessary, when applying the RDC model, as the activation-energy barriers can be overcome more often due to the possibility of multiple reaction attempts, thereby reducing the need for a high amount of meeting events between the reactants. Reactions between two heavier reactants, such as CH_3 + OH → CH_3OH or similar reactions for precursors of methanol, do not contribute significantly.

3.3.3 Introducing $H_2CO + CH_3O \rightarrow CH_3OH + HCO$

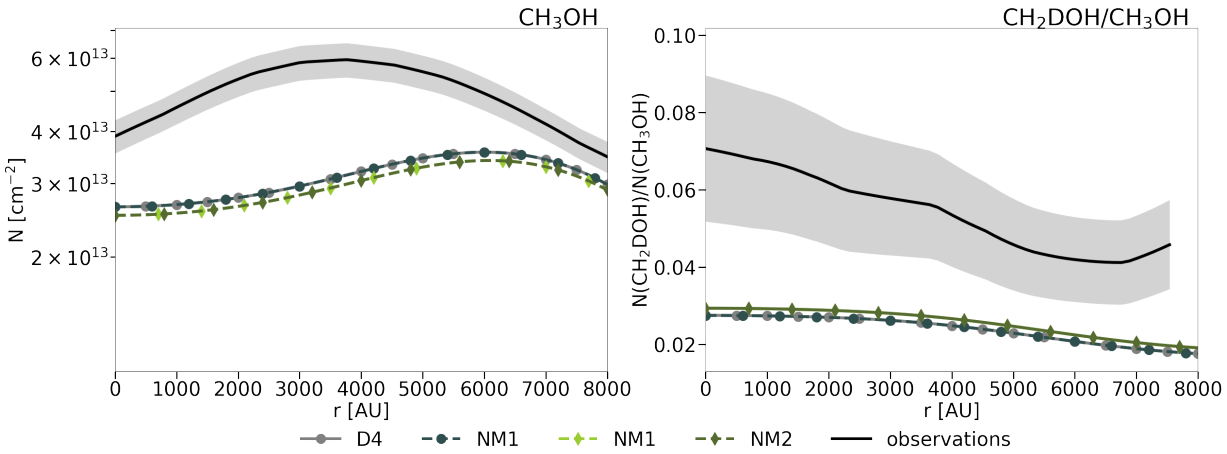

Figure 3.4: Column density profiles of CH_3OH (left) and $N(CH_2DOH)/N(CH_3OH)$ profiles (right) of the diffusive model (D4) and a model including three-body reactions in addition to diffusive reactions (ND9). Both models use the methanol formation scheme presented in Riedel et al. (2023). Subsequently, they were redone with a modified chemical network, including the reaction $H_2CO + CH_3O \rightarrow CH_3OH + HCO$ (NM1 and NM2). The observed profiles are depicted in black (errors as grey-shaded areas).

Typically, the methanol formation pathway solely comprises successive H-addition reactions (or H-abstraction reactions) of atomic H to CO (e.g. Watanabe & Kouchi 2002, Fuchs et al. 2009). The hydrogen atom and its deuterated counterpart are both light enough to efficiently diffuse over the surface of the dust grain even at temperatures ranging around 10 K. If at least one of the reactants can diffuse efficiently, the contribution of non-diffusive reaction mechanisms to the formation yields of a reaction is generally small.

However, as Jin & Garrod (2020) showed, non-diffusive reaction mechanisms can have major contributions for reactions where both reactants are too heavy to efficiently diffuse over the surface. Several such reactions for the formation of methanol were proposed and tested in recent years. In their microscopic kinetic Monte Carlo (KMC) code, Simons et al. (2020) included several H-abstraction reactions between heavy intermediate products of the methanol formation pathway - HCO, H_2CO and CH_3O - with each other. While most of those reactions seem to produce only small methanol yields, Simons et al. (2020) surprisingly derived a contribution of

60% to 90%, depending on the physical conditions, for the reaction between H_2CO and CH_3O:

$$H_2CO + CH_3O \rightarrow CH_3OH + HCO, \tag{3.9}$$

making it the dominant pathway for methanol formation over the simple H-addition reaction. This result was later confirmed experimentally by Santos et al. (2022). These authors performed several H_2CO and H (or other combinations with D_2CO and D) co-deposition experiments with H/H_2CO ratios of either 10 or 30 in a temperature range between 10 K and 16 K. Similar to Simons et al. (2020), they find reaction 3.9 to be the dominant pathway with a contribution of at least 83% independent of the H/H_2CO ratios and temperatures. Additionally, they conclude that forming methanol predominantly by reaction 3.9 would result in a decrease of the expected deuterium fractionation due to the kinetic isotope effect.

Although these findings would signify a major paradigm shift in the methanol formation scheme, most rate-equation codes, unlike microscopic Monte Carlo codes, are not equipped to properly test the efficiency of chemical reactions between two heavy reactants in low temperature regimes, as they do not account for the possibility that the reactants could be already in close proximity by chance. Finally, with the inclusion of non-diffusive reaction mechanisms, we are in a position to test the efficiency of reaction 3.9.

We adopted the branching ratio of 0.4 from Simons et al. (2020) for reaction 3.9. They also include the reaction channel H_2CO+$CH_3O \rightarrow CH_3OCH_2O$ and a nonreactive channel to account for cases where the relative geometry of the reactants is not suitable for a reaction and the reactants are unable to reorient. In the present work, these other reaction channels are only implicitly accounted for by using a branching ratio unequal one. As reaction 3.9 is a radical-molecule reaction, it has an activation-energy barrier, which was estimated to be 2670 K by Álvarez-Barcia et al. (2018). Subsequently, reaction 3.9 is cloned to generate the reactions involving the various deuterated counterparts of the reactant and product species, resulting in 16 distinct versions. After adding the resulting reaction list to the chemical network used above, we run the diffusive model D4, resulting in model NM1, and the non-diffusive model including three-body reactions ND9, resulting in model NM2. The results are depicted in Figure 3.4. The former run is performed to verify that reaction 3.9 is inefficient when assuming purely diffusive reactions to occur, which can be indeed confirmed, as the column density profiles of both CH_3OH and CH_2DOH of model D4 and NM1 are almost identical. The latter run is performed, because non-diffusive reaction mechanisms had the largest contribution for models including three-body reactions in the previous models presented above. In contrast to the results of Simons et al. (2020) and Santos et al. (2022), we only find negligible contributions to the methanol formation yields from reaction 3.9, the majority of methanol is still formed by the addition of atomic hydrogen to CH_3O or to CH_2OH. Our explanation for these contradicting results is that the occurrence rate of either H_2CO or CH_3O being produced in close proximity to the other reactant is much smaller than a hydrogen atom diffusing to a binding site, where a CH_3O molecule is sitting.

Apparently, this is not the case for the other two works by Simons et al. (2020) and Santos et al. (2022). Both groups of authors argue that reaction 3.9 might be the dominant route in their works due to a higher availability of H_2CO and CH_3O close to each other as opposed to hydrogen atoms on the grain's surface. The chemical network in Simons et al. (2020) is limited to a

hydrogen addition chain from CO to form methanol that was extended to also account for some recent experimental results on the formation of larger COMs (see Fedoseev et al. (2015) and Chuang et al. (2016)). Considering significantly more chemical reactions would be prohibitively computationally costly for a microscopic Monte Carlo code to perform. Naturally, the surface of their simulated dust grains only consists of the limited amount of species included in their chemical network, which could cause an overestimation of the occurrence rate of H_2CO and CH_3O molecules in close proximity to each other. Chemical codes that are based on the rate-equation approach are not that severely limited in the same sense. The simulations presented in this work include over 1000 species that are coupled by $\approx$ 75000 reactions, resulting in a more realistic surface composition for interstellar dust grains. Similarly is a H/H_2CO ratio of 30 or 10 used in the H_2CO and H codeposition experiments by Santos et al. (2022) quite low as compared to the interstellar conditions, which could again result in an overestimation of the availability of H_2CO close to CH_3O molecules. In a more recent work by Jiménez-Serra et al. (2025), an adaption of the KMC code used in Simons et al. (2020) was employed to model the ice chemistry in the Chamaeleon I cloud. The chemical network used in this work also includes relevant species and reactions for the formation of CO_2, CH_4, NH_3, and H_2O, in addition to the network used in Simons et al. (2020). Interestingly, with this larger network Jiménez-Serra et al. (2025) derive only a contribution of $\approx$ 10% for reaction 3.9 and $\approx$ 90% for the hydrogenation of CH_2OH and CH_3O. However, since the physical conditions in these two works are not identical, the comparison of both results has to be regarded with some caution.

On the other hand, the specific properties of hydrogen diffusion, its dependency on ice structure, binding sites and -energies and how to include those into chemical codes is still under debate. An overestimation of the hydrogen diffusion rate on the surface could also result in an overestimation of the hydrogenation reaction's efficiency and consequently lower the contribution of reaction 3.9.

3.4 Discussion

In addition to the introduction of non-diffusive reaction mechanisms, we explored various parameter modifications. They proved to be either necessary for the inclusion of non-diffusive chemistry or showed large effects on the CH_3OH column density or $N(CH_2DOH)/N(CH_3OH)$ ratio.

3.4.1 Removing surface H_2

The buildup of an unreasonable amount of H_2 on the surface of dust grains in cold dense cores is a common issue for astrochemical codes. The H_2 adsorption rate is large due to its high abundance in the gas phase, while desorption rates in the extremely cold and highly shielded environments are quite low. The H_2 problem becomes more severe in three-phase models, as H_2 molecules are incorporated into the mantle and locked in, resulting in a very high amount of mantle layers. Additionally, we found in this work that when applying the Eley-Rideal mechanism, the code will not converge to a solution, unless there is also a mechanism in place that removes the excess

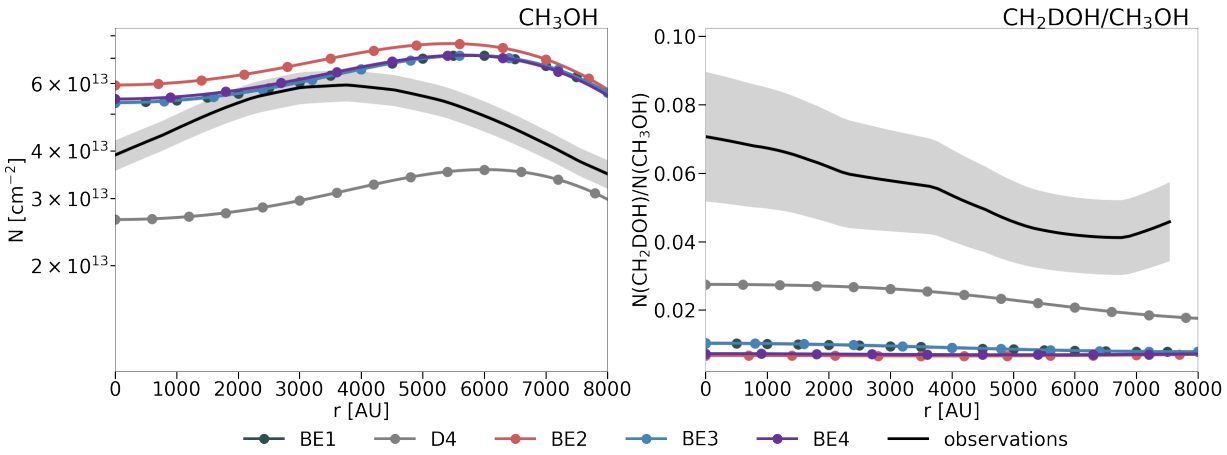

Figure 3.5: Column density profiles of CH_3OH (left) and $N(CH_2DOH)/N(CH_3OH)$ profiles (right) of various diffusive models, that we used to test different approaches to prohibit an unphysical buildup of H_2 on the surface of dust grains. A reference model (BE1) without a H_2 removal method is shown. Additionally, we present a model (D4), where the binding energy of H_2 and its isotopologues were scaled by 0.1 and several models adopting the H_2 removal method proposed by Garrod & Pauly (2011) applied to all species (BE2), only to H_2 (BE3) and only to H and H_2 (BE4). The observed profiles are depicted in black (errors as grey-shaded areas).

H_2 from the surface of the dust grains.

The H_2 excess is likely caused by the usage of binding energies appropriate for a pure water ice surface, while a realistic grain surface is composed of mostly H_2O, CO, CO_2, and ill constrained amounts of H_2. Cuppen et al. (2009) proposed that the binding energy to an H_2 surface could be around 10 times weaker than to other surface types. This motivated Garrod & Pauly (2011) to introduce effective binding $E_{b,eff}$ and diffusion energies $E_{d,eff}$ considering the fractional H_2 surface coverage $\theta(H_2)$:

$$E_{b,eff} = E_b[1 - \theta(H_2)] + 0.1E_b\theta(H_2). \tag{3.10}$$

In equation 3.10, the surface fraction $\theta(H_2)$ that is covered by H_2 contributes only 0.1 times as much to the effective desorption energy as the remaining surface fraction. The main effect of the method is a significant reduction of the amount of H_2 on the surface and in the mantle of the dust grain. However, in Garrod & Pauly (2011), the method is applied to every grain species and consequently also causes a decrease of the binding energies of other species. The same is true for the diffusion energies E_d, as they are usually coupled to the binding energies by the diffusion-to-binding energy ratio E_d/E_b, which is typically due to the lack of sufficient experimental constraints, simply a single, constant value. Therefore, applying the above-described method causes also a decrease in the diffusion energies, increasing the grain species' mobility.

Slightly more complex variations of this method have also been adopted in several other works. Taquet et al. (2014) considers not only H_2 as a surface constituent with distinctly different binding energies from H_2O, but also bare grain and pure ice; Furuya & Persson (2018)

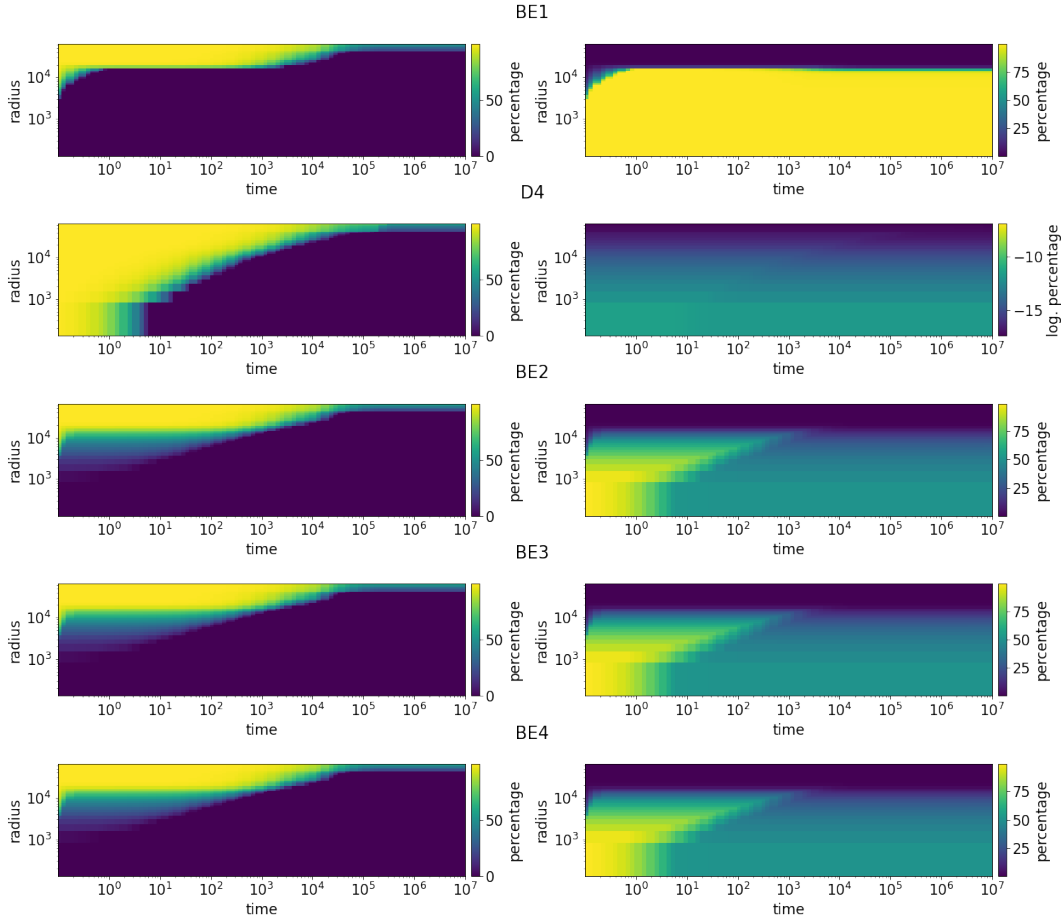

Figure 3.6: Coverage of dust grain as a function of time (x-axis) and radius (y-axis). The left column shows the percentage of empty binding sites, which are typically filled quickly by absorbed and newly formed molecules. The right column shows the percentage of H_2.

also considered CO, CO_2 and CH_3OH. Also, Garrod et al. (2022) propose a refinement of their original formulation, where they assume that every surface species is bound to four adjacent binding partners that collectively contribute to the binding energy. Each of the binding partners can either be an H_2 molecule or not, introducing five types of binding sites of varying strength (1.0 for no H_2 molecules; 0.1 for 4 H_2 molecules). Considering this more intricate version mainly results in a further reduction of the H_2 surface coverage and a lessened influence of the H_2 content on the diffusion and binding energies of other species.

We tested different methods to remove the excess surface H_2: scaling the binding energies of H_2 and its isotopologues by a factor of 0.1 (model D4) and several versions of the original formulation by Garrod & Pauly (2011) applied to all species (model BE2); only to H_2 and its deuterated isotopologues (model BE3); or only to H_2, H, and their isotopologues (model BE4). Model BE3 and BE4 were tested, as heavier species should be able to penetrate through the single monolayer of H_2 and bind as usual to the underlying ice, which is backed by laboratory experiments that do not find evidence for binding energy changes in experiments with H_2 presence in the apparatus (priv. comm. with Gleb Fedoseev). All models presented in Section 3.4.1 apply only diffusive reaction mechanisms. Non-diffusive reaction mechanisms are not included, as we wanted to be able to compare the effects of the various H_2 removal methods to a reference model (model BE1) without one. Figure 3.5 presents the column density profiles of CH_3OH (left) and $N(CH_2DOH)/N(CH_3OH)$ profiles (right), while Figure 3.6 shows the surface coverage of the grain as a function of time (x-axis) and radius (y-axis). In general, the CH_3OH column densities and $N(CH_2DOH)/N(CH_3OH)$ of the modified models (D4 and BE2-BE4) differ only by a factor of around two or less when compared to the reference model (BE1). The largest difference to the reference model is seen when using scaled H_2-binding energies (model D4), which is likely due to the fact that it represents the most extreme H_2 removal method. Its application removes the surface H_2 almost completely, decreases the CH_3OH column density by approximately a factor of two and increases the $N(CH_2DOH)/N(CH_3OH)$ by the same amount. It is noteworthy, that we partially see the opposite trend when this method is applied in the context of the single collision model (see Appendix B.1). The other H_2 removal methods (models BE2-BE4) produce CH_3OH column densities and $N(CH_2DOH)/N(CH_3OH)$ ratios that are closer to the reference model and also each other. For model BE2, where the Garrod & Pauly (2011) method is applied to all grain species, are the CH_3OH column densities slightly higher than in the reference model, while for model BE3 and BE4 the difference to the reference model is negligible. Models BE2-BE4 show a similar level of H_2 removal, with the H_2 coverage being altered from 99,9% to 56% for the best-fit time of $t = 3.0 \times 10^5$ yr at the position of the dust peak. Interestingly, the $N(CH_2DOH)/N(CH_3OH)$ ratio of model BE1 and model BE2-BE4 is lower than that of model D4 with only slight differences between the former models. Overall, Model BE3, where the Garrod & Pauly (2011) method is applied to only H_2 and its isotopologues, shows the smallest difference to the reference model. It is, however, difficult to decide which method is the closest to a realistic description of the grain surface, as we currently still lack good constraints on the amount of surface H_2 in pre-stellar cores. A removal of the excess surface H_2 is mainly necessary to be able to run the Eley-Rideal mechanism, as otherwise the code will not converge to a solution. In principle, all tested mechanisms are able to remove this convergence problem, but the method of scaling the H_2-binding energies (model D4) shows the lowest computative cost and the least

issues with convergence. Therefore, we adopted it for the majority of this work.

3.4.2 Combining H-abstraction reactions and chemical desorption

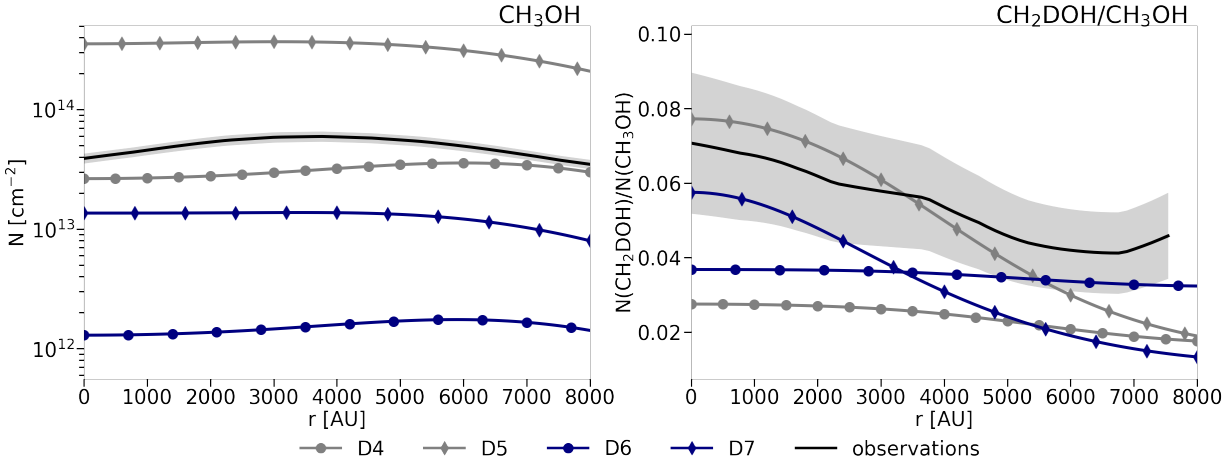

Figure 3.7: Column density profiles of CH_3OH (left) and $N(CH_2DOH)/N(CH_3OH)$ profiles (right) of various diffusive models, either including solely H-addition reactions (round markers) or H-addition and H-abstraction reactions (diamond markers) combined with either a constant reactive desorption efficiency of 1% (grey) or an experiment-based reactive desorption efficiency based on Minissale et al. (2016b) (navy). The observed profiles are depicted in black. Errors are shown as grey-shaded areas.

Various laboratory experiments (Hidaka et al. 2009, Chuang et al. 2016, Minissale et al. 2016c) agree that H-abstraction reactions play an important role in the methanol formation scheme. Theoretically, the inclusion of H-abstraction should have two important effects on the gas phase reservoirs of CH_3OH and CH_2DOH. (I) The reactive desorption rate of methanol increases due to cyclic H-abstraction events (e.g. Jin & Garrod 2020): when a CH_3OH molecule (or a CH_2DOH molecule) is formed, it can be desorbed into the gas phase with a certain probability. However, in the majority of cases, it stays on the grain surface, where it can be subject of H-abstraction reactions that reduce it back to CH_3O or CH_2OH, which can be hydrogenated to methanol again and thereby desorbing with some probability into the gas phase. In principle, the described addition and abstraction steps can be repeated multiple times, thereby amplifying the reactive desorption process beyond what is suggested by the reactive desorption efficiency. (II) The $N(CH_2DOH)/N(CH_3OH)$ is increased due to preferential abstraction of CH_2DOH to CH_2DO and CHDOH (Hidaka et al. 2009): the reaction CH_2DOH + H has three possible outcomes in our chemical network. It can either reduce to CH_2OH, from where a hydrogenation to CH_3OH is more likely to happen than a deuteration to CH_2DOH again, or it can reduce to CHDOH and CH_2DO, from where a hydrogenation to CH_2DOH is more likely to happen than a deuteration to CHD_2OH. The branching ratio (0.17) for the former reaction, likely reversing the deuteration, is lower than for the latter two possibilities (0.33 and 0.5, respectively), preserving the deuteration.

It is noteworthy that the likelihood of hydrogenation versus deuteration reactions depends on the ratio of deuterium to hydrogen atoms and the assumed mode of diffusion on the surface of the dust grains. In case the D/H ratio is sufficient to compensate the slower diffusion of deuterium atoms, deuteration reactions can become more likely than hydrogenation reactions. However, this is not the case for the models presented in this Section.

Figure 3.7 shows the impact of the inclusion of the H-abstraction reactions following the Hidaka et al. 2009-scheme, and their combination with either a simple constant reactive desorption efficiency of 1% (model D5) or the experiment-based reactive desorption efficiencies following Minissale et al. (2016b) (model D7). For the purpose of comparison, we also show the respective models solely including H-addition reactions (model D4 and D6).

Models D4 and D5, using a constant reactive desorption efficiency of 1% show both theoretically expected effects. Model D5, which includes H-abstraction reactions, has higher column densities of both CH_3OH and CH_2DOH. For CH_3OH the increase can be attributed to cyclic H-abstraction (effect I), whereas for CH_2DOH it is a combination of both described effects (effects I and II). In alignment with our expectations, we find that the increase in CH_2DOH is higher than the increase in CH_3OH, resulting in an approximately two percentage points higher $N(CH_2DOH)/N(CH_3OH)$ ratio.

Models D6 and D7 apply an experiment-based desorption mechanism following the proposed equation by Minissale et al. (2016b), which produces an individual desorption efficiency for every product species and surface coverage. In general, they produce lower column densities than model D4 and D5 for both CH_3OH and CH_2DOH, which is expected as the experiment-based reactive desorption mechanism yields much lower desorption efficiencies than 1% for heavier molecules. Given the used values for reaction enthalpies H_{form} and binding energies E_{b} (presented in Table A1 of Riedel et al. 2023), the desorption efficiency is 0.05 for $CH_2OH\rightarrow CH_3OH$ and 0.08% for $CH_3O \rightarrow CH_3OH$ on a pure CO surface.

Models D6 and D7 do not follow the same trend as described above for model D4 and D5. The column densities of CH_3OH and CH_2DOH are both increased due to the cyclic H-abstraction (effect I) in model D7. However, the increase for CH_2DOH is lower than for CH_3OH for radii above 4000 AU, consequently resulting in a lower $N(CH_2DOH)/N(CH_3OH)$ ratio for model D7 compared to model D6. The smaller increase in CH_2DOH is caused by different reactive desorption efficiencies for the different formation reactions of CH_2DOH. Reaction 3.6 ($CH_2OH \rightarrow CH_2DOH$) and reaction 3.7 ($CHDOH \rightarrow CH_2DOH$) both have a reactive desorption efficiency of around 0.05%, while reaction 3.8 ($CH_2DO \rightarrow CH_2DOH$) has a reactive desorption efficiency of around 0.08%. For the inner radii, CH_2DOH formation is dominated by reaction 3.8. For the outer radii, however, the efficiency of reaction 3.6 increases, as the D atoms mobility is increased due to the higher dust temperatures. Therefore, the effective CH_2DOH reactive desorption efficiency is decreased, since this formation route contributes less of its products to the gas phase.

In our previous works, abstraction reactions were left out entirely or were only used for selected parameter sets. Vasyunin et al. (2017) argued that branching ratios between H-addition and H-abstraction reactions were not measured accurately enough to lower the overall uncertainties of their presented model. Therefore, the authors opted to use a simpler network solely including H-addition reactions. Riedel et al. (2023) included H-abstraction reactions

following the scheme proposed by Hidaka et al. (2009) but also tested selected parameter sets with a simpler network comprising only the H-addition reactions. They found the inclusion of H-abstraction reactions to cause a substantial increase in the CH_3OH column densities, while the CH_2DOH column densities were found to be decreased, consequently lowering the N(CH_2DOH)/ N(CH_3OH) to values that are in worse agreement with observations. Admittedly, this result was impacted by the fact that the presented models also used the experiment-based mechanism for reactive desorption proposed by Minissale et al. (2016b) and therefore experienced the same effect as described above for models D6 and D7. The effect could be seen even more pronounced in the models presented in Riedel et al. (2023), as the use of the SC model causes CH_3OH to be formed predominantly by hydrogenation of CH_3O, which has a higher reactive desorption efficiency as the competing reaction involving its isomer CH_2OH. Hence, the effective CH_3OH reactive desorption efficiency is higher than in the RDC model.

Recently, Punanova et al. (2025) pointed out that H_2CO, an important intermediary in the methanol formation chain, is typically strongly overproduced, resulting in an inverse H_2CO: CH_3OH abundance of the chemical models compared to observations. Although formaldehyde is formed efficiently on the grain, its main formation reaction is the gas phase reaction CH_3 + O → H_2CO + H. Punanova et al. (2025) propose to remedy the overproduction of H_2CO by introducing the additional reaction channel CH_3 + O → CO + H_2 + H and constraining its branching ratio (CO+H_2+H:H_2CO+H = 8:1) observationally. Since the publication of this work is very recent, its proposed constraint has not been tested by us. However, we find that it is unlikely to have large consequences for the formation of methanol, as it concerns the gas phase formation of formaldehyde. We also would like to point out that for the models presented in the present work, the H_2CO:CH_3OH ratio strongly depends on the model parameters. Indeed, the H_2CO:CH_3OH ratio for model D5 is not inverse to the observed one.

3.4.3 Varying the initial H abundances

Unfortunately, a direct measurement of the H_2 abundance in cold dense cores is not possible, as the highly symmetric H_2 molecule does not possess a permanent dipole moment and is therefore only directly accessible in the UV and near- and far-infrared regime. Therefore, a commonly used tool is the use of ^{13}CO or ^{18}CO abundances combined with a conversion relation of the respective CO isotopologue's abundance to the one of molecular hydrogen. Simultaneously, the atomic hydrogen abundance can be obtained by accompanying HI narrow self-absorption observations, as was done by Li & Goldsmith (2003). They determined [HI]/[H_2] number density ratios between 10^{-4} and 8×10^{-3} for over 30 dark clouds in the Taurus and Perseus region. Goldsmith & Li (2005) later studied four dark clouds in more detail. There, they obtained an [HI]/[H_2] ratio of 10^{-3} specifically for L1544, resulting in an H abundance of 5×10^{-4} with respect to the total proton density $n_H = n(H) + 2n(H_2)$. Although it is a common modelling approach to start the simulation with no (or very small) atomic hydrogen abundances, in recent years several modellers adopted initial abundances for atomic hydrogen following the values suggested by the above mentioned works (e.g. Jin & Garrod (2020): 5×10^{-4} for L1544; Wakelam et al. (2021): 5×10^{-4}, 1×10^{-3} and 1×10^{-2} for an averaged physical structure representative of TMC1).

In this Section, we investigate the effect of a variation in the initial abundances of atomic and

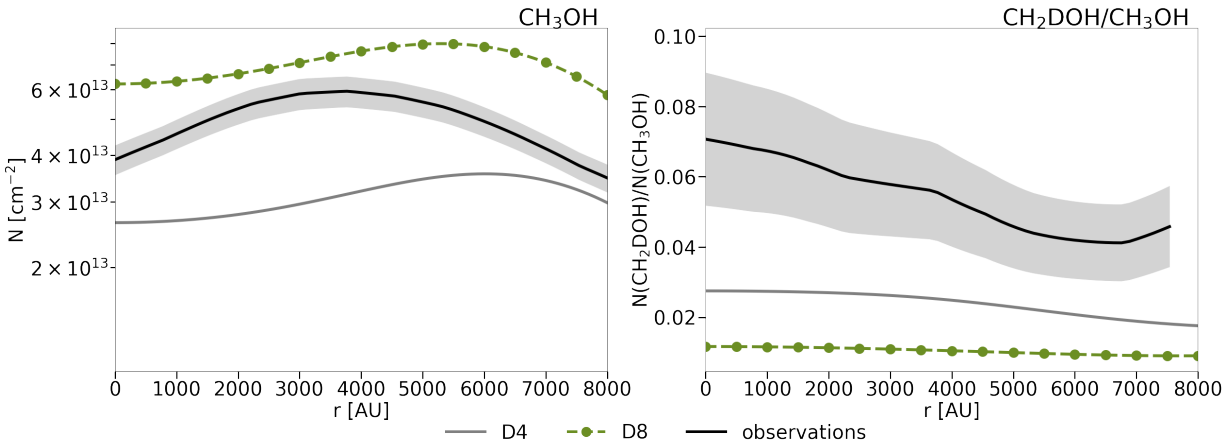

Figure 3.8: Column density profiles of CH_3OH (left) and $N(CH_2DOH)/N(CH_3OH)$ profiles (right) of the diffusive model D4 (grey), with an initial atomic hydrogen abundance of 10^{-8}, and diffusive model D8 (green), with an initial atomic hydrogen abundance of 0.5. The observed profiles are depicted in black (errors as grey-shaded areas).

molecular hydrogen on the CH_3OH column density and $N(CH_2DOH)/N(CH_3OH)$ ratio profile (see Figure 3.8). Here, we adopt an even higher value of 0.5 for atomic hydrogen and 0.25 for molecular hydrogen, which is a ratio more typical of translucent clouds. The initial abundances for pH_2 and oH_2 are adjusted accordingly to preserve an ortho-to-para ratio of 10^{-3}. The HD abundance is divided in half, where one half remains HD and the other is thought to be in the form of H and D atoms, respectively, thereby increasing the D abundance to the same value as the HD abundance. Consequently, the initial D/H ratio is lowered from a value of 1.0 to 1.6×10^{-5}. The modified initial abundances are summarised in Table 3.3. The diffusive model D4, not including H-abstraction reactions, is run again with the modified initial abundances, resulting in model D8.

Table 3.3: Initial H abundances used for a 50/50 H/H_2.

Species	Initial abundance
pH_2	2.4975×10^{-1}
oH_2	2.5000×10^{-4}
HD	8.0000×10^{-6}
H	5.0000×10^{-1}
D	8.0000×10^{-6}

An increased atomic hydrogen abundance is a priori expected to increase the production of molecules that are formed by hydrogenation reactions of common ice species, such as CH_3OH. Indeed, we find that the CH_3OH column density is increased by roughly a factor of 2.5, while the CH_2DOH column density is reduced by that factor, resulting in a slightly lower $N(CH_2DOH)/N(CH_3OH)$ ratio. The decrease of the CH_2DOH column density is caused by the lower initial

D/H ratio. The $N(CH_2DOH)/N(CH_3OH)$ in model D8 is eventually able to reach values similar to those in model D4; however, the two models only converge for evolutionary times past 10^6 yr.

A similar result is obtained in Sipilä et al. (2024) (see Appendix B). There, the authors found a highly increased H_2CO and CH_3OH formation for larger radii, while the variation for inner radii is small. Since the volume density for the outer radii is low, their contribution to the CH_3OH column density is low as well. Therefore, the CH_3OH column density of the 50:50 H/H_2 model is only increased by a factor 1.8 compared to reference model with initially no atomic hydrogen.

3.5 Conclusion

Surprisingly high abundances of methanol and other COMs were found in several surveys targeting dark molecular clouds (e.g. Bacmann et al. 2012; Cernicharo et al. 2012; Jiménez-Serra et al. 2016). Additionally, multiple experiments (Fedoseev et al. 2015; Chuang et al. 2016; Fedoseev et al. 2017; Qasim et al 2019; Ioppolo et al. 2021; Fedoseev et al. 2022; Santos et al. 2022) conducted at low temperatures ($T = 10 - 16$ K) have proposed grain surface COM formation routes involving (at least) one reaction step with two heavy immobile reactants. These kinds of reactions pose a severe bottleneck in a diffusive-only grain chemistry and likely render the formation route inefficient. Including non-diffusive grain chemistry evades the obstacle of immobility of reactants by taking into consideration that in a (small) number of cases, the reactants are already formed in close proximity to each other.

We updated the astrochemical code *pyRate* by including various non-diffusive reaction mechanisms, including Eley-Rideal reactions, photodissociation-induced reactions, and three-body reactions, thereby following closely the proposed formulation by Jin & Garrod (2020) and Garrod et al. (2022). We investigated methanol and its deuterated isotopologues, as methanol and its precursors are considered to be fundamental building blocks for both gas phase and grain surface formation routes of COMs. We presented several models for the prediction of abundance, column density, and deuterium fraction profiles of CH_3OH and CH_2DOH in the prototypical pre-stellar core L1544. Subsequently, we compared our model results to our previous work (Riedel et al. 2023), exploring various methods to increase the efficiency of hydrogen and deuterium atom diffusion and with available single-dish observations presented in Chacón-Tanarro et al. (2019a).

Our main conclusions are as follows. When applying the single collision model (SC model) for the derivation of reaction probabilities of reactions with an activation-energy barrier:

1. Models with a slow diffusion process ($E_d/E_b = 0.55$) cannot reproduce the observed column density profiles.

2. The addition of non-diffusive reaction mechanisms provides only minor contributions to methanol formation, independent of the selected mechanisms. Although the majority of CH_3OH and CH_2DOH is still produced by successive addition of H (or D) atoms, reactions between heavier products (e.g. $OH+CH_3 \rightarrow CH_3OH$, $O+CH_3 \rightarrow CH_3O$ and $OH+CH_2 \rightarrow CH_2OH$) can contribute significantly in certain regions and/or at certain time steps.

3. Increasing the diffusion rate of hydrogen and deuterium atoms by either a slow thermal hopping process ($E_d/E_b = 0.55$) that is accompanied by diffusion by quantum tunneling of H and D atoms or a fast thermal hopping process ($E_d/E_b = 0.2$) results in significantly better agreement with observed profiles.

When applying the reaction-diffusion competition model (RDC model) for the derivation of reaction probabilities:

4. In the RDC model, reactions with an activation-energy barrier are significantly more likely to happen when compared to the SC model, reducing the importance of an efficient diffusion process. Models with a slow diffusion process ($E_d/E_b = 0.55$) match the observed column density profile for CH_3OH within a factor of around two, which is a good agreement.

5. The $N(CH_2DOH)/N(CH_3OH)$ ratio derived with the RDC model is lower by a factor of two to three in comparison to the one derived with the SC model and the observed ratio. This is due to a combination of an increased importance of $H_2CO \rightarrow CH_2OH \rightarrow CH_2DOH$ relative to $H_2CO \rightarrow CH_2DO \rightarrow CH_2DOH$ and a lowered D/H ratio.

6. Similar to the results derived with the SC model, the addition of non-diffusive reaction mechanisms provides only minor contributions to methanol formation, independent of the selected mechanisms.

7. The reaction $H_2CO + CH_3O \rightarrow CH_3OH + HCO$ (reaction 3.9) is theoretically (Simons et al. 2020) and experimentally (Santos et al. 2022) predicted to provide a contribution of 60%-90% to the formation of CH_3OH. Following the introduction of reaction 3.9 to our chemical network, we derived only a negligible contribution for reaction 3.9 due to the fact that the occurrence rate of either H_2CO or CH_3O produced in close proximity to the other reactant is quite low, resulting in a very small reaction rate. Therefore, we cannot confirm the result.

8. Unlike other COMs, methanol can be considered a unique case, as its formation does not include a bottleneck reaction between two heavier reactants, which is the case for other proposed COM formation routes. If at least one of the reactants, for example, hydrogen (or deuterium) atoms, can diffusive efficiently, the contribution of non-diffusive reactions mechanisms is generally small.

9. The inclusion of H-abstraction reactions has two important effects on the gas phase reservoir: (I) The desorption rate of CH_3OH and CH_2DOH increases due to cyclic H-abstraction events, and (II) the $N(CH_2DOH)/N(CH_3OH)$ ratio is increased due to preferential abstraction of CH_2DOH to CH_2DO and CHDOH, instead of CH_2OH. Both effects result in higher CH_3OH column densities and higher $N(CH_2DOH)/N(CH_3OH)$ ratios.

10. A combination of H-abstraction reactions with an experiment-based reactive desorption mechanism (Minissale et al. 2016b), as opposed to a constant 1% reactive desorption efficiency, also increases the formation of CH_3OH. The $N(CH_2DOH)/N(CH_3OH)$ ratio,

however, is lower than in the model without abstraction reactions due to lower effective reactive desorption efficiencies.

11. Increasing the initial amount of atomic H from a very low value (10^{-8}) to 50% of the total H content results in an increase of the CH_3OH column density by roughly a factor of 2.5, while the CH_2DOH column density is reduced by that factor, lowering the $N(CH_2DOH)/N(CH_3OH)$ ratio.

The present work represents the first step in a set of projects exploring the deuteration of COMs. In a future paper, we will expand the chemical network to include COMs larger than methanol (e.g. acetaldehyde, methyl formate, and glycoaldehyde) and constrain their expected level of deuteration. In addition, a closer look into the chemistry of doubly or even triply deuterated forms of methanol could provide valuable additional constraints for the formation of methanol and its deuterated isotopologues.

Chapter 4

Forming deuterated O-bearing COMs in pre-stellar core conditions

The contents of this chapter will be submitted in Astronomy & Astrophysics.

Abstract

Context. Complex organic molecules (COMs) are thought to be the precursors of biologically relevant molecules, such as proteins, lipids and amino acids. The study of their deuteration is an excellent tool to understand their formation in the earliest phase of star formation, the pre-stellar core phase, and their possible inheritance to subsequent phases.
Aims. The aim of this work is the development of models for the formation and deuteration of COMs in the extremely cold conditions of pre-stellar cores, by applying non-diffusive reaction mechanisms promoting an efficient grain surface formation. In this work, we focus our efforts on commonly observed O-bearing COMs with up to eight atoms, namely acetaldehyde (CH_3CHO), methyl formate (CH_3OCHO) and glycoaldhyde (CH_2OHCHO).
Methods. We created a state-of-the-art chemical network, which contains deuterated COMs and spin-states for selected species and is suitable for the application of non-diffusive chemistry. As the resulting network is extremely large, we devised and tested various strategies to manage the computational cost and discuss their advantages and disadvantages. We performed several 1D simulations for the proto-typical pre-stellar core L1544, for which we derived column density profiles for CH_3OH, CH_3CHO, CH_3OCHO, CH_2OHCHO and their deuterated isotopologues. Subsequently, we compared our model results with the available gas-phase observations.
Results. The modelled column densities of the main isotopologues of CH_3OH, CH_3CHO, CH_3O CHO and CH_2OHCHO reproduce the observational column densities within a factor of 2. The modelled column density ratios $N/N_{\rm main}$ of the deuterated isotopologues with respect to their main isotopo-logues are up to a factor 4.8 higher than the observed ratios. A comparison of the modelled column density ratios $N/N_{\rm main}$ for multiple deuterated isotopologues of the investigated COMs with observational constraints obtained towards the protostellar system IRAS 16293-

2422B suggests an overestimation of one to two orders of magnitude by the model.

Keywords: ISM: abundances - ISM: clouds - ISM: molecules - astrochemistry

4.1 Introduction

The existence of complex organic molecules (COMs), which are carbon-based molecules with six atoms or more (Herbst & van Dishoeck 2009), has sparked the interest of many in the astrochemical community. The main motivation is that they constitute a direct measure of the chemical complexity of the molecular content in an astronomical object and are thought to be the precursors of biologically relevant molecules, as e.g. proteins, lipids and amino acids.

In the last decade, it has been established by observations (e.g. Jiménez-Serra et al. 2016) that a variety of COMs are already produced in surprisingly high abundances in the earliest stages of star formation, specifically in the pre-stellar core phase. Nowadays, efforts have been made to confirm their existence and determine their abundance in a multitude of starless and pre-stellar cores, in the Taurus (Scibelli & Shirley 2020, Punanova et al. 2022), Perseus (Scibelli et al. 2024) and Ophiuchus star forming regions (Steffes et al. in prep.). Mostly, the relatively simple O-bearing COMs, methanol (CH_3OH) and acetaldehyde (CH_3CHO) have been detected in a large sample of sources. However, follow-up observations of the most promising objects (Scibelli et al. 2024, 2025) also detect high abundances of other O-bearing COMs, such as methyl formate (CH_3OCHO) and dimethylether (CH_3OCH_3), and N-bearing COMs, such as methyl cyanide (CH_3CN) and vinyl cyanide (CH_2CHCN).

Currently, methanol is the only COM for which deuterated isotopologues have been detected towards pre-stellar cores. While the deuterated isotopologue CH_2DOH has been observed in several low- and high mass sources (e.g. Chacón-Tanarro et al. 2019a, van Gelder 2022), the deuterated isotopologues CH_3OD (Kulterer et al. 2025) and CHD_2OH (Lin et al. 2023a) have only been detected towards pre-stellar cores for the first time in the last years. For other COMs, only their main isotopologues have been detected in the pre-stellar core stage thus far. For the protostellar stage, however, there are observational constraints for multiple deuterated isotopologues of several O-bearing COMs, mostly detected towards the Class 0 triple protostellar system IRAS 16293-2422 (e.g. Jørgensen et al. 2016, 2018, Manigand et al. 2019, 2020, Drozdovskaya et al. 2022, Ferrer Asensio et al. 2023, Ilyushin et al. 2022, 2023).

Here, we present a model that combines non-diffusive reaction mechanisms with deuterium chemistry, focused on the investigation of the formation and deuteration of the three O-bearing COMs - acetaldehyde, methyl formate and glycoaldehyde - in pre-stellar cores. This work represents the continuation of a set of projects exploring the deuteration of COMs, which was initiated by the inclusion of non-diffusive reaction mechanisms into the astrochemical code *pyRate* (Sipilä et al. 2015a, 2019b) and its application to methanol formation, presented in Riedel et al. (2025).

This paper is structured as follows: in Section 4.2, we describe the chemical and physical model and the various chemical networks developed and used in detail. In Section 4.3, we present the column density and deuterium fraction profiles, derived for the physical model of the

Table 4.1: Initial chemical abundances with respect to n_H.

Species	Initial abundance	Species	Initial abundance
He	9.00×10^{-2}	S^+	8.00×10^{-8}
pH_2	5.00×10^{-1}	Si^+	8.00×10^{-9}
oH_2	5.00×10^{-4}	Na^+	2.00×10^{-9}
HD	1.60×10^{-5}	Mg^+	7.00×10^{-9}
H	1.00×10^{-8}	Fe^+	3.00×10^{-9}
D	1.00×10^{-8}	P^+	2.00×10^{-10}
C^+	1.20×10^{-4}	Cl^+	1.00×10^{-9}
N	7.60×10^{-5}	F	2.00×10^{-9}
O	2.56×10^{-4}		

pre-stellar core L1544 and the available observational data for the pre-stellar core stage. Section 4.4 compares them to previous modelling results and provides a comparison to the proto-stellar stage. Section 4.5 presents our conclusions.

4.2 Methods

4.2.1 Chemical model

The chemical evolution of molecular abundances is calculated with the gas-grain astrochemical code *pyRate* (Sipilä et al. 2015a, 2019b). The code is capable of simulating deuterium chemistry and was recently updated to include various non-diffusive reaction mechanisms (Riedel et al. 2025) , following the recipes laid out in Jin & Garrod (2020) and Garrod et al. (2022).

The dust grains are assumed to be spherical with a radius of 0.1 μm. The presented models employ a three-phase model, consisting of gas phase, a chemically active surface phase and an inert mantle phase. The surface phase consists of only one layer. The mantle phase is not layered and its contents do not undergo chemical reactions or diffusion processes. Surface reactions proceed either diffusively, through the Langmuir-Hinshelwood mechanism, or additionally non-diffusively, through Eley-Rideal, photodissociation-induced or three-body reactions. Diffusion of surface molecules proceeds purely by thermal diffusion. The reaction probabilities for reactions with an activation-energy barrier are calculated using the reaction-diffusion competition model introduced by Chang et al. (2007), which considers that reaction partners are confined in the same binding sites until one of them diffuses away again and consequently have multiple opportunities to overcome the barrier.

PyRate includes, besides thermal desorption, various non-thermal desorption mechanisms, including photodesorption, cosmic-ray induced desorption and reactive desorption. The code contains two different options for the reactive desorption mechanism - using a constant reactive desorption efficiency or an individual reactive desorption efficiency for every reaction derived by an experiment-based formula, taking into account the reaction enthalpy and underlying surface

Table 4.2: Overview of the various chemical networks developed in this work.

network	deut.	other features	No. gas reac.	No. grain reac.
BN1	✗	species with ≤ 9 atoms	7,778	3,105
BN2	✗	species with ≤ 9 atoms for gas-phase species with ≤ 7 atoms for grain-surface + selected reactions for CH_3OCHO & CH_2OHCHO	7,778	1,986
DN1	✓	deuterated BN1 network	274,207	82,812
DRN1	✓	deuterated BN1 network with reduction of deuteration to singly and doubly deuterated isotopologues	274,207	66,472
DN2	✓	deuterated BN2 network	274,207	31,864

type (Minissale et al. 2016b, Riedel et al. 2023). In this work, we adopt a constant reactive desorption efficiency of 1% to both increase comparability to the literature and to keep the structure of the differential equations simple. The binding energies for species already present in previously used networks are summarized in Riedel et al. (2023). The binding energy of H_2 and its deuterated isotopologues is scaled by a factor 0.1 to prohibit an unphysical build-up of H_2 on the surface of dust grains. This method was tested and compared to other common H_2 removal methods in Riedel et al. (2025). The diffusion-to-binding energy E_d/E_b is set to a value of 0.55, as suggested by Minissale et al. (2016a) and used in previous works (Vasyunin et al. 2017, Riedel et al. 2023, 2025).

We use atomic initial abundances (see Table 4.1), as also used for previous works (Vasyunin et al. 2017, Riedel et al. 2023, 2025).

4.2.2 Chemical networks

In this work, several distinct chemical networks are used. Their most important properties are summarized in Table 4.2. In general, this work distinguishes between base networks, only containing the chemistry of the main isotopologues, and deuterated networks, containing various degrees of deuterium chemistry. A detailed description of the networks and how they were obtained is presented in detail in this Section.

4.2.2.1 The base network - BN1

The base network BN1 is presented in Bonfand et al. in prep., and is based on that of Garrod et al. (2022). The gas-phase network includes various ion–neutral, neutral–neutral, and electronic recombination reactions. Following Garrod & Herbst (2023), it also incorporates various proton-transfer reactions, such as those between complex organic species and protonated ammonia. Equivalent processes involving other high proton-affinity species are also included, where plausible, based on relative proton affinities. The gas-phase network also includes a selection of radical-radical reactions considered by Tsang et al. (1986), Tsang et al. (1987), and subsequent publications. The network also incorporates the chemical network additions for dimethyl amine

and normal- and iso-propanol, by Müller et al. (2023) and Belloche et al. (2022), respectively. The grain surface network specialises on the formation of several commonly observed COMs with non-diffusive reaction mechanisms and therefore includes many surface reactions with two relatively heavy reaction partners. Commonly, these reactions are not included in chemical networks that focus on the cold-environment chemistry, as their contribution in purely diffusive reaction mechanisms is usually insignificant.

For the present work, the base network is limited to reactions involving only species with up to nine atoms to ensure the feasibility of the simulation once the network has been deuterated. After the restriction, several species and their reaction pathways were removed to ensure conservation of the elemental abundances and closure of the network. None of the removed species are chemically closely related to methanol, acetaldehyde, methyl formate or glycoaldehyde.

The base network contains around 8,000 gas phase reactions and 3,000 grain surface reactions. Abstraction reactions, in which a radical (e.g. H, CH_3, NH_2, OH) abstracts a hydrogen atom from a molecule, thereby resulting in a closed-shell end product (e.g. H_2, CH_4, NH_3, H_2O) and an unsaturated COM, are included for all investigated species. Unfortunately, dedicated measurements concerning their branching ratios are scarce. In the absence of any other information, the branching ratios are weighted equally, so as to not favour any pathway without experimental justification. Molpeceres et al. (2025), however, recently published recommendations for branching ratios concerning the H-addition-abstraction cycle of $CH_3CO \leftrightarrow CH_3CHO$, based on a combined approach of quantum chemical calculations and laboratory experiments. They find the following reactions to have non-negligible branching ratios α:

$$H + CH_3CHO \rightarrow CH_3CO + H_2 \tag{4.1}$$

$$H + CH_3CO \rightarrow CH_3CHO \tag{4.2}$$

$$H + CH_3CO \rightarrow CH_2CO + H_2 \tag{4.3}$$

$$H + CH_3CO \rightarrow CH_3COH \tag{4.4}$$

$$H + CH_3CO \rightarrow CH_4 + CO, \tag{4.5}$$

where they recommend $\alpha = 1.0$ for reaction 4.1 and $\alpha = 0.9$ for reaction 4.2. Constraining the branching ratios of the remaining three channels (reaction 4.3 - 4.5) proved difficult, which is why they recommend equal weighting of $\alpha = 0.03$. Unfortunately, the BN1 network does not contain the molecular species CH_3COH. Introducing another species to a network requires careful consideration of its possible formation and destruction pathways, which is beyond the scope of the present paper. Therefore, we set $\alpha = 0.05$ for reactions 4.3 and 4.5 and omit reaction 4.4.

4.2.2.2 The base network - BN2

After the first stages of tests, it proved necessary to further reduce the amount of species in the base network. To decrease the number of reactions in the grain surface network further, we devised a modification of the BN1 network in which the grain surface network is limited to reactions involving only species with up to 7 atoms. Additionally, we include selected pathways

to reproduce the chemistry of methyl formate and glycoaldehyde. In practice, this is achieved mainly by removing reactions for the formation of nitrogen- and sulfur bearing species with more than 7 atoms from the BN1 network. The same procedure could be also applied to limit the gas phase network. We found it, however, difficult to identify the correct pathways to achieve a good recovery of the larger COMs: methyl formate and glycoaldehyde. Since the size of the gas phase network only marginally affects the duration of the simulation, we simply decided to use the entire gas phase network of the BN1 network. Molecular species that only possess gas phase reactions and no explicit grain surface reactions are allowed to adsorb and desorb to mimic the correct freeze-out behaviour and to avoid sinks.

4.2.2.3 Deuteration of the networks

The deuterated networks, presented in this work, are obtained by a routine that clones the chemical reactions of the base network to include their deuterated counterparts. The branching ratios are calculated as detailed in Sipilä et al. (2015a,b, 2019b). The routine was recently extended to allow the treatment of molecules with up to nine atoms. To this regard, special care was taken to isolate the functional groups of COMs and deuterate them as separate entities. As an example, the routine allows the reaction HCO + $CH_2DO \rightarrow CH_2DOCHO$ to proceed, but not HCO + $CH_2DO \rightarrow CH_3OCDO$, as this would require an exchange of deuterium atoms between functional groups. Additional reactions are added to include specific spin-state chemistry for H_2, H_2^+, H_3^+ and their deuterated isotopologues, as their ortho-to-para ratio strongly influences the efficiency of the deuteration process.

In general, experimental data on the branching ratios and activation energies of deuterated and spin-separated reactions are scarce. They are applied for H_2, H_2^+, H_3^+ and their deuterated isotopologues, incorporating values from Flower et al. (2004), Walmsley et al. (2004), Hugo et al. (2009), Pagani et al. (2009), Le Gal et al. (2014) and Hillenbrand et al. (2019, 2022). The successive hydrogenation and deuteration of methanol follows the experimentally verified proposal by Hidaka et al. (2009).

The deuterated versions of the base networks BN1 and BN2 are called DN1 and DN2, respectively. Additionally, in an effort to keep the computation time of the simulations with the deuterated networks manageable, we developed and tested a reduction scheme to limit the degree of deuteration to singly and doubly deuterated species, resulting in the deuterated network DRN1.

4.2.3 Physical model

We use a one-dimensional static model for H_2 density, gas temperature $T_{\rm gas}$, dust temperature $T_{\rm dust}$ and visual extinction $A_{\rm V}$ of the proto-typical pre-stellar core L1544 (see Figure 2.2.3). It was derived in Keto & Caselli (2010) and explained in more detail in Sipilä et al. (2019a). The chemical evolution is solved for 35 cells. The column density profiles are obtained by an integration along the line of sight for different impact factors and subsequently convolved with a 30″ Gaussian beam, which is the resolution of the observations available in the literature.

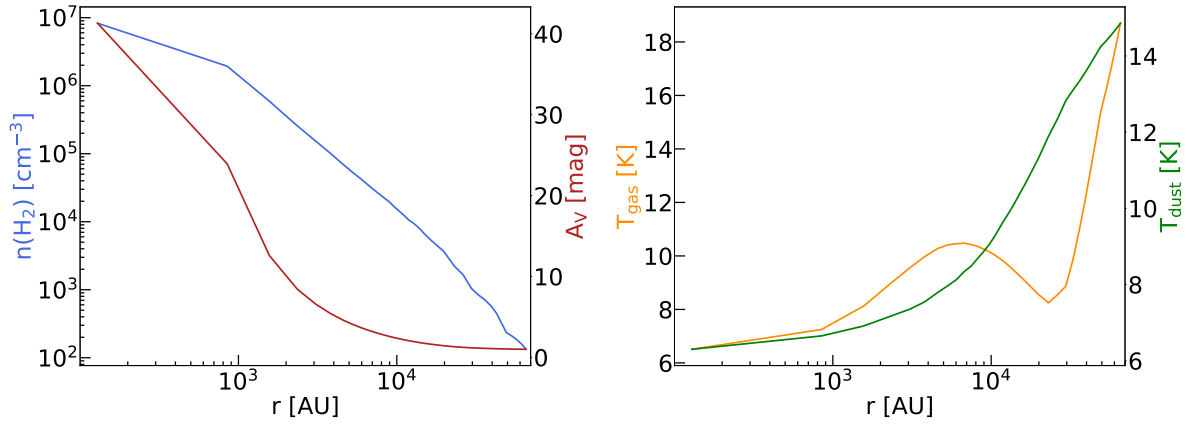

Figure 4.1: Physical model first presented in Keto & Caselli (2010) and described in more detail in Sipilä et al. (2019a) providing static radial profiles of the H_2 volume density, $n(H_2)$ (blue, logarithmic scale), the visual extinction, A_V (red), T_{gas} (orange), and the dust temperature, T_{dust} (green).

4.3 Results

In the following, the results of the various chemical networks (summarized in Table 4.2) are presented and our modelling choices are explained in a step-by-step manner. In general, we adopted the approach to guide the decisions with the help of the base networks, only containing the main isotopologues, with which an exploration of the parameter space is feasible. The main properties of the models discussed in this work are summarized in Table 4.3.

4.3.1 The BN1 network

Figure 4.2 presents the simulated column density profiles of methanol (CH_3OH), acetaldehyde (CH_3CHO), methyl formate (CH_3OCHO) and glycoaldehyde (CH_2OHCHO) for various models including non-diffusive reaction mechanisms at the best-fit time of $t = 3 \times 10^5$ yr. A purely diffusive model with a diffusion-to-binding energy of $E_d/E_b = 0.55$ is shown as a reference. Although it is, in principle, possible to combine all non-diffusive reaction mechanisms, they are only enabled separately and not in combination with each other. The only exception is model B5, where both three-body reactions and three-body reactions with excited formation are applied. Amplification or competition effects are expected to be small. The non-diffusive reaction mechanisms include Eley-Rideal reactions (model B2), photodissociation-induced reactions (model B3), three-body reactions (model B4), and a combination of three-body reactions and three-body reactions with excited formation (model B5).

We find that adding the non-diffusive reaction mechanisms is able to increase the column densities for all investigated COMs to a varying degree. The largest increases are obtained when applying the three-body reactions (model B4) and the three-body reactions with excited formation (model B5). The Eley-Rideal reactions (model B2) and the photodissociation-induced

Table 4.3: Overview of the various models investigated in this work.

Model	ER[a]	PDI[b]	3B[c]	3BEF[d]	network	subroutine size[e]	performed[f]	comp. time[g]
B1	✗	✗	✗	✗	BN1	small	✓	< 1 h
B2	✓	✗	✗	✗	BN1	small	✓	< 1 h
B3	✗	✓	✗	✗	BN1	small	✓	≈ 2 h
B4	✗	✗	✓	✗	BN1	small	✓	≈ 2 h
B5	✗	✗	✓	✓	BN1	small	✓	≈ 2 h
D1	✗	✗	✗	✗	DN1	mid-sized	✓	5-6 h
D2	✗	✗	✓	✓	DN1	22GB	✗	unknown
D3	✗	✗	✗	✗	DRN1	mid-sized	✓	5-6 h
D4	✗	✗	✓	✗	DRN1	16.4 GB	✗	> 2 months
B6	✗	✗	✓	✗	BN2	small	✓	≈ 2 h
D5	✗	✗	✓	✗	DN2	5.1 GB	✓	≈ 22 d

Notes. BX are models performed with a base network, including only the main isotopologues. DX are models performed with a deuterated network. [(a)] Eley-Rideal reactions , [(b)] photodissociation-induced reactions , [(c)] three-body reactions and [(d)] three-body reactions with excited formation . [(e)] The chemical code *pyRate* consists of a Python routine, setting up the differential equations in a subroutine file, which is then compiled and integrated in the programming language C. For the deuterated networks, presented in this work, the compilation of the subroutine proved to be the bottleneck of the simulation. Therefore, the size of the subroutine is used to estimate the feasibility of a given simulation. [(f)] Some simulations are found to not be feasible in a reasonable time frame. [(g)] The computation time for one simulation.

reactions (model B3) only produce orders of magnitude lower column density increases, with the exception of methanol. Methanol, which is mainly produced by successive addition reactions of the highly mobile hydrogen atom to CO, is affected only slightly by the choice of non-diffusive reaction mechanism. The column density ratio $N_{B4;CH_3OH}/N_{B1;CH_3OH}$ of the B4 model to the B1 model at the dust-peak and best-fit time is 1.07. The other COMs show considerably higher increases in column densities: $N_{B4;CH_3CHO}/N_{B1;CH_3CHO} = 62.9$, $N_{B4;CH_3OCHO}/N_{B1;CH_3OCHO} = 1.4{\times}10^6$ and $N_{B4;CH_2OHCHO}/N_{B1;CH_2OHCHO} = 6.8 \times 10^{17}$.

A higher $N_{B4;CH_3OH}/N_{B1;CH_3OH}$ ratio, derived using a similar network, is found in Jiménez-Serra et al. (2025) for temperatures of 10 K. There, the deviation is attributed to an altered efficiency for the conversion of CO into CO_2. Applying non-diffusive reaction mechanisms contributes significantly to the formation of CO_2 by the reaction CO + OH → CO_2, for temperatures below 13 K, which influences the amount of CO available for methanol formation. A possible reason why this effect is not seen in this work is the use of a static physical model, as in contrast to the spherical collapse model applied in Jiménez-Serra et al. (2025). However, the test of time-dependent physical conditions is beyond the scope of this paper.

Model B4, applying the three-body reactions (3B), and model B5, additionally applying three-body reactions with excited formation (3BEF), result in very similar column densities for all investigated COMs. There are several possible reasons for this: (i) The original formulation (Jin & Garrod 2020) of the three-body reactions with excited formation assumed that the entire

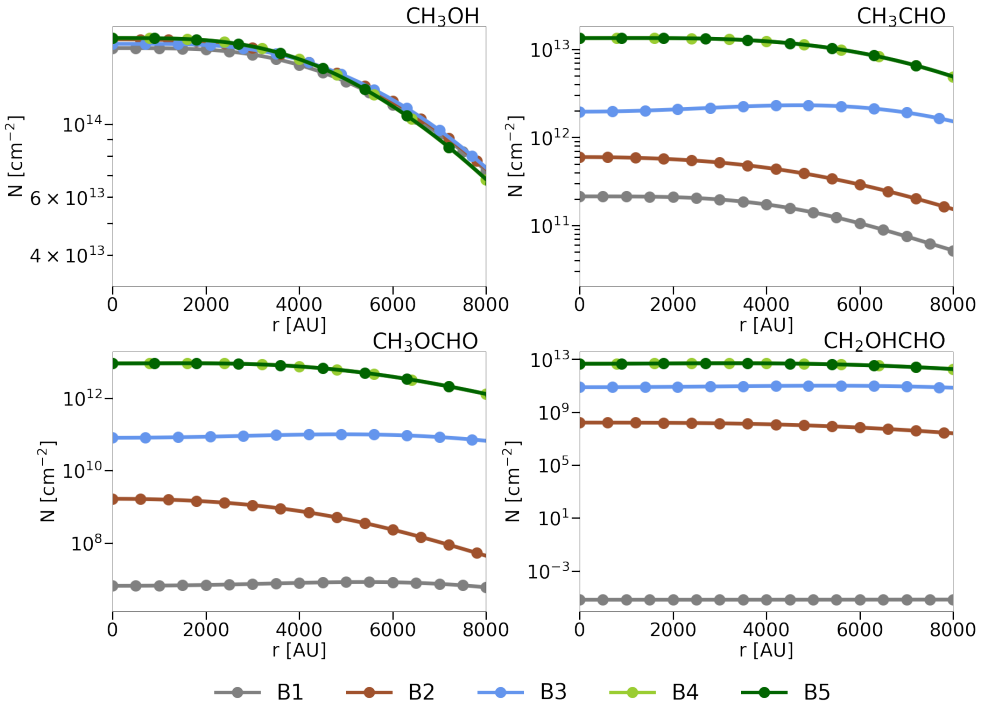

Figure 4.2: Column density profiles of methanol (CH_3OH), acetaldehyde (CH_3CHO), methyl formate (CH_3OCHO) and glycoaldehyde (CH_2OHCHO) for various models performed with the base network BN1. A purely diffusive model (model B1; grey line) is shown as a reference. The other models each include one non-diffusive reaction mechanism: Eley-Rideal reactions (model B2; brown), photodissociation-induced reactions (model B3; light blue), three-body reactions (model B4; light green) and three-body reactions with excited formation (model B5; dark green).

reaction enthalpy of the initiating reaction is available to overcome the activation-energy barrier of the follow-up reaction. A refinement of the mechanism, proposed in Garrod et al. (2022), considered that there is only a probability lower than unity that the required energy is instantaneously present in the correct vibrational mode. Additionally, other competition processes, namely energy loss to the surface and diffusion of the excited species away from the site, decrease the amount of successful reactions. Therefore, the reaction is only treated as 3BEF reaction in a fraction $f_{\rm EF}$ of cases and in $(1-f_{\rm EF})$ of cases as a regular 3B reaction. The fraction $f_{\rm EF}$ is typically smaller than the opposing fraction $(1-f_{\rm EF})$. The mechanism adopted in *pyRate* for the three-body reactions with excited formation is equal to this proposed refinement. (ii) In this work, as in many others, chemical reactions with an activation-energy barrier are assumed to proceed by reactive quantum tunneling through the barrier. *pyRate* applies a rather simple formulation of reactive tunneling, where the tunneling probability is simply described by tunneling through a rectangular barrier of 1 Å width for all surface species. (iii) The investigated COMs are mainly formed by the successive addition of a hydrogen atom, as in the case of methanol, or by radical-radical reactions of intermediary products along the methanol formation chain. Radical-radical

reactions typically do not possess activation energy barriers, as radicals have a high tendency to form stabler molecules. The 3BEF mechanism, however, is only applied to chemical reactions with an activation-energy barrier. If the reaction does not have a barrier, the code switches automatically to the use of the regular 3B mechanism.

4.3.2 The DN1 and DRN1 networks

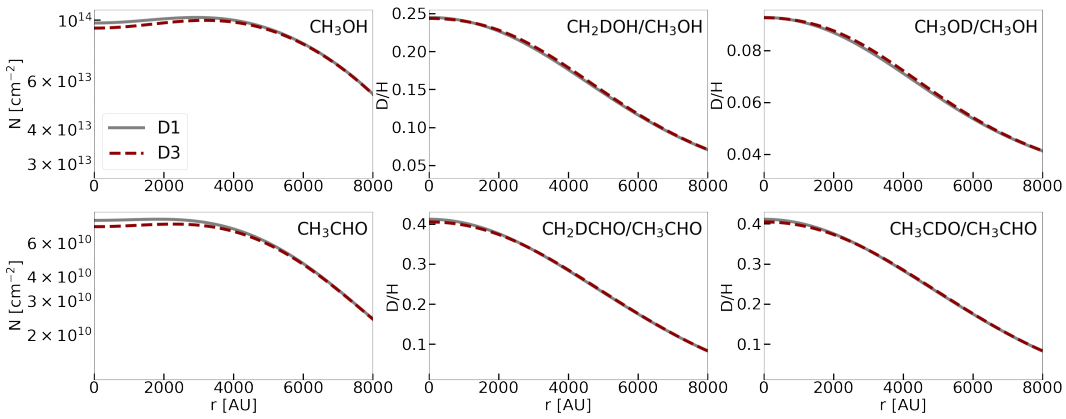

Figure 4.3: Column density profiles of methanol (CH_3OH), acetaldehyde (CH_3CHO) and deuterium fraction profiles of their singly deuterated isotopologues. The figure compares a purely diffusive model (model D1; grey), performed with the full deuterated network DN1, and a purely diffusive model (model D3; dark red), performed with a deuterated network DRN1, where the degree of deuteration is limited to singly and doubly deuterated species.

The cloning of reactions, including species with many hydrogen atoms, results in a large number of deuterated (and possibly spin-separated) counterparts. Additionally, the details of COM formation and deuteration necessitate the inclusion of structural isomers, as reactions with those lead to different end products. For example, methanol is formed both by CH_3O + H $\rightarrow$ CH_3OH and CH_2OH + H $\rightarrow$ CH_3OH, with CH_3O and CH_2OH being structural isomers. Although neglected in some works, including both species into the chemical networks is especially important for (i) the deuteration of methanol, as e.g. CH_3OD only forms from CH_3O and CH_2DOH only from CH_2OH and (ii) the formation of COMs that are structural isomers, as e.g. methyl formate (CH_3OCHO) forms via CH_3O + HCO and glycoaldehyde (CH_2OHCHO) via CH_2OH + HCO. Therefore, the simple reaction of CH_3O/CH_2OH adding a hydrogen atom to form CH_3OH already results in 20 distinct deuterated versions. The deuterated network DN1, which is based on the base network BN1, contains around 280,000 gas phase reactions and 80,000 grain surface reactions, making it substantially larger than chemical networks that do not treat the chemistry of isotopologues explicitly, and also much larger than previously used deuterated networks (e.g. Riedel et al. 2023, 2025).

PyRate uses the programming language Python to set up a system of coupled first-order ordinary differential equations, based on the chemical network and the reaction mechanisms included in the code. The differential equations are written into a file, which is first compiled and then integrated by a subroutine in the programming language C. For the deuterated networks, used in this work, the duration of the compilation of this subroutine file proved to be the bottleneck of the simulation. Hence, the size of the subroutine is used as a measure of the feasibility of the simulations.

Performing a purely diffusive model with this network is possible and takes around 5-6 hours with *pyRate* to complete. However, the simulations with the base network BN1 (see Figure 4.2) showed that the inclusion of non-diffusive reaction mechanisms, especially three-body reactions, is essential to reproduce the observed column densities for acetaldehyde, methyl formate and glycoaldehyde. Combining both non-diffusive reaction mechanisms with the large deuterated networks increases the size of the subroutine dramatically. Interestingly, we found that the size of the larger gas phase network plays only a secondary role in that increase, but that the size of the grain surface network mostly dictates the resulting subroutine size. This is caused by the fact that, when applying the non-diffusive reactions, a single surface reaction can be initiated by a multitude of initiating reactions. Therefore, the larger the base grain surface network, the larger the increase when this network is deuterated and combined with non-diffusive reaction mechanisms.

For this reason, we implemented several measures to minimize the computational effort of this project: (i) Based on the tests with the base network BN1, models B4 and B5 show by far the largest increase for acetaldehyde, methyl formate and glycoaldehyde. There is no significant difference in column densities between models B4 and B5 and the additional use of three-body reactions with excited formation will add more terms to the differential equations. Hence, the most efficient use of computational resources is to run the deuterated network DN2 in combination with the three-body reactions. (ii) A pre-compilation scheme is developed for this work, making it possible to modify the physical parameters without repeating the compilation phase and immediately skipping to the integration phase. Modifications to the chemical parameter, however, necessitate another compilation of the subroutine.

By using (i) and (ii), we found that running the D2 model resulted in a subroutine size of 22 GB, which is around 10x larger than successful simulations that were previously run with *pyRate*. Since the compilation time increases steeply with increasing subroutine size, we decided to additionally restrict the degree of deuteration to singly and doubly deuterated isotopologues. Higher order isotopologues are recombined into an artificial species with a common name, e.g. CHD_2OCDO, CD_3OCHO and CD_3CDO are renamed to $CH_3OCHO^\star$. The renaming creates duplicate reactions in the chemical network, which are then removed from the network in a second step. Figure 4.3 shows the column density profiles at the best-fit time t=3.0×10^5 yr of the purely diffusive model D1, performed with the fully deuterated network DN1 and the model D3, performed with the reduced deuterated network DRN1. We find that both models diverge for late evolutionary times $> 1 \times 10^6$ yr, as the recombination scheme introduces a slight violation of the elemental conservation of hydrogen and deuterium atoms. The cause of this violation is explained by the fact that the network contains many reactions in which larger COMs that have triply or quadruply deuterated isotopologues are split up into smaller

fragments again, thereby also splitting up the molecules of the artificial species. However, since the recombination combined species with different amounts of deuterium atoms and the information of how much molecules belong to the individual species CHD_2OCDO, CD_3OCHO and CD_3CDO is lost, improper assumptions about where the hydrogen and deuterium atoms end up are made. Since the divergence only becomes severe for late time steps, which are beyond our best-fit time (t=3 $\times$ 10^5 yr), we conclude that this recombination is still likely to result in a good approximation of the full network, and can therefore be used.

The reduction scheme is able to reduce the grain surface network by roughly 15,000 reactions. For model D4, which combines the reduced network DRN1 with three-body reactions, the subroutine is 16.4 GB in size, which constitutes a reduction of 25% in comparison with the 22GB of the full network DN1. However, although the recombination scheme is able to reduce the subroutine size, we found that the compilation time of model D4 is still longer than 2 months and we found it is therefore not feasible to be used in the testing phase, when modifications to the chemistry still might be made. Hence, we decreased the amount of reactions in the grain surface network further (see Section 4.3.3).

4.3.2.1 The deuteration of methanol

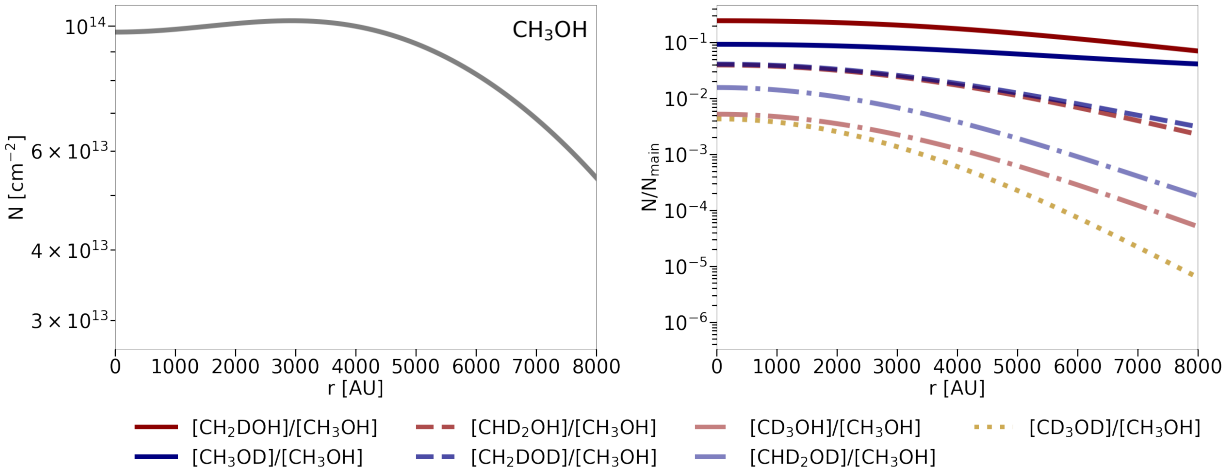

Figure 4.4: Column density profiles of methanol (CH_3OH, left) and column density ratios of its singly- (solid line), doubly- (dashed line), triply- (dash-dotted line) and quadruply (dotted line) deuterated isotopologues, derived with the D1 model. The isotopologues, deuterated at the methyl group are depicted in shades of red, while the isotopologues, where also the hydroxy group is deuterated, are depicted in shades of blue. The fully deuterated isotopologue CH_3OD is shown in yellow.

Although the formation and deuteration of the larger COMs, acetaldehyde, methyl formate and glycoaldehyde is not well described by the purely diffusive model D1, the column density profiles of methanol are reasonably well reproduced by it and hence allow for a first inspection. Figure 4.4 shows the column density profiles of methanol and all of their deuterated isotopologues.

Table 4.4: Column densities of methanol and its deuterated isotopologues, derived with the D1 model.

Molecule	Dust Peak[a] N [cm^{-2}]	mod. $N/N_{\rm main}$[c]	obs. $N/N_{\rm main}$[d]	COM Peak[b] N [cm^{-2}]	mod. $N/N_{\rm main}$	obs. $N/N_{\rm main}$
CH_3OH	9.76×10^{13}	-		9.99×10^{13}	-	
CH_2DOH	2.39×10^{13}	0.24	0.22±0.06	1.76×10^{13}	0.18	0.21 ± 0.05
CH_3OD	9.04×10^{12}	0.09		7.11×10^{12}	0.07	
CHD_2OH	3.86×10^{12}	0.04	0.06±0.01	1.72×10^{12}	0.02	0.03 ± 0.01
CH_2DOD	4.00×10^{12}	0.04		1.85×10^{12}	0.02	
CD_3OH	5.09×10^{11}	5×10^{-3}		1.25×10^{11}	1×10^{-3}	
CHD_2OD	1.53×10^{12}	0.02		3.82×10^{11}	4×10^{-3}	
CD_3OD	4.2×10^{11}	4×10^{-3}		6.04×10^{10}	6×10^{-4}	

Notes. [(a)] $r = 0$ AU [(b)] The off-centre position is set to $r = 4000$ AU, according to the value determined by observations (Chacón-Tanarro et al. 2019a, Jiménez-Serra et al. 2016). The modelled column density peak occurs around 3000 AU, depending on the molecule, with methyl formate peaking closer to the dust peak as the others. [(c)] Column density of deuterated isotopologue relative to that of the main isotopologue. [(d)] N(CH_3OH) from Lin et al. (2022), N(CH_2DOH) from Chacón-Tanarro et al. (2019a), N(CHD_2OH) from Spezzano et al. (2025).

Table 4.4 summarizes the column densities of the various deuterated isotopologues and their ratio relative to that of the main isotopologue at the dust peak ($r = 0$ AU) and the observed COM peak ($r = 4000$ AU). The third column reports the available observed ratios for CH_2DOH and CHD_2OH, which are the only deuterated isotopologues observed in L1544 at this point in time.

The observational column density profile of methanol N(CH_3OH) and the deuterium fraction profile N(CH_2DOH)/N(CH_3OH) have been reported originally in Chacón-Tanarro et al. (2019a). These authors found a N(CH_3OH) = (3.9± 0.4)×10^{13}cm^{-2} at the dust peak and N(CH_3OH) = (5.9±0.6)×10^{13}cm^{-2} at the COM peak and a maximum value of N(CH_2DOH)/N(CH_3OH) = 0.071 ± 0.019 at the dust peak. These values have been also used to compare to our previous modelling work on deuterated methanol (Riedel et al. 2023, 2025). Recently, however, Spezzano et al. (2025) reported N(CH_2DOH)/N(CH_3OH) and N(CHD_2OH)/N(CH_3OH) ratios for the dust and COM peak, where the column densities of CH_3OH have been derived with RADEX non-LTE modelling using multiple lines. The corrected N(CH_3OH) are lower in this work with N(CH_3OH) = (1.30±0.05)×10^{13}cm^{-2} at the dust peak and (1.60±0.03)×10^{13}cm^{-2} at the COM peak. The corrected N(CH_2DOH)/N(CH_3OH) ratios in this work are consequently higher, but still agree within a factor of two with previously published values (Vastel et al. 2014, Bizzocchi et al. 2014, Punanova et al. 2018 and Chacón-Tanarro et al. 2019a). The D1 model obtains a column density of 9.76×10^{13} cm^{-2} at the dust peak and 9.99×10^{13} cm^{-2} at the COM peak, which is higher than the observed values and might point toward an overestimation of the reactive desorption efficiency. It is noteworthy that the COM peak in the models occurs slightly more inwards at 3000 AU with slightly higher N(CH_3OH) of 1.02×10^{14} cm^{-2} in comparison to the 4000 AU that is obtained by the observations. Moreover, the D1 model determines a column density ratio

$N(CH_2DOH)/N(CH_3OH)$ of 0.24 (vs the observed 0.22±0.06) at the dust peak and of 0.18 (vs the observed 0.21±0.05) at the COM peak, which is well within the error margins of the observations. Also the $N(CHD_2OH)/N(CH_3OH)$ ratios are reproduced similarly well with a value of 0.04 (vs the observed 0.06±0.01) at the dust peak and of 0.02 (vs the observed 0.03±0.01) at the COM peak.

The model predicts that for the singly deuterated isotopologues, CH_2DOH, which is deuterated at the methyl group, has higher column densities than CH_3OD, which is deuterated at the hydroxy group. The $N(CH_2DOH)/N(CH_3OD)$ is 2.64 at the dust peak and 2.48 and the methanol peak, which is lower than the statistically expected value of 3. The first robust detection of CH_3OD towards a pre-stellar core has been only reported very recently (Kulterer et al. 2025) towards L1448, determining a $N(CH_2DOH)/N(CH_3OD)$ ratio between 2.8 and 8.5 and a tentative detection towards B213-C6 with a ratio of ≤ 5.7. For L1544, only estimates for upper limits of CH_3OD exist (Bizzocchi et al. 2014), suggesting a $N(CH_2DOH)/N(CH_3OD) \geq 10$. With such a wide range of observational values, one cannot conclude if the model needs to be adjusted in this regard.

4.3.3 The BN2 network

Figure 4.5 shows the column density profiles for methanol, acetaldehyde, methyl formate and glycoaldehyde obtained with the purely diffusive model B1, the model with three-body reactions B4, both performed with the BN1 network, and the model with three-body reactions B6, performed with the BN2 network. This comparison facilitates to estimate the quality of recovery achieved by the BN2 network. We find that model B6 recovers the results of model B4 very well for methanol with $N_{B4;CH_3OH}/N_{B6;CH_3OH} = 1.04$ at the dust peak and $N_{B4;CH_3OH}/N_{B6;CH_3OH} = 1.01$ at the COM peak. The methanol column densities of the B6 model are slightly lower than that of the B4 model and closer to the results of the B1 model, which indicates that the small surplus in the B4 model is produced by a top-down chemistry, in which methanol is produced by splitting up larger molecules. Interestingly, also the column densities of the larger COMs, methyl formate and glycoaldehyde, are reproduced to a reasonable degree with $N_{B4;CH_3OCHO}/N_{B6;CH_3OCHO} = 0.85$ and $N_{B4;CH_2OHCHO}/N_{B6;CH_2OHCHO} = 1.43$ at the dust peak and $N_{B4;CH_3OCHO}/N_{B6;CH_3OCHO} = 0.93$ and $N_{B4;CH_2OHCHO}/N_{B6;CH_2OHCHO} = 1.45$ at the COM peak. Acetaldehyde is reproduced the least well with a factor of $N_{B4;CH_3CHO}/N_{B6;CH_3CHO} = 1.7$ at the dust peak and $N_{B4;CH_3CHO}/N_{B6;CH_3CHO} = 2.0$ at the COM peak, indicating that the BN2 network might be missing some reactions for the formation of acetaldehyde.

4.3.4 The DN2 network

The deuteration of the BN2 network generates the DN2 network. It consists of significantly less grain surface reactions than the DN1 or DRN1 networks, including only around 30,000 reactions. The subroutine size of the D5 model, using the DN2 network and including three-body reactions amounts to 5.1GB instead of 22GB for the D2 model and 16.4GB for the D4 model. This subroutine size is only a factor of approximately 2 larger than previously successful simulations and finishes within around 22 days, making it much faster than simulations of the

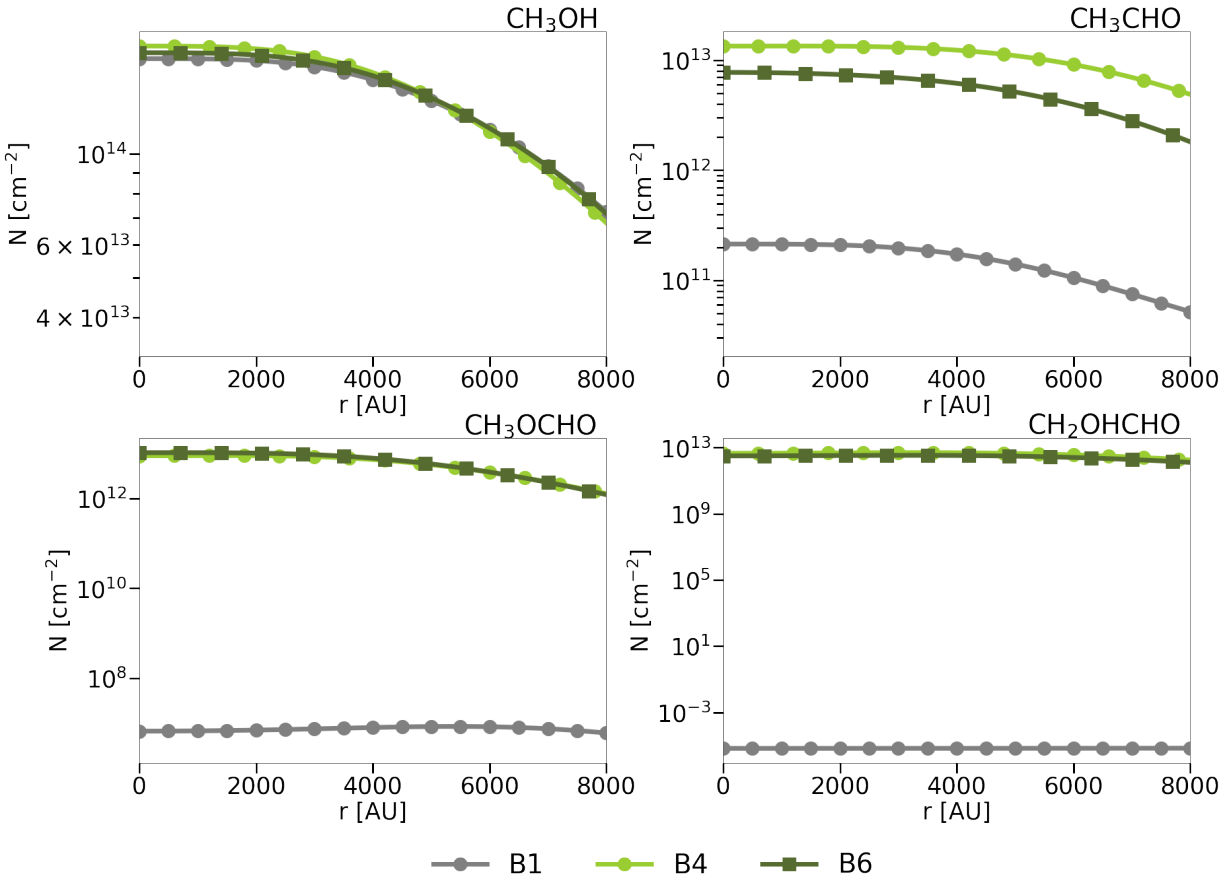

Figure 4.5: Column density profiles of methanol (CH_3OH), acetaldehyde (CH_3CHO), methyl formate (CH_3OCHO) and glycoaldehyde (CH_2OHCHO) for a purely diffusive model (model B1; grey) and a model including three-body reactions (model B4; light green), performed with the base network BN1, and a model including three-body reactions (model B6; olive), performed with the base network BN2.

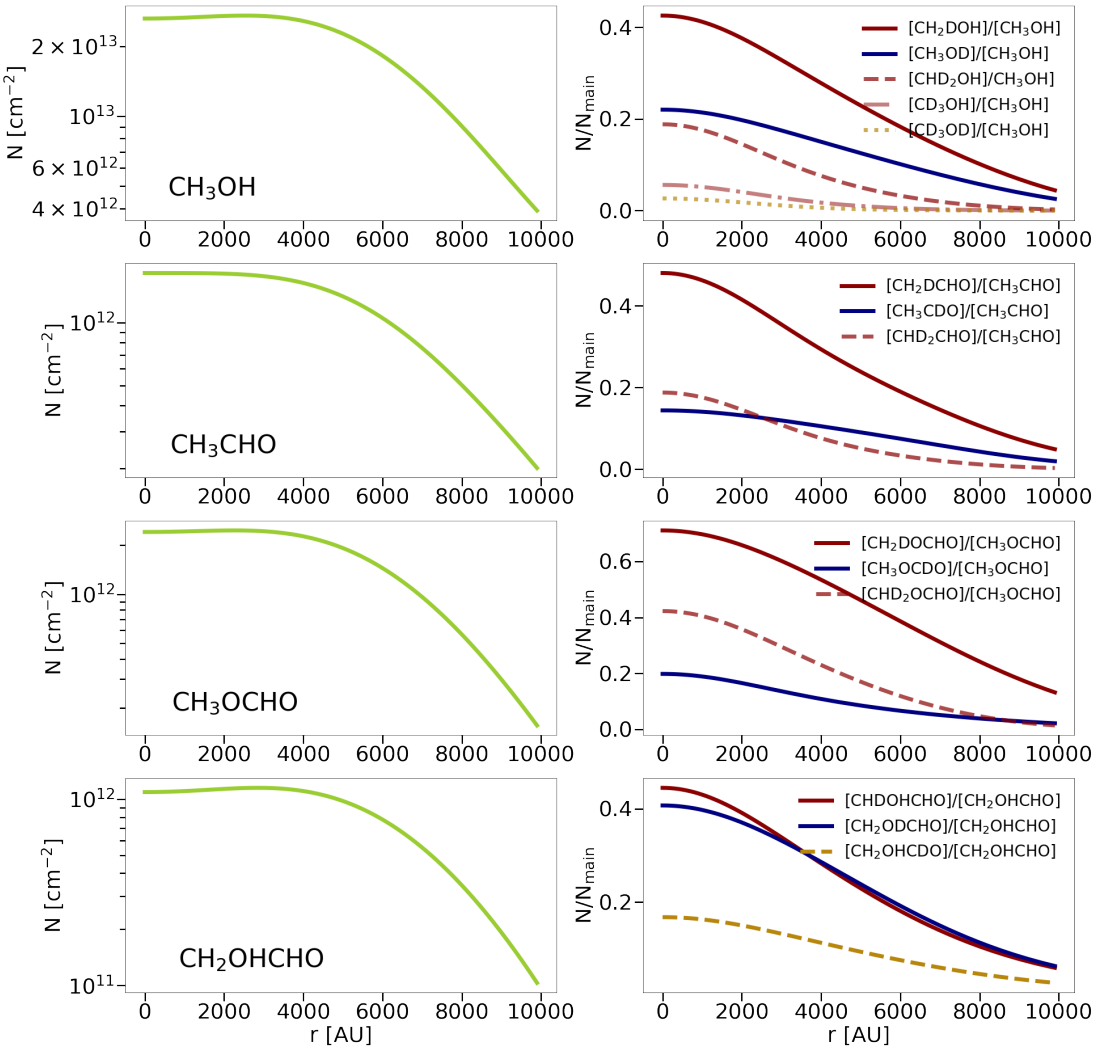

Figure 4.6: Column density profiles of methanol (CH_3OH), acetaldehyde (CH_3CHO), methyl formate (CH_3OCHO) and glycoaldehyde (CH_2OHCHO; left) and column density ratios of their observed deuterated isotopologues (right), derived with the D5 model.

D4 model. An additional advantage of this approach in contrast to the one presented in Section 4.3.2 is that this network is feasible without the reduction of the deuteration degree tested for the D3 and D4 model. It is therefore able to make predictions for all deuterated isotopologues of the investigated COMs.

Table 4.5 [1] lists the column densities N and the column density ratios with respect to the main isotopologues $N/N_{\rm main}$ toward the core center and the COM peak at 4000 AU at the best-fit time of 3×10^5 yr. The few observational constraints available (Jiménez-Serra et al. 2016, Spezzano et al. 2025) from the pre-stellar core stage are included in a third column respectively.

Additionally, Figure 4.6 presents the column density profiles N of methanol, acetaldehyde, methyl formate and glycoaldehyde (left), obtained with the D5 model, and the column density ratios $N/N_{\rm main}$ of the respective deuterated isotopologue with respect to the main isotopologue (right). Here, we present the ratios of deuterated isotopologues for which detections either in the pre-stellar core stage or in the protostellar stage have been reported. This concerns mostly the singly and doubly deuterated isotopologues of the COMs. In the case of methanol, however, there are also detections of the triply deuterated isotopologue CD_3OH (Ilyushin et al. 2022) and a tentative detection of the quadruply deuterated isotopologue CD_3OD (Ilyushin et al. 2023).

We find that the observed column densities (Spezzano et al. 2025, Jiménez-Serra et al. 2016) of the main isotopologues of methanol, acetaldehyde and methyl formate are matched reasonably well by model D5. The modelled column densities reproduce the observed ones within a factor of 2 both at the dust peak and the COM peak. It is noteworthy that the methanol column densities for CH_3OH obtained with the D5 model are lower than the ones obtained by the D1 model (see Table 4.4) by a factor of 3 to 4.

Moreover, we find that the D5 model derives relatively high $N/N_{\rm main}$ values for all investigated molecules. The column density ratios $N/N_{\rm main}$ for methanol obtained with the D5 model are significantly higher than the ones obtained with the D1 model, indicating that the contribution of non-diffusive reaction mechanisms to the deuteration of methanol is not negligible. This result is in contrast to our previous work (Riedel et al. 2025), using another chemical network, in which we concluded that the non-diffusive reaction mechanisms only have minor contributions to methanol formation and deuteration. Unfortunately, there are only very few observational constraints for $N/N_{\rm main}$ from the pre-stellar core stage. Spezzano et al. (2025) reports a column density ratio $N_{\rm obs}(CH_2DOH)/N_{\rm obs}(CH_3OH)$ of 0.22 at the dust peak and 0.21 at the COM peak and a column density ratio of $N_{\rm obs}(CHD_2OH)/N_{\rm obs}(CH_3OH)$ of 0.06 at the dust peak and 0.03 at the COM peak. The modelled column density ratios $N_{\rm mod}(CH_2DOH)/N_{\rm mod}(CH_3OH)$, derived with the D5 model, are a factor of around 2 (dust peak) and 1.3 (COM peak) larger than the observed ones. The modelled column density ratios $N_{\rm mod}(CHD_2OH)/N_{\rm mod}(CH_3OH)$ are a factor

[1] At the submission date of this thesis, the integration phase of cells 0,1 and 4 was not completed. The inner two cells typically have a low contribution to the column densities. The contribution of cell 4 is higher. The column density values presented in this Section assume that the contribution of these three cells is 0. However, we also performed an upper estimate of the missing portion of the column densities for the main isotopologues at the dust peak, assuming that the missing cells have the same abundances as their neighbouring cells: N_{CH_3OH}=3.33 × 10^{13} cm^{-2}, N_{CH_3CHO}=2.27 × 10^{12} cm^{-2}, N_{CH_3OCHO}=3.15 × 10^{12} cm^{-2}, N_{CH_3OCHO}=1.36 × 10^{12} cm^{-2}. Since the upper estimates do not differ significantly from the presented values, we conclude that the derived column densities will already be close to the ones derived by the full model.

Table 4.5: Column densities of the COMs and their deuterated isotopologues, derived with the D5 model.

Molecule	Dust Peak[a] N [cm^{-2}]	obs. N [cm^{-2}]	$N/N_{\rm main}$[c]	COM Peak[b] N [cm^{-2}]	obs. N [cm^{-2}]	$N/N_{\rm main}$
methanol						
CH_3OH	2.63×10^{13}	$(1.3\pm0.05)\times10^{13}$⋄	-	2.57×10^{13}	$(1.6\pm0.03)\times10^{13}$⋄	-
CH_2DOH	1.12×10^{13}	$(2.8\pm0.7)\times10^{12}$⋄	0.43	7.15×10^{12}	$(3.3\pm0.8)\times10^{12}$⋄	0.28
CH_3OD	5.80×10^{12}		0.22	3.86×10^{12}		0.15
CHD_2OH	4.96×10^{12}	$(7.2\pm0.14)\times10^{11}$⋄	0.19	1.95×10^{12}	$(5.4\pm0.15)\times10^{11}$⋄	0.08
CH_2DOD	4.67×10^{12}		0.18	1.82×10^{12}		0.07
CD_3OH	1.48×10^{12}		0.06	4.49×10^{11}		0.02
CHD_2OD	2.41×10^{12}		0.09	6.34×10^{11}		0.02
CD_3OD	7.00×10^{11}		0.03	1.61×10^{11}		0.01
acetaldehyde						
CH_3CHO	1.73×10^{12}	1.2×10^{12}◎	-	1.55×10^{12}	3.2×10^{12}◎	-
CH_2DCHO	8.28×10^{11}		0.48	4.53×10^{11}		0.29
CH_3CDO	2.48×10^{11}		0.14	1.63×10^{11}		0.11
CHD_2CHO	3.24×10^{11}		0.19	1.17×10^{11}		0.08
CH_2DCDO	3.99×10^{11}		0.23	1.37×10^{11}		0.09
CD_3CHO	1.17×10^{11}		0.07	3.28×10^{10}		0.02
CHD_2CDO	1.92×10^{11}		0.11	4.88×10^{10}		0.03
CD_3CDO	4.22×10^{10}		0.02	8.85×10^{9}		0.01
methyl formate						
CH_3OCHO	2.41×10^{12}	$(4.4\pm4.0)\times10^{12}$◎	-	2.27×10^{12}	$(2.3\pm1.4)\times10^{12}$◎	-
CH_2DOCHO	1.71×10^{12}		0.71	1.21×10^{12}		0.53
CH_3OCDO	4.78×10^{11}		0.20	2.47×10^{11}		0.11
CHD_2OCHO	1.02×10^{12}		0.42	5.22×10^{11}		0.23
CH_2DOCDO	5.87×10^{11}		0.24	2.01×10^{11}		0.09
CD_3OCHO	5.89×10^{11}		0.24	2.21×10^{11}		0.10
CHD_2OCDO	3.95×10^{11}		0.16	1.11×10^{11}		0.05
CD_3OCDO	2.89×10^{11}		0.12	7.13×10^{10}		0.03
glycoaldehyde						
CH_2OHCHO	1.09×10^{12}		-	1.11×10^{12}		-
$CHDOHCHO$	4.86×10^{11}		0.45	3.13×10^{11}		0.28
CH_2ODCHO	4.45×10^{11}		0.41	3.17×10^{11}		0.29
CH_2OHCDO	1.83×10^{11}		0.17	1.25×10^{11}		0.11
CD_2OHCHO	1.95×10^{11}		0.18	8.37×10^{10}		0.08
$CHDODCHO$	2.90×10^{11}		0.27	1.17×10^{11}		0.11
$CHDOHCDO$	1.89×10^{11}		0.17	8.02×10^{10}		0.07
CH_2ODCDO	1.45×10^{11}		0.13	5.91×10^{10}		0.05
CD_2ODCHO	6.42×10^{10}		0.06	1.86×10^{10}		0.02
$CHDODCDO$	8.06×10^{10}		0.07	2.35×10^{10}		0.02
CD_2OHCDO	9.26×10^{10}		0.08	2.43×10^{10}		0.02
CD_2ODCDO	2.93×10^{10}		0.03	6.19×10^{9}		0.01

Notes. [(a)] r = 0 AU [(b)] The off-centre position is set to r = 4000 AU, according to the value determined by observations (Chacón-Tanarro et al. 2019a, Jiménez-Serra et al. 2016). The modelled fractional abundance peak occurs between 4500 AU and 6700 AU, depending on the molecule, with methyl formate peaking closer to the dust peak as the others. [(c)] Column density of deuterated isotopologue relative to that of the main isotopologue. ⋄ values are from Spezzano et al. (2025). ◎ values are from Jiménez-Serra et al. (2016).

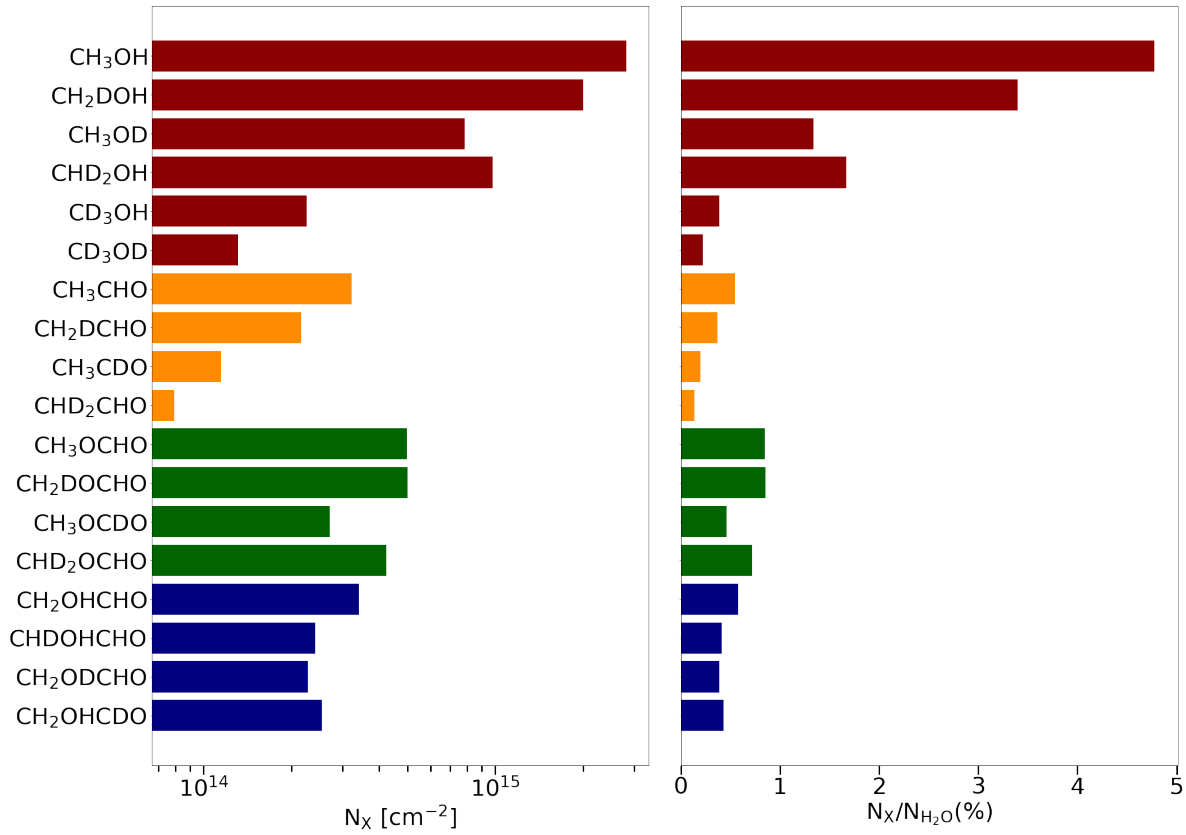

Figure 4.7: Column density profiles of methanol (CH_3OH), acetaldehyde (CH_3CHO), methyl formate (CH_3OCHO) and glycoaldehyde (CH_2OHCHO) of the icy mantles as absolute values (left) and as percentage of the H_2O content (right), derived with the D5 model.

of around 4.8 (dust peak) and 2.7 (COM peak) larger than the observed ones.

Figure 4.7 additionally shows the modelled ice column densities of methanol, acetaldehyde, methyl formate, glycoaldehyde and their observed deuterated isotopologues towards the center of the core in absolute values (left) and with respect to the H_2O column densities (right). The highest column density ratio $N_{\rm mod}(X)/N_{\rm mod}(H_2O) \approx 5\%$ is attained by CH_3OH. Interestingly, the ice column density ratios $N/N_{\rm main}$ tend to be even higher than the gas phase values and their ratios to each other are partially different than in the gas phase. For example, the ice column density ratio $N_{\rm ice}(CH_2DOH)/N_{\rm ice}(CH_3OH)=0.71$ is higher than the gas phase column density ratio $N_{\rm gas}(CH_2DOH)/N_{\rm gas}(CH_3OH)=0.43$. Also, while in the gas phase CH_3OD has a larger column density ($N(CH_3OD)=5.80\times10^{12}$ cm^{-2}) than CHD_2OH ($N(CHD_2OH)=4.96\times10^{12}$ cm^{-2}), the ice column densities for CHD_2OH are larger than the ones for CH_3OD ($N(CHD_2OH)=2.00\times10^{15}$ cm^{-2} vs $N(CH_3OD)=7.87\times10^{14}$ cm^{-2}). In the absence of efficient gas phase formation routes, these differences between gas phase and ice column densities indicate distinct desorption efficiencies for the various isotopologues. Although the model uses a constant reactive desorption efficiency value of 1% for all grain surface species, the desorption process can be amplified by

addition-abstraction cycles and hence the desorption of isotopologues that undergo these cycles more often than others is increased.

4.4 Discussion

Although there are, unfortunately, only very few observational constraints from the pre-stellar core stage, observations of multiple deuterated isotopologues for all investigated molecules in the protostellar stage exist. They were mostly obtained towards the Class 0 triple protostellar system IRAS 16293-2422, close to the center of the B source.

Table 4.6: Comparison of the modelled gas and grain column densities with observational constraints from IRAS 16293-2422 B.

Molecule	mod. gas $N/N_{\rm main}$	mod. grain $N/N_{\rm main}$	obs. gas $N/N_{\rm main}$	references references
CH_2DOH	0.45	0.78	0.071	Jørgensen et al. (2018)
CH_3OD	0.23	0.30	0.018	Jørgensen et al. (2018)
CHD_2OH	0.21	0.42	0.018	Drozdovskaya et al. (2022)
CD_3OH	0.07	0.10	3.7×10^{-3}	Ilyushin et al. (2022)
CD_3OD	0.03	0.06	2×10^{-4}	Ilyushin et al. (2023)
CH_2DCHO	0.51	0.74	0.052	Manigand et al. (2020)
CH_3CDO	0.15	0.39	0.06	Manigand et al. (2020)
CH_2DCHO	0.21	0.29	0.01	Ferrer Asensio et al. (2023)
CH_2DOCHO	0.30	1.06	0.018	Jørgensen et al. (2018)
CH_3OCDO	0.20	0.61	0.061	Jørgensen et al. (2018)
CHD_2OCHO	0.41	0.93	0.042	Manigand et al. (2019)
CHDOHCHO	0.47	0.76	0.10	Jørgensen et al. (2016)
CH_2ODCHO	0.42	0.72	0.047	Jørgensen et al. (2016)
CH_2OHCDO	0.17	0.82	0.052	Jørgensen et al. (2016)

Notes. The modelled column densities are derived with the D5 model and convolved with a 0.5″ Gaussian beam of a source with a distance d = 120 pc.

Table 4.6 compares the modelled gas phase and ice column $N/N_{\rm main}$ with the observed values in IRAS 16293-2422B. The modelled column density ratios are derived with the D5 model, presented in Section 4.3.4. They were convolved with a 0.5″ telescope beam and set to a distance of d = 120 pc, corresponding to the resolution of the observations and the determined distance of the source (Jørgensen et al. 2016). In general, we conclude that model D5 severely overproduces the observed $N/N_{\rm main}$ ratios by one or two orders of magnitude. Although the comparison of observational D/H ratios for methanol between pre-stellar and protostellar stage (e.g.van Gelder 2022, Lin et al. 2023a) hints toward a slight evolutionary trend of decreasing D/H ratios in the protostellar stage, it is not expected that $N/N_{\rm main}$ ratios will undergo a decrease as large as suggested by this comparison.

In combination with the overestimation of the N/N_{main} of CH_2DOH and CHD_2OH in the pre-stellar core stage as compared to the observationally obtained values (Spezzano et al. 2025), these results indicate that the deuteration efficiency is overestimated by the non-diffusive reaction mechanisms. In principle, a higher deuteration efficiency is expected in non-diffusive reaction models with respect to purely diffusive models. The diffusion of the deuterated counterparts in contrast to the main species is generally hampered by their higher mass. However, this effect is expected to be less severe in models that additionally employ non-diffusive reaction mechanisms, as the combination of two heavier reaction partners in cold environments almost exclusively occurs by non-diffusive mechanisms that do not favour the formation of the non-deuterated species in the same manner. The overproduction by model D5 might therefore indicate that diffusive reactions also play a role in the formation of the investigated COMs.

4.5 Conclusion

In this work, we developed multiple deuterated networks, based on a state-of the art chemical network including the chemistry of the main isotopologues, developed in Garrod et al. (2022) and updated in Bonfand et al. in prep. We presented several models for the prediction of abundances, column densities and deuterium fraction profiles of the O-bearing COMs: methanol (CH_3OH), acetaldehyde (CH_3CHO), methyl formate (CH_3OCHO) and glycoaldehyde (CH_2OH CHO) for the prototypical pre-stellar core L1544. They include both models employing purely diffusive reaction mechanisms and models that additionally include various non-diffusive reaction mechanisms, following the recipes laid out in Jin & Garrod (2020) and Garrod et al. (2022) and added to *pyRate* in Riedel et al. (2025).

Our main conclusions are as follows:

1. Non-diffusive reaction mechanisms increase the column densities for CH_3OH, CH_3CHO, CH_3OCHO and CH_2OHCHO to a varying degree. While the column density increases for methanol are only small, the column densities of the other investigated COMs are increased by several orders of magnitude. The largest column density increases are obtained when applying the three-body reactions.

2. Cloning of the base network to incorporate the deuterated counterparts of the chemical reactions results in an extremely large deuterated chemical network DN1, containing 280,000 gas phase and 80,000 grain surface reactions.

3. The simulation of a purely diffusive model with the DN1 network is comparatively costly, but finishes within 5-6 hours. Performing a model, additionally applying the three-body reactions, with the DN1 network is unfeasible within a reasonable time frame.

4. The purely diffusive model, obtained with the DN1 network, allows for an approximate estimation of the column density of methanol and its deuterated isotopologues. The obtained column density ratios N/N_{main} of the deuterated isotopologue with respect to the main

isotopologue reproduce the observationally obtained values (Spezzano et al. 2025) well. The modelled ratios are within the error margins of the observations.

5. Multiple strategies to manage the high computational cost of this project are developed, including the development of a deuterated network containing only singly and doubly deuterated isotopologues (network DRN1), and the development of a deuterated network derived from a reduced base network (network DN2).

6. Performing a simulation, applying the three-body reactions, in combination with the DRN1 network is very computationally costly, taking more than 2 months to finish and is therefore not feasible in the first stages of tests.

7. A simulation, applying the three-body reactions, in combination with the DN2 network takes around 22 days to finish. The modelled column densities of the main isotopologues reproduce the observational column densities (Spezzano et al. 2025, Jiménez-Serra et al. 2016) within a factor of 2. The modelled column density ratios $N/N_{\rm main}$ of the deuterated isotopologue with respect to the main isotopologue, however, are up to a factor of 4.8 higher than the available observations for $N(CH_2DOH)/N(CH_3OH)$ and $N(CHD_2OH)/N(CH_3OH)$.

8. A comparison of the modelled column density ratios $N/N_{\rm main}$ for multiple deuterated isotopologues of methanol, acetaldehyde, methyl formate and glycoaldehyde with observational constraints obtained towards the protostellar system IRAS 16293-2422B suggests an overestimation of one to two orders of magnitude by the model. This might indicate an overestimation of the contribution of non-diffusive reactions to the formation and deuteration of the investigated COMs.

The present work represents the first exploration of the formation and deuteration of the larger O-bearing COMs: acetaldehyde, methyl formate and glycoaldehyde in combination with non-diffusive reaction mechanisms. Further work, introducing diffusive mechanisms to the model that were shown to increase the column densities of COMs in cold environments, as e.g. the one presented in Molpeceres et al. (2024), would provide valuable additions.

Chapter 5

High deuteration of methanol in L1544

The contents of this chapter are under revision in ACS Earth and Space Chemistry. Credit: Spezzano, S., Riedel, W., Caselli, P, et al. 2025, submitted to ACS.

This study was mainly conducted by my colleague Silvia Spezzano. She performed the observations and their entire analysis and discussion. I contributed the modelling data presented in this work, as a means of comparison to the observed values. The models for the pre-stellar core L1544 were developed in Riedel et al. (2025) (see Chapter 3). In addition, I computed the models for the pre-stellar cores HMM1 and L694-2 particularly for the work presented in this Chapter. The text in Section 5.4 and Appendix C.2 was written by me.

Abstract

Isotopic fractionation is a very powerful tool to follow the evolution of material from one stage to the next in the star-formation process. Pre-stellar cores exhibit some of the highest levels of deuteration because their physical conditions (T $\leq$ 10 K and $n(H_2) \geq 10^5$ cm^{-3}) greatly favor deuteration processes. Deuteration maps are a measure of the effectiveness of the deuteration across the core, and they are useful to study both the deuteration as well as the formation mechanism (either in the gas-phase or on grain surfaces) of the main species. Methanol is the simplest O-bearing complex organic molecule (COM) detected in the interstellar medium (ISM). It represents the beginning of molecular complexity in star-forming regions, thus a complete understanding of its formation and deuteration is a necessary step to understand the development of further chemical complexity. In this paper, we use single-dish observations with the IRAM 30 m telescope and state-of-the-art chemical models to investigate the deuteration of methanol towards the prototypical pre-stellar core L1544. We also compare the results of the chemical models with previous observations of deuterated methanol towards the pre-stellar cores HMM1 and L694-2. The spectra extracted from the CHD_2OH map show that the emission is concentrated in the center and towards the north-west of the core. Using deep observations towards the dust and the methanol peaks of the core, we derive a very large deuterium fraction for methanol ($\sim$ 20%) towards both peaks. The comparison of our observational results with chemical models

has highlighted the importance of H-abstraction processes in the formation and deuteration of methanol. Deep observations combined with state-of-the-art chemical models are of fundamental importance in understanding the development of molecular complexity in the ISM. Our analysis also shows the importance of non-LTE effects when measuring the D/H ratios in methanol.

5.1 Introduction

Low-mass stars are formed by the collapse of dense cores within filamentary structures in molecular clouds (Bergin & Tafalla 2007; Hacar et al. 2023). Dense cores are therefore crucial players in our understanding of the physical and chemical conditions at the dawn of star-formation. Pre-stellar cores are dynamically evolved starless cores with centrally concentrated density profiles and central densities higher than a few 10^5 cm^{-3} (Crapsi et al. 2005; Keto & Caselli 2008). Pre-stellar cores are of particular importance in the quest of understanding the initial conditions of low-mass star-formation because they are unstable against gravitational collapse, and hence will certainly form a protostellar system. Conversely, starless cores that are less dense and not centrally concentrated (e.g. B68 and TMC-1 Bergin et al. 2002; Fuente et al. 2019), might eventually evolve into a pre-stellar core and finally form a protostar, or dissolve back into the interstellar medium.

The density structure of pre-stellar cores is generally modelled with a Bonnor-Ebert (BE) sphere (Bonnor et al. 1958; Ebert 1955) with a central plateau and a density decrease outwards that scales with r^{-2} where the size of the central plateau decreases as the core approaches the protostar formation (Keto & Caselli 2010). Pre-stellar cores are also characterized by a steep decrease of temperatures towards their center, where the gas reaches temperatures of 6-8 K (Crapsi et al. 2007; Pagani et al. 2007). As a consequence of the low temperatures and high densities in the centre, molecules readily freeze onto dust grains (Caselli et al. 1999; Bacmann et al. 2002; Caselli et al. 2022), a process that significantly enhances deuterium fractionation (Crapsi et al. 2005; Caselli et al. 2002). H_2D^+ and the other deuterated isotopologues of H_3^+ are the primary sources of deuteration in pre-stellar cores. They form *via* the exothermic reaction

$$H_3^+ + HD \rightarrow H_2D^+ + H_2 \tag{5.1}$$

that strongly favors H_2D^+ production at temperatures below 30 K. Furthermore, the abundance of H_2D^+ is also influenced by the *ortho*-to-*para* ratio of H_2, as the reverse reaction becomes endothermic when H_2 is predominantly in the *para* form (Pagani et al. 1992). H_2D^+ is further deuterated by successive reactions with HD, leading to an enhancement of D_2H^+ and D_3^+ (Caselli et al. 2019). The deuterated isotopologues of H_3^+ are the key players in the gas-phase deuteration, while deuterium atoms, formed from the reactive dissociation of deuterated H_3^+ isotopologues with electrons, drive the deuteration on the icy surface of dust grains. Overall, very high levels of deuteration have been observed in pre-stellar cores, where even multiply deuterated molecules are routinely observed, e.g. *c*-C_3D_2, D_2CO, and CHD_2OH (Spezzano et al. 2013; Bacmann et al. 2003; Lin et al. 2023a).

Complex organic molecules (COMs) are defined as organic molecules with more than five atoms (e.g. Herbst & van Dishoeck 2009). COMs have been observed in a wide variety of

astrophysical environments. In low-mass star-forming regions, they are particularly abundant around protostars, in regions called hot corinos where forming stars heat the surrounding material above the sublimation temperature (100 K) of the water ice mantles on dust grains (Ceccarelli et al. 2007). In the past decade, many observations of COMs toward starless and pre-stellar cores demonstrated that they efficiently form also in very cold environments (Öberg et al. 2010; Bacmann et al. 2012; Vastel et al. 2014; Jiménez-Serra et al. 2016, 2021; Scibelli et al. 2021). According to astrochemical models, COMs in pre-stellar core centres are mainly present in solid-phase within the thick icy mantles of dust grains (e.g. Vasyunin et al. 2017), while observable levels of COMs are found in the outskirts of pre-stellar cores (e.g. Jiménez-Serra et al. 2016, 2021). Lin et al. (2023a) recently reported on the first detection of doubly deuterated methanol (the simplest COM) towards pre-stellar cores, and derived a D/H ratio consistent with measurements in more evolved Class 0/I objects and comet 67P/Churyumov-Gerasimenko(Drozdovskaya et al. 2021), suggesting a chemical inheritance from the pre-stellar stage. There is observational evidence suggesting that the chemical budget present in the pre-stellar phase doesn't undergo a full reset during protostar formation (Müller et al. 2022). Consequently, pre-stellar cores act as a chemical reservoirs, supplying crucial building blocks for stars and planets. To follow the evolution of pre-stellar material from one evolutionary stage to the next in the star-formation process, isotopic fractionation proves to be an exceptionally powerful diagnostic tool(Ceccarelli et al. 2014). It is, in fact, not possible to reproduce the deuterium fractionation observed in water within the Solar System without taking into account the formation and deuteration of water in the pre-stellar phase (Cleeves et al. 2014). Furthermore, recent observations suggest that a fraction of the complex organic molecules (COMs) observed towards protostellar cores are inherited from the pre-stellar phase (van Gelder 2020; Scibelli et al. 2021). Deuteration maps are a measure of the effectiveness of the deuteration across the core, and they are useful to study both the deuteration as well as the formation of the main species (Redaelli et al. 2019; Chacón-Tanarro et al. 2019a; Giers et al. 2022). Furthermore, deuteration maps from multiply deuterated isotopologues (i.e. CHD_2OH or c-C_3D_2) are crucial to assess the effects of the spatial distribution of both deuterated and non-deuterated isotopologues on the deuteration peak that results from using the main isotopologue (e.g. CH_2DOH/CH_3OH). A clear example is the deuteration of c-C_3H_2 observed in the pre-stellar core L1544. While the c-C_3HD/c-C_3H_2 column density ratio peaks at the east of the dust emission peak, the c-C_3D_2/c-C_3HD peaks towards the dust peak (see Figure 2 in Giers et al. 2022). This might suggest that the c-C_3HD/c-C_3H_2 peak could be a consequence of the steep decrease of the c-C_3H_2 towards the North-East in the outer layers of the pre-stellar cores, rather then a location of enhanced deuteration. In Spezzano et al. (2016) we showed that the southern part of the pre-stellar core L1544 is more exposed to the interstellar radiation field (ISRF), and therefore this is where the carbon chain molecules peak. The north-eastern part of the core is more shielded, and as a consequence more carbon will be locked in CO and is not available for the formation of carbon chain molecules. Given that methanol is directly formed from CO on grains (Watanabe & Kouchi 2002), methanol peaks in the North-East of L1544. The deuterated isotopologues of c-C_3H_2, instead, are only present in the inner layers of L1544, and their distribution is not affected by the ISRF.

Observing multiply deuterated molecules is very important to fine-tune our astrochemical models

and allow quantitative comparison among the different evolutionary stages in the star- and planet-formation process. With methanol being the simplest O-bearing COM and the starting point of molecular complexity in star-forming regions (Garrod et al. 2006b; Chuang et al. 2017), understanding its deuteration in pre-stellar cores will provide crucial constraints on its formation and inheritance in the star-formation process. Although the formation of methanol on dust grains is well-established (Watanabe & Kouchi 2002; Vasyunin et al. 2017), the chemical pathways responsible for its deuteration remain unclear, with potential pathways including H-D substitution and hydrogenation of deuterated formaldehyde (Hidaka et al. 2009). In an effort to identify crucial chemical and physical parameters for the formation and deuteration of methanol in the pre-stellar phase, Riedel et al. (2023, 2025) updated a gas-grain chemical code by including various processes such as reactive desorption, diffusion mechanisms for hydrogen and deuterium atoms on the surface of interstellar dust grains, and non-diffusive reaction mechanisms. Such processes are very important to reproduce the observations of COMs in pre-stellar cores.
In this paper we explore the deuteration of methanol towards the prototypical pre-stellar core L1544. This core, located in the Taurus molecular cloud at 170 pc (Galli et al. (2019)), is one of the best studied pre-stellar cores. Its central density is $\sim 10^6$ cm^{-3} and the central temperature is $\sim$ 6 K (Crapsi et al. 2007). The core exhibits a high degree of CO freeze-out and a high level of deuteration towards its center (Caselli et al. 1999; Crapsi et al. 2005). It is chemically rich (Vastel et al. 2014; Jiménez-Serra et al. 2016), showing spatial inhomogeneities in the distribution of molecular emission (Spezzano et al. 2017). For decades, L1544 has been the test bed for studies that have significantly advanced our understanding of the dynamical evolution of dense cores prior to star-formation.
The paper is structured as follows: Section 5.2 presents the observations, the analysis of the single-dish observations is presented in Section 5.3. We use state-of-the art chemical models to reproduce the deuteration of methanol in three pre-stellar cores and our results are described in Section 5.4. We discuss the overall results in Section 5.5 and summarize our conclusions in Section 5.6.

5.2 Observations

The emission map of the $J_{K_a,K_c} = 2_{0,2}$-$1_{0,1}$ e_0 transition of CHD_2OH (E_{up} = 6 K) at 83289.63 MHz (Coudert et al. 2021) towards L1544 was obtained using the IRAM 30 m telescope (Pico Veleta, Spain) in different observing runs between 2022 and 2023 (project codes: 116-21, 043-22, 104-22, PI: S. Spezzano). We performed a 1.4′ × 1.4′ on-the-fly (OTF) map centred on the source dust emission peak (α_{2000} = $05^h04^m17^s.21$, δ_{2000} = +25°10′42″.8). We used position switching with the reference position set at (-180″, 180″) offset with respect to the map centre. The EMIR E090 receiver was used with the Fourier transform spectrometer backend (FTS) with a spectral resolution of 50 kHz. The mapping was carried out in good weather conditions ($\tau_{225\ GHz} \sim 0.3$) and a typical system temperature of $T_{sys} \sim$ 90-150 K. The data processing was done using the GILDAS software (Pety 2005). The emission map has a beam size of 30″, and was gridded to a pixel size of 6″ with the CLASS software in the GILDAS package, which corresponds to ∼1/5 of the beam size. The intensity scale was converted into main beam temperature T_{MB}

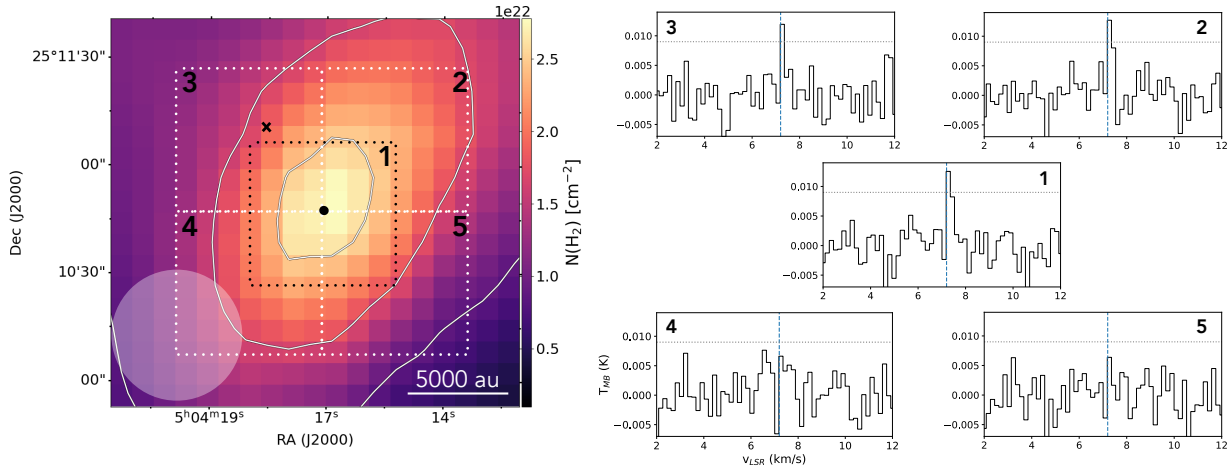

Figure 5.1: Left panel: the five different areas where the CHD_2OH spectra have been extracted from the OTF map observed with the IRAM 30 m telescope are shown as dotted squares on the H_2 column density map of L1544 computed from *Herschel*/SPIRE data at 250, 350 and 500 μm (Spezzano et al. 2016). The solid white contours are the 30%, 60% and 90% of the peak intensity of the N(H_2) map. The *Herschel*/SPIRE beam is shown in the bottom left of the map. The black saltire shows the position of the methanol peak and the full black circle shows the dust emission peak. Right panel: $J_{K_a,K_c} = 2_{0,2}$-$1_{0,1}$ e_0 CHD_2OH spectra extracted from the IRAM 30m OTF map. The vertical dashed lines shows the v_{LSR} of the source (7.2 km/s), and the horizontal dotted lines show the 3σ noise level. The number in each spectra refers to the area where the spectra was extracted from, shown in the left panel of the figure.

assuming the forward efficiency $F_{eff} = 0.95$ and $B_{eff} = 0.81$. The noise level was homogeneous in our map, therefore no weighting was applied to the individual spectra before averaging. While the brightest CH_2DOH transition in the 3 mm band was observed, the line is still too weak to produce an integrated intensity map. The averaged spectra towards five different regions across L1544 are shown in Figure 5.1. The single pointing observations towards the dust peak of L1544 shown in Figure 5.2 are from the IRAM 30 m large program ASAI (Lefloch et al. 2018). The single pointing observations towards the methanol peak ($\alpha_{2000} = 05^h04^m18^s$, $\delta_{2000} = +25°11'10''$) shown in Figure 5.2 were obtained with the 30m telescope in 2024 within the framework of project 022-24 (PI: A. Megías).

5.3 Results

The results of the IRAM 30m project aimed at mapping the $2_{0,2}$-$1_{0,1}$, e_0 transition of doubly deuterated methanol toward the central $1.4' \times 1.4'$ region of L1544 are shown in Figure 5.1. The final rms of the map is ~5 mK and the peak intensity of the CHD_2OH line, towards the dust peak, is ~ 15 mK. Given the weakness of the line, we used the OTF data to average the spectra

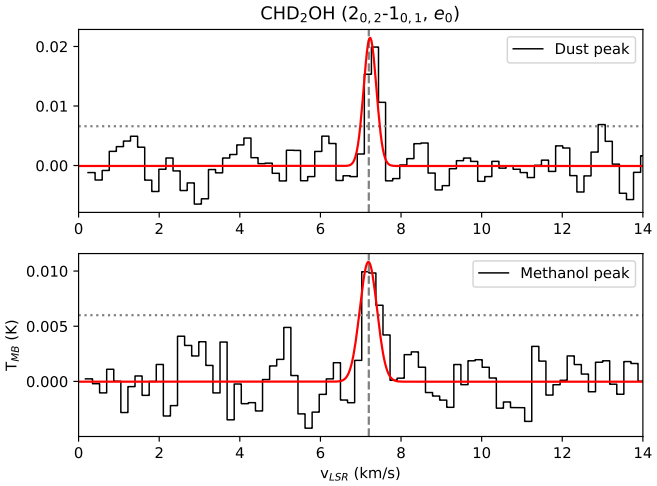

Figure 5.2: Spectra of CHD_2OH observed with single-pointing observations toward the dust peak (upper panel) and the methanol peak (lower panel) of L1544. The vertical dashed line shows the v_{LSR} of the core, 7.2 km/s. The horizontal dotted lines show the 3σ noise level.

Table 5.1: Parameters of the observed CHD_2OH lines in the dust and methanol peak of L1544.

	W mK km s^{-1}	v_{LSR} km s^{-1}	FWHM km s^{-1}	rms mK	N_{TOT} (T_{ex} = 5 K) cm^{-2}	N_{TOT} (T_{ex} = 6.5 K) cm^{-2}	N_{TOT} (T_{ex} = 8 K) cm^{-2}
dust peak	8.4(9)	7.19(2)	0.37(4)	3	$6.7(7)\times10^{11}$	$7.0(8)\times10^{11}$	$8.0(9)\times10^{11}$
methanol peak	6.2(9)	7.18(5)	0.47(9)	3	$5.0(7)\times10^{11}$	$5.2(8)\times10^{11}$	$5.9(9)\times10^{11}$

Note: The laboratory spectroscopy reference for CHD_2OH is Drozdovskaya et al. (2022). The integrated intensities are reported in units of T_{MB}. Numbers in parentheses denote 1σ uncertainties in units of the last quoted digit.

within an area of 40″× 40″ towards five quadrants shown with dotted white lines in Figure 5.1. All spectra in Figure 5.1 are plotted between -0.007 and 0.012 K, and between 2 and 12 km/s, with the emission lines centered at 7.2 km/s. The color map used as background for the spectra is the $N(H_2)$ map of L1544 computed from *Herschel*/SPIRE data (Spezzano et al. 2016). The spectra in Figure 5.1 show that the CHD_2OH line is brightest in the central and the northwest part of the core, where it is detected with S/N¿4 over two channels. The line is barely detected in the North-East (S/N~4) over only one channel, and not detected in the southern part of the core. The result is in agreement with the singly deuterated methanol maps shown in the central and right panels of Figure 2 in Chacón-Tanarro et al. (2019a).

Although the results shown in Figure 5.1 allow us to understand the distribution of doubly deuterated methanol in L1544 and qualitatively compare with OTF maps of CH_3OH, CH_2DOH, and other deuterated isotopologues observed in L1544 (Chacón-Tanarro et al. 2019a; Redaelli et al. 2019; Giers et al. 2022), the poor signal-to-noise ratio of the spectra would make a quantitative comparison rather inconclusive. To overcome this limitation, we use deep observations

towards the dust and methanol peaks of L1544, where the rms is 2.2 and 2.0 mK, respectively. The single pointing observations are shown in Figure 5.2. The results of the Gaussian fit towards the dust and methanol peak of L1544 are reported in Table 5.1. The column densities of CHD_2OH reported in Table 5.1 have been computed from the spectra shown in Figure 5.2 using the formula reported in Mangum & Shirley (2015), assuming optically thin emission and that the source fills the beam:

$$N_{\rm tot} = \frac{8\pi\nu^3 Q_{rot}(T_{ex})W}{c^3 A_{ul} g_u} \frac{e^{\frac{E_u}{kT}}}{J(T_{ex}) - J(T_{bg})}, \tag{5.2}$$

where $J(T) = \frac{h\nu}{k}(e^{\frac{h\nu}{kT}} - 1)^{-1}$ is the Rayleigh-Jeans equivalent temperature in Kelvin, k is the Boltzmann constant, ν is the frequency of the line, h is the Planck constant, c is the speed of light, A_{ul} is the Einstein coefficient of the transition, W is the integrated intensity, g_u is the degeneracy of the upper state, E_u is the energy of the upper state, Q_{rot} is the partition function of the molecule at the given temperature T_{ex}, $T_{bg}$is the background (2.7 K). We calculated the partition function $Q(T_{\rm ex})$ at 5, 6.5, and 8 K using the CHD_2OH catalog from the CDMS (Müller et al. 2005), recently updated based on Drozdovskaya et al. (2022). The resulting partition functions are reported in Table S1. The column densities of doubly deuterated methanol reported in Table 5.2 were calculated considering variations of $T_{\rm ex}$ within 5-8 K and assuming a calibration error of 20% to derive the uncertainties, as done in Lin et al. (2023a). Table 5.2 also reports on the deuteration ratios of methanol at the dust and methanol peaks of L1544, as well as the column densities of the main and singly deuterated isotopologues of methanol reported in Lin et al. (2022) and Chacón-Tanarro et al. (2019a), for completeness. The column densities of the main isotopolog reported in Table 5 of Lin et al. (2022) have been derived with RADEX non-LTE modelling using a total of ten different lines (of which four were obeserved as upper limits) at 3 and 2 mm, and they agree within a factor of two with previous values reported in Vastel et al. (2014), Bizzocchi et al. (2014), Punanova et al. (2018), and Chacón-Tanarro et al. (2019a).

Table 5.2: Column densities and column density ratios at the dust peak and methanol peak of L1544

	Dust Peak	Methanol Peak
$N(CH_3OH)^a$	$1.30(5)\times10^{13}$ cm^{-2}	$1.60(3)\times10^{13}$ cm^{-2}
$N(CH_2DOH)^b$	$2.8(7)\times10^{12}$ cm^{-2}	$3.3(8)\times10^{12}$ cm^{-2}
$N(CHD_2OH)^c$	$7.2(1.4)\times10^{11}$ cm^{-2}	$5.4(1.5)\times10^{11}$ cm^{-2}
$N(CH_2DOH)/N(CH_3OH)$	22(6)%	21(5)%
$N(CHD_2OH)/N(CH_3OH)$	6(1)%	3(1)%
$N(CHD_2OH)/N(CH_2DOH)$	26(8)%	16(6)%

Notes. $^{(a)}$ From Lin et al. (2022). $^{(b)}$ From Chacón-Tanarro et al. (2019a). $^{(c)}$ This work. Numbers in parentheses denote 1σ uncertainties in units of the last quoted digit.

5.4 Chemical models

To compare if our current theoretical understanding of deuterium chemistry can match the observed deuteration trends for methanol, we have tested several models originally developed to reproduce the CH_2DOH/CH_3OH ratio (Riedel et al. 2023, 2025).

The chemical evolution of molecular abundances is computed with the gas-grain astrochemical code *pyRate* (Sipilä et al. 2015a, 2019b). The chemical network for the gas-phase is based on the 2014 public release of the Kinetic Database for Astrochemistry (Wakelam et al. 2015). A recent update to the latest data release (kida.uva.2024, Wakelam et al. 2024) showed no significant deviations from the results reported here. The grain surface network is based on the one presented in Semenov et al. (2010). Reactions were cloned to include deuterated counterparts for species up to seven atoms and spin-state counterparts for selected species. Uncertainties arise when reactions are cloned to describe the evolution of deuterated species. The methanol formation and deuteration scheme follow the experimentally verified proposal by Hidaka et al. (2009). Generally, experimental data is used when it is available; for details on the network and deuteration schemes, we refer to Riedel et al. (2025) and references therein. The models assume a three-phase grain model, including a gas-phase, a chemically active surface-phase, and an inert mantle-phase. Desorption of methanol from the surface of the dust grain occurs predominantly through non-thermal desorption mechanisms in the extremely cold conditions of pre-stellar cores. Usually, reactive desorption is presumed to be the dominant one (Vasyunin et al. 2017; Riedel et al. 2023). All models presented in this work apply a constant reactive desorption efficiency of 1% (Garrod et al. 2007). The formation enthalpies and binding energies used in the model are reported in Table A.1 of Riedel et al. (2023). After a recent update (Riedel et al. 2025), pyRate includes several non-diffusive reaction mechanisms. However, their impact on the chemistry of methanol, which is mainly formed and deuterated by addition and abstraction reactions of highly mobile H and D atoms, was found to be only minor in Riedel et al. (2025), where a factor of non-diffusive/diffusive of 1.07 (dust peak) and 0.95 (methanol peak) is derived at the best fit-time (t=3×10^5 yr). The models presented in this work, therefore, include solely the more conservative diffusive chemistry. Nonetheless, we note that Jiménez-Serra et al. (2025) found that the formation of CO, CO_2 and CH_3OH are tightly linked, so that non-diffusive chemistry may lead to some different results. Surface reactions proceed through the Langmuir-Hinshelwood mechanism relying on thermal diffusion. Riedel et al. (2025) tested over 30 different models while investigating the formation and deuteration of methanol in cold dense cores, like L1544. Here we compare the result of the best four models (D2, D3, D4 and D5) against our observations in L1544. To facilitate the comparison, we kept the same nomenclature as in Riedel et al. (2025). The characteristics of the models used in this paper are listed in Table S2. Models D2, D3 and D4 adopt only H-addition reactions, while model D5 also includes H-abstraction reactions. Model D2 additionally allows for the diffusion of hydrogen and deuterium atoms by quantum tunneling through a rectangular barrier of 1 Å width. The diffusion-to-binding energy E_d/E_b is set to 0.55; with the exception of model D3, where it is set to 0.2, the lowest value debated in the literature (Furuya et al. 2022b). Reactions with an activation-energy barrier play an important role in the hydrogenation (and deuteration) of

methanol. Hence, the approach used to derive their reaction probabilities has a significant impact on the formation of methanol and its deuterated isotopologues. Here, we test two approaches widely used in the literature. Models D2 and D3 apply the single collision approach (Hasegawa et al. 1992), which assumes that the reactant has only one attempt to either thermally hop over the barrier or tunnel through it. Models D4 and D5 apply the reaction-diffusion competition approach (Chang et al. 2007), which considers that the reaction partners are confined in the same binding site until one of them diffuses away again and can therefore undergo multiple attempts to react with each other. The chemical models were run using the physical structure of L1544 (Keto et al. 2015), shown in Figure S2. All models use the initial chemical abundances reported in Table 1 of Riedel et al. (2025), consider a spherical dust grain with a radius of 0.1 μm and a surface density of binding sites of $1.5{\times}10^{15}$ cm^{-2}, and use the canonical value of $\zeta_2 = 1.3{\times}10^{-17}$ s^{-1}. The visual extinction in the models is calculated as $A_V = 10^{-21}\,N(\mathrm{H_2})$; a floor value of 1 mag for L1544 and L694-2, and 3 mag for HMM1, are added to account for the more extended envelope. The external values used for the three cores are 1 mag for L1544 and L694-2, and 3 mag for HMM1. The resulting abundances were converted to column densities including beam convolution with a beam size corresponding to the observations. The results of the models for L1544 and the comparison with the observations are shown in Figure 3.

5.5 Discussion

The spectra on the L1544 map in Figure 5.1 show that the line of CHD_2OH is not detected towards the southern part of the core, and detected at a 2σ level (in integrated intensity) towards the north-east part of the core. The distribution of methanol in L1544 is characterized by a sharp decrease towards the South because of a more efficient illumination from the interstellar radiation field (Spezzano et al. 2016). It is therefore not surprising that we do not observe CHD_2OH in the southern part of the core. On the contrary, it might be surprising that the line is very weak towards the north-east part of the core, given that the methanol peak is located towards the north east with respect to the dust peak of L1544 (Bizzocchi et al. 2014). It is important to note, however, that the quadrants that we used to average the spectra shown in Figure 1 are large and the position of the methanol peak is covered by both the central and the upper-left quadrant. Overall, the spectra in Figure 1 show that our target line for CHD_2OH is observed in a rather small portion of the map around and slightly towards the north of the dust peak.

When comparing the deuteration of methanol towards the dust and methanol peaks in L1544 using the deep observations shown in Figure 2, we do not see significant differences within error-bars. The deuterium fractions measured towards the dust peak, however, tend to be larger than the ones measured towards the methanol peak, as reported in Table 2. The deuteration maps of N_2H^+, HCO^+, and c-C_3H_2 in L1544 also peak towards the center of the core (e.g., Redaelli et al. 2019 and Giers et al. 2022) where the deuteration is more efficient because of the local increase in the abundance of H_2D^+, D_2H^+, and D_3^+, as well as the catastrophic freeze-out of CO (Caselli et al. 1999). The level of deuteration reached by each molecule varies, and it is likely influenced both by the molecule's distribution within the different layers of the core (Redaelli et al. 2019;

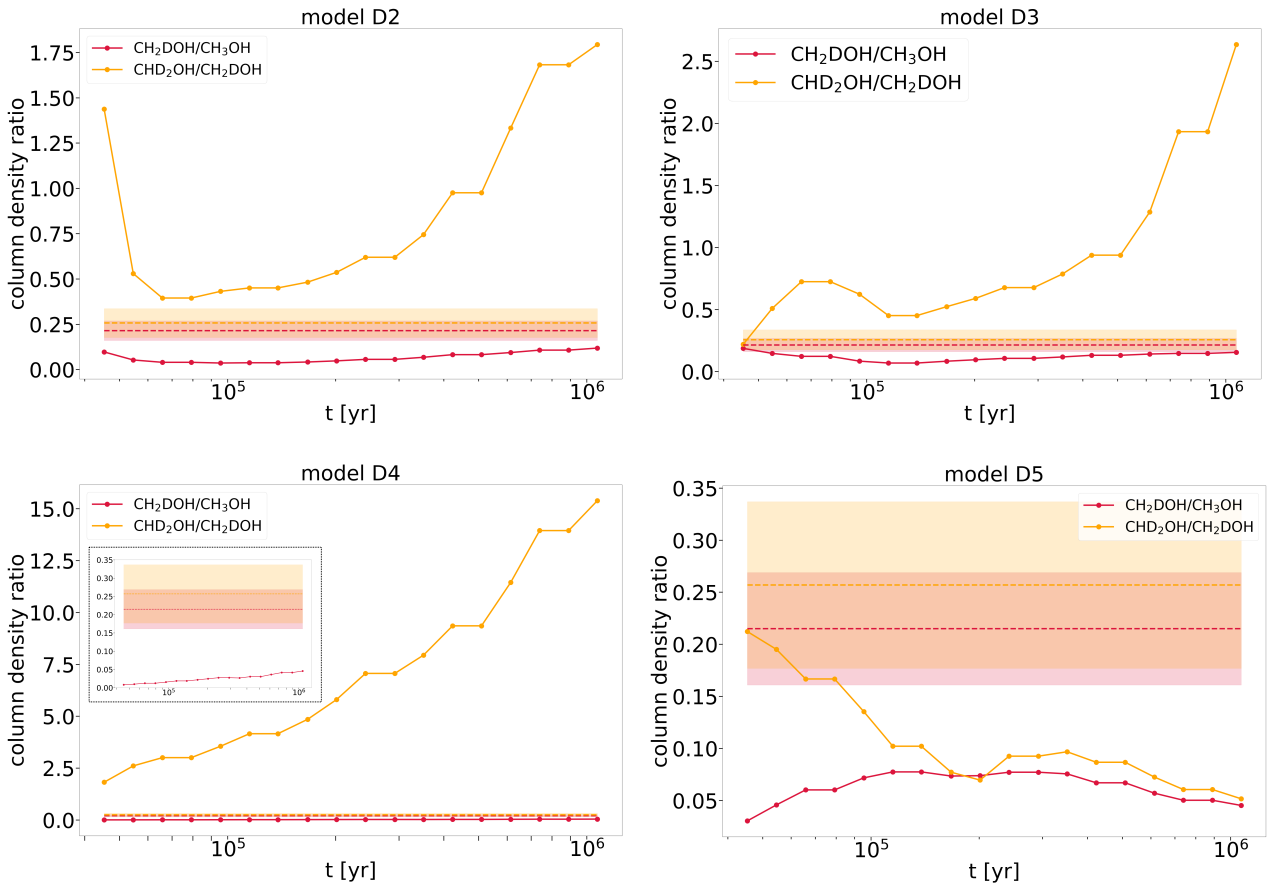

Figure 5.3: Column density ratios for the deuteration of methanol in L1544 computed with four of the models presented in Riedel et al. (2025). The horizontal dashed lines show the result from the observations towards the dust peak of L1544
and the shaded region indicates the error bars of the observed ratios. Models D2 and D3 apply the single collision model proposed by Hasegawa et al. (1992) with either tunnel diffusion (D2) or fast diffusion (D3). Models D4 and D5 apply the reaction-diffusion competition model proposed by Chang et al. (2007). Additionally, D5 allows for H abstraction reactions. For model D4, a zoom-in for low values of column density ratios has been added within the plot.

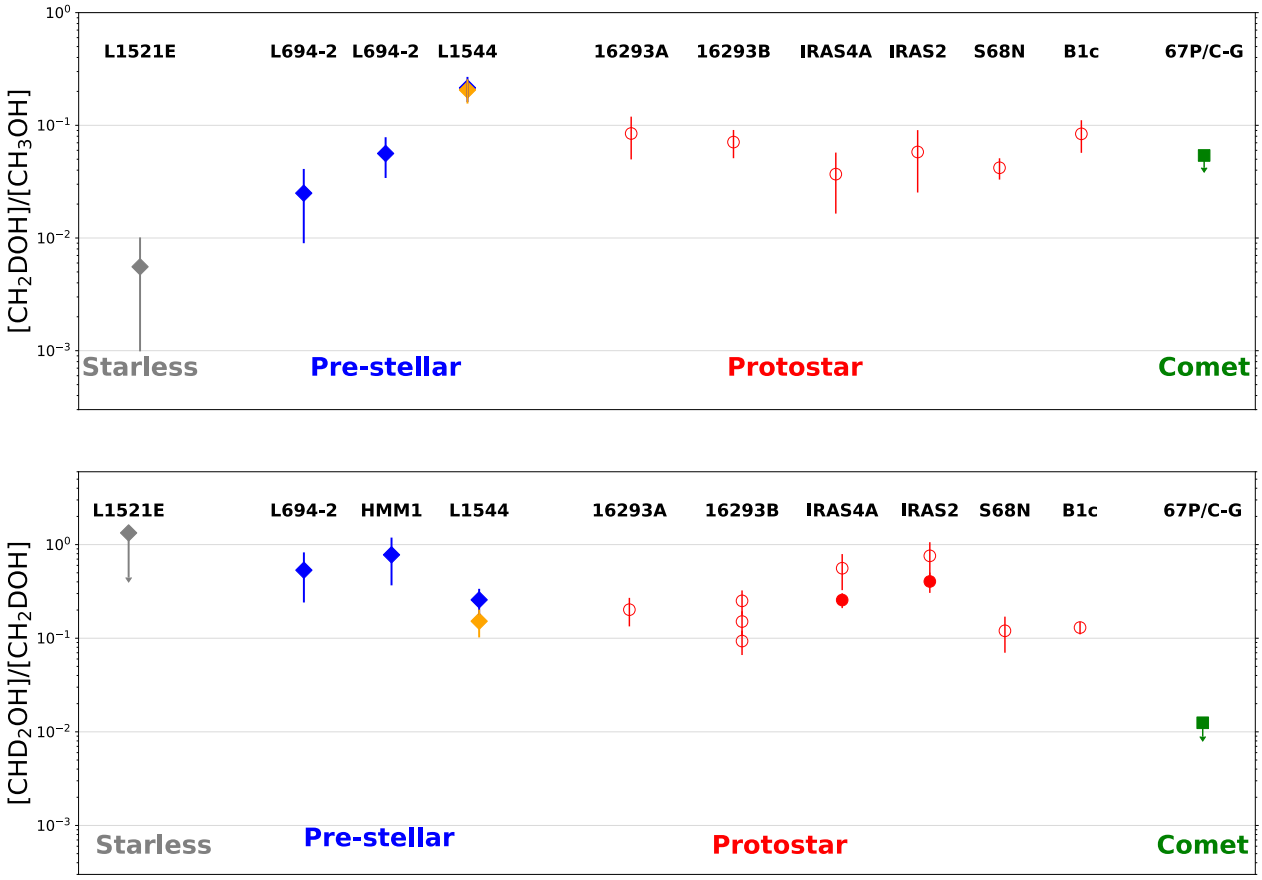

Figure 5.4: The column density ratios of $[CH_2DOH]/[CH_3OH]$ (upper panel) and $[CHD_2OH]/[CH_2DOH]$ (lower panel) as a function of source types, rearranged from Lin et al. (2023a) with L1544 values in the dust (blue) and methanol (orange) peaks (from this work). Filled markers indicate single-dish observations and open markers indicate interferometric observations. The plotted values for L1544 take into consideration T_{ex} variations from 5 to 8 K, and use the CH_3OH column density derived in Lin et al. (2023b) with non-LTE models. The references for S68N and B1c are from van Gelder (2022); for IRAS4A and IRAS2 are Taquet et al. (2019) and Parise et al. (2006); for IRAS16293A and IRAS16293B are Manigand et al. (2019), Jørgensen et al. (2016), Drozdovskaya et al. (2022); for comet 67P/C-G is Drozdovskaya et al. (2021).

Spezzano et al. 2016), as well as by the relevant deuteration processes for each molecule. N_2H^+ has larger levels of deuteration (26%) than c-C_3H_2 (17%) and HCO^+ (3.5%) because it traces best the denser gas in the centre of L1544, where the deuteration is more efficient. The level of deuteration measured in methanol is similar to N_2H^+ even if methanol traces an outer shell of L1544 (Bizzocchi et al. 2014; Vastel et al. 2014; Spezzano et al. 2016), as c-C_3H_2 does. This is indicative of a much more efficient deuteration process taking place in the interstellar ices, where methanol and deuterated methanol are formed, in comparison with the deuteration happening in the gas-phase (e.g. for c-C_3H_2). The deuteration ratio R_D=N(XHD)/N(XH_2) is ∼15% for c-C_3H_2 and ∼20% for methanol, while the R_{D_2}=N(XD_2)/N(XHD) is ∼1% for c-C_3H_2 and ∼25% for methanol, indicating that the second deuteration of methanol, to form CHD_2OH, is also more efficient than the second deuteration of c-C_3H_2, to form c-C_3D_2. Particularly puzzling is the deuteration of H_2CO and H_2CS, whose large R_{D_2} (∼100%) towards the dust peak of L1544. While, unlike methanol, H_2CO and H_2CS can also be formed and deuterated in the gas-phase (e.g. Zahorecz et al. 2021), the large R_{D_2} observed in L1544 cannot be reproduced with chemical models that consider the deuteration on the surface as well as in the gas-phase (Chacón-Tanarro et al. 2019a; Spezzano et al. 2022).

To understand the different deuterium fractions observed in L1544, we use the best models among the ones developed and tested in Riedel et al. (2025) for L1544, as described in Section 5.4, and compared the results against the observed trends. The results, shown in Figure 3 clearly indicate that model D5 is the only one that does not predict very large R_{D_2} ratios that would strongly disagree with our observations. Additionally, model D5 predicts relatively similar values for R_{D_2} and R_D, which is in agreement with our observations. This is a very interesting result because model D5 is the only one that includes the H-abstraction reactions. H-abstraction reactions have been studied in the laboratory (Hidaka et al. 2009; Chuang et al. 2016; Minissale et al. 2016c), and the experimental results showed their importance in the reaction scheme for methanol formation.

Lin et al. (2023a) reported on the first detection of doubly deuterated methanol towards pre-stellar cores and observed deuterium fractions towards L694-2 and HMM-1 that are different than what we observe in L1544. The R_D is 3% in L694-2 and 6% in HMM-1, lower than what we observe for L1544 (20%). On the other hand, R_{D_2} is 50% in L694-2 and 80% in HMM-1, larger than what we observe in L1544 (25%). Figure S1 shows the results of the chemical modelling using model D5 on L694-2 and HMM-1, with the physical structure of the core being the only difference when applying model D5 to the different cores in our sample. It is very interesting to note the effect that the different physical structures of the three cores (L1544, L694-2, and HMM1), shown in Figure S2, have on the predicted ratios. Figure S3 shows the results of the D5 models for the three cores, to facilitate the comparison among them. Additionally, it is worth noticing that the observed R_{D_2} and R_D ratios in L694-2 and HMM1 can also be well reproduced within a factor of 2.

In Figure 4, we have included our results on L1544 to the plots shown in Figure 2 of Lin et al. (2023a). The summary plots in Figure 4 show the values of R_D, and R_{D_2} reported in the literature for starless and pre-stellar cores, protostars, and comets. As already discussed in Lin et al. (2023a), there is a strong observational evidence that the deuteration of methanol is enhanced in dynamically evolved cores, and that the pre-stellar methanol is efficiently inherited

in the protostellar phase. R_{D_2} shows the least variations across the sources in Figure 4 because singly and doubly deuterated methanol are more likely to trace the same gas, while the normal isotopologue is also present in regions of the cores where deuteration is not efficient. A non-LTE analysis for the excitation of CH_3OH was considered for the starless and pre-stellar cores in Figure 4, while for the other objects in Figure 4 the analysis for CH_3OH was done under the assumption of LTE. The differences in R_D that arise from using the LTE vs non-LTE analysis can be significant. In the case of L1544, for example, R_D is 7(2)% assuming LTE (Chacón-Tanarro et al. 2019a, while we derive here a value of 22(6)% using the column density of CH_3OH computed with a non-LTE analysis in Lin et al. (2022). As a consequence, the values shown in Figure 4 for the for the protostars and the comet may differ by a factor of three.

5.6 Conclusions

Isotopic fractionation, and in particular deuteration, is an excellent tool to understand the formation and inheritance of molecules in star-forming regions. Towards the pre-stellar core L1544, methanol exhibits levels of deuteration as large as N_2H^+, highlighting its very efficient deuteration on the icy surface of dust grains.

By comparing our observational results with state-of-the-art chemical models, we are able to gauge the importance of H-abstraction reactions in the formation and deuteration of methanol on the surface of dust grains. Additionally, we have compared the observations of three pre-stellar cores and assessed the large effect that their physical structures have on the deuteration of methanol.

Collisional rate coefficients for deuterated methanol will be necessary to assess non-LTE effects and consequent effects on the column density that we routinely derive in star-forming regions.

Methanol represents the beginning of molecular complexity in star-forming regions, thus a complete understanding of its formation and deuteration is a necessary step to understand the development of further chemical complexity. In this regard, understanding the processes responsible for the very high R_{D_2} measured in H_2CO, an intermediate in the formation of methanol on the surface of dust grains, is of paramount importance.

Chapter 6

Summary and Future Perspectives

In this thesis, I presented three modelling projects (Chapters 2-4) concerning the deuteration of complex organic molecules in the earliest phase of star formation, the pre-stellar core phase. Additionally, I showed collaborative work (Chapter 5) that connects the modelling results with observational constraints. This chapter summarizes the main conclusions of each project and how they relate to each other. Furthermore, I propose several opportunities for further research work.

6.1 Summary of this thesis

In Chapter 2, I introduced an experiment-based reactive desorption mechanism, proposed by Minissale et al. (2016b), into the astrochemical code *pyRate*. The mechanism derives individual reactive desorption efficiencies for every product of a chemical reaction, depending on the reaction enthalpy and type of the underlying surface. I proposed a refinement of the original formula that considers a mass-dependent partitioning of the reaction enthalpy for two-product reactions and removes possible violations of energy conservation. Although this mechanism, in its simpler form, had been incorporated into rate-equation based chemical codes before (e.g. Vasyunin et al. 2017, Wakelam et al. 2021), it had never been applied in combination with a chemical network including deuterium chemistry. I tested several variations both of the chemical and physical model and identified critical chemical and physical parameters, which influence the formation and deuteration of methanol. I found that most variations only had small effects on the CH_3OH and CH_2DOH column density and deuterium fraction profiles. It is, however, essential to use an increased rate of surface diffusion to reproduce the observed order of magnitude of the column densities. To this regard, I tested two options: (i) a slow thermal diffusion process and additional quantum tunneling of hydrogen and deuterium atoms and (ii) a fast thermal diffusion process, resulting from a decrease of the diffusion energy. Both methods are able to increase the methanol column densities by several orders of magnitude to similar levels. Additionally, I found that the inclusion of abstraction reactions, in combination with the experiment-based reactive desorption mechanism, suppresses the deuteration of methanol with respect to the reference model without them. The fiducial model, using tunneling diffusion (option i) and not including

abstraction reactions, produces CH_3OH and CH_2DOH column densities that are roughly an order of magnitude lower than the observed ones, improving the results of the previous model (Chacón-Tanarro et al. 2019a) by a factor of 10. The deuterium fraction is reproduced within a factor of 1.2 for the position of the dust peak and 1.8 for the position of the methanol peak.

In Chapter 3, I incorporated several non-diffusive reaction mechanisms, originally proposed by Jin & Garrod (2020) and Garrod et al. (2022), including Eley-Rideal reactions, photodissociation-induced reactions and three-body reactions. Subsequently, I applied them in the context of methanol formation and deuteration. In this work, I tested two methods for the derivation of reaction probabilities for reactions with an activation energy barrier: (i) the single collision model, originally proposed by Hasegawa et al. (1992), which assumes that the reaction either happens at the first attempt or not at all, and (ii) the reaction-diffusion competition model, proposed by Chang et al. (2007), which considers that reactants are staying in close proximity for an extended period of time, hence having multiple attempts to react with each other. The former model is the one used for the work presented in Chapter 2. I found that the latter model removes the necessity to assume an increased diffusion rate to reproduce the observed column densities, as the higher reaction probabilities compensate for a lower meeting rate. I performed simulations with various combinations of the non-diffusive reaction mechanisms for both models and found that they provide only small contributions to methanol formation and deuteration. In an additional model, I included the methanol forming reaction $H_2CO + CH_3O \rightarrow CH_3OH + HCO$, investigated both theoretically by use of a microscopic kinetic Monte Carlo code (Simons et al. 2020) and experimentally (Santos et al. 2022), and determined to have a high contribution to methanol formation of 60%-90%. In contrast to these works, I found the contribution of this reaction to be negligible, due to a low occurrence rate of H_2CO and CH_3O being produced in close proximity to the other reactant. Additionally, I investigated the effect of H-abstractions reactions in the framework of the reaction-diffusion competition model with purely diffusive models. I found that, the inclusion of H-abstraction reactions, combined with a constant reactive desorption efficiency, both increases the gas phase column densities of CH_3OH and CH_2DOH, due to cyclic H-abstraction events, and the $N(CH_2DOH)/N(CH_3OH)$ ratio, due to preferential abstraction of CH_2DOH to CH_2DO and CHDOH. The latter effect is minimized/reversed when the inclusion of H-abstraction reactions is paired with the experiment-based reactive desorption mechanism developed in Chapter 2, as the formation reactions of CH_2DOH have partially lower reactive desorption efficiencies than the formation reactions of CH_3OH.

In Chapter 4, I extended the chemical network from species with up to seven atoms to nine atoms, facilitating the study of formation and deuteration of larger COMs. In this work, I focused on acetaldehyde (CH_3CHO), methyl formate (CH_3OCHO) and glycoaldehyde (CH_2OHCHO), as they are chemically closely related to methanol. I found that non-diffusive reaction mechanisms increase the column densities for all investigated molecules to a varying degree. While the column density increases for methanol are only small, the other COMs exhibit column density increases of several orders of magnitude, with the largest obtained when applying three-body reactions. Therefore, I conclude that three-body reactions need to be considered to reproduce the observed column densities for the larger O-bearing COMs. The fully deuterated and partially spin-separated chemical network I developed in this work is extremely large. Hence, I tested several approaches to manage the computational cost: (i) restriction of the deuteration degree to

singly and doubly deuterated species and (ii) reducing the amount of reactions in the grain surface network. Unfortunately, I found that performing a simulation including three-body reaction and using option (i) takes more than 2 months and is therefore unfeasible for the first stages of test. Therefore, I employed option (ii) and performed a simulation including three-body reactions, which takes around 22 days to complete. I found that the modelled column densities of the main isotopologues reproduce the observational column densities (Spezzano et al. 2025, Jiménez-Serra et al. 2016) within a factor of 2. The modelled column density ratios $N/N_{\rm main}$ of the deuterated isotopologue with respect to the main isotopologue are up to a factor of 4.8 higher than the observed values.

Chapter 5 includes an observational project conducted by Silvia Spezzano, which was accompanied by the comparison with models I developed in the context of the work presented in Riedel et al. (2025) (Chapter 3). The paper reports the first detection of the doubly deuterated methanol isotopologue CHD_2OH in the pre-stellar core L1544 and derives the resulting N(CH_2DOH)/N(CH_3OH) and N(CHD_2OH)/N(CH_2DOH) ratios. My contribution in this work comprises the supply of modelling predictions for CH_3OH, CH_2DOH and CHD_2OH for L1544 for four different models, tested in Chapter 3. With that, we found that the inclusion of H-abstraction reactions into the methanol formation and deuteration scheme is necessary to derive reasonable values for the N(CHD_2OH)/N(CH_2DOH) ratios. Additionally, I computed models for the pre-stellar cores HMM1 and L694-2, and showed that the models can reproduce the observed trends between different sources within a factor of two.

6.2 Future work

The work presented in this thesis adds to the current knowledge about the processes of formation and deuteration of O-bearing COMs in the pre-stellar core phase. Additionally, the development of the reaction mechanisms presented in Chapters 2 - 5 opens up new pathways for further research. In the following, I discuss several prospective research projects that represent valuable additions to the current models presented in this thesis:

1. As seen in Spezzano et al. (2025) (included in Chapter 5 of this thesis), the detection of previously unobserved deuterated isotopologues of COMs, especially in the same object, provides valuable constraints on the properties of the models and could be used to rule out parameter regimes for various physical and chemical quantities, such as the importance of abstraction reactions or the non-thermal desorption processes ongoing in the extremely low temperatures of pre-stellar cores. Some attainable candidates include CH_3OD, which was very recently detected for the first time towards the pre-stellar cores L1448 and tentatively towards B213-C6 (Kulterer et al. 2025) and the singly deuterated isotopologues of acetaldehyde CH_2DCHO and CH_3CDO, for which at least the main isotopologue has been shown to exist in high abundances towards several pre-stellar cores in the Taurus and Perseus molecular cloud (Jiménez-Serra et al. 2016, Scibelli & Shirley 2020, Scibelli et al. 2024).

2. In addition to various model predictions for the doubly deuterated methanol isotopologue

CHD_2OH in L1544, Spezzano et al. (2025) also included model predictions for the pre-stellar cores HMM1 and L694-2. Extending the amount of modelled cores allows for a dedicated comparison of the influence of physical conditions on the formation and deuteration of COMs. This effort could be aided by the growing number of of observations of deuterated methanol isotopologues in the pre-stellar core phase (e.g. van Gelder 2022, Lin et al. 2023a, Spezzano et al. 2025, Steffes et al. in prep.). Moreover, it would be valuable to expand the modelling efforts also to the protostellar stage, as currently most of observational constraints were obtained in this stage of star formation and there is evidence of partial reprocessing of the molecular content. For that, it is necessary to add a warm-up phase to the physical model. This addition might further promote the formation of COMs on the surface, as diffusion processes of heavy reactants become more efficient for temperatures ≥ 30 K. Once the temperatures are high enough (around 120 K), the molecular content of the mantle phase sublimates in its entirety into the gas phase and the molecules, stored in different mantle layers, mix again.

3. The physical model (Keto & Caselli 2010) used in all of the works included in this thesis is a static, one-dimensional model, meaning that the necessary physical quantities, as e.g. the H_2 density $n(H_2)$, the gas temperature T_{gas}, the dust temperature T_{dust} and the visual extinction A_V, are only dependent on radius, but not on polar and azimuthal angle or on time. Clearly, this physical model only roughly reflects the currently observable quantities along one axis of the core. Reducing the complexity of the physical models, however, was a necessary simplification, making the exploration of an extended parameter space (as done in Chapter 2) or the development of computationally demanding reaction mechanisms (as done in Chapters 3 and 4) possible.

   An obvious prospective project towards a more realistic model is the introduction of time-dependent physical conditions. This could be done in a step-by-step approach, gradually increasing the complexity of the physical model, while monitoring the computation cost and developing new strategies to handle the increasing computational demand. Possible intermediate steps include the use of a spherical free-fall collapse treatment (Brown et al. 1988, Rawlings et al. 1992), as used in many other recent modelling works (e.g. Jin & Garrod 2020, Garrod et al. 2022, Jiménez-Serra et al. 2025). Another increase in complexity includes the use of a hydrodynamic collapse model, as already done for L1544 for simpler molecules (Sipilä et al. 2018, 2022, 2024) that is either chemically processed on the fly or in a post-processing step. Here, the use of the pre-compilation option introduced in Chapter 4 is likely able to procure significant savings regarding the required computational cost as compared to previous works.

4. The inclusion of non-diffusive reaction mechanisms into *pyRate* facilitates other modelling projects that cannot be reproduced with purely diffusive models. Particular examples already on-going include: (i) the simulation of laboratory experiments involving the UV-photon irradiation of CS_2 bearing ices (Martín-Doménech et al. 2024), with particular emphasis on the formation pathways of OCS (Sipilä et al. in prep.) and (ii) the use of astrochemical models to simulate reactivity experiments on ices (Sokolova, Husquinet et

al. in prep.).

5. The current formulation of non-diffusive reactions mechanisms (Jin & Garrod 2020, Garrod et al. 2022) into rate-equation based chemical codes has been criticized, due to the codes' inability to account for the exact position of each molecule at all times. Hence, the amount of suitable reaction partners being formed close to each other, could be overestimated in case only small numbers of the respective species are present on the grain surface. Devising a correction of the equations taking this effect into account would be desirable and could likely be easily added to the existing implementation.

6. Alternative methods to increase the formation of COMs in the pre-stellar core stage, that do not rely on non-diffusive reaction mechanisms, have been proposed in recent years. A particular interesting proposal is presented in Molpeceres et al. (2024), where the authors suggest that a high CO surface coverage could promote the diffusion process of several important surface radicals even at 10 K, due to lower intermolecular forces between CO molecules and the adsorbed molecules as compared to water ice. The proposed formulation of the mechanisms can be easily incorporated into a rate-equation based code. Hence, it would be a valuable addition to *pyRate*, which would facilitate a direct comparison of this modified diffusion process with non-diffusive reaction mechanisms and their possible competition effects.

In conclusion, the work of this thesis paves the way to modelling the deuteration of increasingly complex pre-biotic species, which is of particular interest in combination with the upcoming generation of telescope facilities, providing high sensitivity at the centimeter and millimeter wavelenghts (e.g. ngVLA, ALMA WSU and SKA Low).

Appendix A

Complementary Material for Chapter 2

A.1 Formation enthalpies and binding energies

In Table A.1 we present the formation enthalpies H_{form} and binding energies E_b for all species involved in exothermic surface reactions, to which we applied the newly developed reactive desorption mechanism laid out in Section 2.2.1.

Table A.1: Formation enthalpies, H_{form}, and binding energies, E_b.

Species	H_{form} [kJ mol^{-1}]	E_b [K]	Species	H_{form} [kJ mol^{-1}]	E_b [K]	Species	H_{form} [kJ mol^{-1}]	E_b [K]	Species	H_{form} [kJ mol^{-1}]	E_b [K]
C	716.70	800.0	O_2	0.00	1000.0	HCN	135.10	2050.0	NaH	124.27[a]	12250.0
CH	594.10	925.0	O_2H	2.10	3650.0	HNC	135.10	2050.0	PH	253.55[a]	5000.0
CH_2	386.40	1050.0	O_3	142.70	1800.0	HCO	43.50	1600.0	PH_2	125.94[a]	5000.0
CH_3	145.70	1175.0	OCN	159.40	2400.0	HCS	296.20	2350.0	PH_2	125.94[a]	5000.0
CH_3O	17.00	3800.0	OCS	138.40	2888.0	HNO	99.60	2050.0	SiH	376.66[a]	3150.0
CH_2OH	-9.00	5084.0	OH	39.00	2850.0	HS	139.30	1450.0	SiH_4	34.31[a]	4500.0
CH_3OH	-201.20	5534.0	OD	36.60[a]	2850.0	DS*	138.49[a]	1450.0	NS	263.59[a]	1900.0
CH_4	-74.90	1300.0	S	277.00	1100.0	N	472.70	800.0	CCO	286.60[a]	1950.0
CN	435.10	1600.0	SO	5.00	2600.0	N_2	0.00	1000.0	C_4H	775.02[b]	3737.0
CO	-110.50	1150.0	SO_2	-296.80	3405.0	N_2H	245.20	1450.0	C_6	1261.02[b]	4800.0
CO_2	-393.50	2575.0	C_2	837.74	1600.0	N_2H_2	213.00	4756.0	C_6H	991.80[b]	5337.0
CS	280.30	1900.0	CCH	476.98	2137.0	N_2D_2	207.11[a]	4756.0	C_7	1309.34[b]	5600.0
H	218.00	450.0	C_2H_2	226.73	2587.0	NH	376.60	2378.0	l-C_3H	714.09[b]	2937.0
D*	221.72[a]	450.0	C_3	820.06[a]	2400.0	ND*	375.31[a]	2378.0	c-C_3H	714.09[b]	2937.0
H_2	0.0	500.0	C_4	970.69[a]	3200.0	NH_2	190.40	3956.0	C_5H_2	690.36[b]	4987.0
HD*	0.32[a]	500.0	C_5	979.06[a]	4000.0	$ND_2^\star$	185.35[a]	3956.0	H_2CN	242.23[b]	2400.0
H_2CO	-115.90	2050.0	C_2H_3	299.00[a]	3037.0	NH_2CHO	-186.00	5556.0	l-C_3H_2	650.36[b]	3387.0
H_2O	-241.80	5700.0	C_4H_2	464.00[a]	4187.0	NH_3	-45.90	5534.0	c-C_3H_2	477.96[b]	3387.0
HDO*	-245.37[a]	5700.0	C_2H_4	52.40[a]	3487.0	$ND_3^\star$	-58.58[a]	5534.0	C_4H_3	545.65[b]	4637.0
$D_2O^\star$	-249.20[a]	5700.0	C_2H_5	119.00[a]	3937.0	NO	90.30	1600.0	SiH_2	275.00[b]	3600.0
H_2O_2	-135.80	5700.0	HC_3N	354.00[a]	4580.0	NO_2	33.10	2400.0	SiH_3	204.09[b]	4050.0
H_2S	-20.5	2743.0	H_2CS	118.00[a]	2700.0	O	249.20	1390.0	HOOH	-129.89[b]	5700.0
$D_2S^\star$	-23.89[a]	2743.0	MgH	169.03[a]	5750.0						

Notes. Species marked with a star (*) are newly added formation enthalpies for deuterated isotopologues. If not stated otherwise the formation enthalpies are adopted from Du et al. (2012). The values marked with [a] are adopted from the NIST Chemistry WebBook[1] and the ones marked with [b] are from the Kinetic Database for Astrochemistry[2]. The binding energies are taken from Semenov et al. (2010). (1) https://webbook.nist.gov/chemistry (2) https://kida.astrochem-tools.org

A.2 Applied reaction scheme for CH_3OH and deuterated variants

Figure A.1 depicts the reaction scheme for the formation of methanol that we employed for all the presented models.

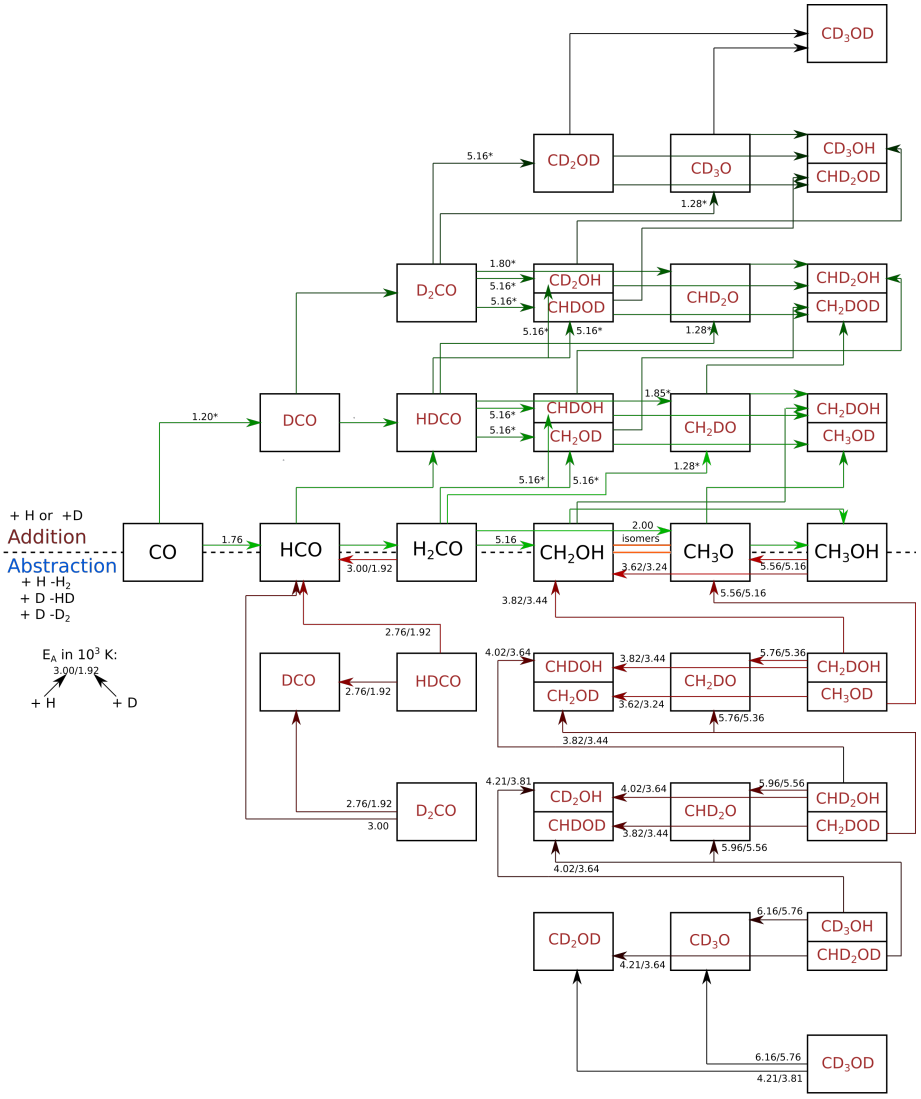

Figure A.1: Reaction scheme for the formation of CH_3OH and its deuterated isotopologues. The upper half shows the applied 'forward reactions' (addition reactions), either adding H (in the horizontal direction) or D (in the vertical direction). The lower half shows the employed 'backward reactions' (abstraction reactions), reacting with H or D and thereby removing a H_2, HD, or D_2 molecule. The values on top of the arrows indicate, if existing, the activation energies, E_A, in 10^3 K. There are always two values for the abstraction reactions. The first one gives the value for the reaction with H, the second for the reaction with D. Note that our reaction scheme also includes two 'substitution reactions', exchanging one D atom for a H atom in H_2CO and HDCO, which are not shown here for the sake of clarity.

A.3 Column density and deuterium fraction profiles

Figures A.2 and A.3 respectively show the modelled column density and deuterium fraction profiles of the models with only small effects. We present the models 1D-9 (decreased activation energy for deuterated isotopologues), 1D-10 (individual formation enthalpies for deuterated isotopologues), 1D-11 (decrease in the gas temperature) and 1D-13 (refinement of cosmic-ray desorption mechanism).

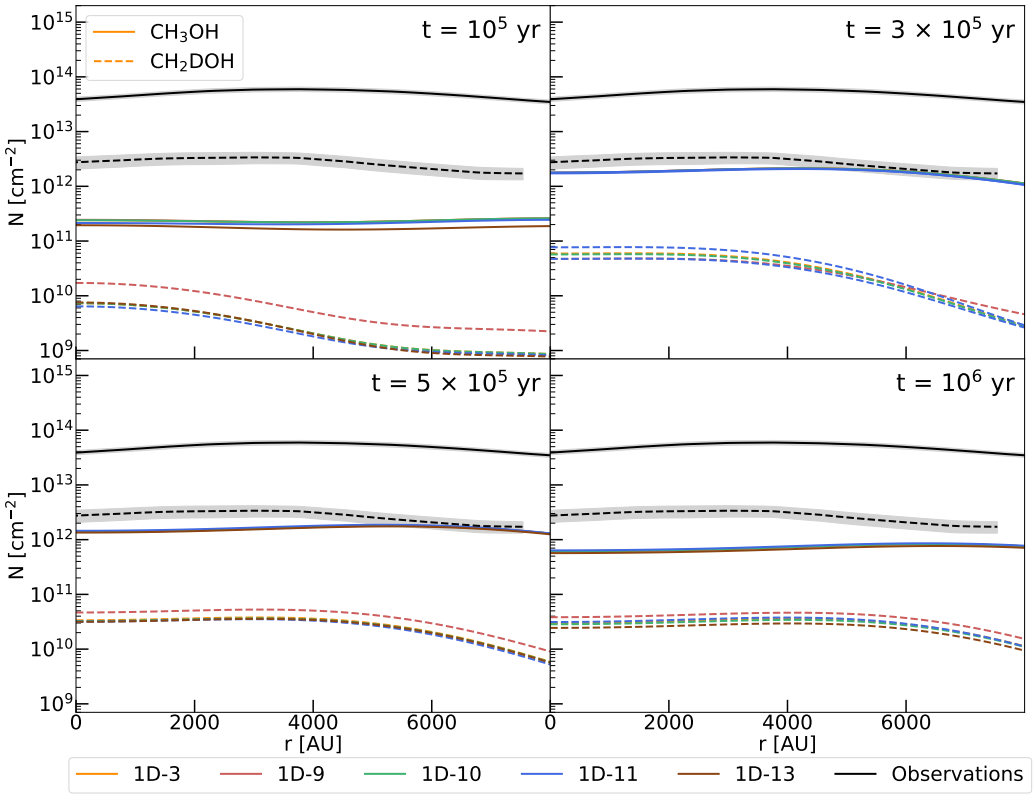

Figure A.2: Modelled column density profiles of non-deuterated methanol (CH_3OH) and singly deuterated methanol (CH_2DOH) for several models at four different time steps ranging from 10^5yr to 10^6yr. The black lines show the observed profiles (errors as grey-shaded areas). The solid lines indicate the CH_3OH column densities, and the dashed lines indicate the CH_2DOH column densities.

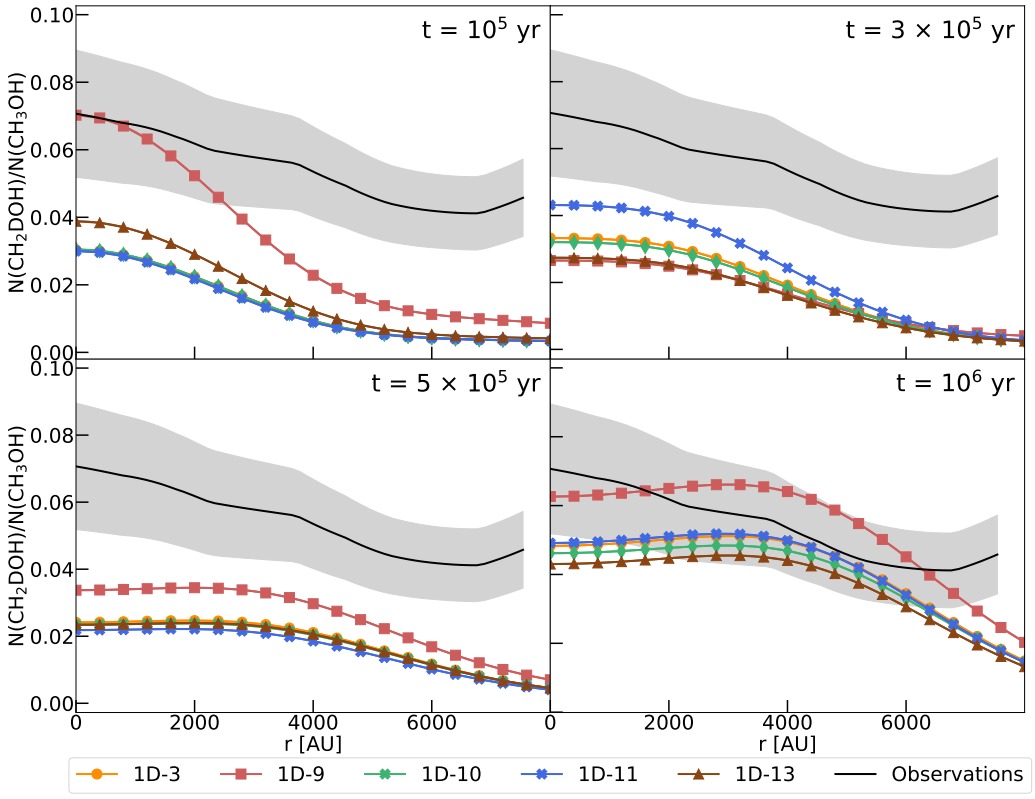

Figure A.3: Modelled ratio between singly deuterated methanol (CH_2DOH) and non-deuterated methanol (CH_3OH) for several models at four different time steps ranging from 10^5yr to 10^6yr. The black line shows the observed ratio (errors as grey-shaded areas).

Appendix B

Complementary Material for Chapter 3

B.1 Scaling the H_2 binding energies

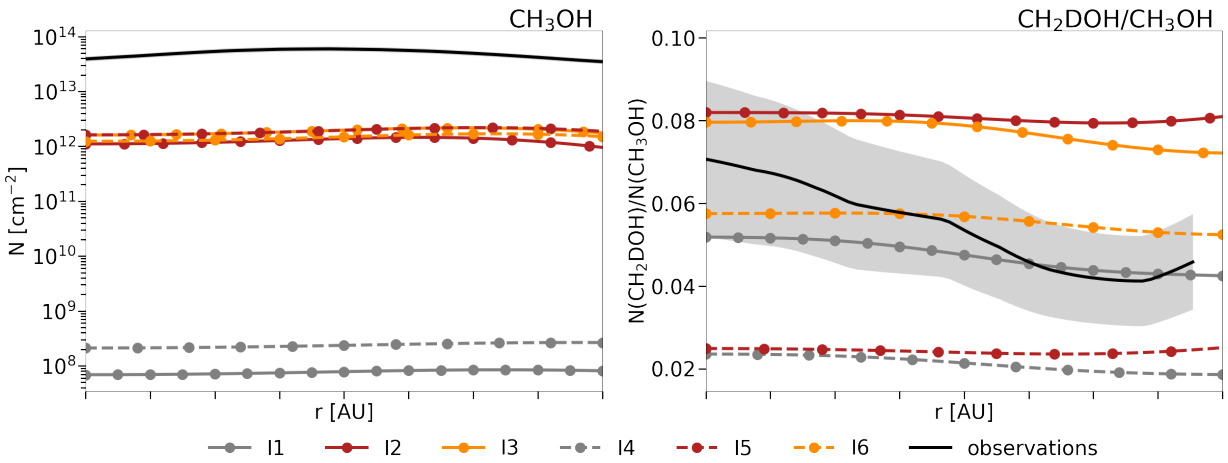

Figure B.1: Modelled column density profiles. Comparison of the main models presented in Riedel et al. (2023) (solid lines) with a respective version of those models with a scaling factor of 0.1 applied to the binding energy of H_2 and its deuterated isotopologues (dashed lines). The results are presented for the best-fit time of $t = 3.0 \times 10^5$ yr. The observed profiles, presented first in Chacón-Tanarro et al. (2019a), are depicted in black (errors as grey-shaded areas).

An important aim of this work is to ensure comparability of the models presented in this work to our previous work (Riedel et al. 2023). Therefore, we decided to introduce all modifications in a step-by-step manner and also present the results of all intermediate steps to enable the reader to follow each modification and its effects. The models, presented in Riedel et al. (2023) were performed by applying a single collision model (Hasegawa et al. 1992) for the derivation of reaction probabilities of reactions with an activation-energy barrier. It was found that a model with only a slow thermal hopping process ($E_d/E_b = 0.55$, model I1) is not able to reproduce the observed methanol column densities, as it underproduces them by several orders of magnitude.

Instead, it proved necessary to introduce a highly efficient diffusion process for H (and D) atoms to ensure that the reactants 'meet' often enough to lead to a sufficient amount of successful reactions. We tested two different options: (I) a model, using a slow thermal hopping process (E_d/E_b = 0.55) accompanied by diffusion by quantum tunneling of H and D atoms (model I2) and (II) a model, using a fast thermal hopping process (E_d/E_b = 0.2; model I3). Since we test each of those models - with slightly different parameters - in this work again, we used them as a starting point for our modifications.

To get models that include the Eley-Rideal mechanism to work, we needed to reduce the amount of H_2 built up on the surface of dust grains. For that purpose, we adopted the scaling of the binding energies of H_2 and its deuterated isotopologues by a factor of 0.1. In Figure B.1, we present the column density profiles of CH_3OH (left) and N(CH_2DOH)/N(CH_3OH) profiles (right) of the most important models (I1, I2, I3) as presented in Riedel et al. (2023) and with scaled H_2 binding energies (I4, I5, I6). The CH_3OH column density of models I4, I5 and I6 is only varied within a factor of less than two compared to the models without the scaling of H_2 binding energies. The N(CH_2DOH)/N(CH_3OH) ratio, however, is decreased by a factor of two to four, depending on the type of diffusion applied to H and D atoms. We find that models I1, I2 and I3 present a larger D/H ratio on the grain surface for the time interval most relevant for the production of CH_3OH and CH_2DOH. Atomic hydrogen (and deuterium) on the surface of the dust grain is formed either by absorption from the gas phase or by surface reactions involving H_2 or its deuterated isotopologues (e.g. $H_2 + OH \rightarrow H_2O + H$, $H_2+CH_2 \rightarrow CH_3 + H$). Naturally, the removal of large quantities of surface H_2 in models I4, I5 and I6 is reducing the importance of the second pathway. Instead, proportionally more of the available surface H and D atoms are absorbed from the gas phase with a typically significantly lower D/H ratio than the one on the grain surface.

B.2 Switching to a simpler reactive desorption mechanism

In Riedel et al. (2023), we adopted an experiment-based reactive desorption mechanism following the semi-empirical equation suggested in Minissale et al. (2016b). It derives an individual reactive desorption efficiency for every product species in a reaction, that depends on the reaction enthalpy and underlying surface. Similar versions of this mechanism were also added in several other works (e.g. Vasyunin et al. 2017, Wakelam et al. 2021). The largest difference to those works is the treatment of multi-product reactions. The method used in Riedel et al. (2023), and partially in this work, also includes a recipe for the mass-dependent partitioning of the total reaction enthalpy in the case of a two-product reaction. However, since most other works use a constant reactive desorption efficiency for every reaction and independent of the surface coverage, we chose, for the sake of comparability to the literature, to switch to this simpler version of reactive desorption. In most models of this work, we adopted a reactive desorption efficiency of 1%.

Figure B.2 presents the column density profiles of CH_3OH (left) and N(CH_2DOH)/N(CH_3OH) profiles (right) of the most important models (I4, I5, I6) presented in Riedel et al. (2023), with scaled H_2 binding energies (see Appendix B.1) and the experiment-based reactive desorption

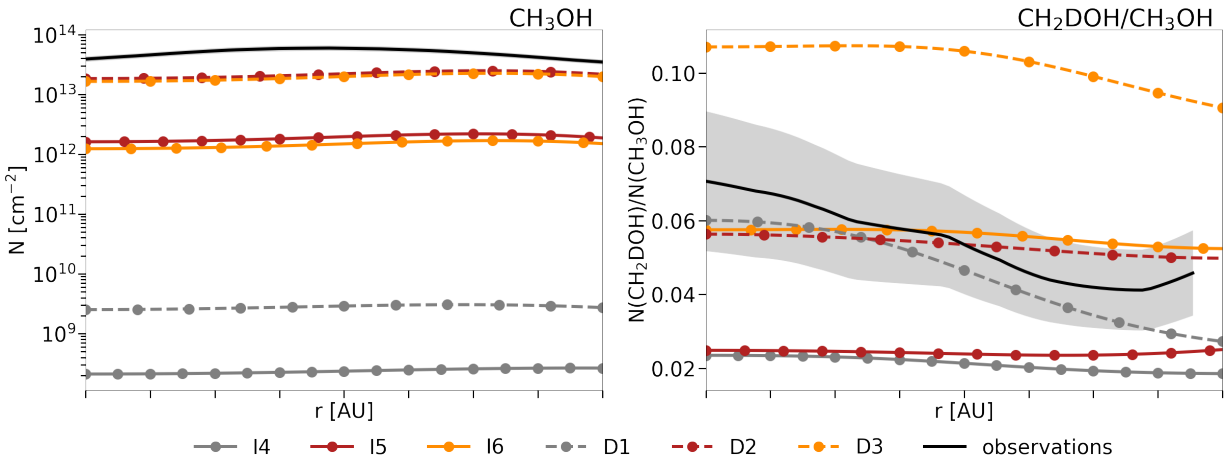

Figure B.2: Modelled column density profiles. Comparison of the models presented in Appendix B.1 (solid lines) with a respective version of those models with a reactive desorption efficiency of 1% independent of reaction and surface coverage (dashed lines). The results are presented for the best-fit time of $t = 3.0 \times 10^5$ yr. The observed profiles, presented first in Chacón-Tanarro et al. (2019a), are depicted in black (errors as grey-shaded areas).

mechanism, and the same models with a constant 1% reactive desorption efficiency (models D1,D2 and D3). The CH_3OH column density of models D1, D2, and D3, using a constant 1% reactive desorption efficiency, is increased by roughly an order of magnitude in comparison to models I4, I5 and I6, using the experiment-based reactive desorption mechanism. The increase is caused by the comparably low reactive desorption efficiencies of the experiment-based reactive desorption mechanism for heavier products. When applying the SC model, CH_3OH is predominantly produced by $CH_3O+H \rightarrow CH_3OH$, which has a reactive desorption efficiency of only 0.08% on a pure CO surface, given the reaction enthalpies and binding energies adopted in this work. Additionally, the $N(CH_2DOH)/N(CH_3OH)$ ratio is increased slightly when switching from models I4, I5, and I6 to models D1, D2, and D3, as the formation reactions of CH_2DOH partially have lower reactive desorption efficiencies than the one leading to CH_3OH ($CH_2DO+H \rightarrow CH_2DOH$: 0.08%; $CHDOH+H \rightarrow CH_2DOH$: 0.05%, and $CH_2OH+D \rightarrow CH_2DOH$: 0.05% on a pure CO surface). Consequently, the higher the relative reaction rates of reactions $CHDOH+H \rightarrow CH_2DOH$ and $CH_2OH+D \rightarrow CH_2DOH$ as compared to $CH_2DO+H \rightarrow CH_2DOH$, the lower the $N(CH_2DOH)/N(CH_3OH)$ ratio.

Appendix C

Complementary Material for Chapter 5

C.1 On the spectroscopy and catalogs of deuterated methanol

The internal rotation of the asymmetric methyl group in the isotopologues of methanol with deuterium in the methyl group leads to complex spectral patterns that require complex analysis. As a consequence, particular care needs to be taken when using data from online catalogs as approximate methods used to produce the catalog might have effects on the interpretation of astronomical data. In the JPL catalog, the rest frequencies of CH_2DOH transitions that are energetically favorable to observe in cold sources like starless and pre-stellar cores have errors in the order of ∼100 kHz with respect to the measured frequencies reported in the supplementary material of Coudert et al. (2014). Such small deviations are significant in cold sources because of the characteristic small line-widths and might induce significant error in the velocity of the line or even misidentification. We therefore suggest to refer to the rest frequencies reported in the spectroscopy papers and compare them to the catalogs, especially in cases of doubts on the interpretation of the astronomical data. The complexity of the rotational ladder also translates into potential errors when extrapolating the values of their partition functions at temperatures not listed in the online catalogs. We therefore list in Table C.1 the partition functions Q(T) for CH_2DOH and CHD_2OH in a large range of temperatures, including temperatures relevant for cold sources like starless and pre-stellar cores. The values reported in Table C.1 have been computed using all torsional levels up to 1700 cm^{-1} for CH_2DOH and 2000 cm^{-1} for CHD_2OH. We note that the partition function reported in Table C.1 for CH_2DOH is very close to the values currently listed in the JPL catalog, despite the catalog only listing transitions from the ground torsional state based on Pearson (2012). It is plausible that a correction factor has been used to correct the partition functions listed in the JPL catalog (Drouin, priv. comm.). This warrants a re-evaluation of the column densities derived with the JPL partition function that used a correction factor (e.g. Jørgensen et al. 2018).

Table C.1: Partition function, Q(T), of CH_2DOH and CHD_2OH

T(K)	CH_2DOH	CHD_2OH
300	16753.496	19331.489
225	9506.242	11256.666
150	4385.771	5255.582
75.0	1294.257	1563.391
37.5	398.999	490.483
18.75	114.589	145.295
9.375	30.388	39.851
8.0	22.447	29.521
6.5	15.210	20.009
5.0	9.603	12.412

Table C.2: Overview of the four models from Riedel et al. (2025) used in this work.

Model	RD[a] efficiency	H_2 removal[b]	other modifications
D2*	1%	scaled E_b	tunnel diffusion
D3*	1%	scaled E_b	fast diffusion
D4†	1%	scaled E_b	
D5†	1%	scaled E_b	H-abstraction reac.

Note: * Models that apply the single collision model proposed by Hasegawa et al. (1992) to derive the reaction probabilities. † Models that apply the reaction-diffusion competition model proposed by Chang et al. (2007) to derive the reaction probabilites. [a] Efficiency of the reactive desorption. [b] To avoid unphysical build-up of H_2 (and its deuterated isotopologues) on the surface, their binding energies have been scaled by a factor of 0.1 (Riedel et al. 2025).

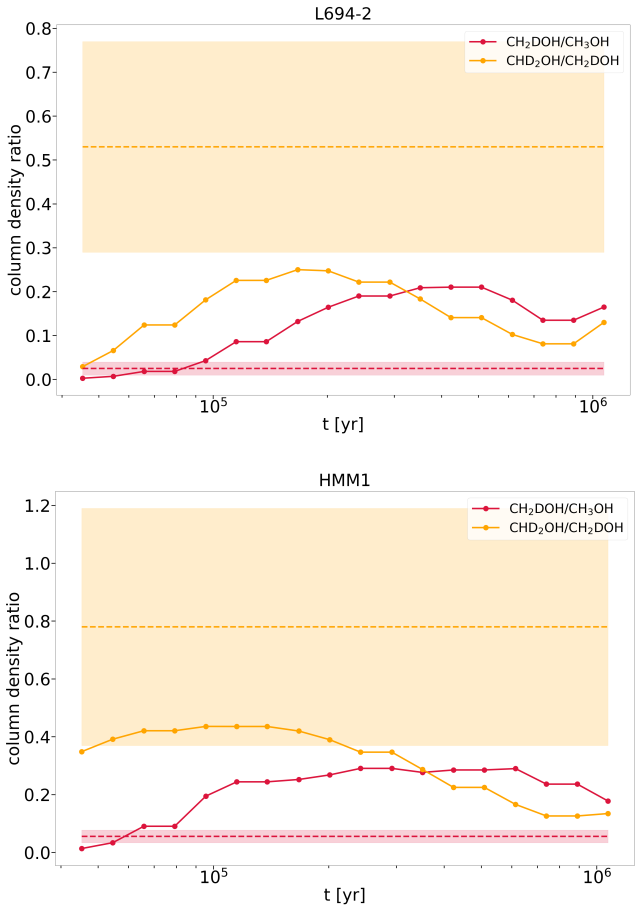

Figure C.1: Results from the best model (D5) from Riedel et al. (2025) for the pre-stellar cores L694-2 and HMM-1. The horizontal dashed lines show the result from the observations and the shaded region indicates the error bars of the observed ratio (Lin et al. 2023a).

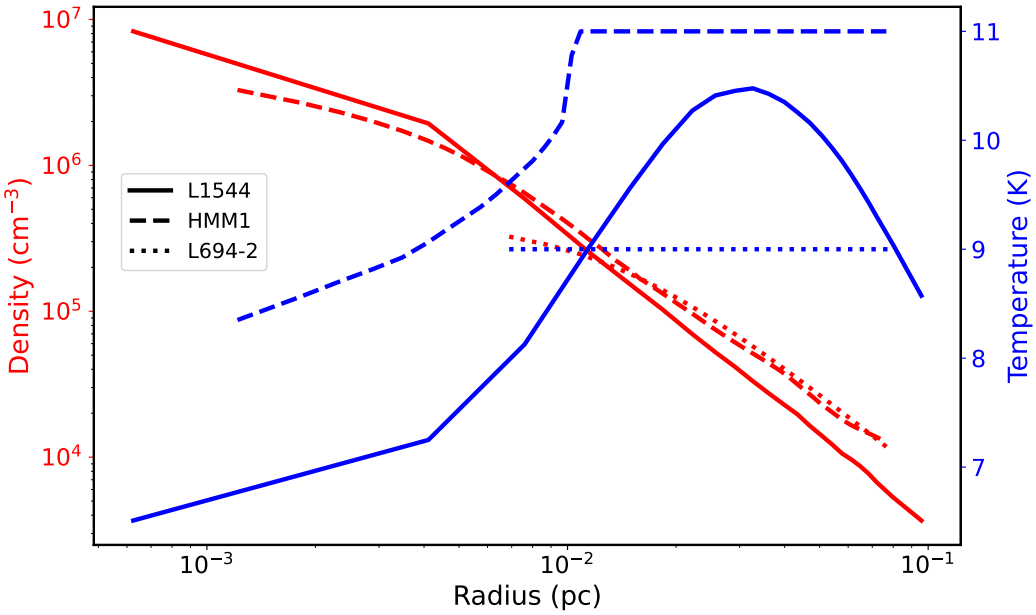

Figure C.2: Physical structures of L1544 (Keto et al. (2015)), HMM1 (Pineda et al. 2022; Harju et al. 2024), and L694-2 (Lin et al. (2023b)) used for the chemical models.

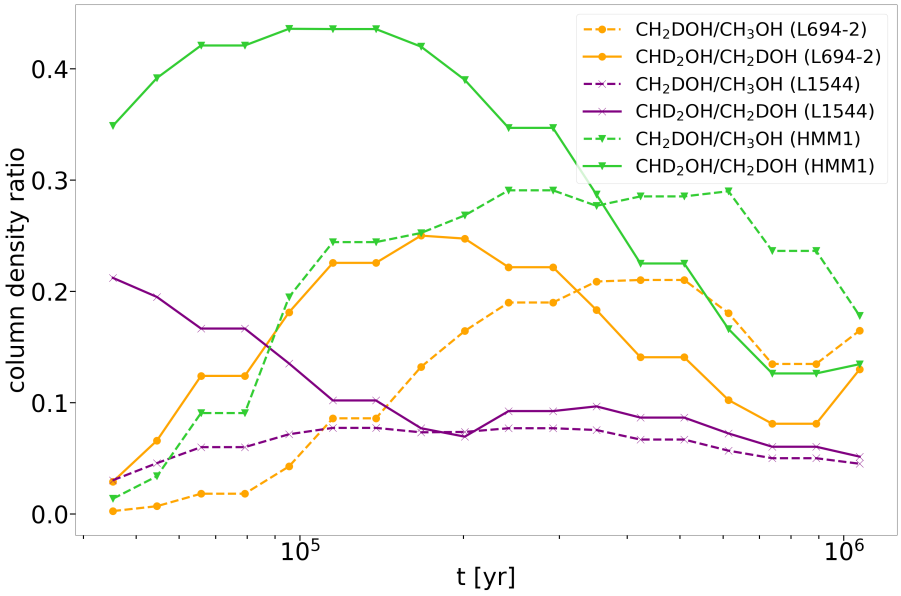

Figure C.3: R_D and R_{D_2} for methanol predicted by the model D5 from Riedel et al. (2025) using the physical structures of L1544 (Keto et al. 2015, HMM1 (Pineda et al. 2022; Harju et al. 2024), and L694-2 (Lin et al. 2023b).

C.2 Dependence of deuteration on physical conditions

The dependence of the modelled R_D and R_{D_2} on the physical properties, mainly the H_2 density and temperature, is a complicated multidimensional problem and a detailed exploration is beyond the scope of this paper.

The fractionation of the deuterium in the gas phase is most efficient in the cold and dense center of the pre-stellar core. H and D atoms are directly adsorbed onto the surface of dust grains from the gas phase, where the atomic D/H ratio is enhanced. However, an increased atomic D/H ratio on the grain by itself does not guarantee, that the deuterium atoms are able to meet their reaction partners successfully. This also depends on the efficiency of the diffusion process, that is dictated by the employed mode of diffusion and the grain temperature. In general, higher grain temperatures allow for a faster diffusion process and a higher reaction rate of potential reaction partners.

To shed some light into the density and temperature dependence, we have run a grid of static 0D simulations (see Figure C.4 and C.5). The H_2 densities range from $3 \times 10^6\,\mathrm{cm}^{-3}$ to $9 \times 10^6\,\mathrm{cm}^{-3}$. The gas and grain temperatures are set to the same value and range from 6.0 K to 9.0 K. The selected range is an appropriate parameter range for the dust peak of the three pre-stellar cores (L1544, HMM1 and L694-2) investigated. This is where the highest levels of deuteration are expected to occur. All other parameters remain constant between individual runs.

We conclude that both H_2 density and temperature affect the R_D and R_{D_2}. The highest R_D and R_{D_2} ratios are determined for high densities $n(H_2) = 9 \times 10^6\,\mathrm{cm}^{-3}$, where fast gas phase reactions promote an efficient fractionation process and short freeze-out timescales quickly deliver the atomic R_D to the grain's surface, and high $T_{\mathrm{grain}} = 9\,\mathrm{K}$ speed up the diffusion process. We also note that partially similar R_D and R_{D_2} can be obtained by multiple parameter pairings.

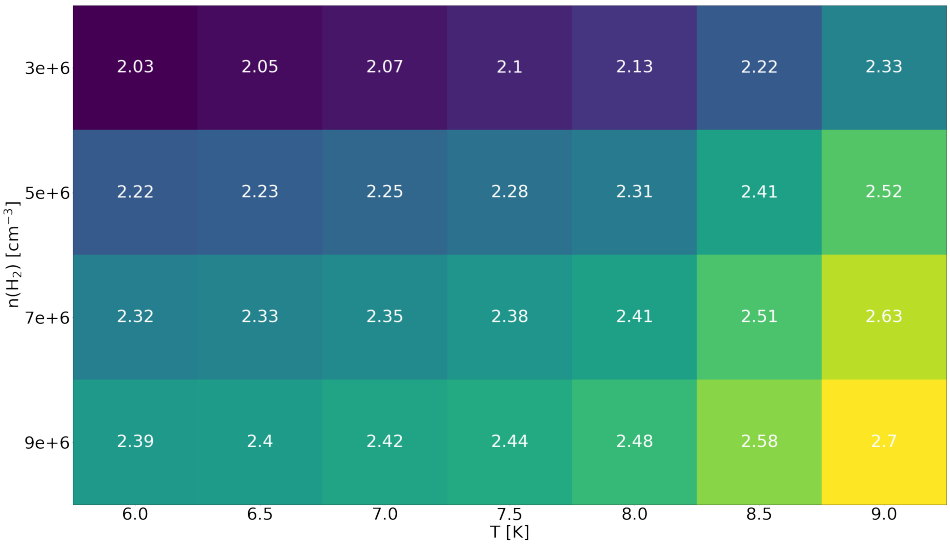

Figure C.4: Heatmap of the abundance ratio of CH_2DOH over CH_3OH for a parameter grid with $n(H_2)$ between 3×10^6 cm^{-3} to 9×10^6 cm^{-3} and T_{gas} and T_{grain} between 6.0 K and 9.0 K.

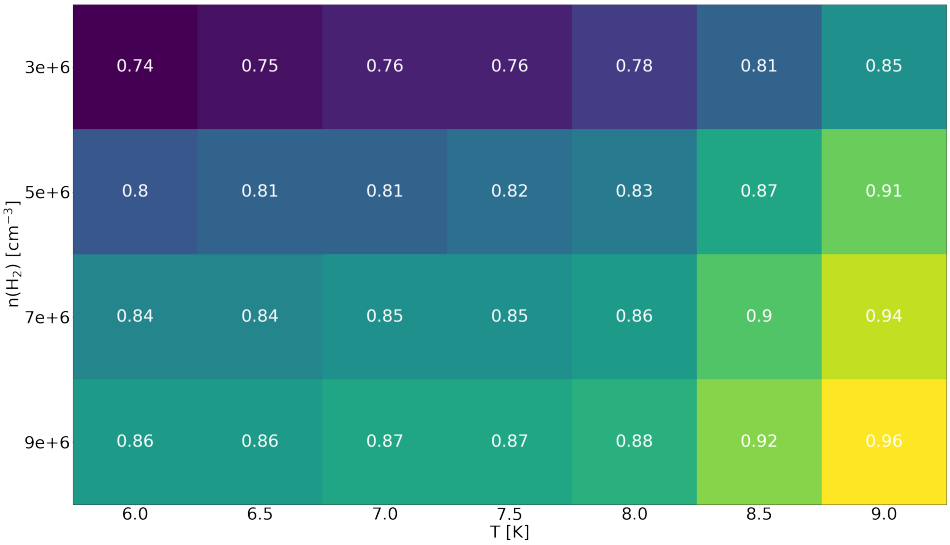

Figure C.5: Heatmap of the abundance ratio of CHD_2OH over CH_2DOH for a parameter grid with $n(H_2)$ between 3×10^6 cm^{-3} to 9×10^6 cm^{-3} and T_{gas} and T_{grain} between 6.0 K and 9.0 K.

Bibliography

Aikawa, Y., Wakelam, V., Hersant, F., et al. 2012, ApJ, 760, 40

Álvarez-Barcia, S., Russ, P., Kästner, J., et al. 2018, MNRAS, 479, 2007

Asplund, M., Grevesse, N., Sauval, A.J., et al. 2009, ARAA, 47, 481

Bacmann, A., Lefloch, B., Ceccarelli, C., et al. 2002, A&A, 389, L6

Bacmann, A., Lefloch, B., Ceccarelli, C., et al. 2003, ApJ Letters, 585, L55

Bacmann, A., Tacquet, V., Faure, A., et al. 2012, A&A, 541, L12

Balucani, N., Ceccarelli, C. & Taquet, V. 2015, MNRAS, 449, L16

Barnard, E.E. 1919, ApJ, 49, 1

Belloche, A., Garrod, R.T., Zingsheim, O., et al. 2022, A&A, 662, A110

Bergin, E.A., Plume, R., Williams, J.P., et al. 1999, ApJ, 512, 724

Bergin, E.A., Alves, J., Huard, T., et al. 2002, ApJ Letters, 570, L101

Bergin, E.A. & Tafalla, M. 2007, ARAA, 45, 339

Bertin, M., Romanzin, C., Doronin, M., et al. 2016, ApJL, 817, L12

Bizzocchi, L., Caselli, P., Spezzano, S. et al. 2014, A&A 569, A27

Bonnor, W.B. 1958, MNRAS, 118, 523

Boogert, A.C.A., Gerakines, P.A. & Whittet, D.C.B. 2015, ARA&A, 53, 541

Borshcheva, K., Fedoseev, G., Punanova, A.F., et al. 2025, accepted in ApJ

Boschman, L., Cazaux, S., Spaans, M., et al. 2015, A&A, 579, A72

Bovino, S. & Grassi, T. (edited), 2024, Astrochemical Modeling, Pratical Aspects of Microphysics in Numerical Simulations, Elsevier Inc.

Bovolenta, G., Bovino, S., Vöhringer-Martinez, E., et al. 2020, Mol.Astr., 21, 100095

Brown, P.D., Charnley, S.B. & Millar, T.J. 1988, MNRAS, 231, 409

Caselli, P., Walmsley, C.M., Terzieva, R., et al. 1998, ApJ, 499, 234

Caselli, P., Walmsley, C.M., Tafalla, M., et al. 1999, ApJ Letters, 523, L165

Caselli, P., Walmsley, C.M., Zucconi, A., et al. 2002, ApJ, 565, 344

Caselli, P. & Ceccarelli, C. 2012, Astron Astrophys Rev, 20, 56

Caselli, P., Pineda, J.E., Zhao, B., et al. 2019, ApJ, 874, 89

Caselli, P., Pineda, J.E., Sipilä, O., et al. 2022, ApJ, 929, 13

Ceccarelli, C., Caselli, P., Herbst, E., et al. 2007, Protostars and Planets V, 47

Ceccarelli, C., Caselli, P., Bockelée-Morvan, D., et al. 2014, Protostars and Planets VI, Henrik Beuther, Ralf S. Klessen, Cornelis P. Dullemond, and Thomas Henning (eds.), University of Arizona Press, Tucson, 859

Ceccarelli, C., Caselli, P., Fontani, F., et al. 2017, ApJ, 850, 176

Ceccarelli, C., Codella, C., Balucani, N., et al. 2023, in Astronomical Society of the Pacific Conference Series, 534, Protostars and Planets VII, eds. S. Inutsuka, Y. Aikawa, T. Muto, K. Tomida & M. Tamura, 379

Cernicharo, J., Marcelino, N., Roueff, E., et al. 2012, ApJL, 759, L43

Chacón-Tanarro, A., Caselli, P., Bizzocchi, L., et al. 2019a, A&A, 622, A141

Chacón-Tanarro, A., Pineda, J.E., Caselli, P., et al. 2019b, A&A, 623, A118

Chang, Q., Cuppen, H.M. & Herbst, E. 2007, A&A 469, 973

Chang, Q. & Herbst, E. 2016, ApJ, 819, 145

Chuang, K.-J., Fedoseev, G., Ioppolo, S., et al. 2016, MNRAS, 455, 1702

Chuang, K.-J., Fedoseev, G., Qasim, D., et al. 2017, MNRAS, 467, 2552

Chuang, K.-J., Fedoseev, G., Qasium, D., et al. 2018, ApJ, 853, 102

Cleeves, L.I., Bergin, E.A., Alexander, C.M.O.D., et al. 2014, Science, 345, 1590

Coudert, L.H., Zemouli, M., Motiyenko, R.A., et al. 2014, Journal of Chemical, Physics, 140, 6

Coudert, L.H., Motiyenko, R.A., Margulès, L., et al. 2021, Journal of Molecular Spectroscopy, 318, 111515

Crapsi, A. Caselli, P., Walmsley, C.M., et al. 2005, ApJ, 619, 379

Crapsi, A., Caselli, P., Walmsley, C.M., et al. 2007, A&A, 470, 221

Crovisier, J., Bockelée-Morvan, D., Colom, P., et al. 2004, A&A, 418, 1141

Cruz-Diaz, G.A., Martín-Doménech, R., Muñoz Caro, G.M., et al. 2016, A&A, 592, A68

Cuppen, H.M., van Dishoeck, E.F., Herbst, E., et al. 2009, A&A, 508, 275

Cuppen, H.M., Kristensen, L.E. & Gavardi, E. 2010, MNRAS, 406, L11

Dartois, E., Augé, B., Boduch, P., et al. 2015, A&A, 576, A125

Dartois, E., Chabot, M., Id Barkach, T., et al. 2019, A&A, 627, A55

Draine, B.T. & Bertoldi, F. 1996, ApJ, 468, 269

Draine, B. 2011, Physics of the Interstellar and Intergalactic Medium, Princeton University Press

Drozdovskaya, M.N., Schroeder I, I.R.H.G., Rubin, M., et al. 2021, MNRAS, 500, 4901

Drozdovskaya, M.N., Coudert, L.H., Margulés, L., et al. 2022, A&A, 659, A69

Du, F., Parise, B. & Bergman, P. 2012, A&A, 538, A91

Dulieu, F., Nguyen, T., Congiu, E., et al. 2019, MNRAS, 484, L119

Ebert, R. 1955, Zeitschrift für Astrophysik, 37, 217

Fedoseev, G., Cuppen, H.M., Ioppolo, S., et al. 2015, MNRAS, 448, 1288

Fedoseev, G., Chuang, K.-J., Ioppolo, S., et al. 2017, ApJ, 842, 52

Fedoseev, G., Qasim, D., Chuang, K.-J., et al. 2022, ApJ, 924, 110

Ferrer Asensio, J., Spezzano, S., Coudert, L.H., et al. 2023, A&A, 670, A177

Ferrero, S., Zamirri, L., Ceccarelli, C., et al. 2020, ApJ, 904, 11

Flower, D.R., Pineau des Forêts, G. & Walmsley, C.M. 2004, A&A, 427, 887

Flower, D.R., Pineau des Forêts, G. & Walmsley, C.M. 2006, A&A 449, 621

Fredon, A., Radchenko, A.K. & Cuppen, H.M. 2021, Acc. Chem. Res., 54, 745

Fuchs, G.W., Cuppen, H.W., Ioppolo, S., et al. 2009, A&A, 505, 629

Fuente, A., Navarro, D.G., Caselli, P., et al. 2019, A&A, 624, A105

Furuya, K. & Persson, M.V. 2018, MNRAS, 476, 4994

Furuya, K., Oba, Y. & Shimonishi, T. 2022a, ApJ, 926, 171

Furuya, K., Hama, T., Oba, Y., et al. 2022b, ApJL, 933, L16

Galli, P.A.B., Loinard, L., Bouy, H., et al. 2019, A&A, 630, A137

Gálvez, Ó., Maté, B., Herrero, V.J., et al. 2011, ApJ, 738, 133

Garrod, R.T., Park, I.H., Caselli, P., et al. 2006a, Faraday Discussions, 133, 51-62

Garrod, R.T. & Herbst, E. 2006b, A&A, 457, 927

Garrod, R.T., Wakelam, V. & Herbst, E. 2007, A&A, 467, 1103

Garrod, R.T., Widicus Weaver, S.L. & Herbst, E. 2008, ApJ, 682, 283

Garrod, R.T. & Pauly, T. 2011, ApJ, 735, 15

Garrod, R.T. 2013, ApJ, 765, 60

Garrod, R.T., Jin, M., Matis, K.A., et al. 2022, ApJS, 259, 1

Garrod, R.T. & Herbst, E. 2023, Faraday Discussions, 245, 541

Geppert, W.D., Hellberg, F., Österdahl, F., et al. 2005, Proc. IAU Symp., No. 231

Giers, K., Spezzano, S., Alves, F., et al. 2022, A&A, 664, A119

Giers, K., Spezzano, S., Caselli, P., et al. 2023, A&A, 676, A78

Goldsmith, P.F. & Li, D. 2005, ApJ, 622, 938

Gould, R.J. & Salpeter, E.E. 1963, ApJ, 138, 393

Grassi, T., Bovino, S., Caselli, P., et al. 2020, A&A, 643, A155

Gredel, R., Lepp, S., Dalgarno, A., et al. 1989, ApJ, 347, 289

Grieco, F., Theulé, P., De Looze, I., et al. 2023, Nature Astronomy, 7, 541

Habart, E. Boulanger, F., Verstraete, L., et al. 2004, A&A, 414, 531

Hacar, A., Clark, S.E., Heitsch, F., et al. 2023, in Astronomical Society of the Pacific Conference Series, 534, Protostars and Planets VII, eds. S. Inutsuka, Y. Aikawa, T. Muto, K. Tomida & M. Tamura, 153

Hama, T., Kuwahata, K., Watanabe, N., et al. 2012, ApJ, 757, 185

Harju, J., Pineda, J.E., Vasyunin, A.I., et al. 2020, ApJ, 895, 101

Harju, J., Vastel, C., Sipilä, O., et al. 2024, A&A, 688, A117

Hasegawa, T.I., Herbst, E. & Leung, C.M. 1992, ApJS, 82, 167

Hasegawa, T. & Herbst, E. 1993, MNRAS, 261, 83

He, J., Acharyya, K. & Vidali, G. 2016, ApJ, 823, 56

Herbst, E. & van Dishoeck, E.F. 2009, ARA&A, 47, 427

Herschel, W. 1785, Philos. Trans. Ser., 175, 213

Hidaka, H., Kouchi, A. & Watanabe, N.J. 2007. Chem.Phys. 126, 204707

Hidaka, H., Watanabe, M., Kouchi, A., et al. 2009, ApJ, 702, 291

Hillenbrand, P.-M., Bowen, K.P., Liévin, J., et al. 2019, ApJ, 877, 38

Hillenbrand, P.-M., de Ruette, N., Urbain, X., et al. 2022, ApJ, 927, 47

Hollenbach, D. & Salpeter, E.E. 1971, ApJ, 163, 155

Hugo, E., Asvany, O. & Schlemmer, S. 2009, Journal of Chem. Phys., 130, 164302

Ilyushin, V.V., Müller, H.S.P., Jørgensen, J.K., et al. 2022, A&A, 658, A127

Ilyushin, V.V., Müller, H.S.P., Jørgensen, J.K., et al. 2023, A&A, 677, A49

Ioppolo, S., Fedoseev, G., Chuang, K.-J., et al. 2021, Nat.Astron., 5, 197

Jiménez-Serra, I., Caselli, P., Martín-Pintado, J., et al. 2008, A&A, 482, 549

Jiménez-Serra, I., Vasyunin, A.I., Caselli, P., et al. 2016, ApJL, 830, L6

Jiménez-Serra, I., Vasyunin, A.I., Spezzano, S., et al. 2021, ApJ, 917, 44

Jiménez-Serra, I., Megías, A., Salaris, J., et al. 2025, A&A, 695, A247

Jin, M., & Garrod, R. T. 2020, ApJS, 249, 26

Jones, A.P. & Williams, D.A. 1985, MNRAS, 217, 413

Jørgensen, J.K., van der Wiel, M.H.D., Coutens, A., et al. 2016, A&A, 595, A117

Jørgensen, J.K., Müller, H.S.P., Calcutt, H., et al. 2018, A&A, 620, A170

Kakkenpara Suresh, S., Dulieu, F., Vitorino, J., et al. 2024, A&A, 682, A163

Keto, E. & Caselli, P. 2008, 683, 238

Keto, E. & Caselli, P. 2010, MNRAS, 402, 1625

Keto, E., Caselli, P. & Rawlings, J. 2015, MNRAS, 446, 3731

Kimura, Y., Tsuge, M., Pirronello, V., et al. 2018, ApJL, 858, L23

Kulterer, B.M., Fuente, A., Drozdovskaya, M.N., et al. 2025, accepted for publication in ApJ

Lefloch, B., Bachiller, R., Ceccarelli, C., et al. 2018, MNRAS, 477, 4792

Le Gal, R., Hily-Blant, P., Faure, A., et al. 2014, A&A, 562, A83

Léger, A., Jura, M. & Omont, A. 1985, A&A, 144, 147

Li, D. & Goldsmith, P.F. 2003, ApJ, 585, 823

Lin, Y., Spezzano, S., Sipilä, O., et al. 2022, A&A, 665, A131

Lin, Y., Spezzano, S. & Caselli, P. 2023a, A&A, 669, L6

Lin, Y., Spezzano, S., Pineda, J.E., et al. 2023b, A&A, 680, A43

Linsky, J.L. 2003, Space Science Reviews, 106, 49

Linsky, J.L., Draine, B.T., Moos, H.W., et al. 2006, ApJ, 647, 1106

Manigand, S., Calcutt, H., Jørgensen, J.K., et al. 2019, A&A, 623, A69

Manigand, S., Jørgensen, J.K., Calcutt, H., et al. 2020, A&A, 635, A48

Mangum, J.G. & Shirley, Y.L. 2015, Publications of the Astronomical Society of the Pacific, 127, 266

Martín-Doménech, R., Cruz-Diaz, G.A. & Muñoz Caro, G.M. et al. 2018, MNRAS, 473, 2575

Martín-Doménech, R., Öberg, K.I., Muñoz Caro, G.M., et al. 2024, MNRAS, 535, 807

Mathis, J.S., Rumpl, W. & Nordsieck, K.H. 1977, ApJ, 217, 425

May, P.W., Pineau des Forêts, G., Flower, D.R., et al. 2000, MNRAS, 318, 809

McClure, M.K., Rocha, W.R.M., Pontoppidan, K.M., et al. 2023, Nature Astronomy, 7, 431

McGuire, B.A. 2022, ApJSS, 259, 30

McKee, C.F. & Ostriker, J.P. 1977, ApJ, 218, 148

McKellar, A. 1940, PASP, 52, 187

Minissale, M. & Dulieu, F. 2014, Journal of Chem. Phys., 141, 014304

Minissale, M., Congiu, E. & Dulieu, F. 2016a, A&A, 585, A146

Minissale, M., Dulieu, F., Cazaux, S. & Hocuk, S. 2016b, A&A, 585, A24

Minissale, M., Moudens, A., Baouche, S., et al. 2016c, MNRAS, 458, 2953

Minissale, M., Aikawa, Y., Bergin, E., et al. 2022, ACS Earth Space Chem, 6, 597

Molpeceres, G., Furuya, K. & Aikawa, Y. 2024, A&A, 688, A150

Molpeceres, G., Nguyen, T., Oba, Y., et al. 2025, A&A, 694, A299

Müller, H.S.P., Schlöder, F., Stutzki, J., et al. 2005, Journal of Molecular Structure, 742, 215

Müller, D.R., Altwegg, K., Berthelier, J.J., et al. 2022, A&A, 662, A69

Müller, H.S.P., Garrod, R.T., Belloche, A., et al. 2023, MNRAS, 523, 2887

Oba, Y., Tomaru, T., Lamberts, T., et al. 2018, Nature Astronomy, 2, 228

Öberg, K.I., van Dishoeck, E.F. & Linnartz, H. 2009a, A&A, 496, 281

Öberg, K.I., Linnartz, H., Visser, R., et al. 2009b, ApJ, 693, 1209

Öberg, K.I., Bottinelli, S., Jørgensen, J., et al. 2010, ApJ, 716, 825

Öberg, K.I. & Bergin, E.A. 2021, Physics Reports, 893, 1

Padovani, M., Ivlev, A.V., Galli, D., et al. 2018, A&A, 614, A111

Pagani, L., Salez, M. & Wannier, P.G. 1992, A&A, 258, 479

Pagani, L., Bacmann, A., Cabrit, S., et al. 2007, A&A, 467, 179

Pagani, L., Vastel, C., Hugo, E., et al. 2009, A&A, 494, 623

Parise, B., Ceccarelli, C., Tielens, A.G.G.M., et al. 2006, A&A, 453, 949

Pety, J. 2005, SF2A-2005: Semaine de l'Astrophysique Francaise, Casoli, F., Contini, T., Hameury, J.M., Pagani, L., 721

Pearson, J.C., Yu, S. & Drouin, B.J. 2012, Journal of Molecular Spectroscopy, 280, 119

Pineda, J.E., Harju, J., Caselli, P., et al. 2022, Astronomical Journal, 163, 294

Pineda, J.E., Arzoumanian, D., André, P., et al. 2023, in Astronomical Society of the Pacific Conference Series, Vol. 534, Protostars and Planets VII, ed. S. Inutsuka, Y. Aikawa, T. Muto, K.Tomida, & M.Tamura, 233

Pineda, J.E., Sipilä, O., Segura-Cox, D.M., et al. 2024, A&A, 686, A162

Planck Collaboration, 2014, A&A, 571, A1

Prasad, S.S. & Tarafdar, S.P. 1983, ApJ, 267, 603

Prodanović, Tijana, Steigman, G. & Fields, B.D. 2010, MNRAS, 406, 1108

Punanova, A., Caselli, P., Feng, S., et al. 2018, ApJ, 855, 112

Punanova, A., Vasyunin, A.I., Caselli, P., et al. 2022, ApJ, 927, 213

Punanova, A.F., Borshcheva, K., Fedoseev, G.S., et al. 2025, MNRAS, 537, 3686

Qasim, D., Fedoseev, G., Chuang, K.-J., et al. 2019, A&A, 627, A1

Ratajczak, A., Quirico, E., Faure, A., et al. 2009, A&A, 496, L21

Rawlings, J.M.C., Hartquist, T.W., Menten, K.M., et al. 1992, MNRAS, 255, 471

Redaelli, E., Bizzocchi, L., Caselli, P., et al. 2019, A&A, 629, A15

Redaelli, E., Sipilä, O., Padovani, M., et al. 2021, A&A, 656, A109

Riedel, W., Sipilä, O., Redaelli, E., et al. 2023, A&A, 680, A87

Riedel, W., Sipilä, O., Redaelli, E., et al. 2025, A&A, 701, A291

Robitaille, T.P. & Whitney, B.A. 2010, ApJL, 710, L11

Rocha, W.R.M., van Dishoeck, E.F., Ressler, M.E., et al. 2024, A&A, 683, A124

Ruaud, M., Loison, J.C., Hickson, K.M., et al. 2015, MNRAS, 447, 4004

Santos, J.C., Chuang, Ko-Ju, Lamberts, T., et al. 2022, ApJL, 931, L33

Santos, J.C., Linnartz, H. & Chuang, K.-J. 2023, A&A, 678, A112

Scibelli, S. & Shirley, Y. 2020, ApJ, 891, 73

Scibelli, S., Shirley, Y., Vasyunin, A., et al. 2021, MNRAS, 504, 5754

Scibelli, S., Shirley, Y. & Megías, A., et al. 2024, MNRAS, 533, 4104

Scibelli, S., Drozdovskaya, M.N., Caselli, P., et al. 2025, A&A, 702, A127

Semenov, D., Hersant, F., Wakelam, V., et al. 2010, A&A, 522, A42

Senevirathne, B., Andersson, S., Dulieu, F., et al. 2017, Mol.Astrophys., 6, 59

Shannon, R.J., Blitz, M.A., Goddard, A., et al. 2013, Nature Chemistry, 5, 745

Shingledecker, C.N., Vasyunin, A., Herbst, E., et al. 2019, APJ, 876, 140

Shingledecker, C.N., Lamberts, T., Laas, J.C., et al. 2020, ApJ, 888, 52

Simons, M.A.J., Lamberts, T. & Cuppen, H. 2020, A&A, 634, A52

Sipilä, O., Caselli, P. & Harju, J. 2015a, A&A, 578, A55

Sipilä, O., Harju, J., Caselli, P., et al. 2015b, A&A, 581, A122

Sipilä, O., Caselli, P. & Taquet, V. 2016, A&A, 591, A9

Sipilä, O. & Caselli, P. 2018, A&A, 615, A15

Sipilä, O., Caselli, P. & Redaelli, E., et al. 2019a, MNRAS, 487, 1269

Sipilä, O., Caselli, P. & Harju, J. 2019b, A&A, 631, A63

Sipilä, O., Silsbee, K. & Caselli, P. 2021, ApJ, 922, 126

Sipilä, O., Caselli, P., Redaelli, E., et al. 2022, A&A, 668, A131

Sipilä, O., Caselli, P., & Juvela, M. 2024, A&A, 690, A280

Skouteris, D., Balucani, N., Ceccarelli, C., et al. 2018, ApJ, 854, 135

Spezzano, S., Brünken, S., Schilke, P., et al. 2013, ApJ Letters, 769, L19

Spezzano, S., Bizzocchi, L., Caselli, P., et al. 2016, A&A, 592, L11

Spezzano, S., Caselli, P., Bizzocchi, L., et al. 2017, A&A, 606, A82

Spezzano, S., Caselli, P., Pineda, J.E., et al. 2020, A&A, 643, A60

Spezzano, S., Sipilä, O., Caselli, P., et al. 2022, A&A, 661, A111

Spezzano, S., Riedel, W., Caselli, P., et al. 2025, submitted to ACS

Stahler, S.W. & Palla, F. 2004, The Formation of Stars, WILEY-VCH Verlag GmbH & Co.KGaA, Weinheim

Tafalla, M., Myers, P.C., Caselli, P., et al. 2002, ApJ, 569, 815

Taquet, V., Ceccarelli, C. & Kahane, C. 2012, ApJ, 748, L3

Taquet, V., Charnley, S.B. & Sipilä, O. 2014, ApJ, 791, 1

Taquet, V., Bianchi, E., Codella, C., et al. 2019, A&A, 632, A19

Tinacci, L., Germain, A., Pantaleone, S., et al. 2022, ACS Earth Space Chem, 6, 1514

Tsang, W. & Hampson, R.F. 1986, Journal of Phys. & Chem. Ref. Data, 15, 1087

Tsang, W. 1987, Journal of Phys. & Chem. Ref. Data, 16, 471

van Dishoeck, E.F. 2014, Faraday Discuss., 168, 9

van Gelder, M.L., Tabone, B., Tychoniec, L., et al. 2020, A&A, 639, A87

van Gelder, M.L., Jaspers, J., Nazari, P., et al. 2022, A&A, 667, A136

Vastel, C., Ceccarelli, C., Lefloch, B., et al. 2014, ApJL, 795, L2

Vasyunin, A.I., Sobolev, A.M., Wiebe, D.S., et al. 2004, Astron.Lett., 30, 566

Vasyunin, A.I., Semenov, D., Henning, Th., et al. 2008, ApJ, 672, 629

Vasyunin, A.I., Caselli, P., Dulieu, F. & Jiménez-Serra, I. 2017, ApJ, 842, 33

Vazart, F., Ceccarelli, C., Balucani, N., et al. 2020, MNRAS, 499, 5547

Wakelam, V., Herbst, E., Le Bourlot, J., et al. 2010, A&A, 517, A21

Wakelam, V., Loison, J.C., Herbst, E., et al. 2015, ApJSS, 217, 20

Wakelam, V., Dartois, E., Chabot, M., et al. 2021, A&A, 652, A63

Wakelam, V., Gratier, P., Loison, J.-C., et al. 2024, A&A, 689, A63

Walmsley, C.M., Flower, D.R. & Pineau des Forêts, G. 2004, A&A, 418, 1035

Ward-Thompson, D., Motte, F. & André, P. 1999, MNRAS, 305, 143

Watanabe, N. & Kouchi, A. 2002, ApJ Letters, 571, L173

Watanabe, N., Kimura, Y., Kouchi, A., et al. 2010, ApJL, 714, L233

Watson, W.D. 1974, ApJ, 188, 35

Weber, A.S., Hodyss, R., Johnson, P.V., et al. 2009, ApJ, 703, 1030

Weinreb, S., Barrett, A., Meeks, M., et al. 1963, Nature, 200, 829

Wilson, R.W., Jefferts, K.B. & Penzias, A.A. 1970, ApJ, 161, L43

Wilson, T.L. 1999, Rep. Prog. Phys., 62, 143

Wolf, M. 1923, Astron. Nachr., 219, 109

Yamamoto, S. 2016, Introduction to Astrochemistry: Chemical Evolution from Interstellar Clouds to Star and Planet Formation, Astronomy and Astrophysics Library (Springer Japan)

Zahorecz, S., Jiménez-Serra, I., Testi, L., et al. 2021, A&A, 653, A45

Zuckerman, B. & Palmer, P. 1974, ARA&A, 12, 279

Acknowledgments

In the past four years, my path was accompanied by a group of incredible people, who introduced me to world of science and academia or who, despite not fully understanding what I was doing, gave me their unwavering support.

First to be thanked are my supervisors Paola Caselli, Olli Sipilä and Elena Redaelli. Paola, you offered me the opportunity to begin my research career in astrochemistry, gave me advice and trust and were always eager to discuss science, despite your extremely busy schedule. Olli, you received me as an unexperienced master student fresh from university and shaped me into the scientist I hope to be today. You certainly had to endure the most of my never-ending questions and concerns about the most tiny details of astrochemical modelling and addressed each of them with unbelievable patience. I cannot thank you enough. And Elena, you always gave me your invaluable advice throughout those years. You were always available and ready to discuss modelling, despite it not directly involving telescopes.

A big thank you also to the entire CAS group for creating such a warm atmosphere, in which I always felt welcome. I enjoyed countless lunches, dinners and coffee breaks with interesting conversations and laughter. Special thanks to all the PhD students of the group, especially to my office mate Farideh, that were suffering through a similar experience with me. Your willingness to hear out my complaints about projects, courses and life in general made this journey much more bearable.

I was also incredibly lucky to be surrounded by long-time (and sometimes new) friends that coincidentally ended up in the same city as me. Thanks to Oliver, Emily, Maxi, Stefan, Maya and Pooja for giving me so much opportunity to take my mind of work.

I am especially grateful for my wonderful family being the best support system I could wish for. My parents, who raised me and supplied me with books and other means to nurture my curiosity. My husband Christopher, who has been by my side for almost my entire educational journey, from being a young bachelor student up to now, who readily accompanied me to Munich and without whose constant love and support I would have never been able to finish this PhD. Ich liebe dich. And my son Levi, who is giving me so much joy and laughter, who puts every struggle at work into another perspective and who even offered to finish this thesis for me.